PERTURBATIVE MEASUREMENTS OF ELECTRON CYCLOTRON RESONANCE ION SOURCE PLASMAS

By

Derek Elwin Neben

A DISSERTATION

Submitted to
Michigan State University
in partial fulfillment of the requirements
for the degree of

Physics—Doctor of Philosophy

2019

ABSTRACT

PERTURBATIVE MEASUREMENTS OF ELECTRON CYCLOTRON RESONANCE ION SOURCE PLASMAS

By

Derek Elwin Neben

Heavy ion accelerators are a valuable resource for the nuclear science community to study atomic physics. One such heavy ion accelerator is the Coupled Cyclotron Facility (CCF) at the National Superconducting Cyclotron Laboratory (NSCL) which relies on Electron Cyclotron Resonance (ECR) ion sources to provide the primary beam to the target. ECR ion sources are essential for the efficient operation of research accelerators such as the CCF, providing high currents of highly charged ions. Highly charged ion beams increase the efficiency of the accelerators, but require longer confinement times and higher temperature plasmas in the ion sources than is necessary to produce singly charged beams. The need to use high temperature and low density plasmas creates challenges including those relating to plasma stability. ECR ion sources provide a good platform to accept metallic vapor ovens and sputtering probes allowing the CCF to accelerate up to 30 types of beams ranging from oxygen to uranium. Furthermore, ECR ion sources use no filaments or cathodes providing a high degree of reliability for the accelerator facility. As the intensity frontier demands ever rarer isotopes from accelerator facilities, the heavy ion beam intensity must increase [70], which creates new demands from the ion sources.

The work presented within this dissertation set out to better understand the mechanism that confines highly charged ions in the ECR plasma. Specifically, it was explored if hot electrons ($E_\gamma \gtrapprox 50$ keV) contribute to ion confinement by generating an electrostatic well in the plasma potential [68]. Perturbative measurements of 2^{nd} and 3^{rd} generation ECR

ion sources are presented with the aim to explore ion confinement times: pulsed sputtering (Chapter 4) and amplitude modulation (Chapter 5).

Chapter 3 explores the geometry of the sputtering probe with respect to the magnetic field which was crucial to produce reliable pulsed sputtering results on the ECR ion source. Axial pulsed sputtering, which could be conveniently implemented on 3^{rd} generation fully superconducting sources, incorporated a bias disc effect that highly perturbed the plasma. Radial sputtering was emulated on the 3^{rd} generation source by placing a semi-shielded probe along the plasma chamber wall in between the electron loss surfaces.

Ion confinement time was characterized through the decay time of the beam current, which is proportional to ion confinement time. Ion beam decay times were measured for different charge states of gold in an oxygen plasma in Chapter 4. Decay time always increased with increasing charge state. Decay time also increased with hot electron temperature for lower frequency operation (13 GHz), but reached an optimized value for higher frequency operation (18 GHz) due to plasma instabilities. Electrostatic confinement of ions appeared to be the most plausible mechanism to explain the observed decay time behaviors.

A novel perturbative measurement technique was developed for ECR ion sources using Amplitude Modulation (AM) of microwave power. The AM measurement was originally motivated by whether or not 50 kHz modulation in microwave power (from the microwave source) would be observable in the beam current. A systematic study was organized on the University of Jyväskylä Physics Department (JYFL) 2^{nd} generation ECR ion source in Jyväskylä Finland. Chapter 5 presents the beam current response to AM on the 14 GHz 2^{nd} generation source for different weights of noble gases, magnetic fields, and vacuum pressures. The beam current amplitude generally decayed exponentially for frequencies higher than around 400 Hz with the modulation highly suppressed at 10 kHz.

To my wife Kimberley and my son Wesley who I hope will read at least this part.
Hi Mom and Dad, I hope you read this part too.

ACKNOWLEDGMENTS

I would like to acknowledge foremost Guillaume Machicoane and Daniela Leitner whose continued support was crucial for the generation of the work presented within this dissertation. I would like to acknowledge the generous support from the National Science Foundation award number PHY-1415462, the National Superconducting Cyclotron Laboratory, and Michigan State University which made this work possible. I would like to also acknowledge the support of Olli Tarvainen, Hannu Koivisto, and The Academy of Finland under the Finnish center of excellence program 2012-2017 Project No. 213503 that made possible all of Chapter 5 within this dissertation.

I would like to acknowledge the efforts of the academic advisory committee Norman Birge, Guillaume Machicoane, Steven Lund, Daniela Leitner, and John Verboncoeur whose administrative and editorial support was invaluable. Finally, I would like to acknowledge the many colleagues and advisors not explicitly named earlier whose help made this work possible: Dallas Cole, Jesse Fogleman, Bryan Isherwood, Taneli Kalvas, Risto Kronholm, Alain Lapierre, Kasey Lund, Guy Parsey, Alfonse Pham, Shane Renteria, Jeffry Stetson, Michael Syphers, Larry Tobos, and Dirk Weisshaar. Thank you all very much!

TABLE OF CONTENTS

LIST OF TABLES

LIST OF FIGURES

KEY TO SYMBOLS

θ	Angle
B	Magnetic field
v	Speed
τ_e	Electron Confinement Time
R	Magnetic Mirror Ratio B_{max}/B_{min}
f_{coll}	Collision Frequency
ω_c	Cyclotron angular frequency
q	Charge
γ	Relativistic Lorentz factor
m_e	Electron mass
m_i	Ion mass
λ_d	Debye length
ϵ_0	Vacuum permittivity
k	Boltzmann constant
T_e	Electron temperature
T_i	Ion temperature
e	Unit charge
n_e	Electron density
ω_p	Electron plasma angular frequency
c	Speed of light
$\tilde{E}$	Electric field
ω_{rf}	electromagnetic frequency (applied) angular frequency
r_e	Classical electron radius
f	Frequency
σ	Cross section

L	Length
π	Archimedes' constant
α	Polarizability coefficient
Q	Charge state
μ	Reduced mass
E_{bind}	Electronic binding energy
Λ	Ratio of characteristic interaction radii
r	Radius
f_{e-e}	Electron-electron Spitzer collision frequency
f_{e-i}	Electron-ion Spitzer collision frequency
f_{i-i}	Ion-ion Spitzer collision frequency
Φ	Electrostatic potential
D_i	Ion coefficient of diffusion
A_i	Mass number of the i^{th} ion species
τ_i	Ion confinement time for the i^{th} ion
n_i	Ion density for the i^{th} ion
I_i	Ion current for the i^{th} ion
σ_a	Beam current emission area
δ_i	Source rate increasing i^{th} ion density from ionization
ϵ_i	Source rate increasing i^{th} ion density from charge exchange
ζ_i	Effective sink rate decreasing the density of the i^{th} ion
τ_{im}	Measured decay time of the i^{th} ion
X	Element undergoing a reaction

KEY TO ABBREVIATIONS

LINAC	LINear ACcelerator
ECRIS	Electron Cyclotron Resonance Ion Source
LBNL	Lawrence Berkeley National Lab
ATLAS	Argonne Tandem Linear Accelerator System
CCF	Coupled Cyclotron Facility
NSCL	National Superconducting Cyclotron Laboratory
FRIB	Facility for Rare Isotope Beams
ECR	Electron Cyclotron Resonance
MSU	Michigan State University
SuSI	Superconducting Source for Ions
CSD	Charge State Distribution
CW	Continuous Wave (steady state)
AM	Amplitude Modulation
ANL	Argonne National Laboratory
EEDF	Electron Energy Distribution Function
IEDF	Ion Energy Distribution Function
JYFL	Jyväskylän Yliopiston Fysiikan Laitos (University of Jyväskylä Physics Department)
FFT	Fast Fourier Transform

Chapter 1

Introduction

This dissertation studies plasma characteristics of ion sources dedicated to supplying high charge state and high intensity ion beams for research accelerators. Positively charged atoms or molecules ionized from physical, chemical, or nuclear reactions (commonly known as ions) play a wide role in contemporary accelerators driving discovery and industry. In the manufacturing of contemporary semiconductor technology ions are implanted into substrate wafers using ion beams in the KeV range as discussed in Ref. [12]. Ion beams are also used to propel satellites and space vehicles with ion engines. Ion engines typically provide less than a newton of thrust (see Ref. [19]) but can be highly efficient for their weight as compared to chemical engines. Ions are also useful in contemporary medicine where short lived radioactive isotopes such as ^{18}F, the most requested for positron emission tomography, are produced with ion beams (typically proton beams) [7]. Beams of ions have contributed greatly to fundamental scientific knowledge, famously, the nucleus was discovered by the use of MeV He^{2+} produced from the radioactive decay of radon scattering off a thin foil in Ref. [76]. All of these uses for ions require some mechanism or machinery to produce them. Some ions such as protons and helium nuclei can be produced from radioactive decay, while heavier ions such as boron, commonly used to dope some semiconductor substrates, need to be produced through chemical reactions. Most heavy ions are not found from natural sources (radioactive decay) and so they are produced with ion sources.

The earliest ion sources for research accelerator applications which were sources such as the Penning ion source [17], relied on a plasma discharge between a cathode and anode to produce ions. These sources wear out quickly due to electrode erosion requiring replacement on a regular basis. The Electron Cyclotron Resonance (ECR) ion source was developed, in part, to increase reliability of ion sources for accelerators and was an application of magnetically confined fusion research with mirror machines [18]. ECR ion sources have the added benefit that the lower vacuum pressures and the efficient ECR heating process allowed for the production of high intensity beams of highly charged ions. ECR ion sources see continued development and are used to supply heavy ion accelerators because of their ability to provide large currents, relative to competing technologies, of highly charged ions. Furthermore, ECR ion sources can be operated in pulsed modes for injection into synchrotrons such as at CERN in Ref. [28], and for steady state operation as at the National Superconducting Cyclotron Laboratory (NSCL) [36].

Accelerator technologies such as cyclotrons and LINear ACcelerators (LINACs) are based on the use of synchronized harmonically varying radio frequency voltages (in time) to accelerate charged particles such as ions. In the case of protons and electrons, the beam energy gain is limited by the accelerating structures. For example, the final beam energy of a LINAC is determined by the type, quantity, and operating electric field of the accelerating cavities. In the case of cyclotrons, the final beam energy is determined by the maximum magnetic field the bending dipole magnet produces. In either case, the physical structure of the accelerator defines the total cumulative electric field the particles witness traveling in the accelerator. The beam energy of LINACs and cyclotrons can be increased on an existing machine by using multiply charged ions. In this case, the beam energy scales as the ion charge state Q for LINACs and Q^2 for cyclotrons. Therefore there is a strong incentive to use highly charged

ions to increase existing accelerator efficiency and to reduce the overall cost of accelerator designs (see Ref. [18]). Highly charged ions are produced by stripping as many electrons from the nucleus as possible but this requires specialized ion sources. Electron Cyclotron Resonance Ion Sources (ECRIS) are capable of providing high intensity highly charged ion beams and, at the time of writing, are used as injector source for the 88 inch cyclotron at Lawrence Berkeley National Lab (LBNL) [100], the Argonne Tandem Linear Accelerator (ATLAS) [78], The Cyclotron Institute at Texas A&M University [98], and the Facility for Rare Isotope Beams (FRIB) [50], in the United States.

Highly charged ions are produced efficiently by stepwise ionization from collisions with free electrons, but the probability to ionize an atom decreases with increasing charge state [43]. Therefore, in order to produce highly charged ions they need to have a long interaction time with the electrons. Ions need long confinement times to become highly charged. Experiments in Ref. [47] on a 3^{rd} generation superconducting ECR ion source found that an oxygen plasma, when optimized for O^{7+} beam current, preferred a magnetic field generating a higher hot electron temperature than when optimized for O^{6+} beam current. Hot electrons ($E_\gamma \gtrapprox 50$ keV) are long lived in the plasma and largely non-collisional so they do not play a significant role in ionization. The increased O^{7+} beam current performance may have been the result of increased ion confinement due to hot electrons. The idea that hot electrons contribute to ion confinement is a well established concept. C. Petty et al. in Ref. [68] posed that the well-confined hot electrons ($T_e = 450$ keV) in the ECR plasma created a small (15 V) electrostatic well to describe ion confinement time measurements with oxygen on the Constance-B quadrupole mirror. The electrostatic ion confinement model has been used to quantitatively model ECR plasmas in Refs. [83, 56]. However, measurement of ion confinement on the Caprice ECR ion source by G. Douysset et al. in Ref. [9], for argon

charge states, suggested a diffusion model instead of an electrostatic one.

The work presented within this dissertation set out to probe the mechanism of ion confinement in an ECR ion source. In particular, we set out to correlate the presence of hot electrons to increased ion confinement in the ECR plasma. Hot electrons are produced naturally in the ECR heating process and are generally observed in coincidence with the best performances of highly charged ions. The latest 3^{rd} generation ECR ion sources are fully superconducting designs and are vulnerable to intense x-ray radiation. The x-rays create a heat load on the heat sensitive cryogenic magnetic coils. Techniques to shield the x-rays from the magnets include tantalum cylinders such as that used on the VENUS ECR ion source which is 2 mm thick [44]. Such heavy metal shielding is effective at stopping low energy x-rays but is expensive and increases the distance between the plasma chamber wall and hexapole magnet decreasing the radial magnetic confinement field available. If hot electrons are necessary for good confinement of ions, then x-ray heating needs to be considered when designing superconducting ECR ion sources.

An introduction to basic physical processes governing ECR ion sources is provided in Chapter 2 along with descriptions of the ECR ion sources used in this dissertation. Chapter 3 discusses the development of the pulsed sputtering method on a 3^{rd} generation superconducting ECR ion source. The placement of the sputtering probe with respect to the magnetic field was important to minimize excessive perturbation of the plasma. Systematic pulsed sputtering experiments are presented in Chapter 4. The results are discussed within the context of ion confinement in Sect. 4.4. A novel perturbative measurement method is presented in Chapter 5. Designed to probe ion confinement, the technique appeared to probe electron processes and is discussed in Sect. 5.6.

Chapter 2

Fundamental Physics and Experimental Systems

2.1 Introduction to ECR Ion Sources

ECR ion sources can range in size and complexity from permanent magnet 2.45 GHz sources commercially available that are about 13 cm long [65] to custom built fully superconducting designs for research accelerators such as VENUS at LBNL [40] that are the size of a car. Each of these sources, although different in design and intended function are built upon the same operating principles. The work presented in this dissertation was focused on ECR ion sources for heavy element highly charged ion beam production where processes such as ion confinement play a more significant role than for smaller sources designed around high intensity low charge state beam production. Section 2.2 and Sect. 2.3 provide an introduction to the reader unfamiliar with ECR plasmas through the example of an 18 GHz ECR ion source operating with hydrogen. Section 2.4 outlines some of the tools available to the experimenter on 2^{nd} and 3^{rd} generation ECR ion sources. Section 2.5 discusses the specific ECR ion sources used during the experiments presented in Chapter 3 and Chapter 4 of this dissertation, while Sect. 2.6 provides an overview of the experimental apparatus used.

2.2 Basic Plasma Properties

2.2.1 Electron Confinement

The magnetic mirror problem is well known and will be briefly covered here, a more thorough treatment is available from Ref. [6]. Assuming the charged particle moves adiabatically in the magnetic field, the magnetic flux contained within a gyro-orbit is conserved. The particle trades longitudinal velocity for rotational velocity when moving from a region of low to high magnetic field. Some particles in velocity phase space have the right initial conditions to be stopped and reflected back in the high magnetic field region. In the case of a simple magnetic mirror (without additional multipole fields) and particles born at the magnetic minimum the line separating unbound and bound motions is described by

$$sin(\theta) = \sqrt{\frac{B_{min}}{B_{max}}} = \frac{v_{\perp}}{v}, \tag{2.1}$$

where θ is the angle in velocity space separating between confined and unconfined electrons, B_{max} the maximum magnetic field, B_{min} the minimum magnetic field, $v_{\perp}$ particle velocity perpendicular to the magnetic field line (gyro motion), and v the magnitude of the particle velocity. In the plasma, collisions between charged particles and between charged particles and neutral gas redistribute velocities amongst particles leading to finite confinement life-times. The electron confinement time for a simple magnetic mirror may be estimated using the Pastukhov theory of confinement in a magnetic bottle [66] applied to electrons in an ECR ion source [79]:

$$\tau_e = 1.48 \frac{\ln R + \sqrt{\ln R}}{f_{coll}}, \tag{2.2}$$

R is the mirror ratio $R = B_{max}/B_{min}$, and f_{coll} the total electron collision frequency. Mirror ratios at extraction for ECR ion sources typically provide the best performance when in the range between 1.8 and 3.2 [29], R=2.7 is used to estimate electron confinement times (corresponding to the value used for 18 GHz operation with B_{min}/B_{ecr}=0.7 in Chapter 4). For a Maxwellian distribution of energies with temperature of 5 keV the total electron collision frequency is about $f_{coll} = 110$ Hz which would result in electron confinement times at extraction of τ_e=25 ms. Similarly, for an EEDF temperature of 50 keV the total collision frequency is approximately $f_{coll} = 15$ Hz resulting in confinement times of τ_e=200 ms. Classical electron collision frequencies for ECR ion sources are estimated in Sect. 2.3.3.

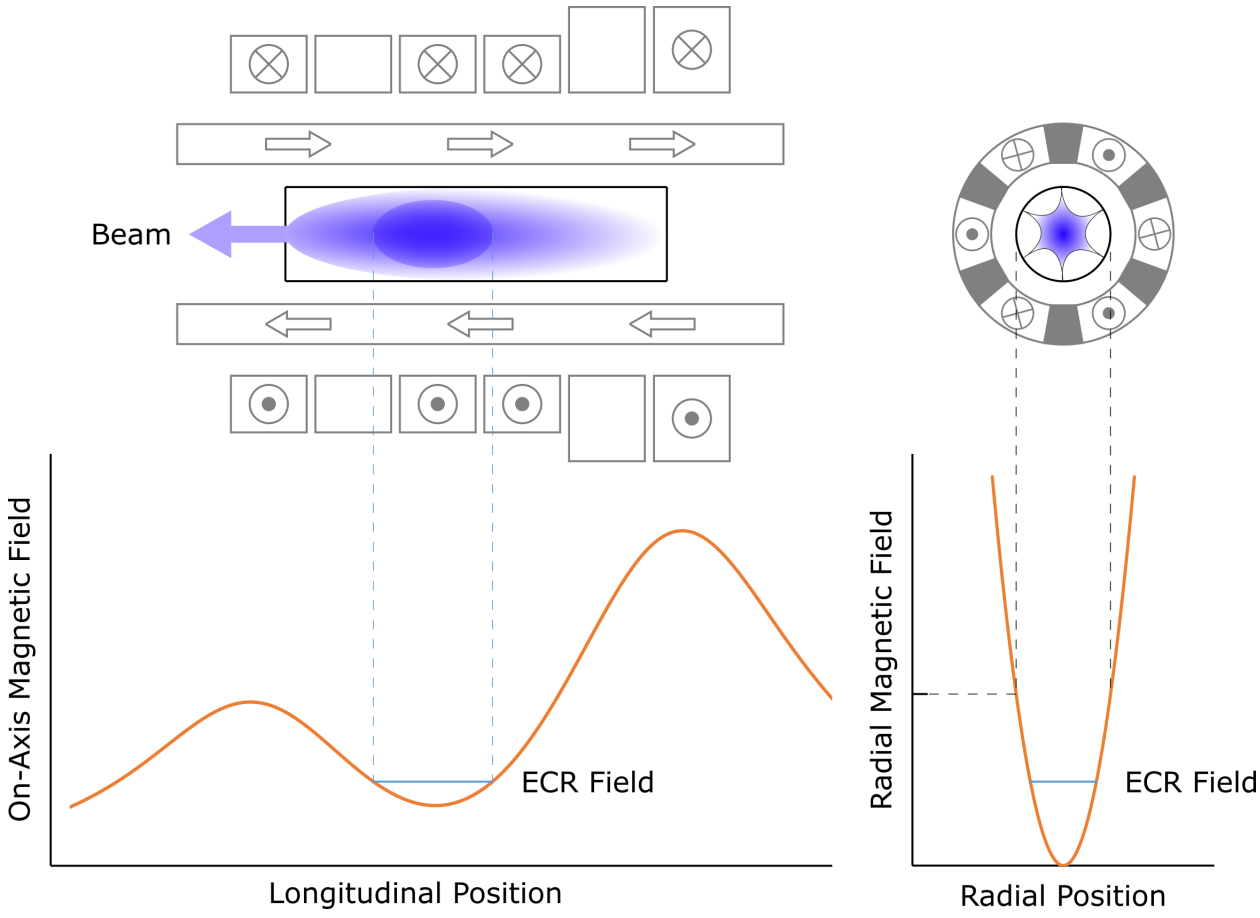

Figure 2.1: Schematic of the magnetic field of an ECR ion source in reference to the coils generating the field. Labeled are the plasma chamber wall and cold electron resonance zone.

The magnetic mirror works well to confine particles along the axis of solenoids but the particles are free to diffuse radially. The magnetic field retards the diffusivity of charge particles, classically [6], as $D \propto 1/B^2$ or as demonstrated by D. Bohm in Ref. [38], as $D \propto 1/B$. The radial diffusivity of the particles are maximized at the minimum magnetic field necessary to confine particles axially. The solution is to add a multipole magnetic field to reduce the diffusivity of particles particularly in the region where the solenoidal field is minimized. The superposition of the two magnetic fields is referred to as a minimum-B configuration because the magnetic field strength increases in all directions from a minimum. Higher order transverse multipoles generate fields that increase more rapidly with radius but require higher coil current densities. Most ECR ion sources use a hexapole magnet to maximize the magnetic field strength and for reasons of beam formation [18]. The sextupole magnet suppresses radial losses of electrons increasing electron density, and modifies the loss cone from a purely symmetric mirror.

2.2.2 Electron Cyclotron Resonance Heating

The electron confinement minimum-B magnetic field in ECRIS provides a convenient setting to heat electrons using Electron Cyclotron Resonance (ECR). An electron in a magnetic field will gyrate at the cyclotron frequency as a function of the local magnetic field and electron kinetic energy with the well-known relation:

$$\omega_c = \frac{qB}{\gamma m_e}. \tag{2.3}$$

Here, γ is the usual relativistic gamma factor, and B is the magnitude of the local magnetic field. For the case of a cold electron ($\gamma = 1$) in a 0.5 T magnetic field (a typical field value

in ECRIS) the rotational frequency of the electron is 14 GHz leading to the widespread use of microwave generators commercially developed for use in radar and communications applications. Conveniently, the electromagnetic plane waves produced by magnetrons and klystrons are composed of right-hand and left-hand circulating components in linear superposition [69] allowing for one of the wave components to efficiently resonate with electrons if the radiation is injected parallel to the magnetic field. Most microwave generators provide useful amplitudes for only a single operating frequency, or in some special cases such as traveling wave tubes, the frequency is tunable within a narrow operating range. Therefore, in practice the experimenter typically selects the frequency and the electrons deposit energy on resonant surfaces by the magnetic field geometry.

Electrons undergo resonance with the co-circulating electric fields for a specific energy and magnetic field, and with the right phase allowing for energy transfer from the microwave field to increase the particle rotational energy. However, other phases extract energy from the electron increasing that of the electromagnetic wave. For electrons moving in a mirror trap the random phase walk between ECR surfaces will, on average, lead to heating even though cooling may occur locally in time [33, 74]. ECR heating combined with the minimum-B magnetic field configuration leads to a favorable electron confinement condition where heating pushes the electrons further into the confinement condition described in Eq. (2.1). This effect results in an "ECR plug" [18] where electrons reflect preferentially off a narrow band of magnetic fields about the ECR field.

Stochastic ECR heating stops above a certain energy limit where the electron energy becomes oscillatory in the case of a magnetic mirror [33]. Estimation of the energy electron limit for long heating times was made by M. Lieberman et al. in Ref. [42]. In particular, the ECR zone length was a key parameter to estimate the energy limit for stochastic

ECR heating. However, as demonstrated in Chapter 4 Sect. 4.3.1, the highest energy electrons measured within this dissertation on the SuSI source were sufficiently energetic that there existed no closed ECR surface (according to magnetic field calculations). One such explanation for these relativistic electrons with no closed ECR surface is the magnetic autoresonance effect [20] or the gyrac effect [18] named after the proposed electron accelerator The Gyrac [21]. In magnetic autoresonance, an electron undergoing ECR heating at a fixed RF frequency in a time increasing magnetic field may (based on initial phase with the RF) become phase locked [22] as the relativistic mass of the electron increases with the magnetic field. The fundamental limit in electron energy due to the balance between the synchrotron radiation damping force and the resonant acceleration is found in Ref. [21] to result in a maximum relativistic γ of:

$$\gamma_{max} = \sqrt[4]{2.68 \cdot 10^8 \ \tilde{E}(kV/cm) \ \lambda^2(cm) \ < \cos\theta >}. \tag{2.4}$$

This theoretical limit from the radiation force far exceeds the highest electron energies observed for ECR ion sources. For example the SuSI source operating at 18 GHz and with 200 W transmitted into the 100 mm diameter plasma chamber resulting in an approximate electric field amplitude inside the plasma chamber of 44 V/cm (found assuming a uniform plane wave) produces an absolute electron energy limit of 44 MeV according to Eq. 2.4. The relativistic electron radius at that energy (44 Mev) at a typical peak injection magnetic field strength of 2.55 T is 50 mm, so 44 MeV is possible, but highly unlikely to form in the plasma chamber due to electron interaction with the chamber. Typical electron energies for SuSI were measured in Chapter 4 Sect. 4.3.1 to fall in the 100s of kiloelectronvolt range.

If autoresonance is the limiting mechanism responsible, then the practical electron energy

limit in ECR ion sources is determined by the destruction of the electron phase locking with the electric field

$$\frac{dB}{dt} \leq \omega_{rf} \frac{\tilde{E} \cos\theta}{c}, \tag{2.5}$$

where θ is the phase angle between electron and RF electric field $\tilde{E}$, c the speed of light in vacuum, and ω_{rf} the RF angular frequency. If the electron is completely in phase with the electric field (highest electron energy scenario) then $\cos\theta = 1$. Equation 2.5 specifies the smallest magnetic field rate of change where electrons experience phase locking. In ECR ion sources the magnetic field is static but spatially varying, the electron "sees" the magnetic field as time varying by the particle's movement in the magnetic field. The electron must slip out of autoresonance in regions such as the two maxima in Fig. 2.1 because $dB/dx \to 0$ resulting in $dB/dt \to 0$ no longer satisfying the phase stability condition in Eq. 2.5. Electrons off the ideal phase will slip out of autoresonance sooner and reach lower energies due to the reduced electric force.

Autoresonance is a good candidate to explain the highest energy electrons observable in the plasma, however the exact nature of the Electron Energy Distribution Function (EEDF) as a whole in "steady state" is, at the time of writing, an active area of research [58, 73, 32]. Frequently, the EEDF is approximated as Maxwellian with a temperature in the keV to tens of keV range [81, 56], a bi-Maxwellian EEDF [79], or a tri-Maxwellian [83]. Non-Maxwellian EEDFs are proposed as being more physical such as the superadiabatic [73] or domed EEDF suggested in Ref. [58]. For the purposes of estimating plasma parameters for an 18 GHz ECR ion source within this chapter, the EEDF will be approximated as bi-Maxwellian with a warm population responsible for plasma shielding, ionization, and maintaining charge neutrality at 5 keV, and a hot largely non-interacting hot population with a temperature around 50 keV

responsible for ion confinement.

2.2.3 Plasma Frequency

Like a classical harmonic system, plasmas undergo oscillations when perturbed. The characteristic frequency of collective plasma oscillations for cold plasmas are described by the plasma frequency [6]:

$$\omega_p = \sqrt{\frac{n_e e^2}{\epsilon_0 m_e}}. \tag{2.6}$$

Here, m_e is the electron mass and ω_p is described in units of radians per second. For externally applied right hand circularly polarized electromagnetic waves with propagation vector parallel to an externally applied magnetic field, the electromagnetic waves will be reflected when the plasma frequency equals the electromagnetic frequency [6]. This effect allows estimation of electron density in ECRIS for a fixed operating frequency [18]. ECR ion sources considered herein typically operate in the 10-28 GHz range. Consequently, rearranging Eq. 2.6 for electron density and using a fixed frequency $\omega_p = \omega_{rf}$ the electron densities n_e are limited by $8 \cdot 10^{10}$ particles/cm^3 and $6 \cdot 10^{11}$ particles/cm^3 respectively. It is unlikely these densities are reached for operational ECR ion sources because extracted beam currents have not been found to saturate even for the most intense applied microwave powers studied [47, 89] suggesting the critical density has not been reached or other microwave coupling mechanisms contribute to sustain the plasma. The cold plasma frequency is a useful tool to estimate electron density, albeit one that should be taken with a grain of salt because ECR plasmas are not cold nor do they appear to saturate with microwave power.

2.2.4 Debye Length

In addition to electron temperature and density, the Debye length or plasma screening length is often used to characterize the plasma. Like a conductor, plasmas screen out external electric fields and the characteristic screening length is known as the Debye length described in Ref. [6]:

$$\lambda_d = \sqrt{\frac{\epsilon_0 k T_e}{n_e e^2}}. \tag{2.7}$$

Here, ϵ_0 is the vacuum permittivity constant, k is the Boltzmann constant, T_e the electron temperature, n_e electron density, and e the unit charge. Equation 2.7 is derived considering a test charge perturbing a homogeneous, quasi neutral, fully ionized plasma with the electron temperature much larger than the ion temperature and massive ions are considered to be effectively static [6]. A perfect electrical conductor has a Debye length of zero. A typical Debye length in an 18 GHz ECR ion source may be estimated with electron density of $2.5 \cdot 10^{11}$ cm^{-3} (estimated in Sect. 2.2.3) and warm electron temperature of 5 keV (covered in Sect. 2.2.2) the Debye length is 1 mm.

2.3 Particle Collisions

Collisions between plasma particles are particularly important for ECR ion sources. Elastic collisions preserve the plasma particles but change the direction of the particle impacting the velocity distribution (leaving the total energy fixed). Inelastic collisions such as ionization and charge exchange are responsible for producing the highly charged ions useful for accelerators. Inelastic collisions can involve both the creation or destruction of particles (ionization and charge exchange) and involve free electrons doing work against the the electronic bind-

ing energy in the case of ionization, and ions gaining kinetic energy in the case of charge exchange [57]. Collisions can be characterized by the collision frequency,

$$f = n\langle \sigma v \rangle, \tag{2.8}$$

where the collision cross section σ is averaged over the collision velocity v via the distribution of velocities in the system and then multiplied by the density n.

2.3.1 Stepwise Ionization

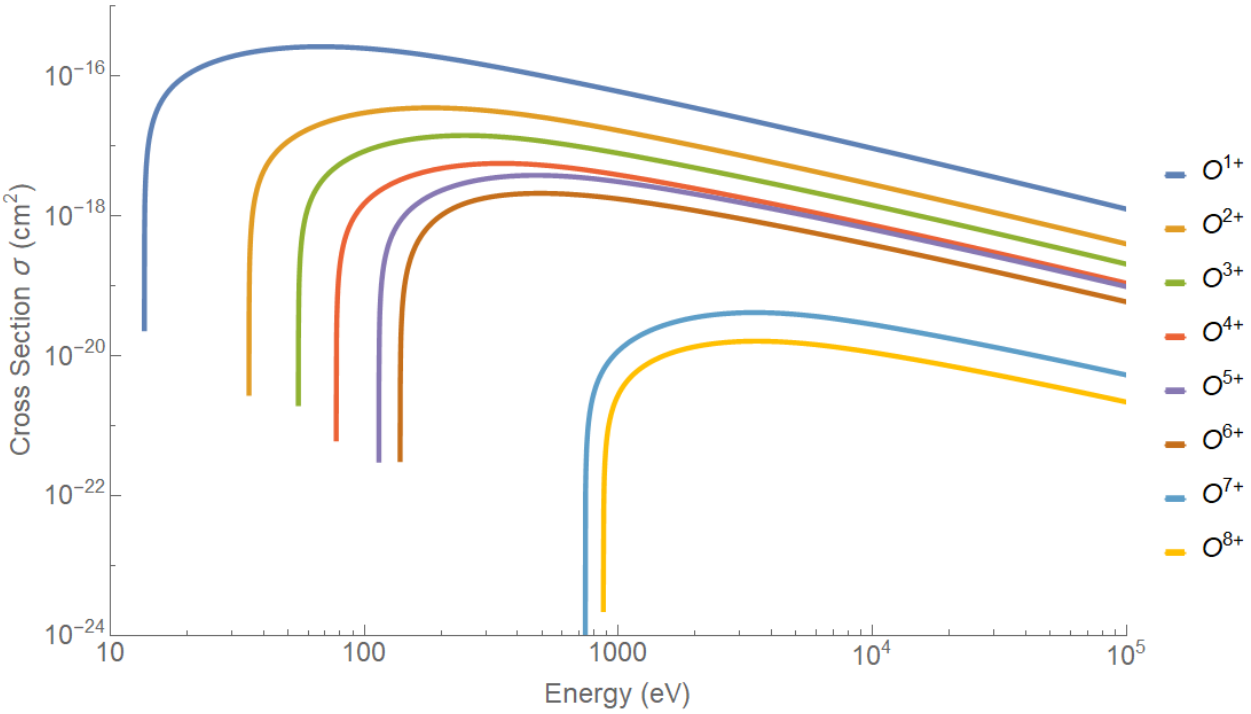

Figure 2.2: Single impact ionization cross sections using the formula and tabulated values from Ref. [43] for monatomic oxygen.

Stepwise ionization involves a collision and energy exchange between a free electron and an ion or neutral resulting in a new free electron and ion. The probability of the reaction taking place, often denoted as a cross section, is dependent on the collision energy and

the electronic structure of the reactants. Stepwise ionization cross sections are shown for monatomic oxygen in Fig. 2.2. Note how there is no probability for ionization if the collision energy is below the binding energy of the electron. It is necessary for the ionization reaction to occur for the free electron kinetic energy to be at least the binding energy of the relevant charge state. The largest cross sections for stepwise ionization are generally found to occur at around three times the binding energy of the bound electron. Therefore for efficient production of O^{6+}, for example, free electron energies should be 100s of eV to keV range. Electrons at higher charge states of the electronic structure become more tightly bound by the nucleus and the ionization cross section decreases. Consequently, highly charged ions have a lower probability for ionization at any collision energy than any previous charge state (see Fig. 2.2). Therefore, to push the ion Charge State Distribution (CSD) to higher charge states the ions need to spend a maximum amount of time in the region where ionization is taking place in addition to having collision energies above the binding potential of the desired charge state. Equally important, the electrons doing ionization should be dense to increase the rate of the reaction. As shown in Eq. 2.8, the ionization reaction frequency is proportional to the electron density so the highest electron density possible is desirable for production of highly charged ions. The electron density is increased in many ECR ion source plasmas by use of magnetic field configurations discussed in Sect. 2.2.1.

2.3.2 Charge Exchange for Highly Charged Ions

Charge exchange is one of the inverse processes to ionization, but is only applicable to ions (ionized atoms or molecules). Ions colliding with neutral gas may pull an outer shell electron off the gas molecule to reduce the charge state of the ion and ionize the neutral gas molecule. Frequently in ECR ion sources, charge exchange takes place with highly charged ions where

the products of the reaction are both positively charged. In this case, the difference in binding energy of the ion state is traded between ions increasing the kinetic energy of the system. The products of the reaction also Coulomb repel.

Charge exchange cross sections for collision velocities less than 10^5 cm/s may be estimated by half the Langevin capture cross section in Ref. [14]:

$$\sigma = \frac{1}{2}\sqrt{\frac{\pi\alpha Q e^2}{\epsilon_0 \mu v^2}}. \tag{2.9}$$

Here, α is the polarizability coefficient of the neutral molecule, μ the reduced mass, v the magnitude of the collision velocity, and Q the charge state. Quantum mechanical effects must be considered for velocities larger than 10^5 cm/s [14] with the cross section converging to a constant. Charge exchange cross sections were measured in Ref. [60] for noble gas systems with impact energies in the keV to hundreds of keV range finding the cross sections to be constant and following the empirical relation

$$\sigma[cm^2] = 1.43 \cdot 10^{-12} Q^{1.17} E_{bind}^{-2.76}[eV]. \tag{2.10}$$

This reaction depends only on the charge state Q and the first ionization potential of the neutral particle E_{bind}. The ions in ECRIS are believed to be in thermal equilibrium because they are not heated directly by the RF and have large collision frequencies (see Sect. 2.3.3). Ion temperature estimates range from a few tens of meV [57] to eVs [58, 55] for steady state. The most probable speeds for an oxygen atom thermalized at 10 meV and 3 eV are $4 \cdot 10^4$ cm/s and $6 \cdot 10^5$ cm/s respectively. These speeds are low enough where the velocity dependence of the collision should be considered.

2.3.3 Long Range Collisions

One consequence of interacting via Coulomb force is that particles preferentially deflect by small angles at long range. The cross section of a single test charged particle "1" colliding with many other charged particles "2", the cross section over a 90° angle from Ref. [18] is

$$\sigma_{90^\circ} = \frac{\ln \Lambda}{2\pi} \left(\frac{Q_1 Q_2 e^2}{\epsilon_0 \mu \langle v \rangle^2} \right)^2, \tag{2.11}$$

where $\langle v \rangle$ is the average collision speed, μ the reduced mass, and $\ln \Lambda = \ln r_{max}/r_{min}$ is the Coulomb logarithm defined by the distance of closest approach r_{min} and the distance where the Coulomb force becomes significant r_{max}. Frequently, collective values of r_{max} and r_{min} defined by plasma properties are used. Often the Debye length is used for r_{max}, and for r_{min} the classical limit for distance of closest approach is taken with:

$$r_{min} = \frac{2 Q_1 Q_2 e^2}{4\pi \epsilon_0 \mu v^2}. \tag{2.12}$$

A characteristic collision frequency can then be calculated using $f_{90^\circ} = n_2 \sigma_{90^\circ} \langle v \rangle$ with n_2 the total density of "2" particles participating in the collisions. The collision frequency depends on the charge and mass of the interacting particles making collision frequencies distinct between plasma species. A convenient expression for Spitzer collision frequency may be found in Ref. [8] for Maxwellian distribution functions:

$$f_{e-e}[Hz] \approx 5 \cdot 10^{-6} \frac{n_e[cm^{-3}] \ln \Lambda}{T_e^{3/2}[eV]}. \tag{2.13}$$

Considering an estimated electron temperature $T_e = 5$ keV with density $2.5 \cdot 10^{11}$ cm^{-3} electron-electron collisions would have an average Coulomb logarithm of $\Lambda = 22$ and undergo about $f_{e-e} = 76$ Hz. This number is small because the average is skewed by a large number of largely non-interacting hot electrons. For cold electrons (≈ 1 eV) with a similar density, the electron-electron collision frequency is about 140 MHz meaning that cold electrons may undergo on average about 130 gyro cycles at the resonance frequency (18 GHz) before undergoing a collision with another electron. As the electron temperature drops below around 1 eV in ECR ion sources the electron-electron collision frequency increases rapidly approaching and exceeding typical gyro frequencies in the magnetic field.

Ion-electron and ion-ion collision frequencies are in general more complicated because the long-range 90° collision cross section must be summed over each unique ion species accounting for particle weight and charge. The total electron-ion collision frequency f_{e-i} for a multi-species plasma is described in Ref. [55] simplified for a constant Coulomb logarithm

$$f_{e-i}[Hz] \approx 3.2 \cdot 10^{-9} \frac{\ln \Lambda_{e-i}}{T_e^{3/2}[eV]} \sum_j \frac{1}{A_j} \sum_k n_k[cm^{-3}] Q_k^2, \tag{2.14}$$

where A_j is the mass number of the j^{th} ion species, and the contributions from each of the k^{th} charge states Q_k are accounted for. The Coulomb logarithm $\ln \Lambda_{e-i}$ is a composite value for interactions between electrons and ions in the plasma. A simpler single species ion-electron collision frequency from Ref. [8] is:

$$f_{e-i}[Hz] \approx \frac{2}{5} Q_i f_{e-e}. \tag{2.15}$$

For the simple case of a hydrogen plasma in an 18 GHz ECR ion source, the electron-

ion collision frequency would be about 30 Hz based on contributions from the warm 5 keV electron population. Collision times for hot (50 keV) electrons are substantively lower than those for warm electrons with $f_{e-e} \approx 12$ Hz and $f_{e-i} \approx 3$ Hz. With such a small electron-ion collision frequency the electrons do not directly heat the ions. In general, ECR ion source plasmas are comprised of many different gas and ion species each with a different mass and charge. The ion-ion collision frequency summed over all ion plasma species [93, 55] is given by

$$f_{i-j}[Hz] \approx 6.8 \cdot 10^{-8} \frac{\ln \Lambda_{i-j} Q_i^2}{A_i T_i^{3/2}[eV]} \sum_j \sqrt{A_j} \sum_k n_k[cm^{-3}] Q_k^2, \tag{2.16}$$

which is simplified from that presented in Ref. [79] for constant ion temperature and Coulomb logarithm. Here i, j, k are indices, A_i is the mass number of the i^{th} ion species, and the sum over k is taken for every j^{th} ion species. Equation 2.16 is cumbersome to use and for the purposes of ballpark estimates of a pure hydrogen 18 GHz ECR ion source plasma a simpler relation for a single species ion-ion collision frequency is provided in Ref. [8] with

$$f_{i-i} = Q_i^4 \sqrt{\frac{m_e}{m_i}} \left[\frac{T_e}{T_i}\right]^{3/2} f_{e-e}. \tag{2.17}$$

This expression for f_{i-i} is a function of the electron-electron collision frequency weighted by ratios of mass and temperature. The ions in ECRIS are colder (meV-eV range) and much heavier than electrons, ion-ion collisions happen much more often. The collision frequency for hydrogen thermalized at 1 eV with the previous parameters is about $f_{i-i} = 640$ kHz. For comparison, the ion cyclotron frequency for the ECR magnetic field at 18 GHz (0.64 T) is 10 MHz so the ions collide about once every 16 gyro orbits and compared to electrons are much less confined by the magnetic field. Collision frequencies generalized for multi-species plasmas may be found in Refs. [79, 99].

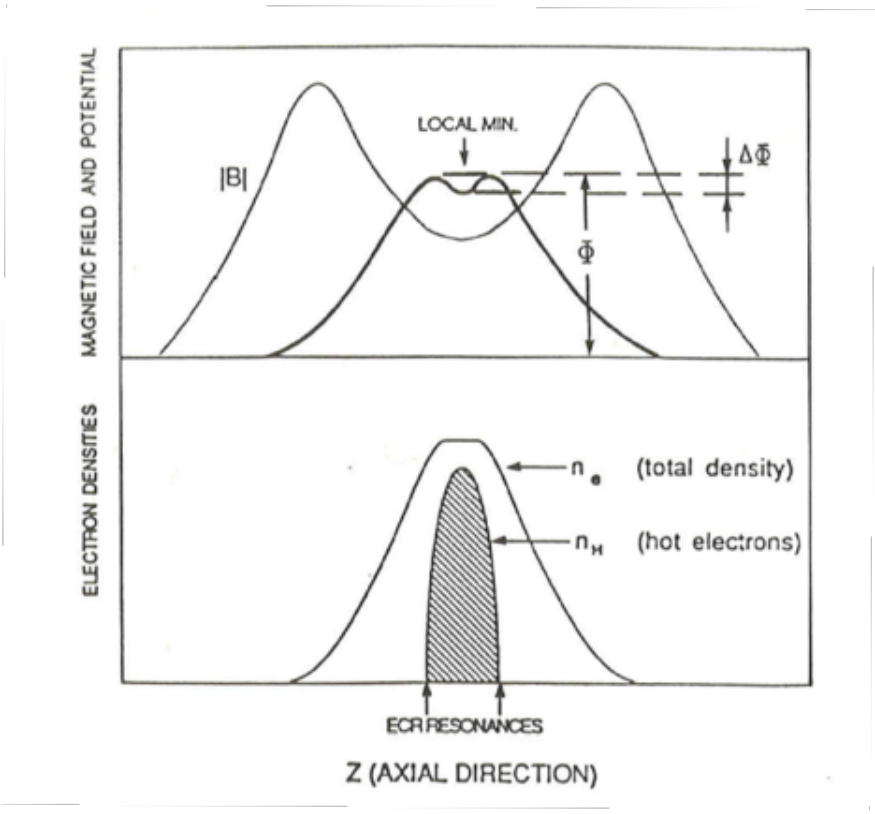

Figure 2.3: Schematic of the electrostatic ion confinement potential $\Delta\Phi$ in relation to electron density, magnetic field, and plasma potential from Refs. [68, 18]. Republished with permission of Taylor and Francis Group from Ref. [18] permission conveyed through Copyright Clearance Center, Inc.

2.3.4 Ion Confinement

Ions need to survive for a long time in the regions where energetic electrons can perform ionization in order to reach high charge states as covered in Sect. 2.3.1. Since the ionization cross sections decay with increasing charge state, and require higher electron energies, it takes an increasing amount of time to produce highly charged ions. The ions are assumed to be too collisional to benefit from confinement due to the minimum-B magnetic bottle.

Two main ion confinement mechanisms have been proposed: electrostatic and diffusive. The electrostatic model [68, 18, 82] relies on a hot electron population that is well confined by the magnetic field so that it creates a potential well as shown in Fig. 2.3. Thermalized

collisional ions escape from the well with a characteristic time from Ref. [71] modeled by

$$\tau_i = RL\sqrt{\frac{\pi m_i}{2kT_i}}e^{\frac{eQ_i\Delta\Phi}{kT_i}}, \tag{2.18}$$

where R is the mirror ratio, L the axial length of the system, $\Delta\Phi$ the depth of the potential well (see Fig. 2.3) and, T_i is the ion temperature. The ion temperature T_i assumed to be spatially uniform for each ion charge state.

In the ion diffusion model the ions diffuse naturally from the plasma according to the collision relations described in Sect. 2.3.3. The transit time of ions to diffuse through a thick plasma was suggested by D. Whaley et al. in Ref. [99] as a means of describing ion lifetimes τ_i in an ECR ion source plasma with $\tau_i = \frac{L^2}{D_i}$. Wherein L is a characteristic length of the plasma (ECR zone length) and D_i is the ion diffusion coefficient. If the diffusion of ions in ECR plasmas is governed by free diffusion [6] then the diffusion coefficient

$$D_i = \frac{kT_i}{m_i f_{i-i}}. \tag{2.19}$$

The diffusion coefficient D_i is weighted by the ion-ion collision time f_{i-i} that scales as Q^4 for a single species (see Eq. 2.17). A diffusion model proposed in Ref. [9] (along with another diffusion based model including the electric field of the plasma potential which was favored by the authors) supported measurements of ion confinement times for argon with the ion lifetime:

$$\tau_i[s] = 1.8\cdot 10^{-20}L^2[cm]Q_i^2\ln\Lambda\sqrt{A_i}\frac{\sum Q_i^2 n_i[cm^{-3}]}{T_i^{5/2}[eV]}. \tag{2.20}$$

This expression can be simplified assuming $\sum Q_i n_i = n_e$. L represents the ECR zone length. Ions must follow the magnetic field lines where the plasma conductivity (and therefore mo-

bility) is high [6] from the plasma core to extraction. It is reasonable to imagine that free diffusion is the dominant phenomenon for extracted (and measured) ions from the plasma. However, recent measurements of ECR ion sources in the afterglow mode [93] (a measurement where microwave power is abruptly dropped from high power to zero power, see Sect. 2.4.3) suggests the diffusion constant is linear in collision frequency as is the case for a strongly magnetized plasma [1].

The example of a hydrogen plasma does not make much sense in this section with ion confinement times being particularly valuable for the production of highly charged ions of the heavy elements. Furthermore, there exists at the time of writing, no model capable of predicting the potential dip in Eq. (2.18) from fundamental properties. Estimates for the potential dip from Ref. [56] for various plasmas on a 14 GHz source fall in the 2 mV to 1 V range and ion temperatures in the 200 meV to 3 eV range. Ultimately, V. Mironov et al. in Ref. [56] estimate the confinement time for Kr^{17+} to fall in the range of 2.4 ms and 5.1 ms. The diffusion model in Eq. (2.20) was fitted to experimental measurements on the 10 GHz Caprice source [9] with the confinement times for Ar^{16+} falling in the range of 900 μs to 3 ms.

2.3.5 Characteristic Parameters for an ECR Ion Source

A picture of an ECR plasma may be formulated using the physics covered in the previous sections. As the electron density increases in an ECR plasma from RF heating at a fixed frequency, the plasma frequency will increase up to where it begins to reflect the RF from penetrating into the resonance zone providing an estimate for the electron density. Using Eq. 2.6 with a fixed frequency of 18 GHz provides a maximum estimate of the cold electron density $n_e = 2.5 \cdot 10^{11}$ particles/cm^3. ECR heating drives the electron temperature up into

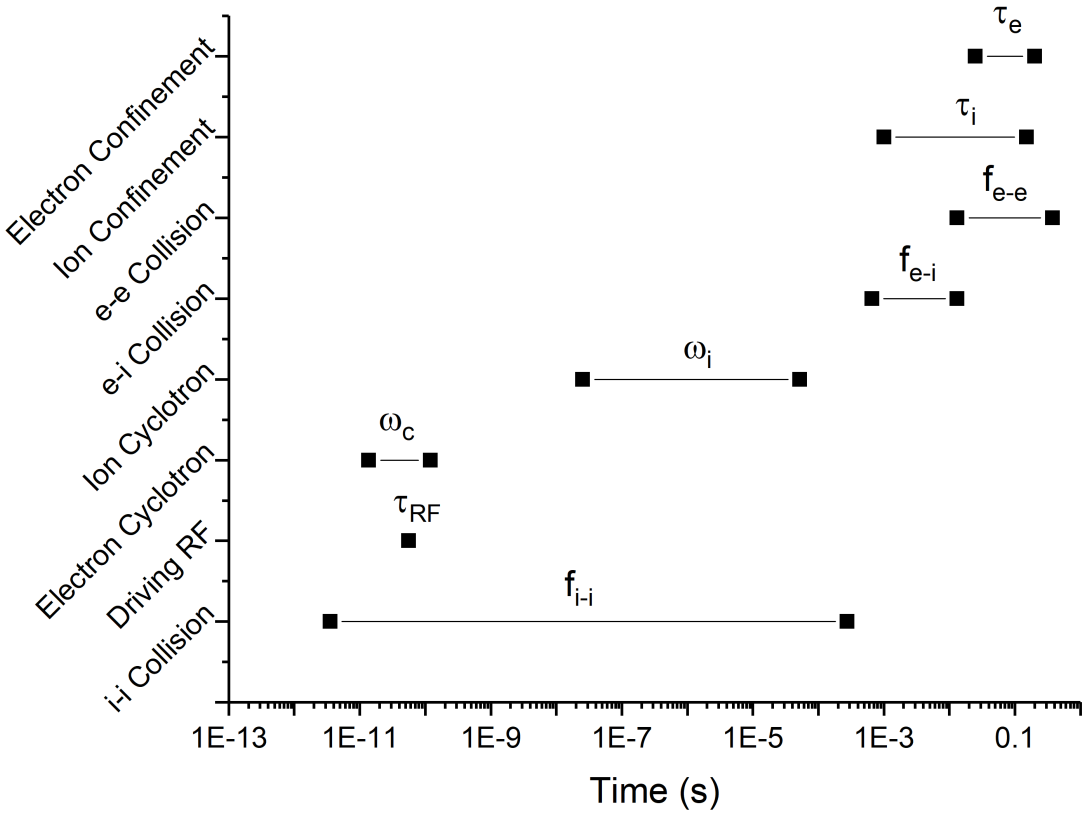

Figure 2.4: Upper and lower timescale ranges of various ion and electron processes for an 18 GHz ECR ion source based on calculations from Eqs. (2.2), (2.13), (2.15) and (2.17) and measurements from Refs. [9, 97] and Chapter 4. Plasma parameters were assumed to fall in the following ranges: ion temperature between 0.5-5 eV, average charge state between 1-20, ion mass number between 1-238, electron temperature between 5-50 keV, electron density $2.5 \cdot 10^{11}$ cm^{-3}, Coulomb logarithm between 21.5-23.9, magnetic field between 0.3-2.6 T, and a driving RF frequency of 18 GHz.

the keV range as covered in Sect. 2.2.2 and for simplicity a bi-Maxwellian EEDF is assumed with 5 keV and 50 keV temperatures. Assuming these temperatures, the hot electrons are largely non-collisional and have a characteristic confinement time of about 200 ms given a mirror ratio of $R = 2.7$. The warm electrons at 5 keV responsible for ionization (covered in Sect. 2.3) have a confinement time of 25 ms and are about 7 times more collisional than the hot electrons. The 5 keV electrons have a density of $2.5 \cdot 10^{11}$ cm^{-3} and distribute to shield electric fields generating a Debye length of about 1 mm. Long range Coulomb collisions with other charged particles generate a 90° deflection 110 times per second for the 5 keV warm electrons (with a longitudinal mirror ratio at extraction of $R = 2.7$). The ions are indirectly heated by electrons and ion temperatures fall in the meV to eV range. With a low ion temperature, the ion-ion collision frequency is about $f_{i-i} = 640$ kHz far exceeding the electron-ion collision frequency estimated to be about $f_{e-i} = 30$ Hz.

ECR ion sources are not typically used to generate hydrogen plasmas (although a nicely solvable situation) and a range of plasma conditions are explored in Fig. 2.4. Single charge state formulae in Eqs. (2.13), (2.15) and (2.17) were used substituting an average charge state for the more complete sums over charge and density in Eqs. (2.14) and (2.16).

2.4 Diagnostic Tools for ECR Ion Sources

2.4.1 Beam Current Measurement

The most commonly used diagnostic for ECR ion sources are the extracted ion currents. The currents are typically plotted verses mass to charge ratios to form Charge State Distributions (CSDs) in electrical current. The distribution of charge states can be used to compare simulations against experiment [84, 10, 83, 56]. Beam current for individual charge states

extracted from the ion source can provide valuable information about ion diffusion [93, 61], ion confinement [81, 25, 97, 9], and the plasma potential [94, 90]. A simple relationship between ion current and density may be written from Ref. [18]

$$I_i \approx \frac{1}{2}\frac{q_i L \sigma_a n_i}{\tau_i}, \tag{2.21}$$

where σ_a denotes the emission area, τ_i the ion confinement time, L the plasma length, q_i the ion charge, and n_i the ion density. Most commonly, ions extracted from ECR sources are used to supply ion accelerators with high intensity heavy ion beams. The ion source is coupled to a low energy beamline to species separate, transport, and bunch the ions into the first accelerating structures. Increasing the intensity of heavy ion beams is an area of active development at the time of writing evident in Refs. [47, 34, 15, 105, 101, 27].

2.4.2 Bias Disc

The bias disc on an ECR ion source is a small electrically charged disc placed on axis at the injection baffle of the source. Figure 2.5 shows where the bias disc appears in an ECR ion source. Negative electrical bias is typically applied to the disc for production of highly charged ions. Bias discs are useful for steady state operation to increase the beam current of ions and particularly for high charge states [53, 16]. Additionally, the bias disc was demonstrated in Ref. [63] to increase beam brightness of U^{35+} produced by off axis sputtering by about a factor of two.

The bias disc, useful for steady state beam production, can also be used as a "primitive planar Langmuir probe" [92] to probe plasma breakdown and plasma potential wherein the bias disc current (for fixed voltage) was monitored with time and changing plasma conditions.

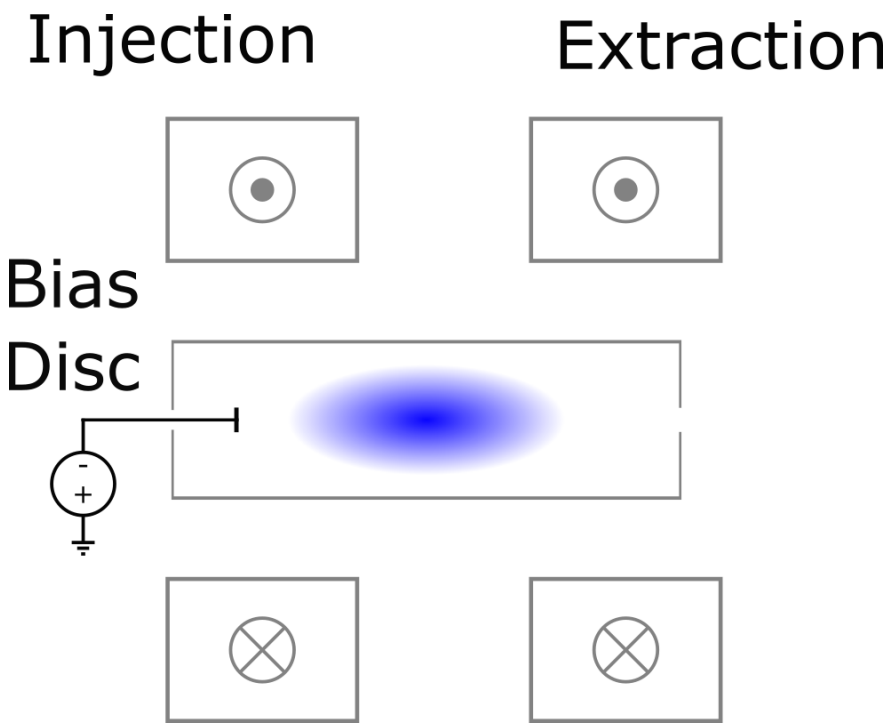

Figure 2.5: Schematic of the bias disc on an ECR ion source. The disc is shown negatively biased with a power supply at the injection side of the ion source. In practice the disc can be biased at either polarity, grounded, or allowed to float, although negatively biased discs typically produce the highest ion beam currents.

The bias disc voltage can also be modulated and the beam current transient measured [88, 75] resulting in waveforms with short (< 100 μs) characteristic times. The bias disc function may be generally attributed to that of an electron reflector and as posed by R. Geller in Ref. [18] specifically for secondary electrons produced on the disc.

2.4.3 Afterglow

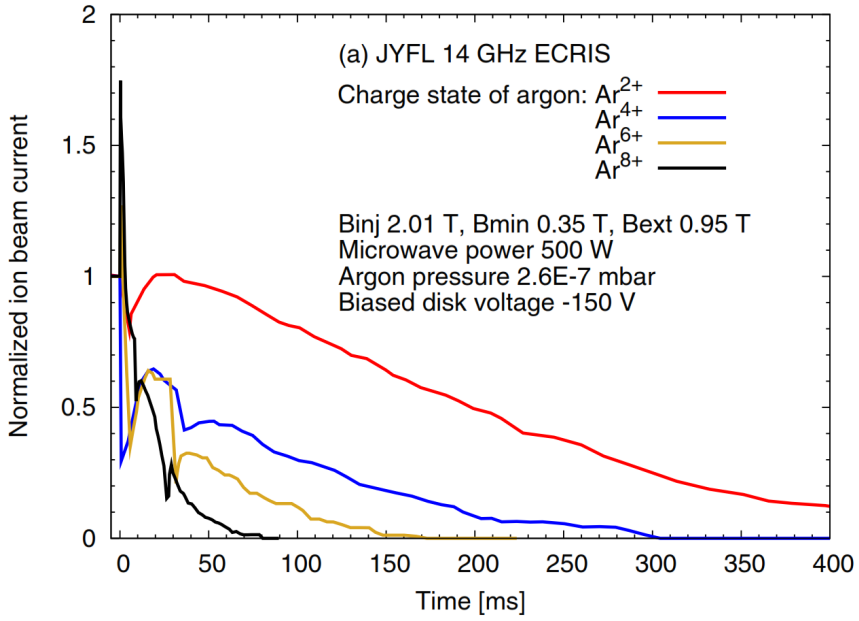

Figure 2.6: Example of an afterglow beam current response shortly after the microwave power is stopped (time $t = 0$). The beam current of four charge states are plotted normalized to the steady state current from Ref. [93]. Copyright IOP Publishing, reproduced with permission, all rights reserved.

Afterglow describes a short (approximately milliseconds duration) burst of ion current (generally around a factor of 2-8 times the steady state current) immediately after the discontinuation of RF into the ion source [54, 96, 93]. Afterglow is used for high current injection into pulsed accelerators notably the LHC at CERN [28, 95]. The CSD during afterglow is notably shifted towards higher charge states when compared to steady state, and the burst of ions is stronger for higher charge states [96, 93]. Several [96, 54, 61, 81]

suggest a collapsing electrostatic confinement well as the source of the ion current bursts. Additionally, the decay times measured during afterglow increase for lower charge states and O. Tarvainen et al. in Ref. [93] suggested this structure is the result of ion diffusion linear in collision frequency.

2.4.4 Fast Sputtering and Laser Ablation

The use of a metal contaminant to study ionization and ion confinement processes arose organically out of research and development to produce steady state beams of a wider range of elements. During laser ablation experiments on the 10 GHz PII-ECRIS at Argonne National Laboratory (ANL), a bismuth target was ablated using short (200 ns) infrared laser pulses repeating every second. The beam current was observed to rise and fall reaching peak current milliseconds after the laser pulse. Notably, higher charge states of bismuth reached peak current later in time than lower charge states. The long repetition rate of the laser coupled with millisecond beam current peaking times made steady state bismuth production for an accelerator impractical [25]. However, the authors noted: "The immediate success of the laser ablation technique has been its use in allowing us to make direct time measurements which verify and quantify sequential, step-by-step ionization taking place in an ECRIS."

It was demonstrated at ANL on the ECR2 ion source by R. Vondrasek et al. in Ref. [97] that sputtering could be used to quantify the step-by-step ionization process in a similar manner to laser ablation. Short sputtering pulses (500 μs) produced a burst of sputtered material that was tracked through the measured ion current. Figure 2.7 from Ref. [97] illustrates how beam current of gold in an oxygen plasma responded as a function of charge state for 500 μs sputtering times. Extracted gold ion current (as measured on a Faraday cup after mass to charge separation) rose and fell peaking tens of milliseconds after the

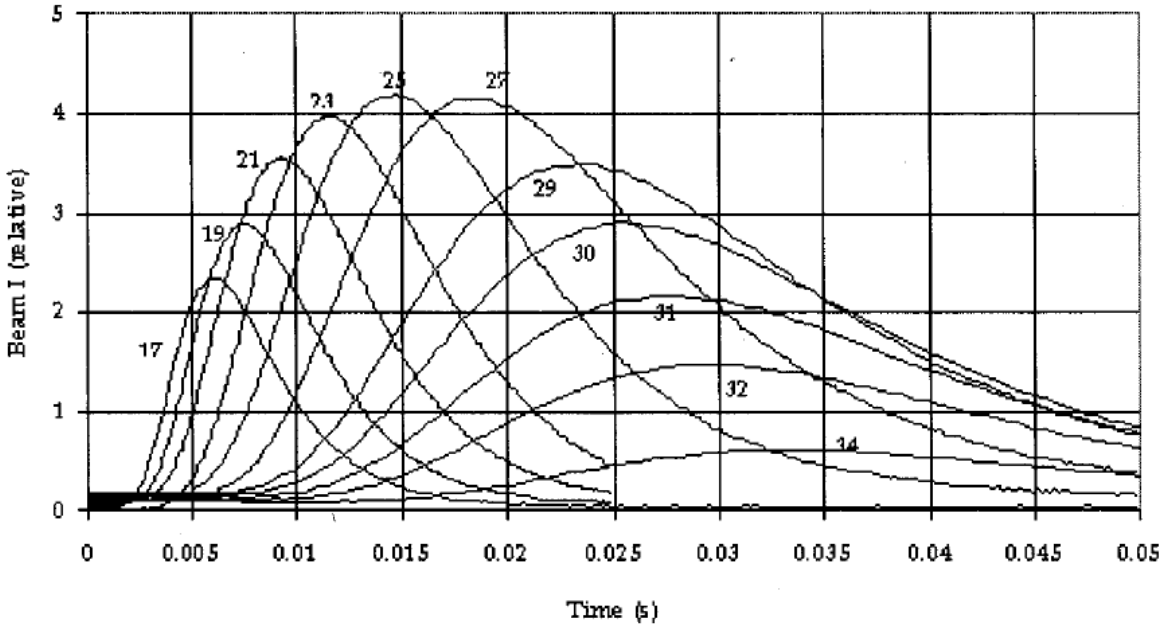

Figure 2.7: Gold beam current response after radial fast sputtering events on ECR2 at ANL [97]. A sputtering voltage of -1.8 kV was applied for 500 μs at time zero. The gold waveforms are plotted as a function of time for eleven different charge states. Reprinted from from Ref. [97], with the permission of AIP Publishing.

sputtering voltage was applied shown in Fig. 2.7. In addition, the authors of Ref. [97] found that increasing the microwave power reduced the peaking time. Sputtering times longer than 500 μs increased the time at which charge states reached their peak values. The beam current waveforms in Fig. 2.7 were similar to the ones produced from laser ablation experiments [25, 59].

Both laser ablative and fast sputtering methods were considered for systematic study of ion confinement times on the SuSI ECR source at Michigan State University (MSU) (see Sect. 2.5.1). An advantage of the laser ablation method is it introduces the contaminant independently of the plasma. However, laser ablation was demonstrated to drill around a millimeter into several targets such as iron and alumina in relatively few laser shots (300-200 k) [64] leading to issues of shot-shot reproducibility. Laser ablation is an inherently

complicated system to implement on an ECR ion source. The laser and optical network required for it to function is sensitive to vibrations and the ablative target is difficult to place in an accessible location. In contrast, fast sputtering is an attractive method because many of the components such as cathode power supplies and sputtering probes are already readily available to the experimenter from the common usage of steady state sputtering to produce metallic beams for accelerator facilities. One main downside is that the time structure of the metal contaminant cannot be evaluated independently of the ECR plasma. Therefore the time required for the sputtering process to stabilize is unknown. However, measurements from Ref. [97] suggest that it is likely less than 500 μs for a 14 GHz ECR ion source. Fast sputtering was selected for use on SuSI because of its simplicity relative laser ablation and an existing sputtering apparatus could be used.

2.4.5 Emittance Measurements

Generally, ECRIS are used as injectors to linear accelerators and cyclotrons that can only accept for acceleration a finite (and usually restrictive) beam emittance. Emittance is a statistical measure of the phase-space area of a particle beam. It is usually measured for each species and more detailed explanations may be found in Ref. [11]. The primary contribution to the beam emittance from an ECR ion source is generated by the particle rotation induced by the strong magnetic field of the source [40]. However, the measured emittances of highly charged ions in ECRIS appears to decrease with increasing charge state [41]. This led to the idea that highly charged ions must be produced at smaller average radii than their lower charge state counterparts. The substantive efforts of experiments covered in Chapter 4 and Chapter 5 do not include emittance measurements because the optical properties of the extracted ion beam were beyond the scope of the experimental goals.

2.4.6 X-Ray Measurements

Energy resolved x-ray measurements of ECR plasmas predate the first ECRIS for highly charged ions SUPERMAFIOS [18]. Notably, experiments on a 9.75 GHz simple mirror ion source looked at bremsstrahlung produced on the plasma chamber wall at an oblique angle to the source axis of symmetry [5]. An important finding, demonstrated in part through x-ray measurements, was heating on a higher ECR harmonic was very inefficient. Consequently, the fundamental electron cyclotron frequency and driving RF frequency must match somewhere on the magnetic surface for efficient heating.

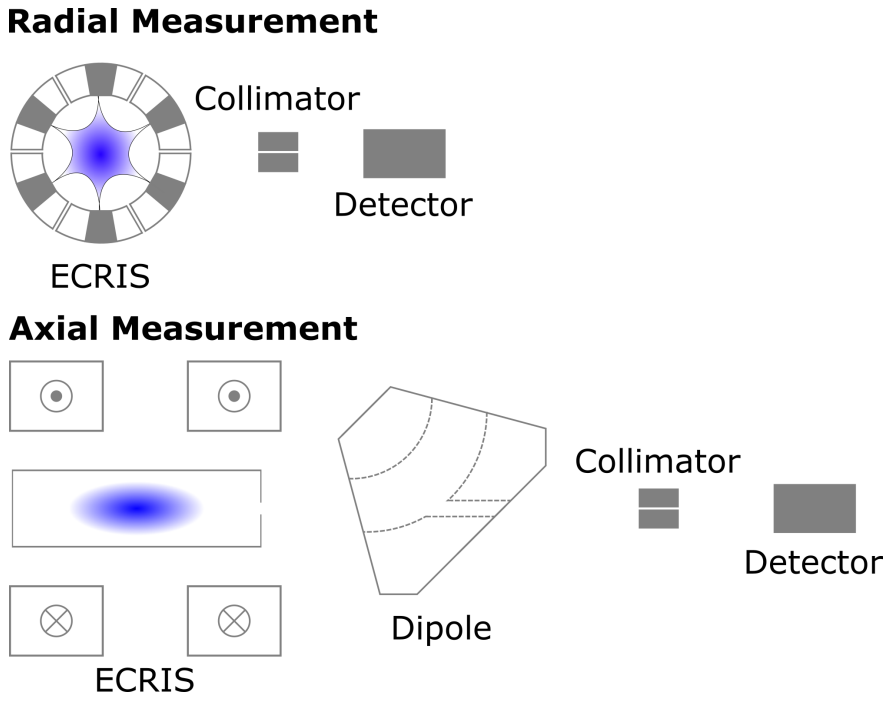

Figure 2.8: Schematic of axial and radial x-ray detection schemes commonly used for ECR ion sources.

Bremsstrahlung produced by electrons impinging on the plasma chamber wall can be sampled in two different geometries: axial and radial. Axial measurement looks at x-rays illuminating a detector along the axis of symmetry of the ion source typically through the bending magnet, while radial measurement is performed on radial port of the source and looks

in between coils of the hexapole magnet. ECR heating is anisotropic and the bremsstrahlung intensity along with electron temperature is observed to be much greater in the radial direction than in the axial one [62]. Bremsstrahlung spectra from ECR ion sources are characterized by a high energy tail that extends into the hundreds of keV as shown in Fig. 2.9 or out to MeV energies as measured on the 28 GHz ECR ion source VENUS [44]. Bremsstrahlung spectra from ECR plasmas exhibit exponential decay in the high energy tail. This can be fitted with an exponential function to arrive at an electron temperature for a Maxwellian EEDF [39]. The hot electron temperature was demonstrated to scale as the magnetic minimum in ECRIS by J. Benitez et al. in Ref. [3] as opposed to the magnetic gradient at the cold electron resonance zone.

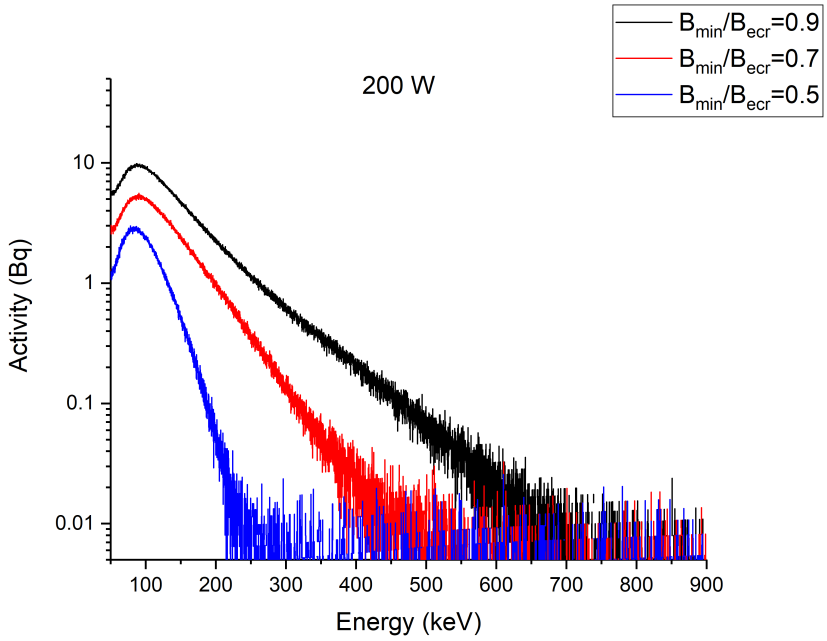

Figure 2.9: Axial bremsstrahlung spectra taken on SuSI over a half hour with an oxygen plasma at 200 W steady state microwave power and three magnetic minima. The spectra is typical of those obtained for ECR plasmas.

Time resolved and energy resolved x-ray measurements are performed with time steps as short as 100 μs and used to characterize ECR heating and EEDF in combination with beam

current measurement in both the afterglow mode and steady state [73]. Time resolved x-Ray power flux (integrated over energy) is used effectively to characterize kinetic instabilities and their effects on ECR ion source operation [91].

The SuSI source (see Sect. 2.5.1) allows for a clear line of sight on the axis of the source. Radial measurements on SuSI are impractical due to the layers of thick x-ray shielding obscuring the view. A tantalum cylinder located between the plasma chamber and the cryostat protects the superconducting magnet from x-rays which can provide several watts of heat load to the cryogenically cooled superconducting magnet [44].

2.5 ECR Ion Sources Used for Experiments Presented Within this Dissertation

2.5.1 The Superconducting Source for Ions (SuSI)

The Superconducting Source for Ions (SuSI) is an 18 GHz fully superconducting ECR ion source. Six superconducting coils each 8 cm in length axially and with the two injection coils having 2628 turns producing a stronger magnetic field for the same current than the two mid and extraction coils having 1626 turns each [103]. Figure 2.1 was generated from the SuSI coil design with the injection coils visible from the increased size relative to the other four coils. For the experiments presented in this dissertation, four of the six solenoidal coils were in operation. The first injection coil and second extraction coil were energized. Other injection and extraction coils were shorted. The configuration used is shown in Fig. 2.1 in Sect. 2.2.1. As a result of the reduced number of coils in operation only certain magnetic field configurations could be used. The four operable coils produced fields that vary in

magnetic minimum while maintaining fixed injection and extraction field strengths. The role of the hexapole was not studied within the experiments presented in this dissertation. The hexapole was set to provide 1.25 T at the plasma chamber wall for 18 GHz operation and 0.93 T for 13 GHz operation.

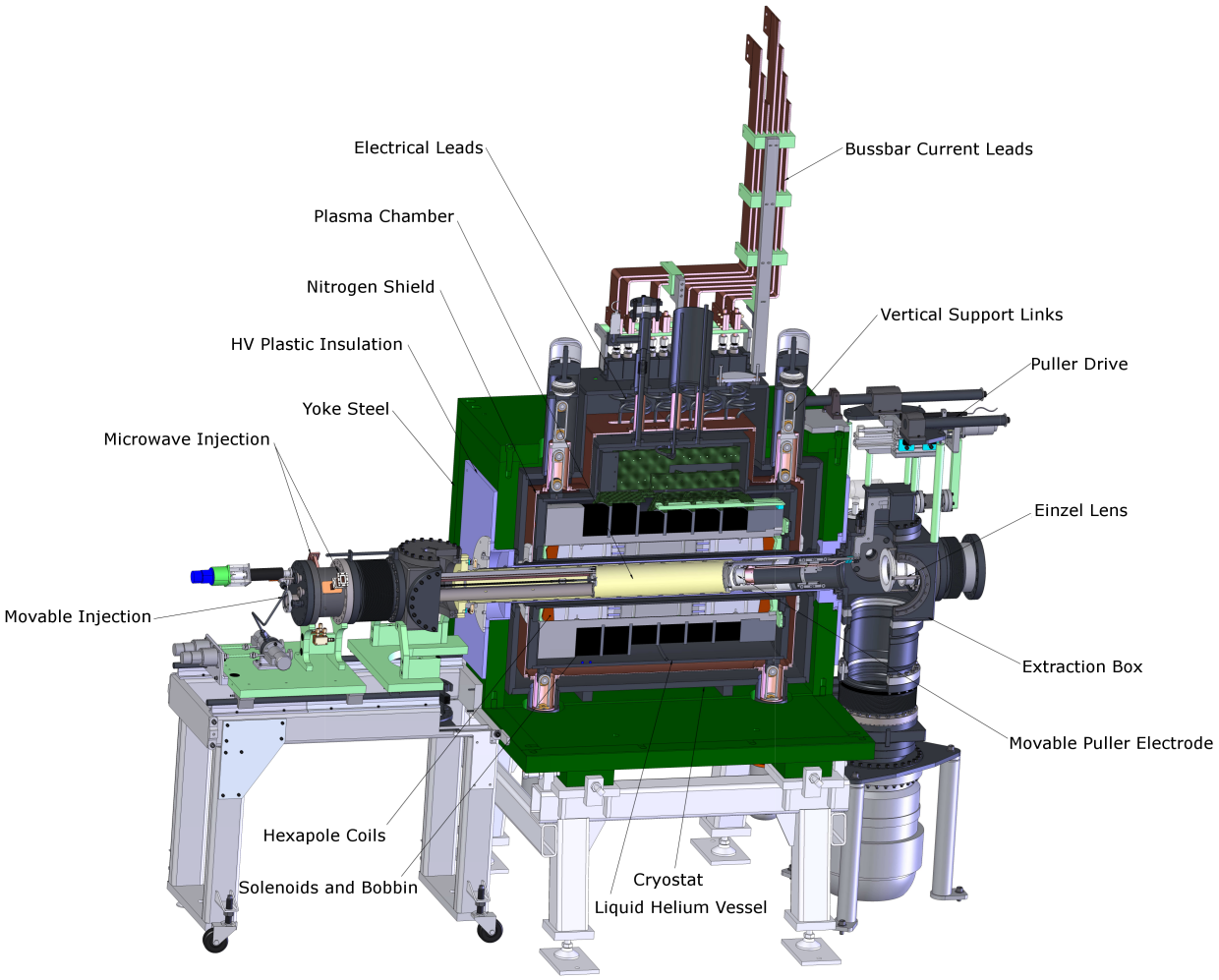

Figure 2.10: Isometric view of the SuSI source cut away to show the plasma chamber, superconducting coils, and cryostat [46].

SuSI was normally powered with a single 18 GHz klystron capable of supplying up to 2 kW microwave power. However, no more than 700 W was injected into the source over the course of the experiments presented. During the experiments covered in Chapter 4, a 13 GHz Traveling Wave Tube (TWT) was coupled to the source through a 18 GHz DC break

and microwave vacuum window. The frequency mismatch of the transmission line in this configuration resulted in high reflected power which limited the attainable power at 13 GHz to 100 W. Figure 2.10 shows a more detailed view of the source with key components labeled. The plasma chamber is 10 cm in diameter and has a volume of about 3.2 L between injection baffle and extraction electrode.

An 8 mm extraction aperture was used for all experiments presented within this dissertation. The ions passed through the extraction electrode and into an accel-decel electrode system [104]. The first transverse focusing element the ion beam encountered was a negatively biased Einzel lens which was critical to reduce beam loss on the dipole separating magnet downstream. The dipole magnet radius of curvature was 51 cm and the SuSI platform voltage was 20 kV for all experiments presented within this dissertation. Between the Faraday cup where current is collected (measured) and the dipole magnet, there were a series of circular apertures and transverse focusing solenoids with the apertures positioned in between the solenoids. Figure 2.11 illustrates the beamline elements and distances. The solenoid currents were scaled with the dipole current to maintain the desired optical properties for different measured charge states.

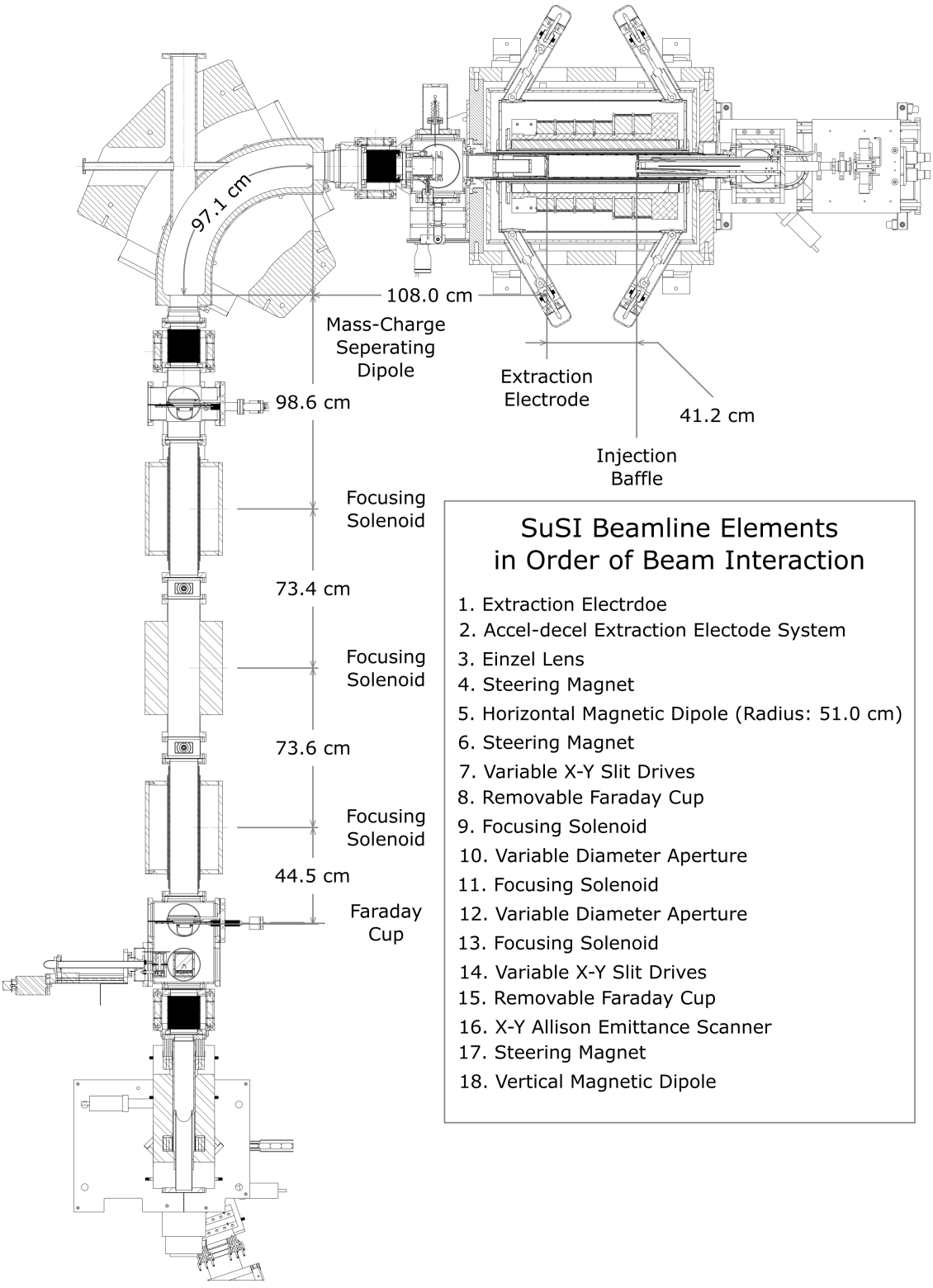

Figure 2.11: Schematic of the SuSI beamline up until the Faraday cup. The solenoid triplet currents were scaled with the dipole current proportional to the mass to charge ratio of the beam. The maximum solenoid current was reached (around $A/Q = 11$).

2.5.2 The Advanced Room TEMperature Ion Source (ARTEMIS)

ARTEMIS is a 2^{nd} generation ECR ion source based on the AECR-U source [36]. Two normal conducting solenoid magnets provide the axial mirror field while a permanent magnet hexapole provides radial confinement. Iron yokes are used at injection and extraction to increase the mirror confinement field strength. Depending on the injection assembly used, peak fields of up to 1.8 T at injection were attainable. Typical injection and extraction field strengths for the experiments presented in this dissertation were 1.28 T and 0.89 T respectively. A hole was drilled through the iron yoke (on axis) at injection to accommodate the axial sputtering probe covered in Sect. 2.6.6. Poles of the hexapole magnet were separated by slots that both improved vacuum pumping of the plasma chamber and also allowed access for instrumentation to be placed radially with respect to the plasma chamber. The permanent magnet hexapole had a fixed strength of 0.65 T at plasma chamber wall [49]. ARTEMIS was powered by a 2 kW 14 GHz klystron with RF power injected from injection through the iron yoke. Figure 2.12 details some key aspects of the source [48].

The ARTEMIS beamline used electrostatic focusing elements, primarily consisting of two quadrupole doublets separated by an octupole. Figure 2.13 highlights beamline elements up until the Faraday cup. Electrostatic focusing elements maintain the same focus for beam species of different A/Q. The double quadrupole doublet was found to increase brightness of the low energy beam particularly below 50 π·mm·mrad an emittance beneath which corresponded to increased transmission efficiency out of the K500 cyclotron [87].

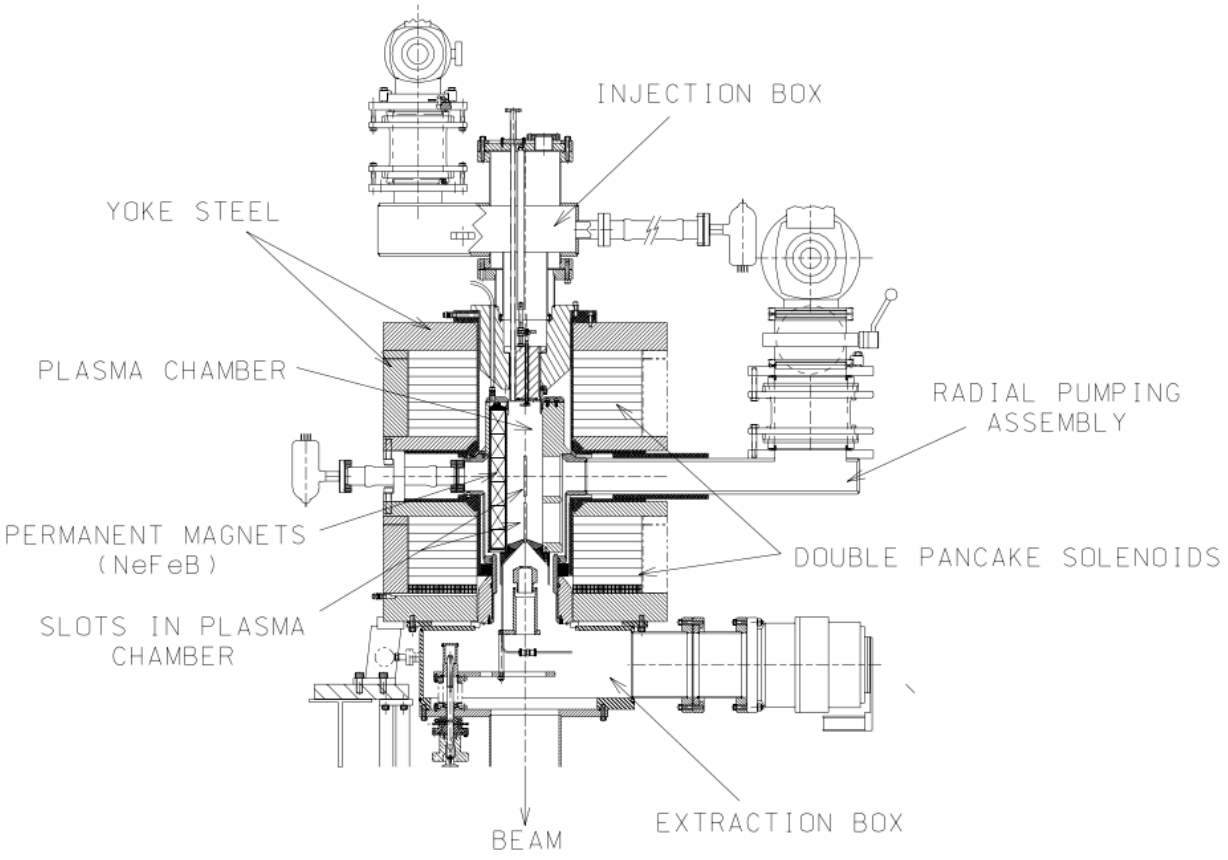

Figure 2.12: Schematic of the ARTEMIS source detailing the vacuum vessel, plasma chamber, magnet design, and microwave waveguide from Ref. [36].

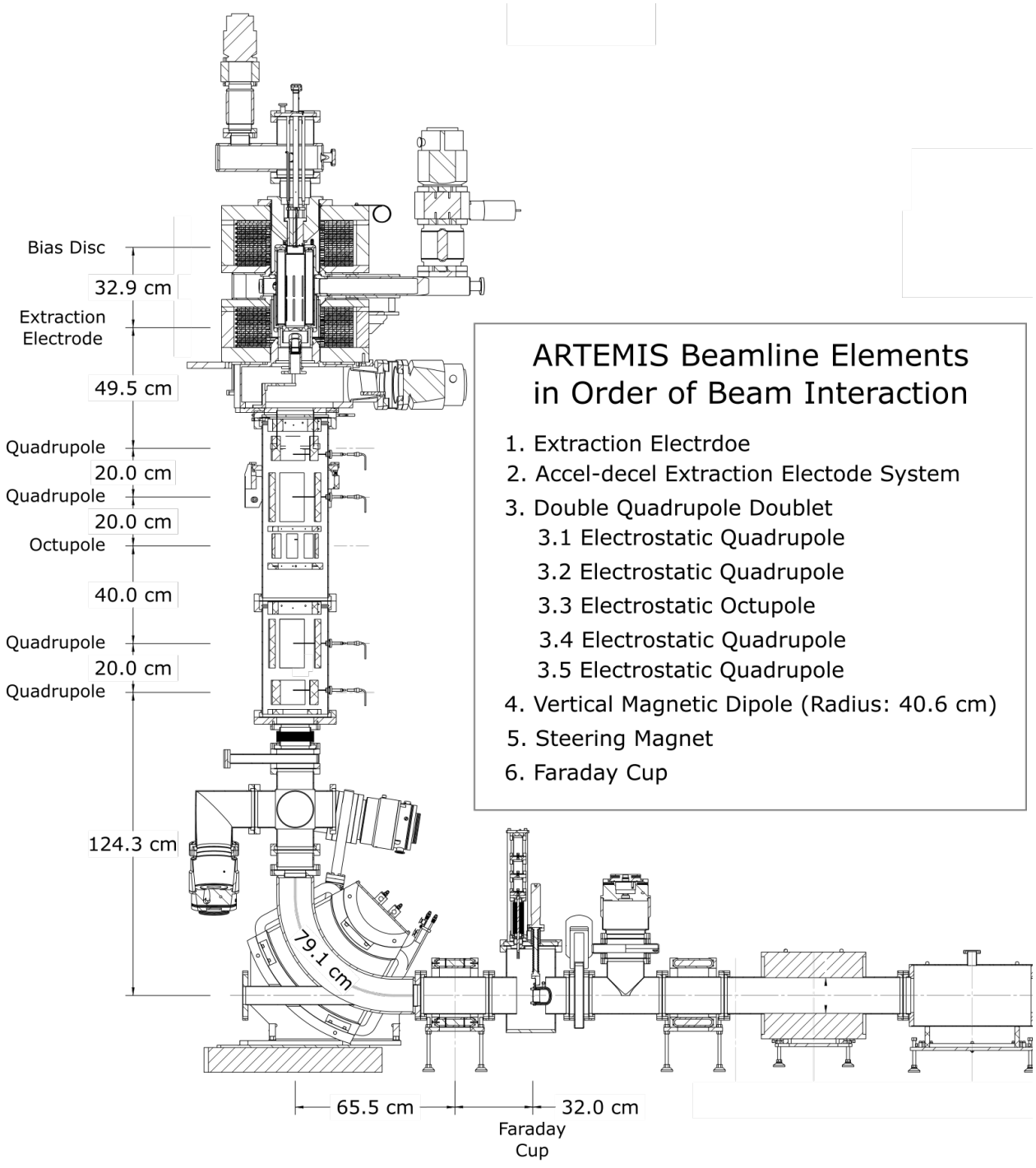

Figure 2.13: Schematic of the ARTEMIS beamline. The electrostatic focusing elements were tuned for maximum transmission and act independently of A/Q on the beam from the source.

2.5.3 The University of Jyväskylä 14 GHz ECR Ion Source: ECR2

ECR2 is a 14 GHz 2^{nd} generation normal conducting ECR ion source operating at the University of Jyväskylä Finland. Figure 2.14 illustrates ECR2 and is based on the ARTEMIS and AECR-U designs [37]. The minimum-B magnetic field configuration was achieved with two normal conducting solenoids providing around 2 T at injection and 1 T at extraction (current depending) with with a permanent magnet NdFeB hexapole providing about 0.9 T at the plasma chamber wall (at the pole tip). ECR2 coil currents at injection allow a maximum current of 500 A allowing it to surpass the 1.8 T injection field of ARTEMIS. Like other AECR type ion sources, slots are cut in the hexapole assembly in between the poles to allow for better vacuum pumping visible (see Fig. 2.14). A three electrode accel-decel extraction system is used and the source can operate at a platform voltage of up to 30 kV [37]. The beamline consisted of an Einzel lens and focusing solenoid immediately downstream from the extraction electrode. A dipole magnet separated the ions by A/Q before measurement on a Faraday cup.

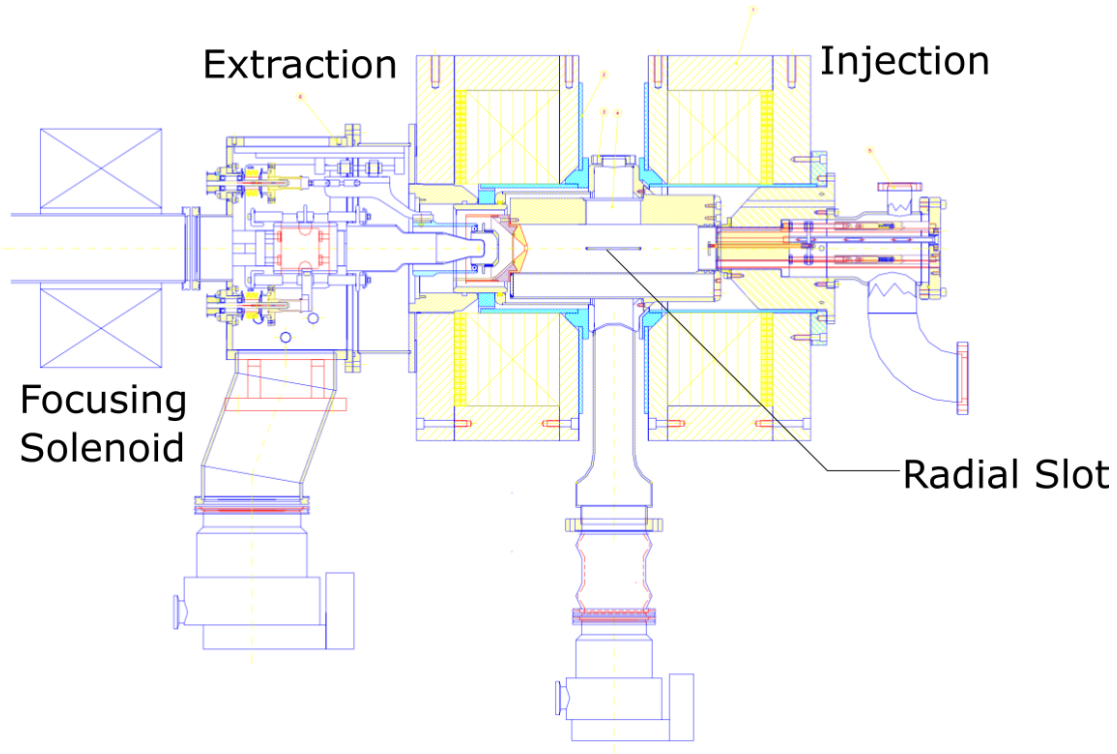

Figure 2.14: Schematic of the ECR2 source at the University of Jyväskylä detailing the vacuum vessel, plasma chamber, magnet design, and extraction solenoid from Ref. [90].

2.6 Instrumentation for Pulsed Sputtering Experiments

2.6.1 Time Resolved Beam Current Measurement

Beam current was measured at a Faraday cup from the voltage drop across a 109 kΩ resistance. For more information about the SuSI beamline, see Sect. 2.11. Long cables were used from the Faraday cup to an oscilloscope and the current across the resistor was measured through a RC low pass filter. LTspice simulations of the circuit in Fig. 2.15 predicted a -3 dB cutoff frequency of 150 Hz. Additionally, a step current was simulated to take 560 μs for the voltage to reach 95% of the steady state value, a 250 μs long square pulse was found to reproduce 76% of the peak amplitude and deform the square edges. The Faraday cup capacitance was measured by [30] using a LCR (Inductance Capacitance Resistance) meter,

and the LTspice simulation was originally developed by J. Stetson [86] to explain oscilloscope observations during bias disc voltage modulation experiments. The simulation input values were modified to better represent the experimental set-up cable lengths. Voltage to current calibrations were performed on the physical circuit with a calibrated direct current source between 10 nA and 80 μA.

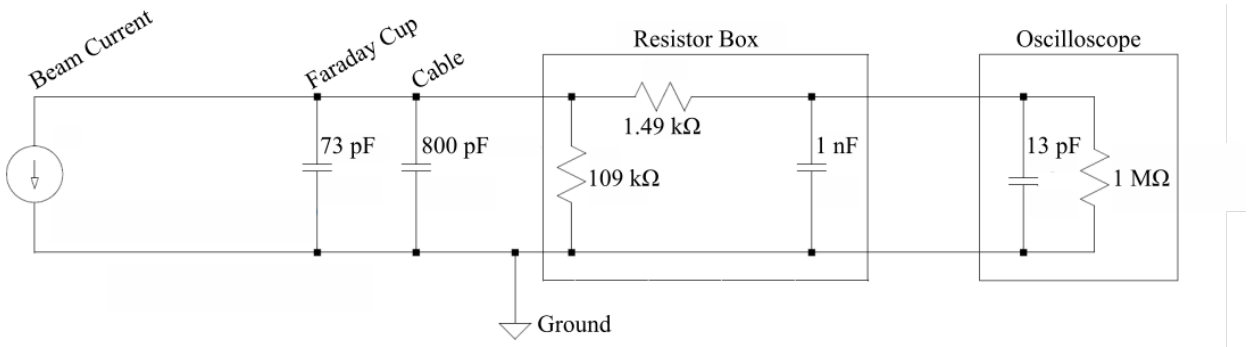

Figure 2.15: Schematic of the electronic circuit used for pulsed sputtering experiments as simulated with LT spice. The Faraday cup current was measured across a 109 kΩ resistor as a voltage on an oscilloscope. A low pass RC filter was used to suppress the influence of megahertz background radiation on the beam current signal.

2.6.2 SuSI X-Ray Detector and Collimation Set-up

X-ray radiation produced by bremsstrahlung from the ECR plasma and on the extraction electrode passed through a collimation system of thick lead and tungsten apertures. The system accepted x-rays emitted longitudinally within a 16 mm circle at the extraction electrode into a cone with geometric opening angle of 25 minutes. The extraction electrode aperture was 8 mm in diameter so x-rays were likely produced by thick target bremsstrahlung by plasma electrons impinging on the aluminum extraction electrode surface. At the end of the collimation system, a High Purity Germanium (HPGe) detector was placed to collect and measure the x-rays. The HPGe detections were recorded with a multi channel analyzer. This solid state detector was selected because its energy calibration is insensitive to variations in

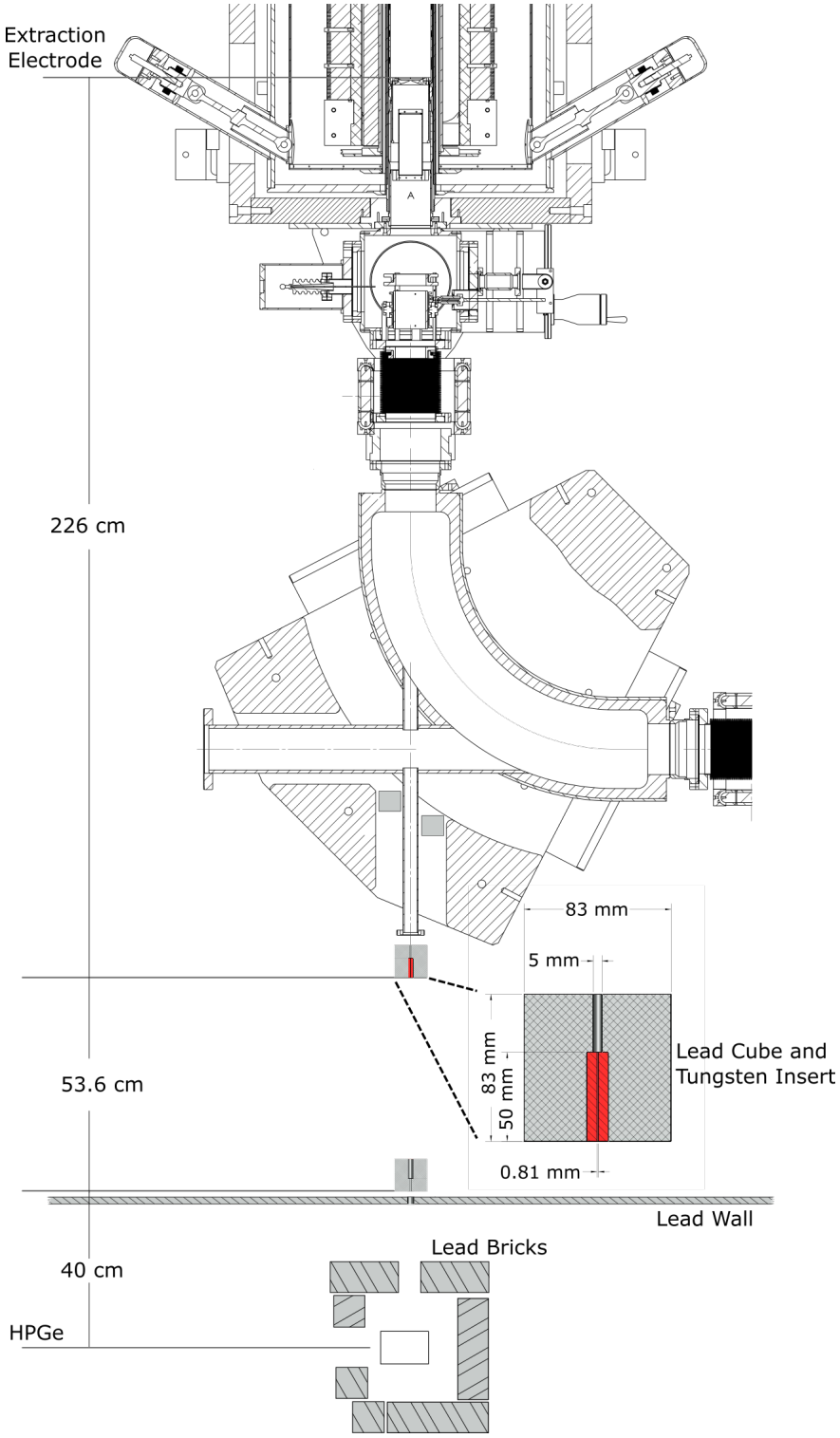

Figure 2.16: Lead and tungsten (red) x-ray collimators. Placing two collimator cubes (one with a tungsten insert and one without) 54 cm apart produced an opening angle of 25 minutes.

local magnetic field. Figure 2.16 shows a schematic of the collimation system in reference to SuSI used in the experiments.

2.6.3 Fast High Voltage Switch

To quickly charge and ground high voltage to the sputter probe a fast (50 ns) high voltage switch (Directed Energy PVX-4140) was connected in series with the DC high voltage power supply floating at the platform potential. A 5 V TTL signal was used to trigger the high voltage switch to fire a bank of MOSFET transistors connected in series to toggle between two reference potentials. We chose our reference potentials to be the platform potential (+20 kV for these experiments) and the negative DC high voltage sputter supply (floating at the ion source platform potential). The positive high voltage input on the switch was shorted, the negative power supply was connected to the negative input on the switch, and the switch output was connected to the sputter probe as shown in Fig. 2.17. The switch was controlled using a fiber-TTL converter for high voltage isolation allowing beam current to be synchronized to the sputtering voltage. This set-up was used for all the pulsed sputtering experiments presented. The TTL-Fiber converter and multi-mode fiber optic cable added an additional 130 ns of time delay. The total time to apply the sputtering voltage in reference to the signal generator was 220 ns, with the TTL-Fiber converter system. The characteristic timescales of interest are four orders of magnitude longer, this time delay is neglected.

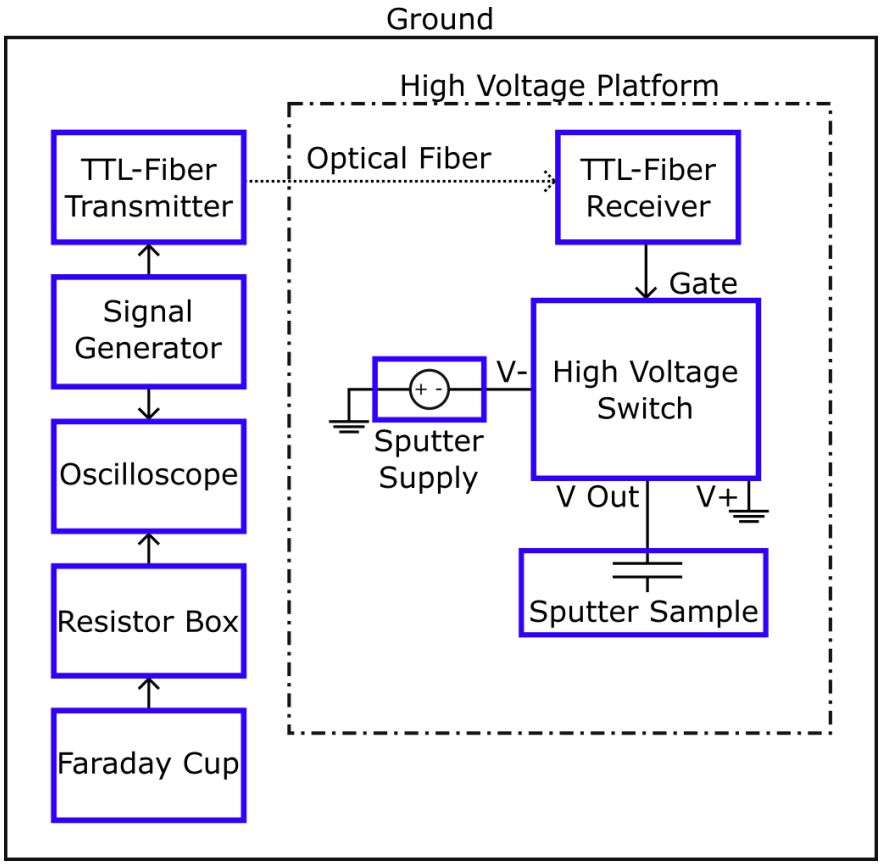

Figure 2.17: Block diagram of the high voltage switch and control infrastructure used for pulsed sputtering experiments. The total time delay between the signal generator output and the application of the high voltage to the sputter sample was 220 ns.

2.6.4 SuSI Axial Sputtering Probe

Axial sputtering on SuSI was performed with sputter sample press fit into an aluminum holder that is threaded onto a water cooled and electrically isolated rod. The entire rod (including sputter sample) was charged with a negative high voltage power supply. The sample longitudinal position was movable and could be adjusted to allow the sputter sample either to protrude out from or be recessed into the injection baffle as shown in Fig. 2.18. The whole injection assembly (and therefore the injection baffle) was mounted on a movable track. If the sputter probe was too close to the plasma then direct feeding, a process where the plasma etched the sputter sample without the sputtering voltage, was observed. If the sputter probe was too far away from the plasma, then the local ion density was too low to provide sputtering rates that produced observable beam currents. Therefore, the sputter probe depth was selected to minimize direct feeding and maximizing uranium current when the sputter voltage was applied. This optimal setting was found iteratively by selecting a depth and then turning the source (magnetic field, high voltage, microwave power, oxygen gas feed), and then measuring the sputter sample current with and without sputtering voltage.

The axial sputter probe high voltage connection consisted of a metal tab and was not suitable for the transmission of nanosecond rise time high voltages. Therefore, a cylindrical metal wire cage was erected around the sputter probe (in atmosphere) and a panel mount SHV connector mounted to the wire cage transferred the high voltage pulse to the sputter probe with about 6 inches of coaxial inner core wire. This modification ensured the sputter probe appeared as a mostly capacitive load. Using a high voltage monitor, -3 kV could be applied to the sputter probe and removed within 90 ns as measured with an oscilloscope at the platform potential.

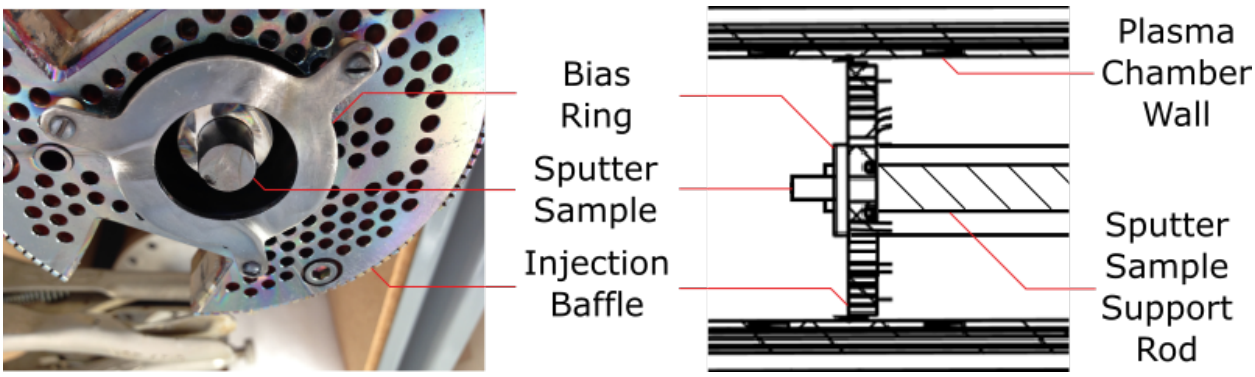

Figure 2.18: Image and schematic of the axial sputter probe for SuSI. A uranium sample is pictured.

2.6.5 SuSI Radial Sputtering Probe

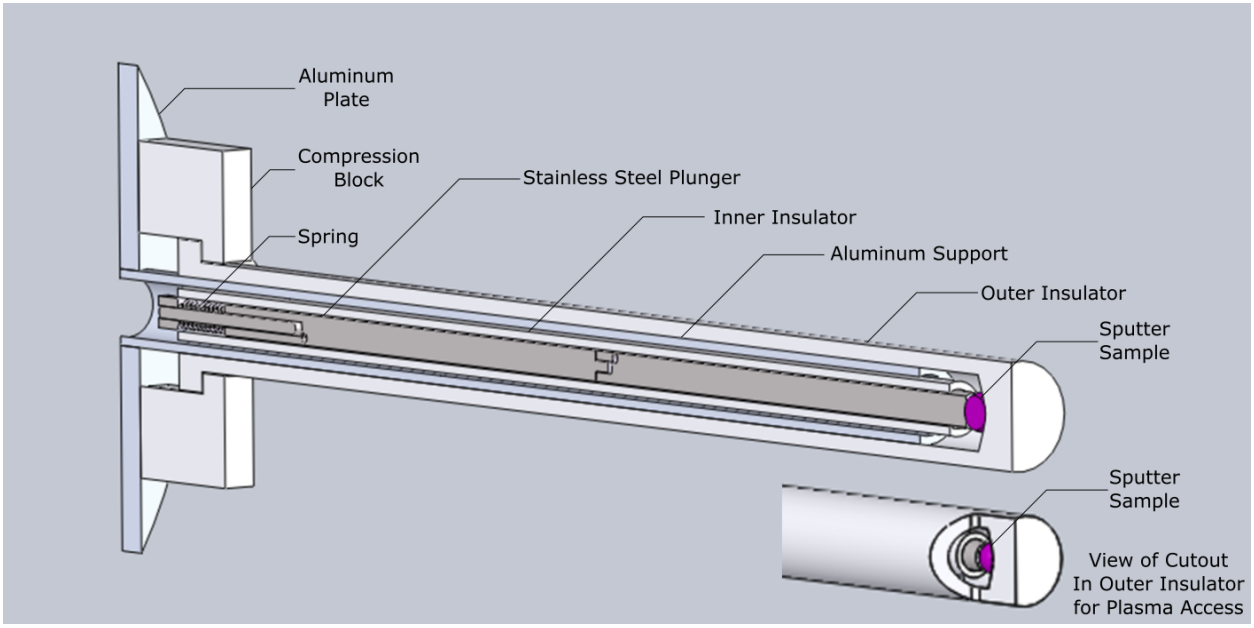

Figure 2.19: Cross section of radial sputtering probe for SuSI. The sputtering voltage is passed from the spring and plunger assembly through a wire inside the oven port to a vacuum feedthrough. The outer insulator protruded 14.5 cm from the injection baffle and was 11.4 mm in diameter.

Radial sputtering on SuSI was performed by inserting a dielectric probe with a metallic sample at the end along the plasma chamber wall. The probe was made primarily of a machinable glass ceramic insulator 11.4 mm in diameter and 14.5 cm long with a coaxial metal plunger and spring assembly both holding the sample mechanically in place and elec-

trically connecting the sample to the high voltage supply as shown in Fig. 2.19. A window in the insulator at the sample location was machined so the plasma would interact with the sputter sample exclusively when biased. A small (≈4 mm) spheroidal metal sample (bead) was held mechanically in place with a spring loaded metal plunger that also provided the electrical connection to the sample. The probe was installed on the injection baffle in between the electron loss surfaces (flutes) between the magnetic poles.

2.6.6 ARTEMIS Axial and Radial Sputtering Probes

Sputtering on ARTEMIS was performed with both radial and axial geometries. The axial sputtering system works in a similar manner to the system on SuSI with a sample attached to an electrically biased longitudinally movable rod. The sputter sample was water cooled and interchangeable with samples on the SuSI assembly. However unlike on SuSI, ARTEMIS relies on an iron yoke to increase the magnetic field at injection. Drilling a hole through the center of the iron yoke (visible in Fig. 2.20) to accommodate the sputter probe, resulted in the magnetic field on axis being reduced by about 30%.

Radial sputtering was performed by inserting a conductive rod with sputter sample at the end into the radial port on the source visible in Fig. 2.21. The sputter probe was mounted on a linear drive allowing for radial movement of the probe. Use of the radial ports place the probe azimuthally in between pole tips of the hexapole and longitudinally near the magnetic minimum.

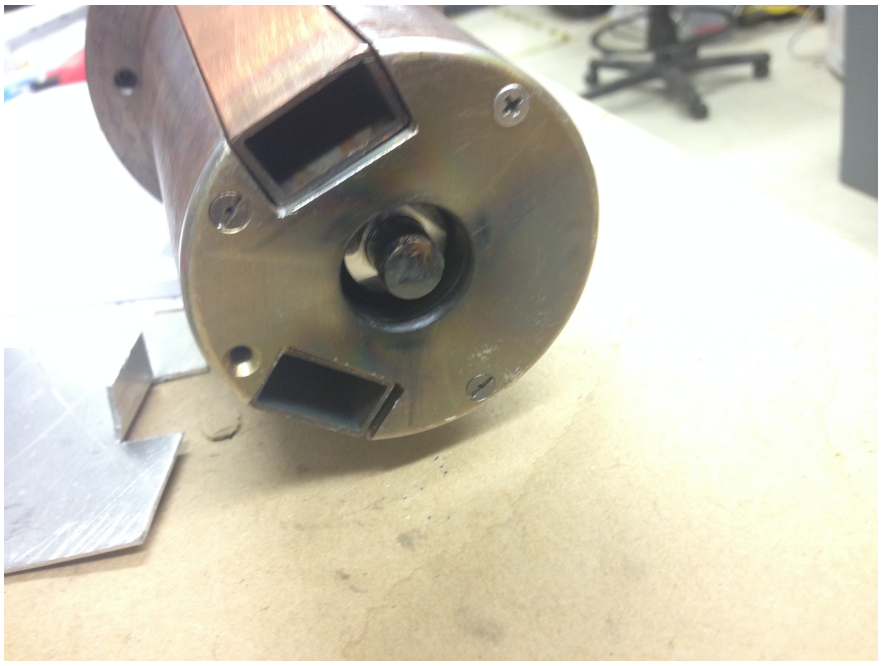

Figure 2.20: ARTEMIS axial sputtering probe viewed from the end of the injection assembly. Note the the copper waveguides for RF power input on the periphery of the iron plug. The axial sputter probe with uranium sample was along the axis of the injection assembly.

Figure 2.21: ARTEMIS radial sputtering probe with aluminum sample holder and uranium sample attached. The sputter probe was passed through the radial slots in the plasma chamber and was positioned at a depth within millimeters of the plasma chamber wall.

Chapter 3

Initial Experiments with Pulsed Sputtering

The purpose of this chapter is to highlight the engineering challenge that went into performing a pulsed sputtering experiment on SuSI. The first pulsed sputtering experiments were carried out using an axial sputter probe further described in Sect. 2.6.4. The axial sputter probe was designed to allow SuSI to provide high intensity steady state uranium beams to CCF at MSU. Over the course of experiments using the axial sputtering geometry, it became clear that some process other than ionization and ion confinement was dominating the beam current waveforms. The clear trends with peaking time increasing with charge state observed in Refs. [97, 25] did not materialize using the axial sputtering probe on SuSI. Notably, characteristic times did not vary with charge state or magnetic field.

In order to determine if axial sputtering was appropriate to conduct a pulsed sputtering experiment, the effect of sputter probe position with respect to the magnetic field on the beam current waveform was investigated using the 14 GHz normal conducting ion source ARTEMIS. Radial and axial sputtering assemblies were installed simultaneously on the ion source. As further explained in Sect. 2.6.6, axial sputtering produced fast (< 1 ms) bursts of beam current whereas radial sputtering did not. Furthermore, radial sputtering exhibited an increase in time structure with extracted charge states, whereas axial sputtering did not.

As a result, radial sputtering was selected as the preferred method to conduct the pulsed sputtering experiment.

A radial sputtering probe, developed for steady state beam production, became available for SuSI concurrently with the experiments on ARTEMIS comparing axial and radial pulsed sputtering geometries (see Sect. 3.2). A short pulsed sputtering experiment was conducted using extra time at the end of a molybdenum CCF run. The results, covered in Sect. 3.3 of this chapter, demonstrated that the radial sputtering apparatus could be pulsed and the resulting beam current waveforms were free from the beam current bursts described in Sect. 3.1 and Sect. 3.2 of this chapter. The position of the sputter sample with respect to the magnetic field was essential to probe the ion production and confinement processes free from unnecessary perturbation. Specifically, a radial geometry with the sputter sample positioned in between the hexapole tips was the preferred location. The sputter sample did not need to be located at the magnetic minimum to emulate radial pulsed sputtering such as that performed with AECR type ion sources such as ARTEMIS or ECR2. This demonstration cleared the way to perform a systematic study of ion timescales on SuSI specifically designed to determine if there was a correlation between a hotter, denser electron population and ion confinement.

3.1 Axial Sputtering on SuSI

3.1.1 Overview

The pulsed sputtering experiments were designed to determine if the bremsstrahlung produced by hot electrons could be correlated to beam current peaking time (discussed in Sect. 2.4.4). The hot electron temperature was envisioned to be controlled with the mag-

netic minimum as demonstrated by J. Benitez et al. in Ref. [3] and if hot electrons played a role in ion confinement then higher temperatures should increase the confinement well of ions increasing their characteristic timescales in the ion source. Additionally, the time structure of the beam current waveforms was sampled as a function of charge state. If the waveform timescales increased with charge state then pulsed sputtering was probing ion production and confinement times. The axial sputtering probe was used for SuSI and it was quickly found that sputtering times on the order of 500 μs did not produce a measurable beam current response for any charge state necessitating the use of longer millisecond sputtering times. The beam current waveforms from the millisecond sputtering times did not manifest any features that scaled with charge state or magnetic field. Suspicions about the similarities with axial pulsed sputtering and pulsed bias disc experiments resulted in a direct comparison of axial and radial pulsed sputtering geometries on ARTEMIS covered in Sect. 3.2.

3.1.2 Experimental Set-up

For these experiments the sputtering voltage was -500 V applied for 2-3 ms. Shorter sputtering times were briefly explored, but the beam current waveforms were too low in amplitude for measurement. Long repetition periods (30-50 times the pulse duration) were taken to ensure that the uranium current would decay away before the next pulse arrived. Sputtering was done in an oxygen plasma and care was taken to ensure the CSD was peaked on O^{6+} for each of the two magnetic fields explored in the experiment. The least aggressive probe depth and lowest voltage that produced usable (hundreds of nano-amperes) of uranium currents were used. Therefore, the uranium was a small perturbation to the oxygen plasma and constituted no more than 1% of the extracted oxygen current for constant application of sputtering voltage. The sputter probe was driven with a high voltage switch using the

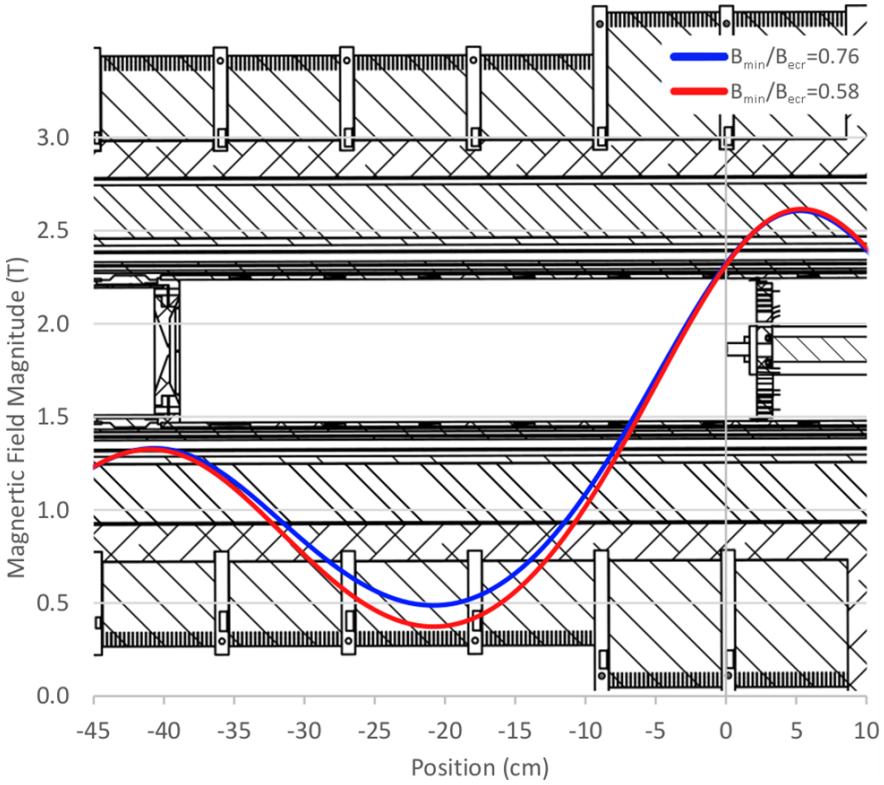

Figure 3.1: SuSI axial uranium sputter probe and injection baffle with respect to the solenoidal magnetic field. The axial projection of the two different magnetic fields used in Figs. 3.4 and 3.5 are plotted from POISSON simulations.

set-up described in Sect. 2.6.3.

Two magnetic field configurations were selected with B_{min}/B_{ecr}=0.58 and B_{min}/B_{ecr}=0.76. Care was taken to keep the injection and extraction peak field magnitudes fixed to less than a percent of each other. The magnetic minimum was changed as shown schematically from POISSON [24] magnetic field simulations in Fig. 3.1. The hexapole magnet remained constant and was set to 1.25 T at the chamber wall. Axial bremsstrahlung measurements showed that raising the minimum also generated higher energy x-rays, and the Kβ1, Kα1, and Kα2 emission lines of uranium were clearly observed in descending order of energy in Fig. 3.2. This was likely caused by fluorescence off of the uranium sputter target within the geometric acceptance cone of the x-ray collimators. In both cases the same microwave power of 700 W

Parameter	B_{min}/B_{ecr}=0.58	B_{min}/B_{ecr}=0.76
Injection Pressure	$6.9{\cdot}10^{-8}$ mbar	$7.2{\cdot}10^{-8}$ mbar
Extraction Pressure	$5.3{\cdot}10^{-9}$ mbar	$6.5{\cdot}10^{-9}$ mbar
Microwave Power	700 W	700 W
Sputter Voltage	-500 V	-500 V
Platform Potential	+20 kV	+20 kV
Drain Current	0.73 mA	0.89 mA
O^{8+} (μA)	3.6	11
O^{6+} (μA)	53	99
O^{4+} (μA)	34	64
O^{2+} (μA)	38	87

Table 3.1: Table of operating parameters for axial sputtering of uranium on SuSI

was applied and oxygen gas flow unchanged. Basic source parameters are tabulated in Table 3.1. The magnetic field minimum in addition to increasing total axial x-ray emission and shifting the recorded bremsstrahlung spectra to higher energies, moves the uranium CSD to peak on higher charge states as shown in Fig. 3.3. Oxygen also responded to the change in magnetic field by producing 63% more O^{7+} current for B_{min}/B_{ecr}=0.76 as compared to B_{min}/B_{ecr}=0.58.

3.1.3 Results and Discussion

The uranium current was characterized by current bursts at the leading and trailing edge of the pulse as shown in Figs. 3.4 and 3.5 for all charge states and magnetic fields selected. The beam current waveforms were averaged over 16 events and have been normalized to the steady state uranium current of each charge state. The current bursts (on leading and trailing edge of the sputtering pulse) occurred at the same time for every charge state and the full width at half maximum of the current burst after the sputter voltage was turned off was 2.5±0.3 ms for B_{min}/B_{ecr}=0.58 and 3.6±0.5 ms for B_{min}/B_{ecr}=0.76. The decay

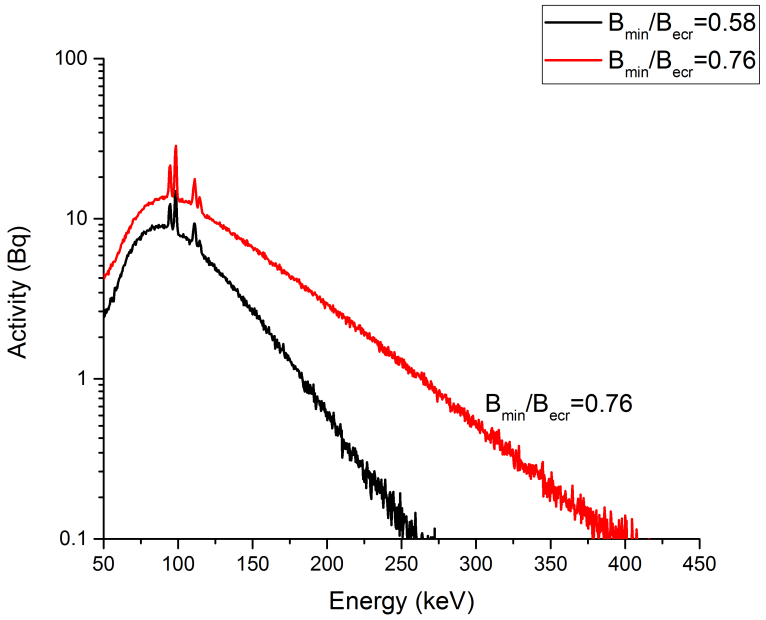

Figure 3.2: Axial bremsstrahlung emission from SuSI for 700 W applied microwave power and for the two magnetic fields shown in Fig. 3.1. The K shell uranium lines were likely caused by x-ray fluorescence of the uranium sputter sample.

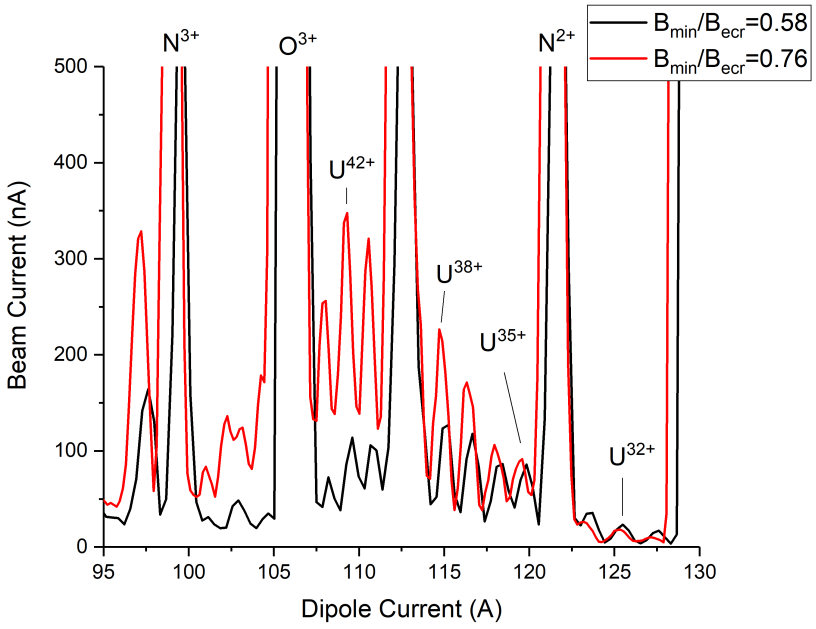

Figure 3.3: Charge state distribution of steady state uranium for -500 V applied to the sputter sample. A clear shift to higher charge states was observed with the higher B_{min}/B_{ecr}(magnetic field minimum), and produced brighter and higher energy x-rays as shown in Fig. 3.2.

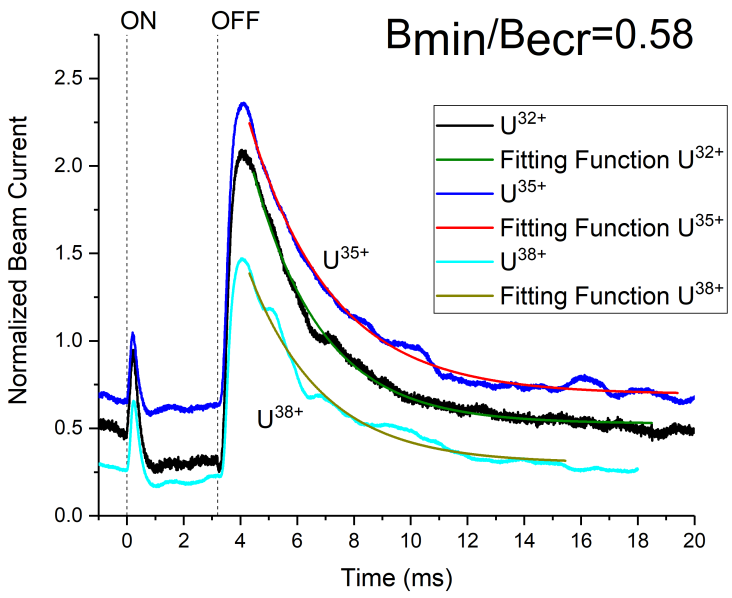

Figure 3.4: Uranium beam current normalized to the steady state current at -500 V applied to the sputter sample (see Fig. 3.3 for current magnitudes). The high voltage was applied for 3.2 ms, and with the beam current decay fitted with an exponential function.

portion following the high voltage pulse contains information about ion confinement when fitted with an exponential decay function (see Sect. 4.2.2). The beam current waveform was fitted between 97% of the peak current and when the average pre-pulse current was reached. Decay times from fitting the waveforms in Figs. 3.4 and 3.5 are shown in Table 3.2. The decay times did not show a trend with either charge state or magnetic field, therefore it is unlikely the measured beam current structure was correlated to stepwise ionization or confinement processes in a manner to extract additional information.

Peaking time did not scale with charge state for either B_{min}/B_{ecr}=0.58 or B_{min}/B_{ecr}=0.76 magnetic field configurations. Instead, fast bursts of uranium current were observed hundreds of microseconds after the leading and trailing edge of the high voltage sputtering pulse. The decay time of the trailing edge pulse was fitted with an exponential decay function but no trend was observed as a function of charge state leading to major doubts about the valid-

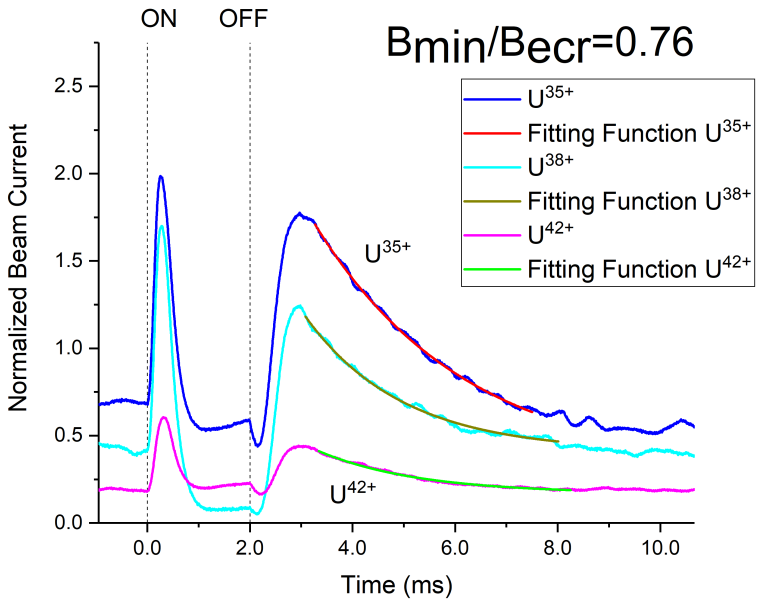

Figure 3.5: Uranium beam current normalized to the steady state current at -500 V applied to the sputter sample (see Fig. 3.3 for current magnitudes). The high voltage was applied for 2.0 ms, and with the beam current decay fitted with an exponential function.

	Decay Time (ms)	
Charge State	**B_{min}/B_{ecr}=0.58**	**B_{min}/B_{ecr}=0.76**
U^{32+}	2.4	N/A
U^{35+}	2.9	2.9
U^{38+}	2.6	1.9
U^{42+}	N/A	1.9

Table 3.2: Characteristic decay times from fitting of the beam current waveforms. No clear trend was observed in either charge state or magnetic field.

ity of our set-up to probe ion processes. Similar effects were observed during pulsed bias disc experiments [75, 88] suggesting the beam current waveforms were more strongly correlated to electrons responding to the negative sputtering voltage.

3.2 Direct Comparison of Axial and Radial Sputtering Geometries on ARTEMIS

3.2.1 Overview

Experiments on SuSI with axial pulsed sputtering (see Sect. 3.1) found the beam current waveforms to have similar structure with charge state and magnetic minimum. The axial pulsed sputtering method produced waveforms (see Figs. 3.4 and 3.5) similar to pulsed bias disc waveforms in Refs. [75, 88]. The axial sputtering probe was similar in geometry to a bias disc.

To investigate the impact of pulsed sputtering geometry on beam current waveform the 2^{nd} generation 14 GHz ECR ion source ARTEMIS was loaded with an axial and radial uranium sputter probe. A clear difference between radial and axial pulsed sputtering was observed, with axial sputtering generating a current burst as the sputtering voltage was removed, whereas radial sputtering did not. Radial sputtering was the best method to perform a pulsed sputtering experiment.

3.2.2 Experimental Set-up

The axial sputter system on ARTEMIS was designed to support CCF operations and was heavily influenced by the axial sputter system for SuSI. The same sputter sample used in

Parameter	Axial Sputtering	Radial Sputtering
Injection Pressure	$1.3{\cdot}10^{-7}$ mbar	$1.2{\cdot}10^{-7}$ mbar
Extraction Pressure	$1.2{\cdot}10^{-7}$ mbar	$1.3{\cdot}10^{-7}$ mbar
Microwave Power	200 W	200 W
Sputter Voltage	-400 V	-600 V
Platform Potential	+17.5 kV	+17.5 kV
Drain Current	2.03 mA	2.09 mA

Table 3.3: ARTEMIS parameters used for the comparison between axial and radial sputtering. Care was taken to ensure they were as similar as possible, the different sputter voltages were used to match the uranium CSDs

Sect. 3.1 was used used. Additional information about the axial sputter probe for ARTEMIS may be found in Sect. 2.6.6.

The high voltage pulse was transferred to both the axial and radial sputter probes via a split coaxial cable. The central conductor was attached to the sputter probe and the return path was bolted to the ion source vacuum vessel. This configuration was found to have rise and fall times of 50 ns and 60 ns respectively for -400 V applied to the radial probe. The axial probe was connected in a similar manner, but a copper grounding bar was installed to the vacuum vessel allowing for the shortest electrical return path possible. The axial sputter probe exhibited the same characteristic rise and fall times as the radial probe.

Both probes were initially installed in the fully retracted position. The sputter depths were adjusted independently in steps of 1 mm and the sputter voltage turned on to see if uranium was present in the CSD. The process continued until hundreds of nanoamperes were observed for about -500 V applied and negligible direct feeding was observed. At this point the axial probe protruded 6 mm from the iron plug face and the radial probe 2 mm from the plasma chamber wall. The probes and operational depths are shown schematically in Fig. 3.6 in reference to the simulated axial magnetic field.

Axial and radial sputtering geometries were compared with each other with an oxygen plasma using the same magnetic field. Care was taken to ensure similar plasma conditions and are summarized in Table 3.3 where the difference in axial sputter voltage ensured the axial steady state uranium CSD matched that measured for the radial geometry. The CSDs in both cases were peaked on U^{27+} and O^{6+}. However, only one sputter probe could be pulsed (biased) at a time and the transition between the two methods was performed within a half hour with the ion source turned off. The sputter probe not in use was shorted to the platform potential to make sure that any charge transferred by the plasma would not build up and perturb the measurement. The magnetic field of the operating point was adjusted to provide the highest charge states of uranium (and oxygen) to better emulate the oxygen plasma sampled on SuSI in Sect. 3.1.

3.2.3 Results

The primary difference between radial and axial pulsed sputtering waveforms was a strong rapid current burst (up to 10 times the steady state current) was observed with the axial sputtering in Fig. 3.7a and was absent with radial sputtering in Fig. 3.7b. The waveforms were fitted with an exponential function 18 ms after the high voltage probe was turned off to generate 1/e decay times that treated each method consistently. The constant delay removed all effects of the current burst characteristic of axial sputtering. The 1/e decay times from the fitting function are presented in Fig. 3.8. The 1/e decay times with radial sputtering increased with charge state. Neither the axial or radial measurements exhibited strong separation of decay time with charge state and was likely due to the combined effects of shot-shot variance and the narrow range of charge states sampled. The waveforms generated with the axial probe decayed faster for any charge state than that generated with the radial

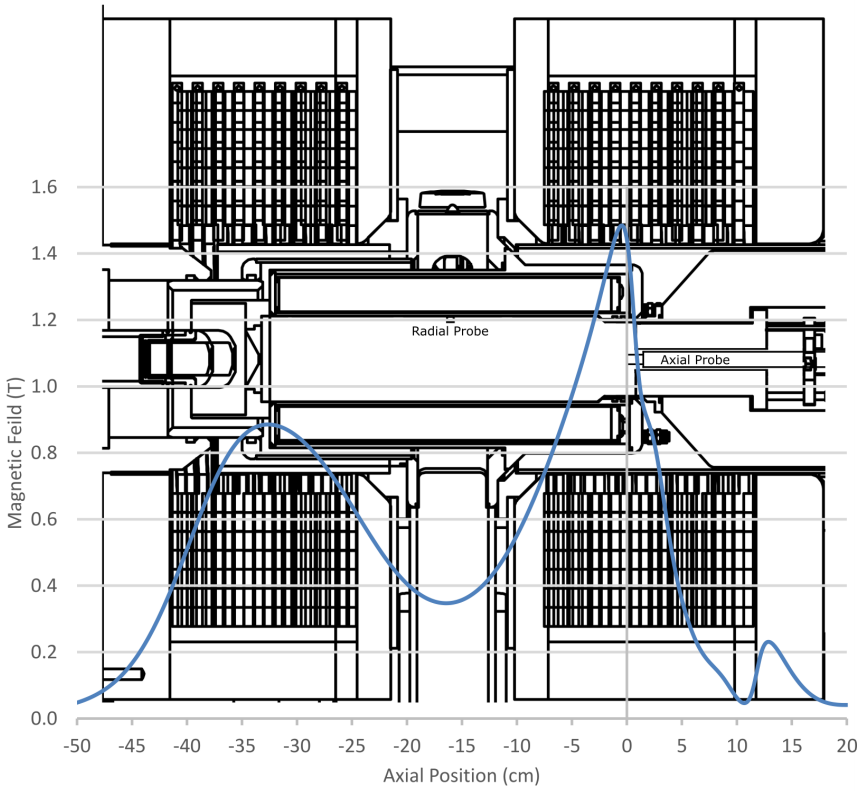

Figure 3.6: The on-axis projection of the ARTEMIS magnetic field used to compare axial and radial sputtering geometries. The axial and radial sputtering probes appear at the corresponding positions used in the experiment.

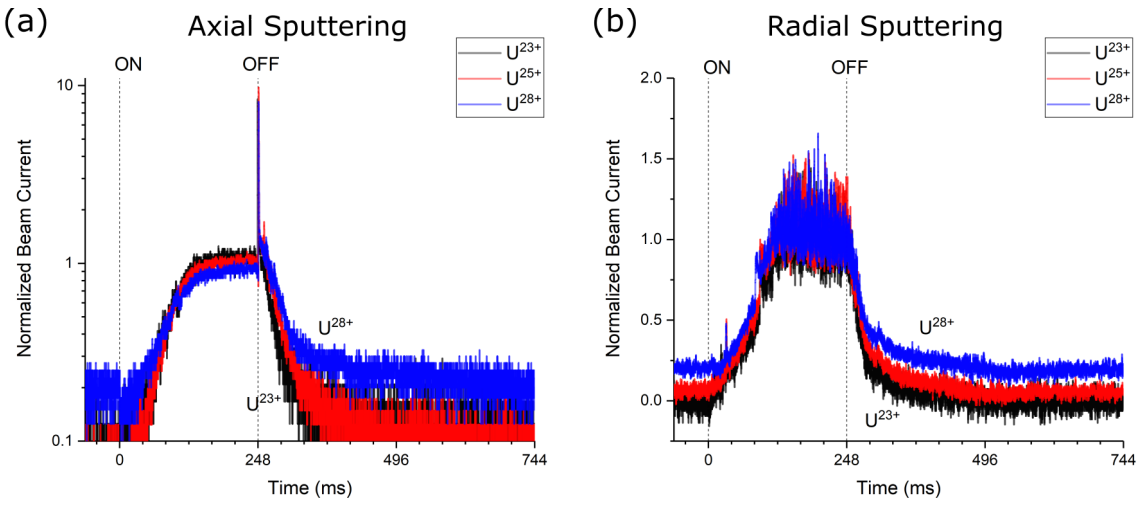

Figure 3.7: Uranium beam current normalized to the steady state current on ARTEMIS for axial sputtering (a) and radial sputtering (b). The sputtering pulse was applied every 1.2 seconds. An exponential decay function was fitted 30 ms after the high voltage was turned off to remove the current burst from the fitting.

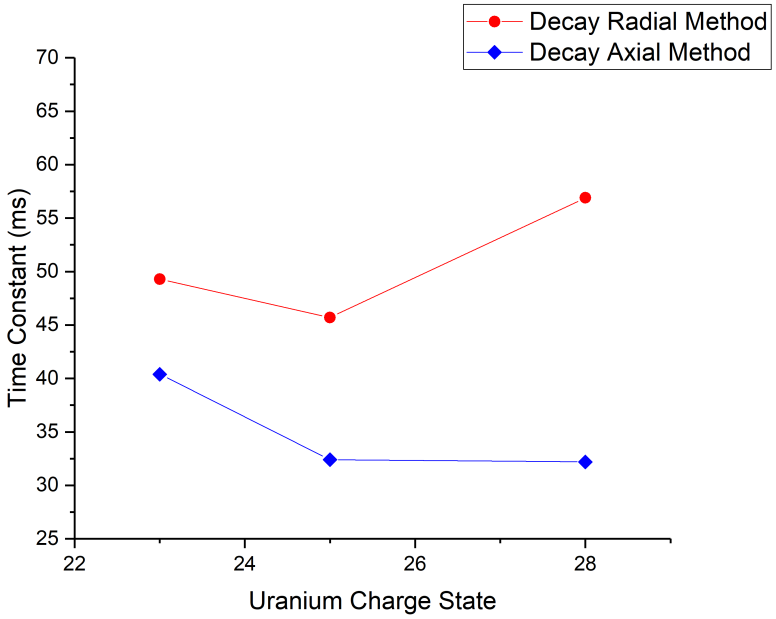

Figure 3.8: Exponential decay time constants from fitting of beam current waveforms in Figs. 3.7a and 3.7b.

probe (on similar plasma conditions) suggesting that the axial sputtering voltage changed the plasma in a significant way.

High voltage pulse duration impacted the amplitude of the current pulse observed for both the radial and axial sputtering geometries. In both cases, pulse durations shorter than about 2 ms produced current bursts that were undetectable. Axial sputtering of U^{25+} exhibited a strong burst of current when the sputter sample was grounded as shown in Figs. 3.7a and 3.9, current amplitudes peaked at 8 times the steady state beam current for an applied sputter voltage duration of 120 ms. The axial beam current bursts decreased in amplitude with decreasing pulse duration, and had Full Width at Half Maxima (FWHM) that decreased with increasing pulse duration as shown in Fig. 3.9. The 19 ms pulse FWHM was 4.8±0.4 ms decreasing to 0.8±0.2 ms for 200 ms pulse width. The shortest axial pulse, 2 ms, did not match the trend and had a FWHM of 2.1±1 ms. In the cases where beam

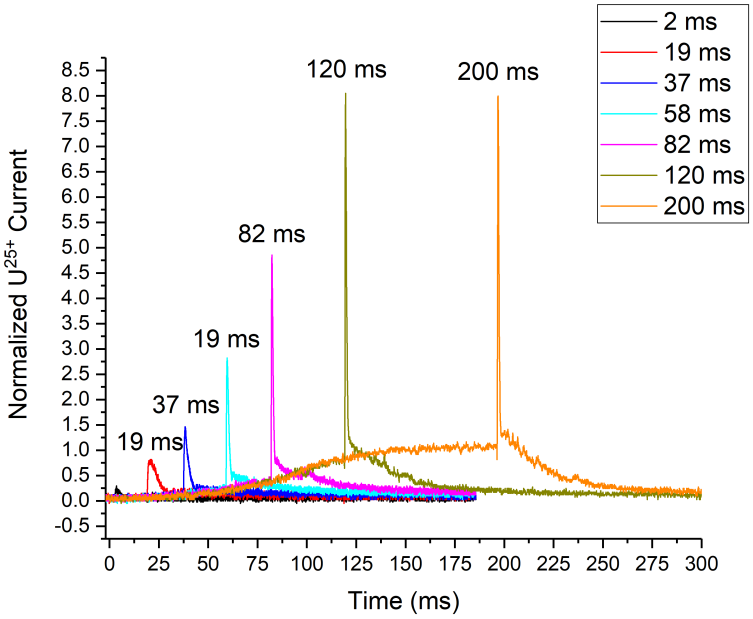

Figure 3.9: Response of U^{25+} beam current to axial sputtering on ARTEMIS normalized to the steady state current. Pulses up to and less than 82 ms duration repeated every 600 ms whereas pulses longer than that repeated five times longer than the pulse length (20% duty cycle).

current was allowed to build up to steady state values, U^{25+} was observed to decay away after the current burst at a rate slow enough to be suggestive of ionization or confinement processes.

Radial sputtering rose and fell without any beam current bursts as can be seen in Fig. 3.10, furthermore sputtering with a 2 ms pulse length generated a peaking time in U^{28+} current about 23 ms after the voltage was removed. This was similar to the behavior reported in Ref. [97], however 2 ms was the shortest sputtering time that produced a measurable beam current response on ARTEMIS.

The comparison between radial and axial pulsed sputtering on ARTEMIS suggests that radial pulsed sputtering is the least perturbative method. Radial sputtering did not produce fast (< 5 ms) bursts of beam current that was characteristic of axial pulsed sputtering. These

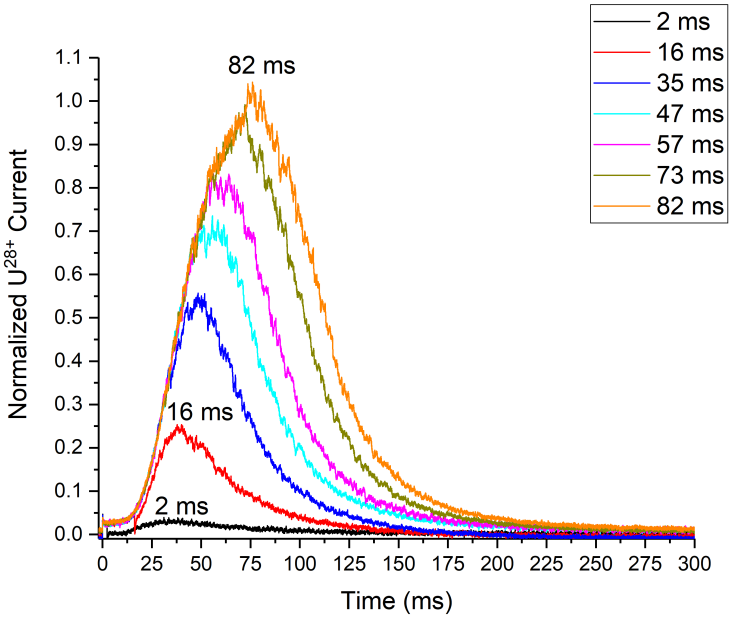

Figure 3.10: Response of U^{28+} beam current to radial sputtering on ARTEMIS normalized to the steady state current. Sputtering pulses repeated every 600 ms.

beam current bursts most closely resembled the waveforms observed on SuSI with an axial uranium probe (see Figs. 3.4 and 3.5) and the waveforms characteristic of pulsed bias disc experiments in Refs. [75, 88]. Since the axial sputter probe was in the same location and was of similar size to a bias disc it makes sense that electron modulation analogous to that induced by bias discs would be a characteristic behavior of this geometry. The bias disc and its purpose is described in Sect. 2.4.2.

3.3 Radial Sputtering on SuSI with Molybdenum

3.3.1 Overview

Experiments comparing radial and axial sputtering geometries on ARTEMIS covered in Sect. 3.2 suggested that radial sputtering was the ideal technique to probe ion confinement

time. Lacking radial ports, radial sputtering on SuSI represented a unique challenge. Fortuitously, a radial sputtering apparatus for SuSI became available concurrently with the experiments in Sect. 3.2. The new radial sputter probe for SuSI is described in Sect. 2.6.5. It was not known if such an apparatus would produce pulsed sputtering characteristics more closely related to radial or axial sputtering since the probe was passed from the injection baffle and did not reach the magnetic minimum. Preliminary tests were conducted with molybdenum in symbiosis with the CCF metallic beam development program.

A short experiment was devised to evaluate the pulsed sputtering properties of the radial probe on SuSI. Magnetic field configurations were borrowed from a preceding experiment for the development of steady state molybdenum beams for the CCF. Two magnetic field configurations were used: B_{min}/B_{ecr}=0.58 and B_{min}/B_{ecr}=0.49 selected so to maintain constant injection and extraction magnetic fields while changing the magnetic minimum. The magnetic field configuration B_{min}/B_{ecr}=0.49 was optimized during the beam development experiment for steady state molybdenum production and differs from the fields used in Sect. 3.1.

3.3.2 Experimental Set-up

The sputter probe was pulsed with -1.5 kV for 80 ms repeating every 9 s. The beam current response is plotted in Fig. 3.11 for the two different magnetic field configurations. The beam current behaved in a similar manner to purely radial sputtering on ARTEMIS (covered in Sect. 3.2 of this chapter). Three independent sputtering events were sampled, fitted independently, and averaged for the 1/e decay time. Single sputtering events are shown in Fig. 3.11 along with the exponential fitting function.

Parameter	**B_{min}/B_{ecr}=0.49**	**B_{min}/B_{ecr}=0.58**
Injection Pressure	$1.3{\cdot}10^{-7}$ mbar	$1.6{\cdot}10^{-7}$ mbar
Extraction Pressure	$2.4{\cdot}10^{-8}$ mbar	$2.7{\cdot}10^{-8}$ mbar
Microwave Power	400 W	400 W
Sputter Voltage	-1500 V	-1500 V
Platform Potential	+20 kV	+20 kV
Drain Current	1.74 mA	1.76 mA
O^{8+} (μA)	0	0
O^{6+} (μA)	23	17
O^{4+} (μA)	50	83
O^{2+} (μA)	98	68

Table 3.4: SuSI source parameters used to compare the two different magnetic field configurations.

3.3.3 Results and Discussion

The radial probe for SuSI produced beam current waveforms free from the current bursts observed in Sect. 3.1 and Sect. 3.2. Mo^{18+} decayed with a characteristic time of 34±4 ms and 66±1 ms for B_{min}/B_{ecr}=0.49 and B_{min}/B_{ecr}=0.58 respectively. The clear increase in beam current decay time with magnetic minimum was encouraging, specifically because the magnetic minimum scales linearly with hot electron temperature [3]. This suggested a correlation between hot electron temperature and decay time for Mo^{18+} current in spite of the fact that no x-ray detector was used coincidentally with this measurement. The combination of a pulsed radial sputtering measurement coincidental with bremsstrahlung measurement was implemented in experiments on SuSI covered in Chapter 4.

The initial success with radial pulsed sputtering on SuSI paved a way for systematic measurements probing different magnetic field configurations and microwave powers. The radial probe for SuSI eliminated the fast bursts of current (FWHM $<$ 5 ms) that were seen during axial sputtering on SuSI (see Sect. 3.1) and ARTEMIS (see Sect. 3.2). A comparison

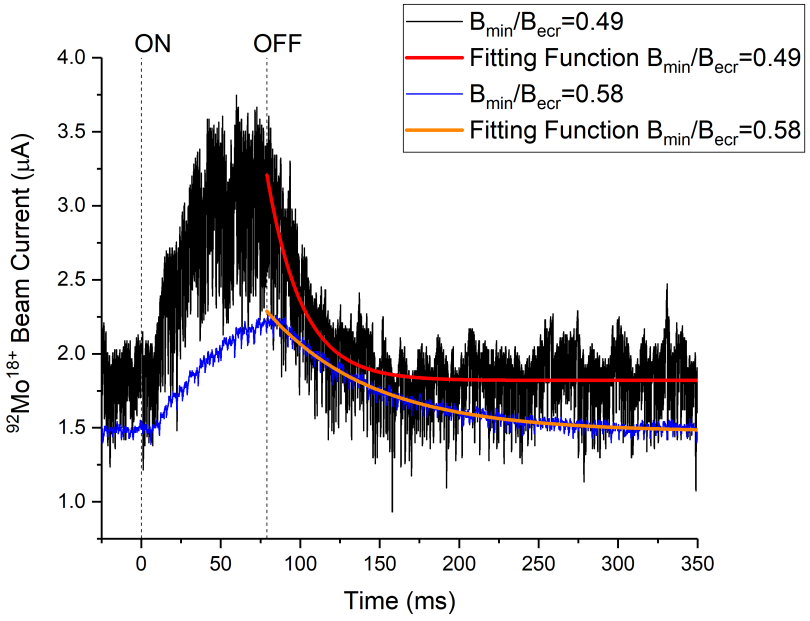

Figure 3.11: Beam current waveforms before, during, and after the application of -1.5 kV to the sputter sample for 80 ms. Fitting with exponential decay function starting after the high voltage was turned off. Mo^{18+} decayed with a characteristic time of 22±2 ms and 66±1 ms for B_{min}/B_{ecr}=0.49 and B_{min}/B_{ecr}=0.58 respectively.

between sputtering waveforms of Mo^{18+} produced at B_{min}/B_{ecr}=0.49 and B_{min}/B_{ecr}=0.58 when controlled for microwave power and pressure indicated that raising the magnetic minimum increased the decay time by a factor of two.

3.4 Final Remarks and Conclusions

Axial pulsed sputtering did not result in useful information about ionization or confinement timescales in either ARTEMIS or SuSI ECR ion sources. Axial sputtering was compared directly to radial sputtering on ARTEMIS to determine if the sputter probe placement with respect to the plasma chamber mattered. These experiments found a significant difference between axial and radial locations and short (< 5 ms) current bursts that could exceed the steady state beam current by a factor of eight in some cases. These bursts were observed for

only the axial sputtering geometry. Therefore, the sputter probe location was found to be crucially important to minimize impact on the plasma.

A proof of concept experiment of a radial sputtering probe for SuSI demonstrated scaling of the characteristic beam current waveform with magnetic minimum. This advance paved a way for systematic experiments further exploring the relationship between characteristic ion timescales and bremsstrahlung from hot electrons as will be presented in Chapter 4.

Chapter 4

Study of Pulsed Sputtering Correlating Hot Electron Temperature to Ion Confinement Time

The objective of the experimental campaign presented herein was to investigate if hot electrons played a role in ion confinement. The SuSI ECR ion source described in Chapter 2 was used exclusively. X-rays were monitored to quantify the hot electron temperature and ion confinement timescales were probed with pulsed sputtering. The plasmas studied were selected to explore the relationship between characteristic ion timescales and magnetic minimum (which determines the hot electron temperature [3]). If hot electrons play a role in ion confinement, then a hotter and better confined electron population should increase the ion confinement time. The extremes of magnetic minimum were explored, in part, because it was not known how sensitive the pulsed sputtering method would be with a variable magnetic field which influences changes in plasma parameters. One consequence was that some plasmas exhibited signs of instability that impacted the pulsed sputtering results.

This chapter will cover in depth how the extracted beam current reacted to different

sputtering times along with analysis on why beam current decay was selected as the figure of merit for confinement time as opposed to the more traditional peaking time. The beam current decay rate is interpreted within an ion density model prescribing an exponential decay as the correct function to fit the beam current. The solution within this simple model relates fitted decay times to ion confinement time showing that beam current decay time is less than the ion confinement time. The decay times are then presented for eleven different plasmas organized by changing microwave heating power and the magnetic field. These decay time measurements are complemented by measured bremsstrahlung spectra and charge state distributions.The chapter concludes with a summary and discussion of the dataset within the context of ion confinement models.

4.1 Experimental Set-up on SuSI

4.1.1 Magnetic Field

The magnetic field was the basis around which the experiment was constructed. Due to the interest in the hot electrons and their relationship with ion confinement, the magnetic field minimum was varied (see Fig. 4.1) thereby varying the hot electron temperature [3]. Six magnetic field configurations were selected: three for 13 GHz operation and three for 18 GHz operation. For a specified frequency, only the magnetic minimum was allowed to change with care taken to maintain injection and extraction field strengths. Each magnetic field was characterized by the ratio of magnetic minimum to the cold electron resonance field or B_{min}/B_{ecr}. The three magnetic field configurations selected for operation at 18 GHz are shown in Fig. 4.1 and three fields selected for 13 GHz operation are shown in Fig. 4.2 from POISSON simulations. Convenient metrics of each of the magnetic field configurations are

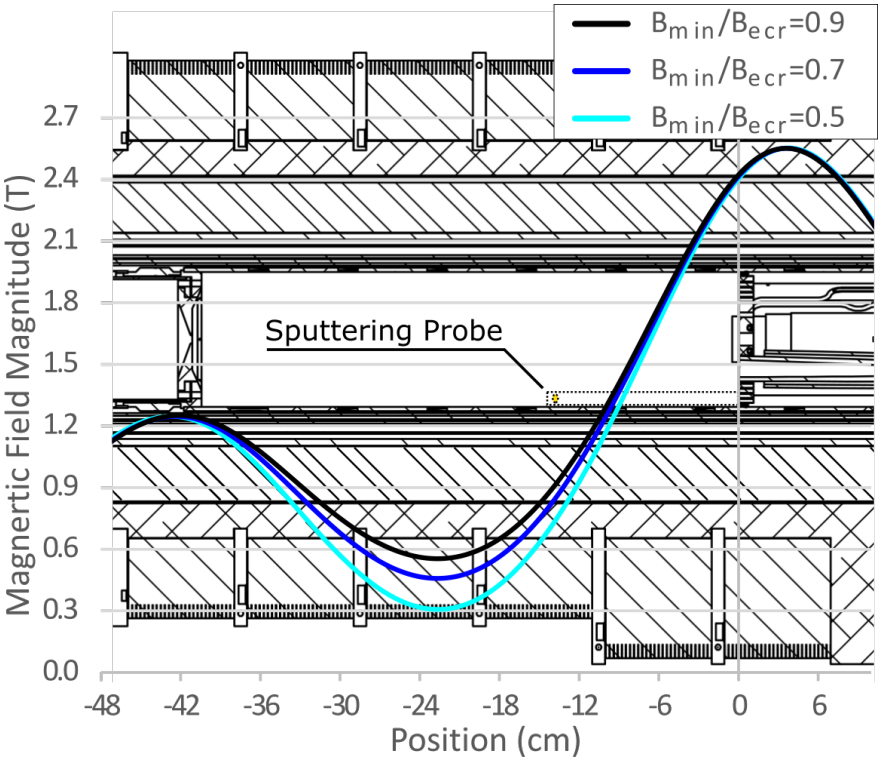

Figure 4.1: Axial magnetic field for 18 GHz operation in reference to the radial sputter probe and ion source.

summarized in Table 4.1. The magnetic field configurations used in the study were scaled by the ratio of the operating frequencies (18/13) to compensate and maintain similar ECR zone sizes. Similarly, the hexapole was scaled with the solenoid field, corresponding to 1.25 T and 0.93 T at the plasma chamber wall for 18 GHz and 13 GHz respectively [45].

The radial sputter probe described in Sect. 2.6.5 appears in Figs. 4.1 and 4.2 as a dotted line offset from the plasma chamber edge because it was mounted out of the cross-section plane in between the pole tips of the hexapole. The sputter probe was not inserted all the way from the injection end to the magnetic minimum at the center of the source. In that regard, it is different from traditional radial sputtering set-ups on AECR type sources [77, 37, 102] where a radial port is available in the vacuum vessel at the location of the magnetic minimum.

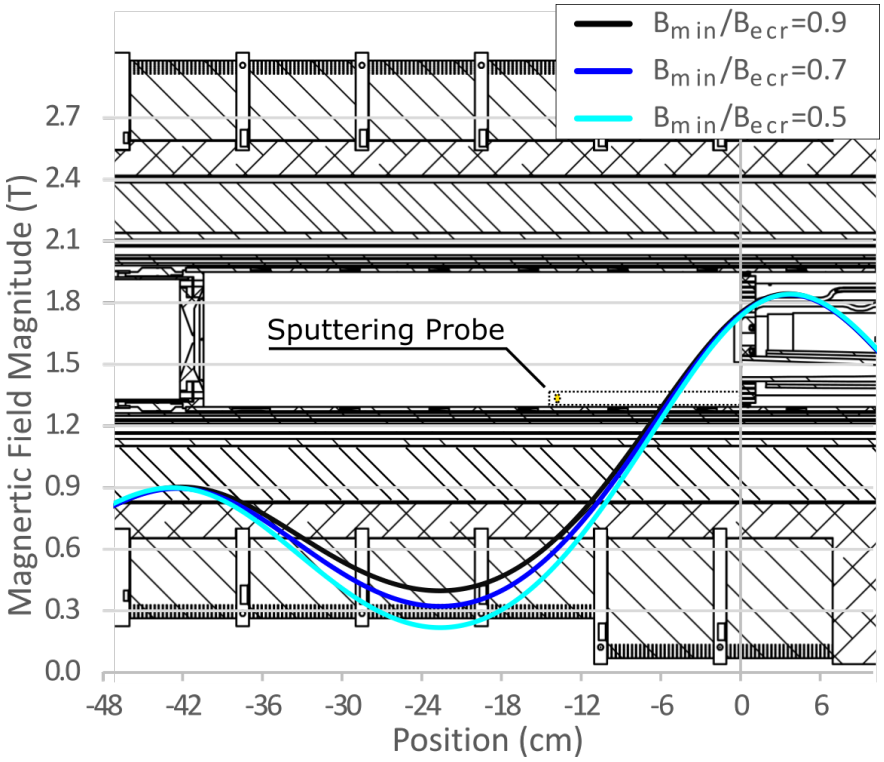

Figure 4.2: Axial magnetic field for 13 GHz operation in reference to the radial sputter probe and ion source.

Frequency	18 GHz				13 GHz		
Rounded B_{min}/B_{ecr}	0.5	0.7	0.8	0.9	0.5	0.7	0.9
B_{min}/B_{ecr}	0.48	0.72	0.77	0.86	0.47	0.69	0.86
B_{min} (T)	0.31	0.46	0.49	0.55	0.22	0.32	0.40
B_{inj} (T)	2.55	2.55	2.55	2.55	1.84	1.84	1.84
B_{ext} (T)	1.25	1.25	1.25	1.25	0.90	0.90	0.90
B_{rad} (T)	1.25	1.25	1.25	1.25	0.93	0.93	0.93
ECR Length (cm)	16.3	12.8	12.3	9.3	16.5	13.0	9.3
B_{ext}/B_{min}	4.03	2.72	2.55	2.27	4.09	2.81	2.25

Table 4.1: Table of magnetic field parameters calculated using POISSON.

Frequency	18 GHz				13 GHz		
Rounded B_{min}/B_{ecr}	0.5	0.7	0.8	0.9	0.5	0.7	0.9
100 W	✓	✓		✓	✓	✓	✓
200 W	✓	✓		✓			
400 W	✓	✓	✓				

Table 4.2: The parameter space in magnetic field and microwave power that was explored during the experiment, no fewer than six charge states of gold were sampled for operating points.

4.1.2 ECR Ion Source Parameters used for the Pulsed Sputtering Experiment

In addition to the magnetic field configuration, the microwave power into the source was varied with 100 W, 200 W, and 400 W coupled into the magnetic fields at 18 GHz. In the special case of B_{min}/B_{ecr}=0.9, 400 W could not be applied without risk of sputter sample damage (discussed in more detail within this section) and instead the field B_{min}/B_{ecr}=0.8 was used. Operation at 13 GHz was assigned only 100 W of microwave power because of high reflected power from the transmission line. In all conditions, oxygen was used to sustain the ECR discharge. Each combination of magnetic field, microwave power, and driving frequency provided different plasmas for the measurements. In total 12 different oxygen plasmas were studied the parameters of which are summarized in Table 4.2.

The radial probe for SuSI as described in Sect. 2.6.5 was used throughout the study. Initially, bismuth was used as the sputter sample. As the source was being conditioned at microwave powers above 400 W at 18 GHz, direct feeding was observed. Direct feeding, wherein the ECR plasma etches the sputter assembly including the sputter sample and insulator material regardless of the applied voltage on the probe was a major limiting factor for optimizing the microwave power injected into the ion source throughout the experiment.

Operating the ion source at microwave powers of around 500-600 W triggered the expansion of the edge of the plasma that lead to the etching of the machinable glass outer insulator and sputter sample. One instance of this is shown in Fig. 4.3 where the plasma melted the bismuth sample. Most likely this event was triggered by an instability that caused a run-away of the plasma parameters once the edge plasma touched the bismuth. The platform voltage drain current and injection pressure are plotted and show the strong response to the direct feeding event. This occurred when the ion source was conditioning at a B_{min}/B_{ecr} ratio of 0.7 and 600 W applied microwave power.

After this event, the source had to be vented and the sample was changed to gold which has a much higher melting temperature than bismuth: 1064°C versus 271°C respectively from Ref. [67]. To avoid direct feeding, the highest microwave power explored in the study was capped at 400 W. This limit provided reliable data, except that the magnetic minimum could not be raised to B_{min}/B_{ecr}=0.9 at 400 W without increasing plasma density to a value that made instabilities likely. In order to maintain three different magnetic minima at the 400 W power level a new field was used: B_{min}/B_{ecr}=0.8. However, this magnetic field configuration and microwave power combination proved to be unreliable due to signs of poor conditioning. Figure 4.4 shows how for this operating point the injection and extraction vacuum pressures increased by about 20% when compared to B_{min}/B_{ecr}=0.7. The increased vacuum pressure could have been caused by direct plasma interaction with the radial sputtering probe because the emitted x-ray power (see Sect. 4.2.1) increased by 4.5 times from B_{min}/B_{ecr}=0.7 to B_{min}/B_{ecr}=0.8. In addition, the steady state charge state distribution of gold did not further shift to higher charge states for B_{min}/B_{ecr}=0.8 at 400 W as was consistently observed for 100 W and 200 W datasets (see Table 4.3).

The most consistent beam currents, from systematic variation of the magnetic field,

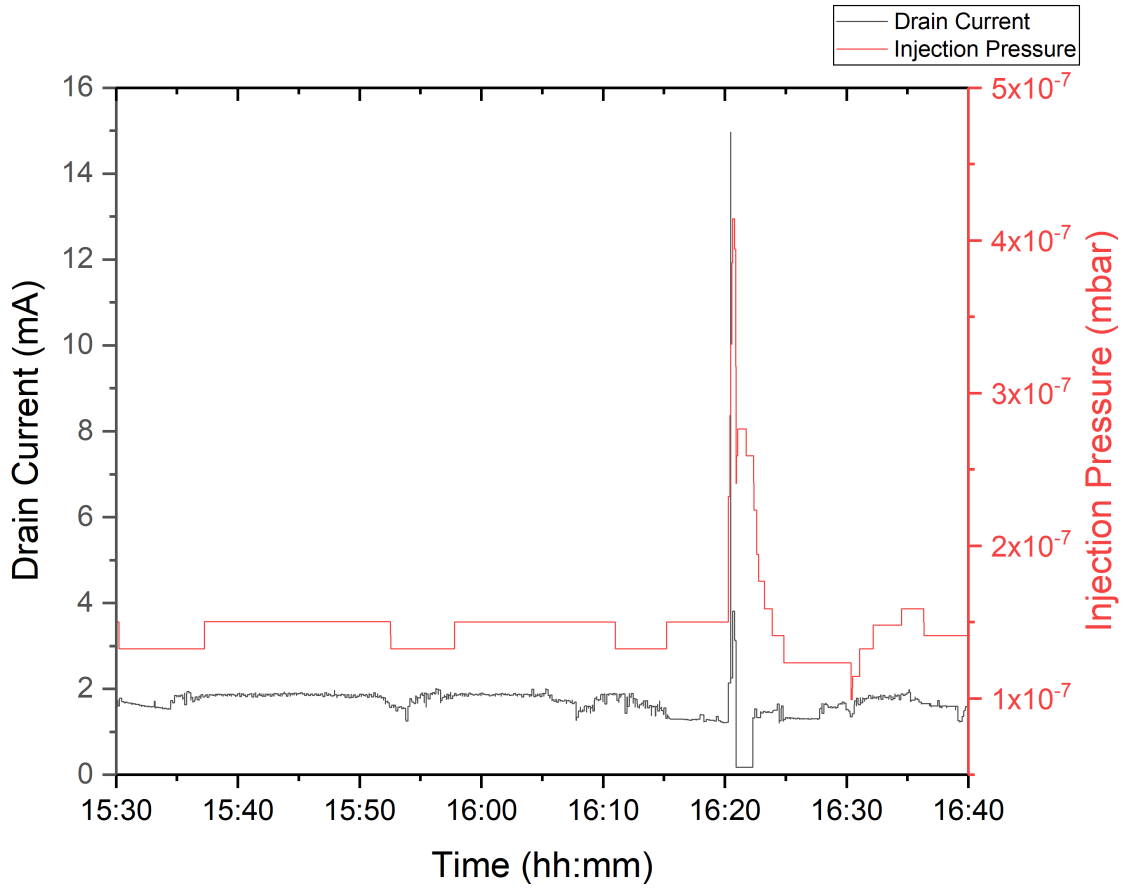

Figure 4.3: Drain current and injection pressure on SuSI before, during, and after the plasma instability that melted the half gram bismuth sputter sample. The instability occurred at approximately 16:20, and was characterized by a sharp increase in the source pressure and drain current. The microwave power was then turned off to investigate what happened resulting in the drain current falling near zero.

were obtained at 100 W and 200 W where the source parameters remained approximately constant with increasing magnetic minimum as shown in Table 4.3. Even at these relatively low microwave powers, when compared to the kilowatts of power needed for the best beam current performances from the source [47], instabilities were observed for B_{min}/B_{ecr}=0.9. The combination of 200 W operation at 18 GHz with B_{min}/B_{ecr}=0.9, the beam current instabilities necessitated masking a portion of the beam current waveform to arrive at an accurate decay time.

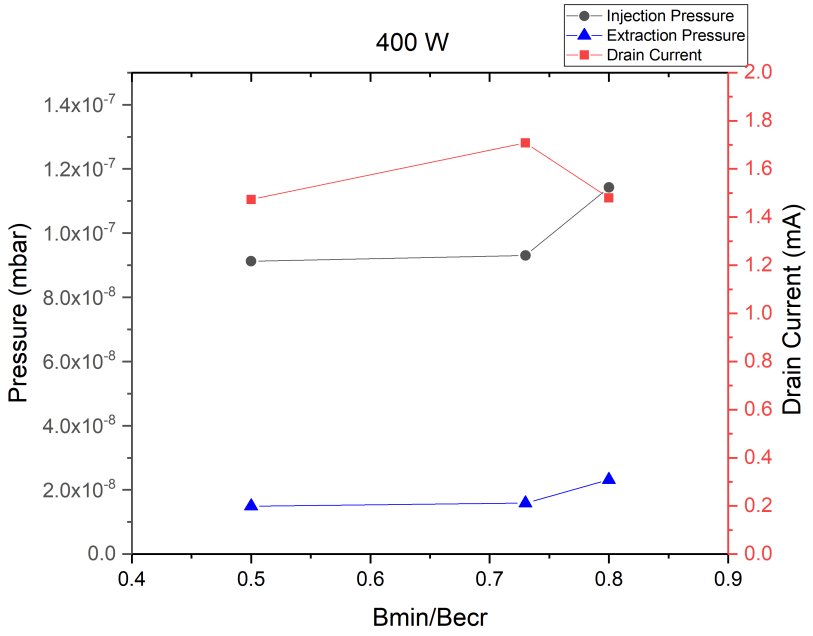

Figure 4.4: Injection and extraction vacuum pressures and high voltage platform drain current plotted as a function of magnetic field for operation at 400 W applied microwave power. Note how pressure increased at B_{min}/B_{ecr}=0.8 indicating the source was poorly conditioned at this field and power combination.

The steady state current produced by sputtering was lower for 13 GHz operation than for 18 GHz. Figure 4.5 shows clearly the reduced currents (by a factor of 6) when controlled for microwave power, magnetic minimum, and ECR zone size. The extracted current from the ion source is proportional to the ion density (see Eq. (2.21)), and sputtering is highly sensitive to plasma density: the sputtering yield depends on the ion density at the sputter sample [35] as well as the probability for sputtered neutrals to be captured by the plasma (ionized) scales with electron density (see Sect. 2.3.1). The measured steady state charge state distributions of gold ions extracted from SuSI provide evidence that higher frequency operation (18 GHz rather than 13 GHz) generated a denser plasma, and is in agreement with well established ideas [18] that higher microwave frequency produces a denser plasma and more beam current.

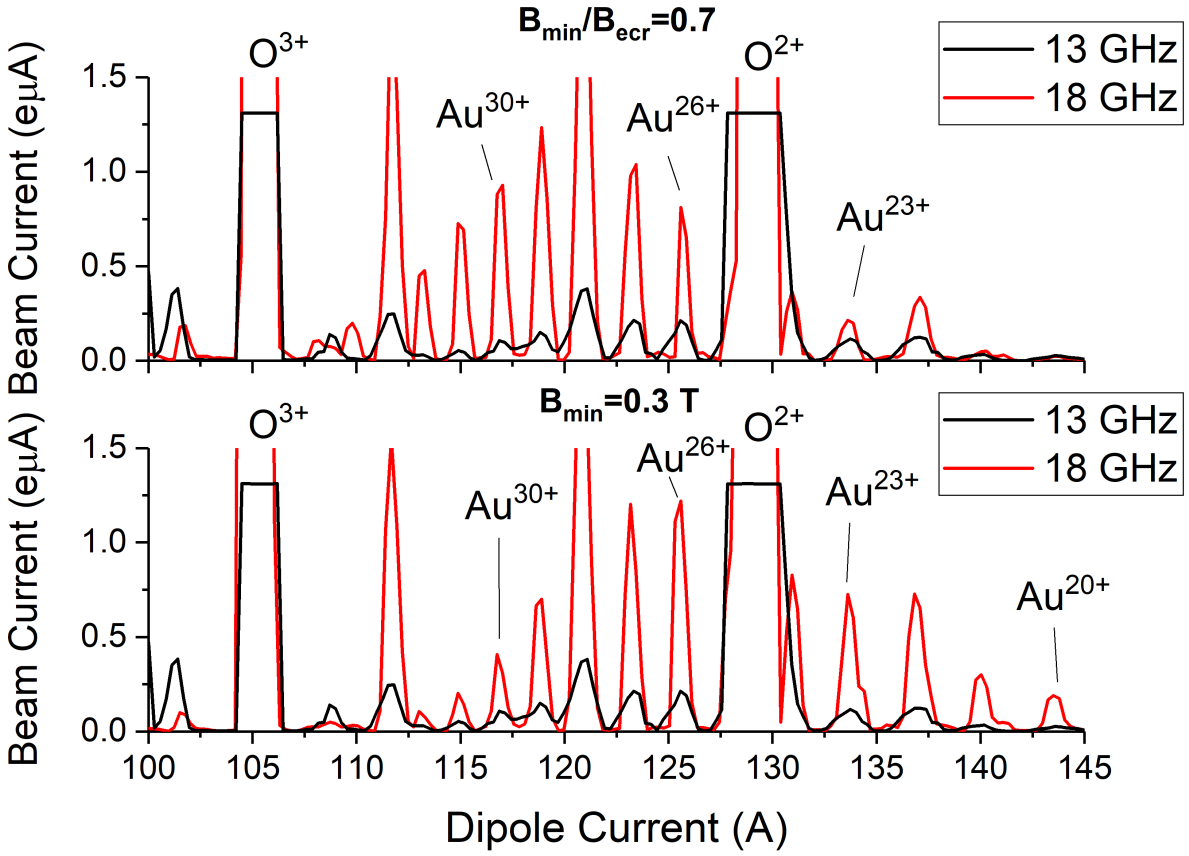

Figure 4.5: Measured extracted gold currents comparing 13 GHz and 18 GHz operation for 100 W of microwave power. Two situations are plotted: constant B_{min} (upper plot) and constant ECR zone size (lower plot).

Frequency	18 GHz									13 GHz		
Microwave Power	400 W			200 W			100 W			100 W		
Rounded B_{min}/B_{ecr}	0.5	0.7	0.8	0.5	0.7	0.9	0.5	0.7	0.9	0.5	0.7	0.9
Drain Current (mA)	1.47	1.71	1.48	1.44	1.4	1.33	0.94	1.08	1.08	1.03	1.03	1.03
Injection Pressure (10^{-8} mbar)	9.1	9.3	11	13	14	13	8.7	8.9	8.7	6.3	6.1	6.6
Extraction Pressure (10^{-8} mbar)	1.5	1.6	2.3	1.9	1.9	1.8	1.6	1.3	1.6	0.94	0.74	0.92
O^{6+} Current ($e\mu$A)	59	61	65	35	64	68	13	30	39	4	17	21
O^{4+} Current ($e\mu$A)	64	65	70	81	66	71	32	60	48	42	59	47
O^{2+} Current ($e\mu$A)	75	78	42	83	79	63	60	73	64	73	53	43
Au^{35+} Current ($e\mu$A)	0.4	0.9	0.9	0.1	0.1	0.6	0	0.1	0.4	0	0	0
Au^{32+} Current ($e\mu$A)	1.6	1.7	2.5	0.3	0.5	2.0	0.1	0.5	1.2	0	0.04	0.06
Au^{30+} Current ($e\mu$A)	3.1	2.1	3.5	1.1	1.2	2.5	0.4	1.0	1.4	0.08	0.10	0.16
Au^{26+} Current ($e\mu$A)	1.9	0.6	1.7	1.9	1.3	0.8	1.2	0.9	0.4	0.27	0.19	0.26
Au^{23+} Current ($e\mu$A)	0.7	0.2	0.4	0.6	0.4	0.1	0.7	0.2	0.1	0.44	0.09	0.11

Table 4.3: Plasma parameters for each combination of magnetic field, microwave power, and frequency explored in the study. Oxygen currents were measured with the sputter probe off, and steady state gold currents with the sputter probe at -500 V. Parameters such as vacuum pressure and drain current were insensitive to the sputter voltage and the presence of gold in the plasma.

4.2 Framework for Pulsed Sputtering Study

4.2.1 Hot Electron Temperature Deconvolution

The hot election population was monitored via bremsstrahlung emission measured axially from SuSI. X-rays were detected with an High Purity Germanium (HPGe) detector placed 3.2 m from the SuSI extraction electrode. An axial line of sight to the ECR plasma was available through a fused quartz window mounted to the analyzing magnet. Lead and tungsten collimators were used to reduce the amplitude of scattered x-rays and pile-up that appear artificially as a bump in the spectra [4, 72]. From geometric optics, the acceptance angle was 25 minutes, projecting a 16 mm diameter circle on the 8 mm diameter extraction electrode aperture. Therefore, the bremsstrahlung measured was mostly produced by electrons colliding with the extraction electrode. X-rays were attenuated primarily by the 3.3 mm thick fused quartz vacuum window. According to the online x-ray transmission resource in Ref. [26], SiO_2 transmits 57% of 30 keV photons. Extrapolation of the transmission data suggests that the x-rays beyond 50 keV were fully transmitted to the detector. The bremsstrahlung spectra was cut for the low energy range as this was not the subject of the experimental campaign. Every day of the measurements, the x-ray detector was energy calibrated with an ^{152}Eu source and a 30 minute background spectra taken (with the ion source off). The background x-ray spectra and energy calibration did not change over the course of the duration of these measurements that lasted 14 days. The x-ray detector was efficiency calibrated with an hour exposure by placing a ^{152}Eu radioactive source with a known activity 1 m from the detector end cap. Each bremsstrahlung data set was corrected for the detector efficiency curve measured from the ^{152}Eu radioactive source using a 6^{th} order polynomial.

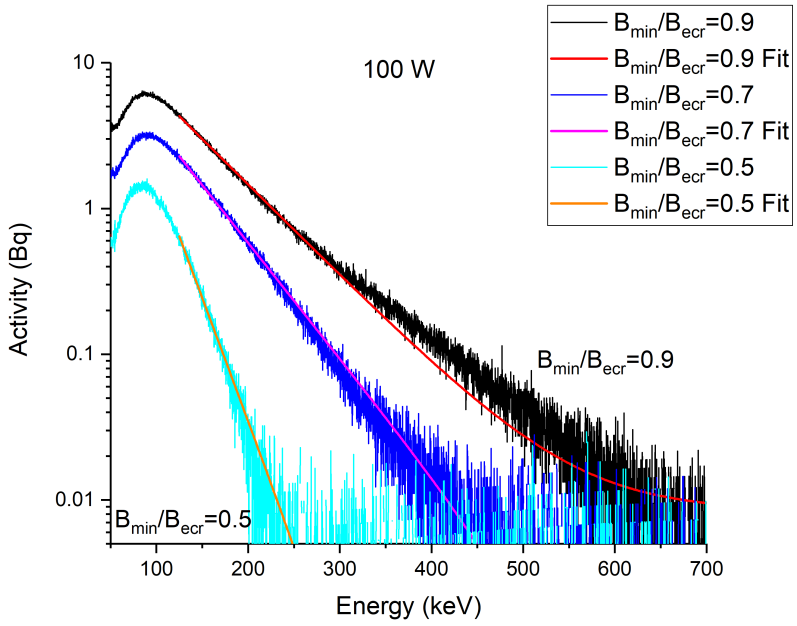

Figure 4.6: X-ray spectra at 18 GHz for 100 W applied microwave power. Three different magnetic fields are compared and the exponential fitting function used to generate hot electron temperature.

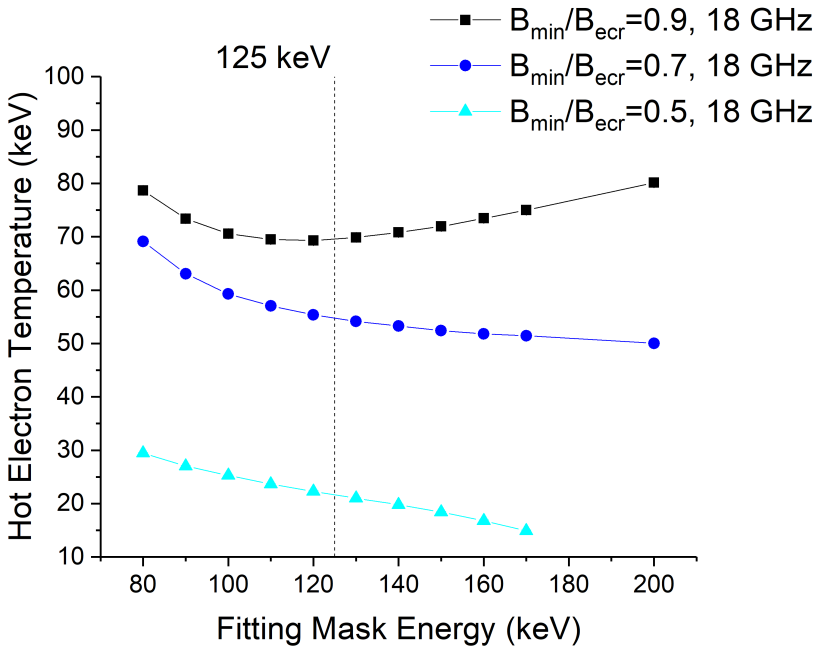

Figure 4.7: Hot electron temperature from fitting of the bremsstrahlung spectra with different starting energies for the exponential fitting function.

Figure 4.6 shows the typical form of the bremsstrahlung spectra for constant microwave power and variable magnetic minima. Each spectra was background subtracted and energy efficiency corrected, thereby representing the x-ray emissions that propagated through the collimation system. The exponentially decaying part of the bremsstrahlung spectra may be deconvoluted with a Maxwell-Boltzmann electron distribution impinging on a thick wall as demonstrated in Ref. [39]. The average electron temperature of the assuming Maxwellian plasma is found from fitting the exponentially decaying part of the spectrum. The decay constant is the temperature. It is widely surmised that there are several populations of electrons in thermal equilibrium in the ECR plasma [18, 32]. For the purposes of the study only the hottest population was sampled. The exponential fit was performed between 125 keV and 1440 keV (file termination) for all plasmas except for 13 GHz operation at B_{min}/B_{ecr}=0.5 where masking began at 100 keV instead of 125 keV. The change in mask start location was done to accommodate for the low energy bremsstrahlung spectra generated from the magnetic field configuration with the lowest magnetic minimum studied.

A consequence of the non-Maxwellian features of the bremsstrahlung spectra from an ECR ion source is that the calculated temperature depends on the choice of fitting mask for the exponential deconvolution function. The relationship between fitting region and calculated temperature was explored by incrementally changing the starting energy for the exponential fitting function. Different magnetic field configurations were studied because the shape of the bremsstrahlung spectra (hot electron temperature) depends on magnetic minimum and is independent of microwave power [3]. Figure 4.7 illustrates the changes in hot electron temperature with fitting mask energy for three different magnetic field configurations. The calculated temperature tends to increase as the fitting mask was reduced below 120 keV because the peak in the bremsstrahlung spectra (around 80-110 keV) artificially flat-

tens the exponential decay increasing the calculated temperature. The behavior as fitting mask energy increased beyond 120 keV depended on the magnetic minimum. For plasmas generated with a higher B_{min} such as B_{min}/B_{ecr}=0.9, the temperature increases again due to the "kink" in the spectra (see Fig.4.6) around 300 keV suggestive of a bi-Maxwellian EEDF. For lower B_{min}, the calculated hot electron temperature decreased with increasing fitting mask energy. The hot electron temperature error was estimated by a 10% deviation in fitting mask energy about the mask generating the reported value. The error bars are not indicative of the usual statistical 68% confidence interval from the standard deviation, but rather a means to quantify the change in hot electron temperature about a somewhat arbitrary fitting range. Given the unique shapes of bremsstrahlung spectra with each magnetic field configuration, the error bars helped quantify uncertainties in the measured temperature.

The exponential decay functions used to determine the hot electron temperature were used to estimate the highest energy electron in the plasma. The exponential decay functions were solved for energy given an activity of 10 mBq (approximately 50 detections) to zero out the vertical offset the fitting function converged onto in some cases. The fitting function was useful to estimate the hot electron temperature, but due to the low statistics for the high energy tail and multi-Maxwellian features that were not accounted for the fitting function did not produce reliable results. Rather, the high energy limit was determined by visual inspection of the bremsstrahlung spectra to within an error of about 50 keV which was the typical maximum energy width of the high energy tail at 5 mBq. Visual inspection was more reliable because the fitting function was strongly weighted to the bulk of the bremsstrahlung spectra and can deviate from the measurement at the high energy tail. This effect can be seen in Fig. 4.6 for B_{min}/B_{ecr}=0.9. A similar 10 mBq low limit was used to extract the high energy limit by visual inspection.

In addition to hot electron temperature and electron energy limit, the axial x-ray power measured through the collimation system was calculated. The x-ray energy and activity were multiplied to find x-ray power per x-ray energy bin, and then summed from 50 keV to the spectrum termination (1440 keV). The error associated with x-ray power involved applying the $1/\sqrt{N}$ Poisson distribution fractional error [35] on x-ray counts for each energy bin wherein N refers to the number of counts. The fractional errors were then multiplied by the x-ray power calculated for the x-ray energy bin, and finally each x-ray power error was summed in quadrature to estimate the total error.

4.2.2 Interpretation of Beam Current Decay Time

The method presented was primarily performed to prescribe what kind of fitting function should be applied to the beam current waveforms for analysis. The result serves as a simple fitting model to provide insight to how the measured 1/e decay time changes with ionization and charge exchange. A straightforward alternative derivation is given by M. Marttinen in Ref. [52] leading to a similar result.

A zero dimensional (physical dimension such as length) plasma model is employed. Complete numerical solutions of zero dimensional models have been used to generate charge state distributions of currents and perform sensitivity analysis of parameters such as electron density, temperature, and neutral pressure [82, 84]. Zero dimensional models were used to compare to experimental CSDs on the 10.5 GHz Constance B Quadrupole Mirror in Ref. [68] and to fit experimental CSDs measured on the 18 GHz superconducting source SERSE in Ref. [83]. The gold ion probe was assumed to be a small perturbation and not to change the global electron density or neutral density. Additionally the applied sputter voltage was assumed to set-up a static source of gold neutrals within a characteristic time much shorter

than plasma ion production and confinement times. In this context the sputtering process is regarded as effectively instant. An ion extraction model is not considered. The assumption is that any differences impacting ion extraction between plasmas are much smaller than the scale of ion production or confinement times. Two primary reactions were considered:

$$\begin{aligned} &\text{Stepwise Ionization: } X^i + e = X^{i+1} + 2e, \\ &\text{Charge Exchange: } X^i + X = X^{i-1} + X^+. \end{aligned} \tag{4.1}$$

Here, X refers to an element undergoing the reaction (ex. Gold), i represents the charge state with $i = 0$ being neutral, and e the electron. An ionization reaction rate is defined by

$$n_e < \sigma v >_{i \to j} = \int_0^\infty \sigma_{i \to j}(E) v f_e(E) dE, \tag{4.2}$$

where f_e is the isotropic Electron Energy Distribution Function (EEDF) as a function of energy E, σ is the ionization cross section (also as a function of energy), v is the speed between collisional particles, and n_e is the electron number density. Charge exchange reaction rates are treated in a similar way, but by replacing the EEDF with the Ion Energy Distribution Function (IEDF), ionization cross section for charge exchange cross section, and electron density for the neutral density of the oxygen plasma. Within this context, the source and sink rates for a single probe ion species may be written as

$$\begin{aligned} \frac{dn_i}{dt} = {} & n_e n_{i-1} < \sigma v >_{i-1 \to i} + n_s n_{i+1} < \sigma_{cx} v >_{i+1 \to i} \\ & - n_e n_i < \sigma v >_{i \to i+1} - n_s n_i < \sigma_{cx} v >_{i \to i-1} - \frac{n_i}{\tau_i}, \end{aligned} \tag{4.3}$$

where, n_i is the density of the i^{th} probe ion (gold in this case), n_s is the density of neutrals supporting the plasma and participating in charge exchange, σ_{cx} is the charge exchange cross

section for the specified reaction pathway (ex. $i \rightarrow i-1$), and ion confinement time for the i^{th} charge state is denoted as τ_i. The individual reaction rates may be expressed as

$$\frac{dn_i}{dt} + \zeta_i n_i = \delta_i n_{i-1} + \epsilon_i n_{i+1}, \tag{4.4}$$

where ζ_i is the effective sink rate, and δ_i and ϵ_i are effective source rates defined by the following relations:

$$\begin{aligned} \delta_i &= n_e < \sigma v >_{i-1 \rightarrow i}, \\ \epsilon_i &= n_s < \sigma_{cx} v >_{i+1 \rightarrow i}, \\ \zeta_i &= n_e < \sigma v >_{i \rightarrow i+1} + n_s < \sigma_{cx} v >_{i \rightarrow i-1} + \frac{1}{\tau_i}. \end{aligned} \tag{4.5}$$

Eq. (4.3) is written in the form of Eq. (4.4) with the reduced rate constants (of unit inverse time) δ, ϵ, and ζ defined in Eq. (4.5). In this form, cross coupling with neighboring charge states becomes more apparent. A complete analytical solution requires solving an equation for every charge state possible for the ion probe. For gold, there are 80 possible states (including neutral) making the full solution not practical for an analytical technique. The simplest solution of Eq. 4.4 is to treat the neighboring densities $n_{i-1} << n_i$ and $n_{i-1} << n_i$ as small resulting in:

$$\frac{dn_i}{dt} + \zeta_i n_i = 0. \tag{4.6}$$

The ion density n_i is assumed to decay from a constant value. Implicit in Eq. 4.6 are some key assumptions:

1. There exists an ion probe to witness the plasma that does not significantly perturb the electron density or electron energy distribution function. This allows

   (a) constant electron density n_e, and

   (b) constant ionization and charge exchange rate terms.

2. Ion probe neutral density is small compared to that of the support plasma being measured, so that

   (a) ion probe to support plasma charge exchange is considered and

   (b) ion probe to ion probe charge exchange is neglected.

3. The ion densities of n_{i-1} and n_{i+1} are assumed much smaller than n_i and are neglected.

4. The ion probe density n_i decays immediately when the sputtering voltage is removed.

5. Only step-by-step ionization and charge exchange are considered, due to the low probability of multi-step reactions.

6. Ion drift times between leaving confinement and measurement on the Faraday cup are neglected. The lowest charge state of gold studied (Au^{13+}) has a time of flight through the SuSI beamline (see Fig. 2.11) with a 20 kV platform potential of 9.7 μs.

7. Ion density decay from steady state is considered.

   (a) The solution presented is not applicable to ion rise times.

The solution of Eq. 4.6 for constant coefficients follows as

$$n_i = c_1 e^{-t\zeta_i} + c_2 \tag{4.7}$$

with density constants c_1 and c_2. Note that ζ_i is real and positive, so n_i must decay from its initial value at time $t = 0$. Two boundary conditions are specified for Eq. (4.7): Time

zero begins when the sputter voltage is removed where the ion density is constant and then decreases in time to another constant. In an ideal system the density decays to zero. However, either due to some small amount of direct feeding or some leftover ion probe material from a previous pulse, a small offset current is accounted for. Therefore, $c_1 = n_{i0}$ the starting ion density and c_2 the density associated with constant direct feeding of the sputter sample. The extracted beam current and ion density from Eq. (4.7) are related by

$$I_i \approx \frac{eiL\sigma n_i}{2\tau_i}, \tag{4.8}$$

where e denotes the charge of an electron, L plasma length, σ emission area, and I_i beam current of the i^{th} charge state from Ref. [18]. Eq. (4.8) pertains to steady state emission from the plasma and is use here by incorporating the time dependence on ion density with the assumptions that ion confinement and plasma emission volume are time independent.

In summary, Eq. (4.8) states that beam current is proportional to ion density by constant factors. This result combined with Eq. (4.7) for the beam current decay relates the rate of current decay τ_{im} with ζ_i containing the ion confinement time τ_i. Importantly, the measured decay time (τ_{im}) can be related to ion confinement time by

$$\tau_{im} \approx 1/\zeta_i = \frac{\tau_i}{1 + \tau_i(n_e < \sigma v >_{i\rightarrow i+1} + n_s < \sigma_{cx} v >_{i\rightarrow i-1})}, \tag{4.9}$$

where the ion confinement time τ_i has been explicitly written, and the denominator in Eq. (4.9) is dimensionless. The measured decay time τ_{im} is less than the ion confinement time τ_i in this approximation because reaction rate coefficients ($n_e < \sigma v >_{i\rightarrow i+1}$ and $n_s < \sigma_{cx} v >_{i\rightarrow i-1}$ are real and positive.

There are two key results contained within this analysis: ion density changes exponen-

tially in time, under the approximations considered, and ion confinement time is greater than the measured 1/e decay time. In steady state, the beam current is related to ion density by the confinement time and constant factors from Eq. (4.8). For a pulsed sputtering experiment, the measured ion current decay τ_{im} is set equal to the ion density rate of decay $1/\zeta_i$. The decaying portion of the beam current should be fitted with an exponential function of the form in Eq. (4.7). It is important to add the disclaimer that Eq. (4.9) considers the n_{i+-1} densities to be equal to zero. For a heavy element like gold with extractable charge state distributions typically spanning twelve or more charge states, additional ion densities beyond the n_{i+-1} charge states should be considered for quantitative analysis.

4.2.3 Behavior of the Oxygen Plasma in the Presence of Gold

Three charge states of oxygen (O^{2+}, O^{4+}, and O^{6+}) were selected to monitor how their currents deviated from steady state during a pulsed sputtering event. These charge states were selected because they were present in all sampled plasma parameters with sufficient amplitude to be measured reliably above background while also covering a large range of oxygen charge states. Measured steady state currents of oxygen and gold are given in Table 4.3 for every plasma studied. A summary of the extent to which oxygen currents changed for each plasma is presented in Table 4.4. Currents are presented with respect to the steady state current.

In all the plasmas studied, the oxygen current did not respond to the leading and trailing edge of the high voltage pulse (unlike axial pulsed sputtering). Instead, the oxygen currents were perturbed by the presence of gold in the plasma. For example, Fig. 4.8 shows waveforms of the oxygen charge states overlaid with Au^{31+} which was one of the highest charge states in the distribution for the plasma operating point (13 GHz operation at B_{min}/B_{ecr}=0.7).

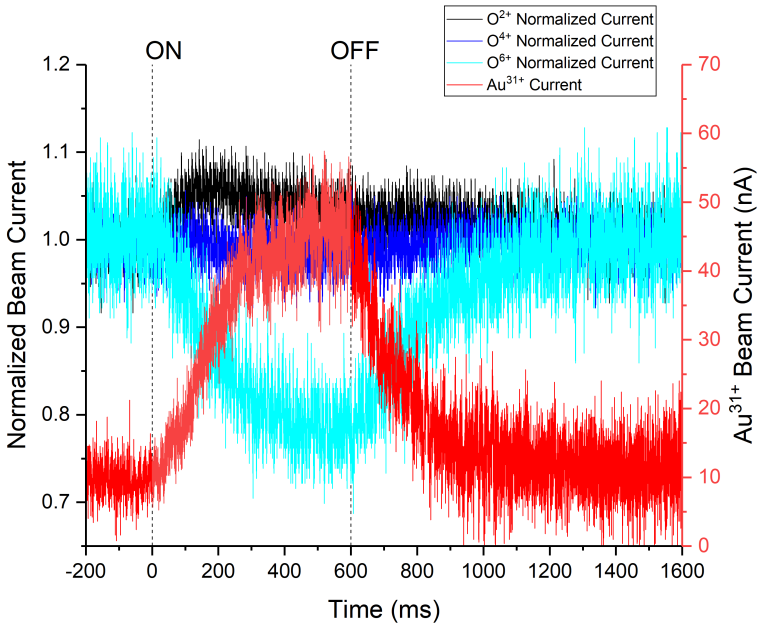

Figure 4.8: Oxygen beam currents relative to the applied sputtering voltage for 100 W applied microwave power, 13 GHz, and B_{min}/B_{ecr}=0.7. The currents have been normalized to their steady state value with the sputtering probe off.

The oxygen currents responded with an inverted waveform to the gold and on the same time scale. This suggests that gold was more perturbative than the sputtering voltage to the oxygen plasma.

In around half of the plasmas O^{6+} was the most sensitive to gold. In five out of the seven plasmas the O^{6+} current decreased. An example is shown in Fig. 4.8, where the oxygen currents dip progressively lower with increasing charge state with the time structure mirroring that of the highest gold charge state (Au^{31+}). The oxygen beam currents did not respond to the high sputtering voltage but rather to the gold current, suggesting in the radial configuration that the sputtering voltage is less perturbative than the sputtered material. Furthermore, the amount of gold resulting in a perturbation to the oxygen current was relative to the plasmas studied. Microamperes of gold current were produced in 18 GHz operation while tens of nanoamperes were produced for 13 GHz operation. Despite the dis-

parity in magnitudes, similar perturbations to the oxygen currents occurred (see Table 4.4). O^{6+} also exhibited a similar behavior during fast sputtering experiments of copper on the University of Jyväskylä 14 GHz ECR ion source in Ref. [52].

O^{6+} was likely the most sensitive to gold (as compared to O^{4+} and O^{2+}) because the ion-ion collision frequency scales as approximately charge to the fourth power [8], so O^{6+} will collide with plasma ions more frequently than O^{4+} or O^{2+} and therefore interact with the gold more frequently. Additionally, this is consistent with theories of electrostatic confinement that explain the gas mixing effect [56, 80, 18] were a lighter plasma species (oxygen) cools a heavier one (gold) through collisions ejecting oxygen.

Gold sputtering currents were intentionally minimized by the use of a relatively small sputtering voltage (-500 V) to reduce the degree to which the oxygen plasma was perturbed by gold during the sputtering event. Table 4.4 suggests that every plasma was perturbed by gold during the sputtering process and with varying degrees of severity. This was an unfortunate consequence of using long sputtering times to reach the highest precision measurement possible to highlight changes in 1/e decay time with charge state and hot electron temperature. Further research is needed to relate the accuracy of 1/e decay time and oxygen current perturbation. Section 4.2.5 addresses the accuracy of the decay time measurement by using shorter sputtering times to reduce the gold contamination for two plasma operating points. Ultimately, it is not clear that the extracted oxygen currents were an indicator of 1/e decay time accuracy in part due to low sample size. Determining this would be an area of further research for similar measurements. For example, 13 GHz operation for B_{min}/B_{ecr}=0.7 found the 1/e decay time to decrease by about a factor of two as the sputtering time was increased to 600 ms. The oxygen beam current during the sputtering event is plotted in Fig. 4.8 showing O^{6+} to decreasing by about 20%.

Frequency	18 GHz									13 GHz		
Microwave Power	400 W			200 W			100 W			100 W		
Rounded B_{min}/B_{ecr}	0.5	0.7	0.8	0.5	0.7	0.9	0.5	0.7	0.9	0.5	0.7	0.9
O^{6+} Deviation (%)	-15	+4	-10	-5	-10	-15	N/A	-15	-15	+10	-20	-25
O^{4+} Deviation (%)	-15	+4	-15	-10	-5	+4	N/A	0	+4	0	0	0
O^{2+} Deviation (%)	-15	0	0	-15	-5	0	N/A	0	+2	-5	+5	+5

Table 4.4: Oxygen beam current deviation from steady state measured at the most extreme magnitude during the high voltage sputtering pulse.

4.2.4 Characteristics of Beam Current Waveforms

Previous studies of ion confinement in Refs. [25, 97] relied on the beam current peaking time as a probe for ion processes. Peaking time is defined (see Fig. 4.10) as the time necessary for the beam current to reach its maximum value after the metal contaminant was first introduced. These measurements explore whether peaking time was a viable figure of merit to study ion confinement time on SuSI.

Two plasmas were selected because they spanned the range of plasma density probed in the study while having approximately the same ECR zone size: 400 W at 18 GHz and 100 W at 13 GHz with a magnetic field configuration of B_{min}/B_{ecr}=0.7. The charge state with the largest steady state current was selected and provided the best chance to measure the peaking time with the largest beam currents. This resulted in Au^{27+} being studied for 13 GHz operation (see Fig. 4.9), and Au^{30+} for 18 GHz operation at 400 W (see Fig. 4.28). Peaking time was estimated by visual inspection, and the error was estimated by dividing beam current noise by the steepest rate of rise on the leading edge of the beam current waveform.

The 13 GHz plasma beam current response to sputtering time at 100 W is summarized in Fig. 4.11. Six different sputtering times are presented in reference to the steady state

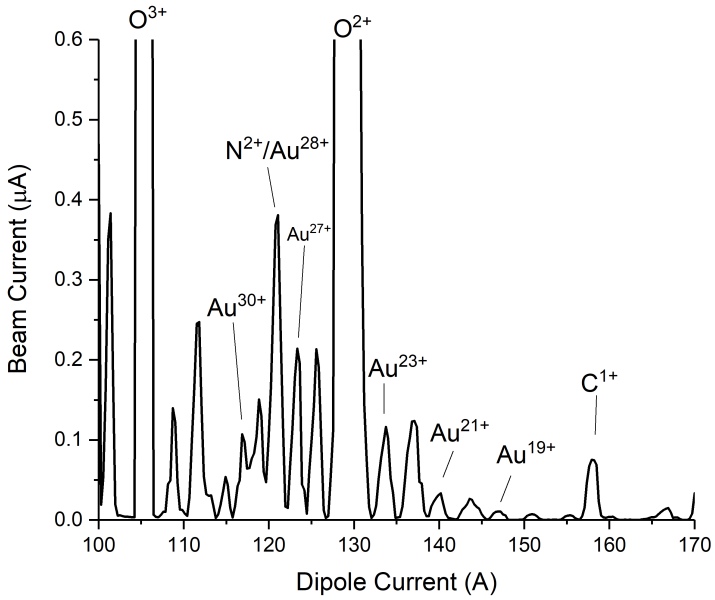

Figure 4.9: Charge state distribution of gold for steady state sputtering with 13 GHz operation and a magnetic field configuration of B_{min}/B_{ecr}=0.7. The peak charge state in the current distribution was Au^{27+}.

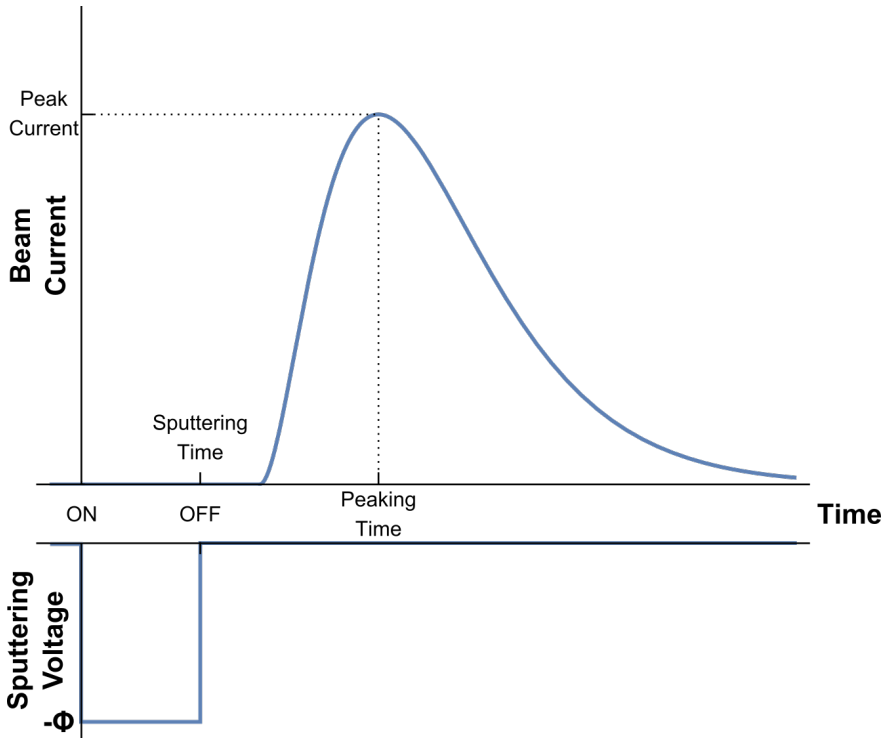

Figure 4.10: Schematic of beam current responding to sputtering times that were too short for the beam current to saturate. The beam current reaches its peak value after the sputter probe was turned off.

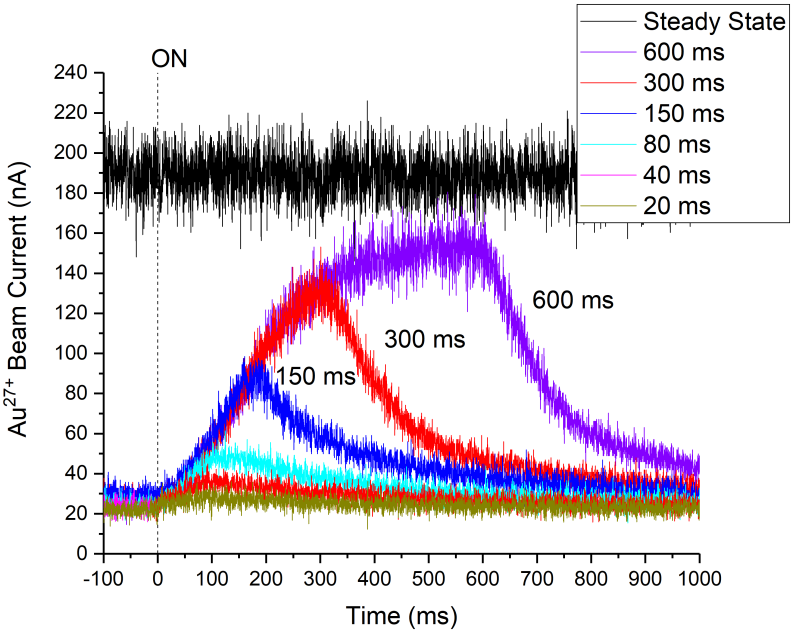

Figure 4.11: Au^{27+} current in reference to the sputtering voltage pulse leading edge (time zero) for different sputtering times for operation at 100 W of 13 GHz microwave power and a magnetic field of B_{min}/B_{ecr}=0.7. The beam current did not saturate to the steady state current for 600 ms sputtering times.

current for Au^{27+}. Notably, the beam current did not rise above the noise for the 20 ms sputtering time and peaking time was not recoverable. However, the sputtering time of 40 ms shown in Fig. 4.12 produced a beam current response strong enough to extract a peaking time which was measured as 90±25 ms. Conversely, pulses 600 ms long were not of sufficient duration to completely saturate the beam current to its steady state value. Sputtering times on the order of 1.1 s would likely have been required to reach the steady state current, as estimated from the 600 ms beam current waveform in Fig. 4.11. This conclusion is based on steady state current measurements, and mathematical analysis with a logistic function. The peaking time increased with sputtering time up to the longest pulse used and became equal for sputtering times of several hundred milliseconds.

The beam current responded to sputtering time in a similar way to the 13 GHz operating

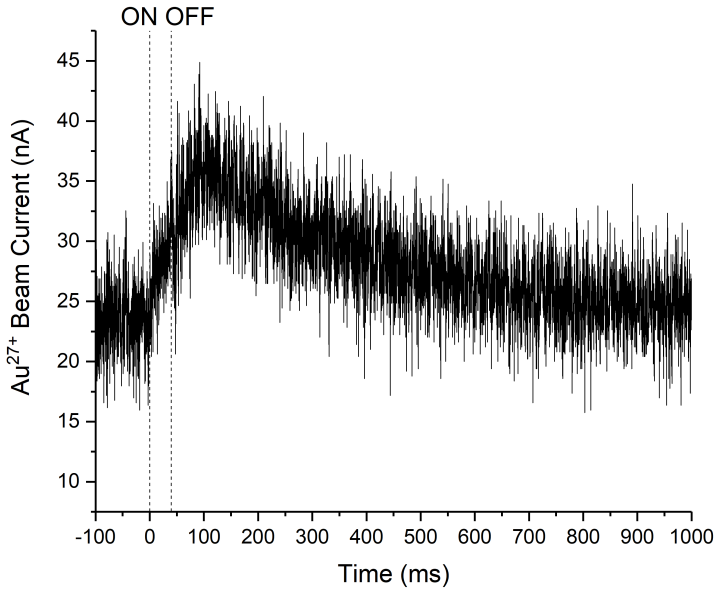

Figure 4.12: Au^{27+} current for 40 ms sputter pulse, 100 W applied microwave power, at 13 GHz, and a magnetic field configuration of B_{min}/B_{ecr}=0.7. The beam current reached its peak value 90±25 ms after the high voltage was applied (50±25 ms after the pulse ended).

point when the source was operated at 18 GHz with 400 W microwave power. The peak charge state, Au^{30+}, responded more quickly and with higher current when compared to the 13 GHz case. See Fig. 4.13 for a summary of the measurement. The beam current response to seven different sputtering times were sampled. The shortest was 1 ms, but the beam current did not rise significantly from the noise and peaking time could not be extracted. Peaking time was extracted for the 5 ms sputtering time and was found to be 30±8 ms as shown in Fig. 4.14. Sputtering times longer than 5 ms increased the beam current peaking time until 160 ms, where the peaking time was set by the sputtering time.

The beam current responded weakly to sputtering times in the 5-40 ms range and beam noise was present due to unavoidable sample direct feeding (caused by a fixed sample position). This unfortunately, limited the usefulness of peaking time. For the case of 18 GHz at 400 W microwave power, the 5 ms sputtering time provided a peaking time of 30±8 ms, but

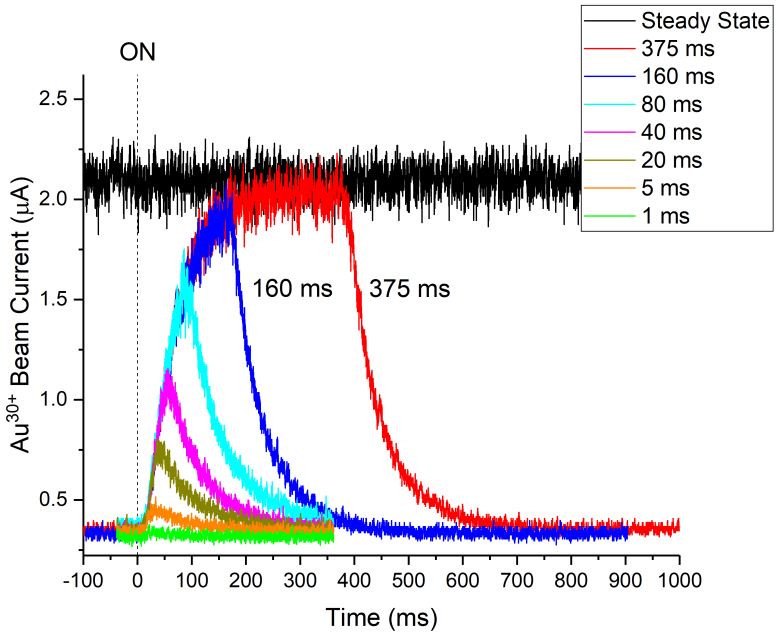

Figure 4.13: Au^{30+} current for the sputtering voltage pulse leading edge (time zero) for different sputtering times for operation at 400 W of 18 GHz microwave power and a magnetic field of B_{min}/B_{ecr}=0.7. The beam current saturated to its steady state level after about 350 ms.

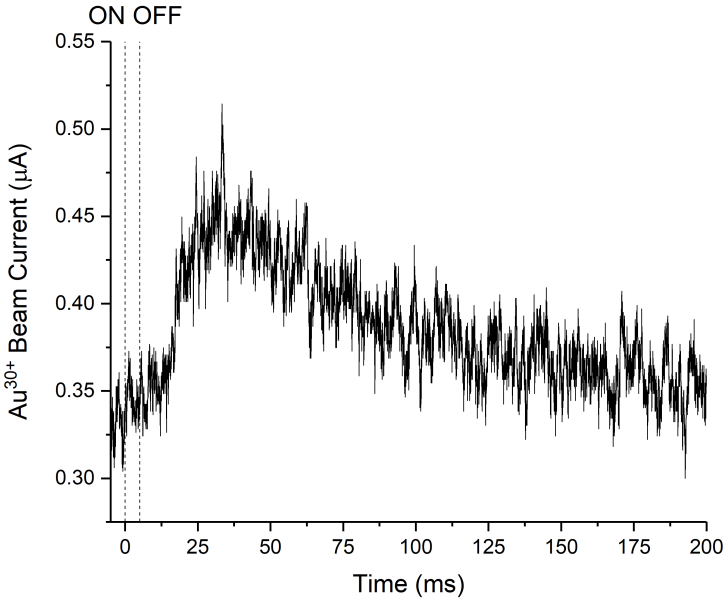

Figure 4.14: Au^{30+} current for a 5 ms sputter pulse for 400 W applied microwave power, at 18 GHz, and a magnetic field configuration of B_{min}/B_{ecr}=0.7. The beam current reached its peak value 30±8 ms after the high voltage was applied (25±8 ms after the pulse ended).

the signal amplitude was only about 1.3 times the background current. Figure 4.15 illustrates how the peaking time increased with sputtering time for the 18 GHz operating point. The same issue was present on both 13 GHz and 18 GHz plasmas, with the 13 GHz having poorer signal fidelity than the higher power 18 GHz plasma. However, in either case, the peaking time always depended on the sputtering time because they had to be long enough for the beam current to overcome the direct feeding current (see Fig. 4.16). Increasing the sputtering time increased signal fidelity but artificially increased the beam current peaking time up until it was completely described by the sputtering time. This phenomenon was described in Ref. [97].

One interesting result was that the 13 GHz plasma required a sputtering time 8 times longer than the 18 GHz plasma to produce enough current to measure even with the charge state in each case selected for the largest electrical currents. This suggests that the 13 GHz plasma is interacting much less with the sputter sample than the 18 GHz plasma. This assertion is supported by the steady state current measurements reported in Table 4.3.

This study and in Ref. [52], the 1/e decay time was used to quantify the degree to which ionization and confinement processes change with different plasmas studied. Decay time was particularly important because the constant current offset due to direct feeding of the sputtering sample (a consequence of sputter sample placement and geometry that could not easily be modified) required sputtering times longer than the natural peaking time of the system to produce measurable current amplitudes.

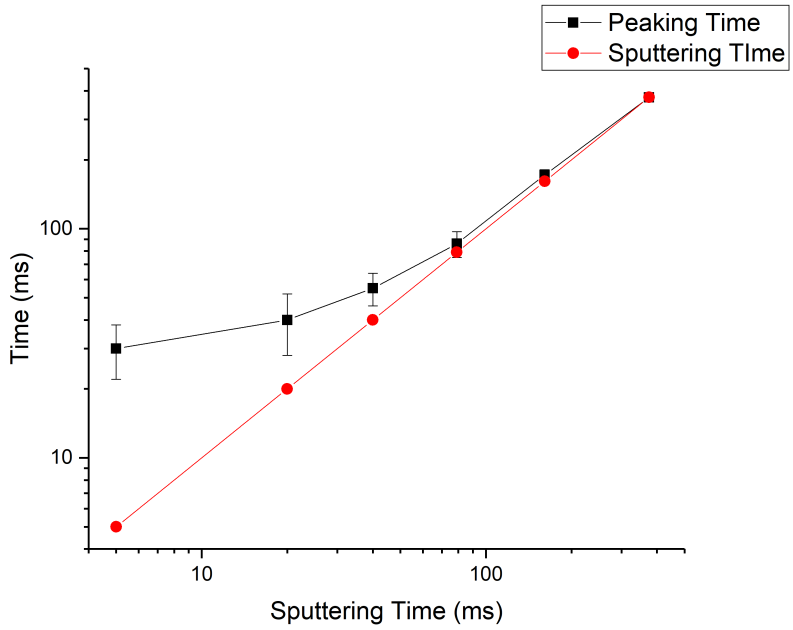

Figure 4.15: Beam current peaking time as a function of sputtering time from the data in Fig. 4.13 for 18 GHz operation at a microwave power level of 400 W. The peaking time converges to the sputtering time for pulses up to and longer than about 100 ms.

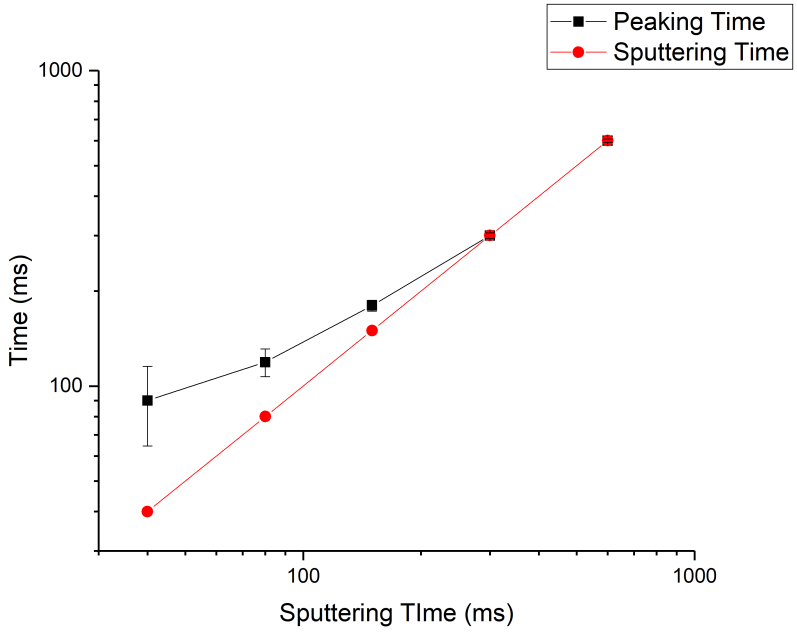

Figure 4.16: Beam current peaking time as a function of sputtering time from the data in Fig. 4.11 for 13 GHz operation at a microwave power level of 100 W. The peaking time converges to the sputtering time for pulses up to and longer than about 300 ms.

4.2.5 Decay and Sputtering Time

The relationship between decay time and sputtering time was explored for 13 GHz operation at B_{min}/B_{ecr}=0.7 with a microwave power level of 100 W, and for 18 GHz operation at B_{min}/B_{ecr}=0.7 with 400 W of microwave power. The beam current measurements for the two operating points are summarized in Figs. 4.11 and 4.13 in Sect. 4.2.4. The two different frequencies and microwave powers were chosen to span the range of plasma density encountered in the study. Each operating point maintained about the same ECR zone size (see Table 4.1). The 1/e decay time was evaluated by fitting the beam current waveform with an exponential decay function starting from the peaking time, or in the case of long sputtering times, from the sputtering time. The decay time error was estimated by the ratio of the steady state beam current noise to the peak beam current measured during the sputtering event.

For 18 GHz operation, the decay time remained approximately fixed as a function of sputtering time. This suggests the amount of gold introduced did not significantly perturb the system (set-up by the oxygen plasma) as evident in Fig. 4.17. Additionally, the charge states O^{2+}, O^{4+}, and O^{6+} did not respond strongly to 375 ms sputtering times for this plasma as seen in Table. 4.4 in Sect. 4.2.3. The fitted 1/e decay time from a 375 ms sputter pulse from Fig.4.13 at 18 GHz was found to be 62±3 ms.

However, for the less dense 13 GHz plasma at 100 W, The fitted decay time in Fig. 4.18 decreased with increasing sputtering times. Notably, the decay time resulting from a 600 ms sputtering time was 145±10 ms while sputtering times of 40 ms produced decay times of 340±100 ms, or about a factor of two longer. As sputtering time increased the amount of gold in the plasma also increased, further suggesting that gold poisons the plasma. Ideally,

the amount of gold introduced to the plasma should be small enough to not change the measurement of decay time. The 13 GHz example shows that by allowing beam current to saturate to its steady state current, some operating points were more impacted than others. In particular the low density 13 GHz plasma studied here was more sensitive to gold than the 18 GHz plasma of comparatively higher density.

It is interesting that when comparing the steady state gold and oxygen currents of the two plasmas studied, (18 GHz with 400 W and 13 GHz with 100 W) the steady state currents did not predict the increased sensitivity to gold for the 13 GHz case. Specifically, 13 GHz operation produced 59 μA of O^{4+} and 0.21 μA of Au^{27+} making the peak gold current (of the CSD) 280 times smaller than the peak oxygen current. When comparing the peak oxygen and gold currents (O^{2+} and Au^{30+}) for the denser 18 GHz plasma, the peak gold current was only 77 times smaller than the peak oxygen current. Steady state currents and their ratios did not provide predictive power as to the extent to which gold perturbed the plasma.

Short 200 ns and 500 μs sputtering times used in [25] and [97] respectively, although ideal for fast sputtering did not produce detectable beam currents on SuSI with the radial sputter probe and gold sample. The beam currents instead responded to much longer sputtering times of 5-40 ms. The most precise decay times were found with maximum differential between high and low currents, so the sputtering times were selected to be long enough for the beam current to saturate. It was thought that measurement of the plasma from (a contaminated) steady state would treat the systematic errors equally, but this assumption was incorrect. Instead, some plasmas appeared to be more sensitive to gold than others from monitoring of the oxygen currents, and in particular, the 13 GHz plasma where decay time decreased significantly with increasing sputtering time. It is not clear if perturbations to

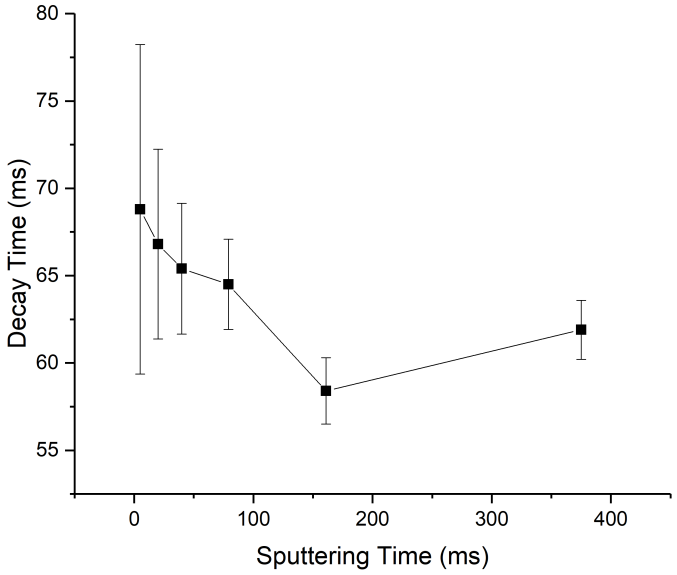

Figure 4.17: Decay time of the peak charge state (Au^{30+}) in the extracted current distribution for 400 W of 18 GHz microwave power with a magnetic field characterized by B_{min}/B_{ecr}=0.7. There is no change of decay time within the fitting error for any sputtering time selected, suggesting the introduction of gold did not perturb the bulk (oxygen) plasma properties.

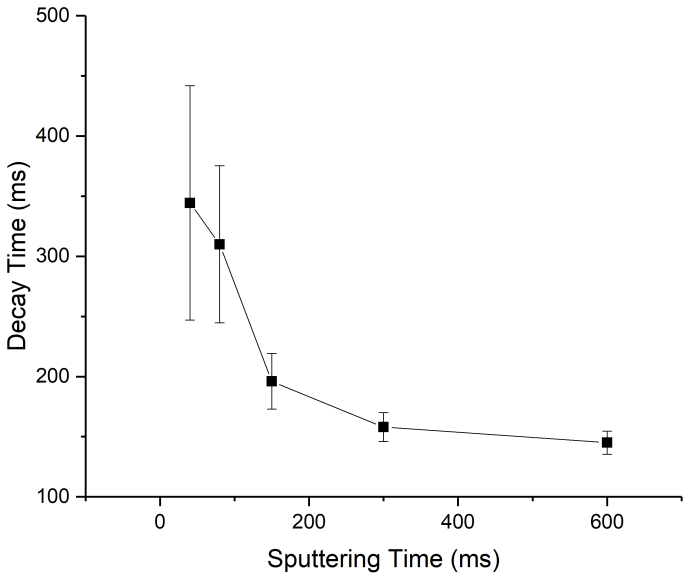

Figure 4.18: Decay time of the peak charge state (Au^{27+}) in the extracted current distribution for 100 W of 13 GHz microwave power with a magnetic field characterized by B_{min}/B_{ecr}=0.7. The decay time steadily decreases with an increase in sputtering time indicating the introduction of gold changed the plasma.

the extracted oxygen currents held an indication of the extent to which gold poisoned the source. Determining this would be an area of further research for similar measurements. In addition, steady state currents were ineffective as a metric to predict which plasmas were the most sensitive to gold poisoning.

Ultimately, long sputtering times were selected in spite of the potential systematic error from gold poisoning, because the larger gold currents increased the precision of the decay time measurement. Given the need for good separation of decay time with magnetic field configuration, it was deemed more important to resolve changes in decay time with different plasmas than it was to minimize the systematic error that could exist in decay time.

Fitting of the beam current decay waveform was performed at the termination of high voltage on the sputtering probe and each decay waveform was treated equally. However,

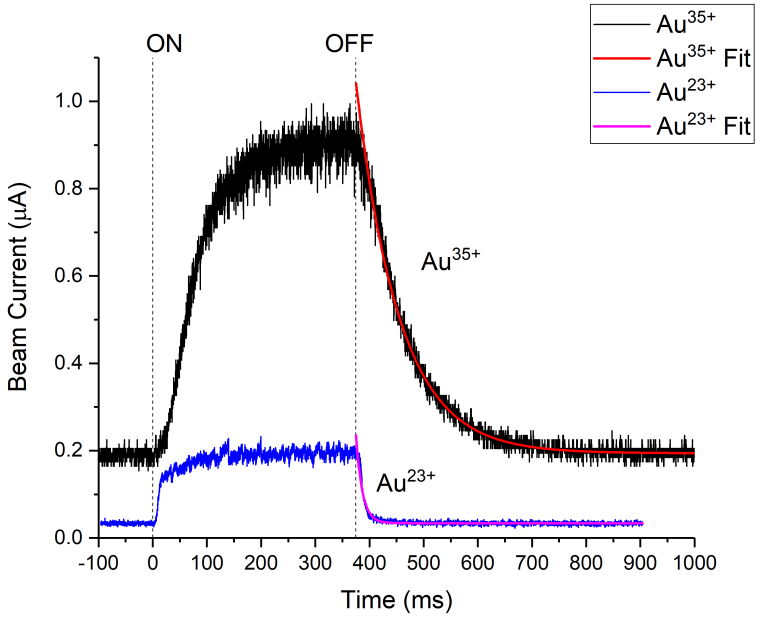

Figure 4.19: Au^{35+} and Au^{23+} beam currents produced by a plasma with 400 W applied microwave power at 18 GHz and a magnetic field with B_{min}/B_{ecr}=0.7. The sputtering voltage (-500 V) was turned on for 375 ms and repeated every 2.75 s. An exponential decay function was fit to the beam current starting when the sputter voltage was turned off through the end of the oscilloscope file. Three sputtering events (also referred to as shots) were saved and fitted to help quantify the shot-shot variation in 1/e decay time.

other methods of waveform fitting have been reported such as in a range at a short time delay from the sputtering time [52].

The 1/e decay times were extracted from the beam current waveform by a least squares fit with an exponential decay function. The fitting function was generally a very good match for the data and is shown in Fig. 4.19 for 400 W of 18 GHz microwave power and B_{min}/B_{ecr}=0.7. To estimate shot-shot "statistics", three sputtering events were recorded and fitted independently (see Appendix for additional information). The decay times reported in Sects. 4.3.2 to 4.3.5 are the result of averaging three independent sputtering events. Decay time error for each charge state was calculated by adding in quadrature: the standard deviation from the mean and steady state beam noise. An example of the beam current fitting function is shown in Fig. 4.19 for Au^{35+} and Au^{23+} charge states produced from an 18 GHz plasma at 400 W with B_{min}/B_{ecr}=0.7. It is notable in Fig. 4.19 that the low charge states such as Au^{23+} saturate faster than the high charge states (Au^{35+}).

4.3 Results

4.3.1 Hot Electron Temperature and X-ray Power

The hot electron temperature increased with magnetic minimum, independent of microwave power and operating frequency as seen in Fig. 4.20 mirroring the result in Ref. [3] (for a direct comparison see the Appendix). For the special case where B_{min} = 0.3 T was fixed between two different frequencies (18 GHz and 13 GHz), the same hot electron temperature was measured.

X-ray power increased linearly with microwave power for the two magnetic field configurations, B_{min}/B_{ecr}=0.5 and 0.7, where all three power levels were measured (see Fig. 4.21).

This same relationship was demonstrated as linear from dynamic heat load measurements on the VENUS cryostat in Ref. [44]. Since the hot electron temperature remains fixed for constant B_{min} (see Table 4.5) the increased x-ray power was likely caused by increased plasma density, due to the increased electron losses for the same magnetic confinement condition.

The highest energy x-ray observed in the bremsstrahlung spectra may be used to estimate the energy of the highest energy electrons participating in the production of the spectra [85]. The highest energy electron measured was estimated, in this dissertation, by visual inspection of the bremsstrahlung spectra. The highest energy electrons generated for 18 GHz operation at B_{min}/B_{ecr}=0.9, 650-800 keV did not have a closed ECR surface. The relativistic cyclotron resonance magnetic field for these electrons ranged between 1.5-1.7 T, which exceeds the 1.25 T extraction magnetic field. This suggests that the magnetic autoresonance effect (discussed in Sect. 2.2.2) plays a role in generating the highest energy electrons observed in ECR plasmas.

A comparison of x-ray power with mirror ratio seems straightforward at first but its important to consider the change in the distribution of energies with each new magnetic minimum (and therefore mirror ratio). Bremsstrahlung emission represents the electron plasma losses and is weighted by the distribution of energies in the spectra, which both depend on the magnetic field (see Fig. 4.20 and Sect. 2.2.1). The x-ray power increased nonlinearly with mirror ratio as seen in Fig. 4.22, however because the hot electron temperature was also changing with B_{min}, the increased x-ray power does not directly equate to increased electron losses. A future measurement could select magnetic fields that control for mirror ratio (B_{ext}/B_{min}) to better differentiate bremsstrahlung energy distribution from its emitted x-ray power. However, for the special case where 18 GHz and 13 GHz operation shared a similar B_{min}=0.3 T (and hot electron temperature) but with different mirror ratios,

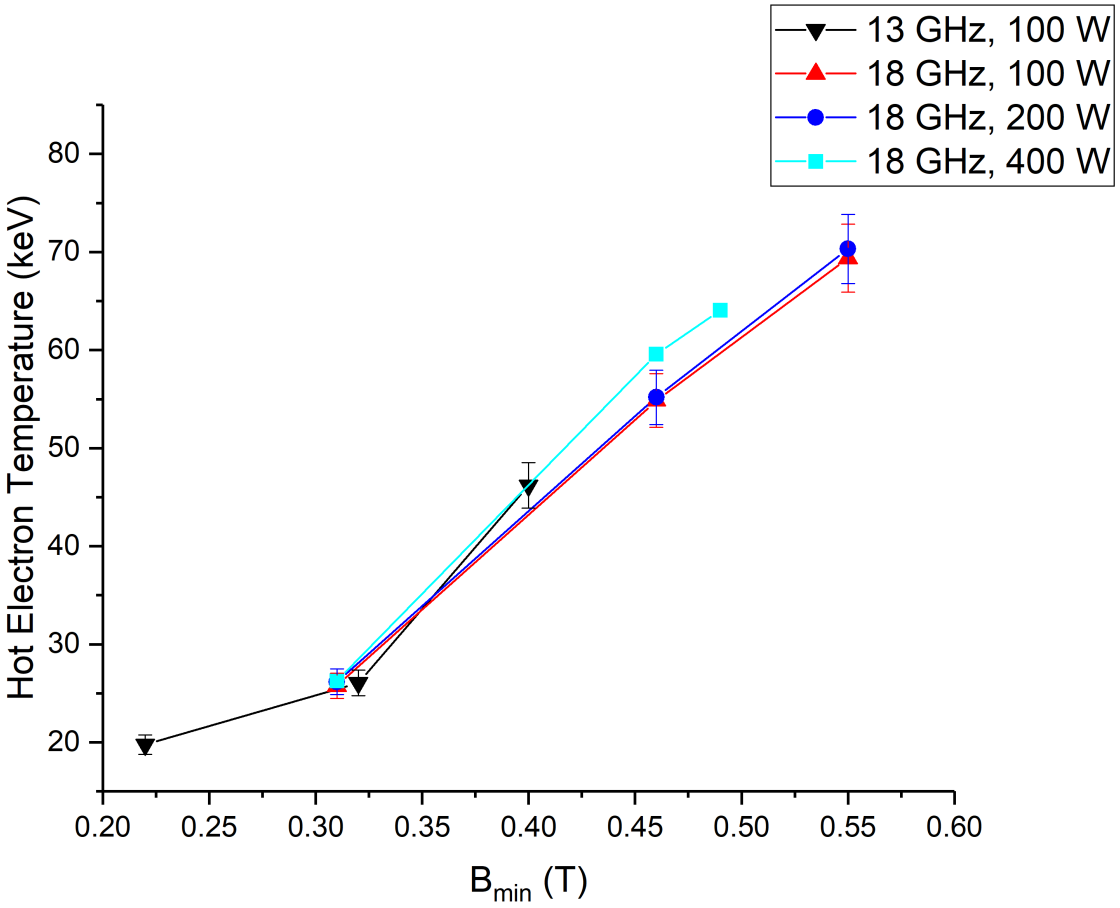

Figure 4.20: Hot electron temperature as a function of the minimum field for 13 GHz and 18 GHz operation. The magnetic minimum was the primary predictor of hot electron temperature across all operating points.

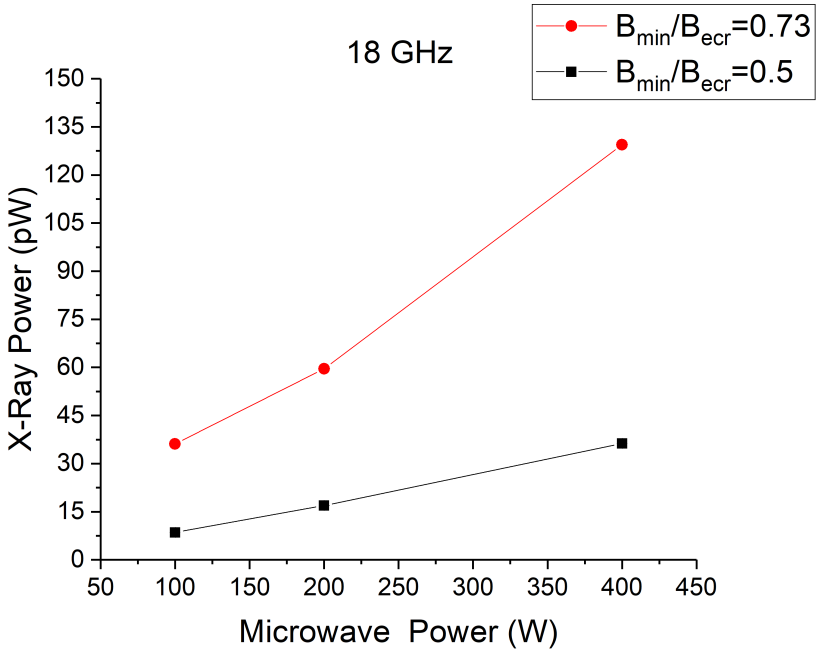

Figure 4.21: Energy integrated x-ray power with applied microwave power for 18 GHz operation.

the plasma with the smaller mirror ratio (13 GHz, B_{min}/B_{ecr}=0.7) produced more x-ray power and was likely the result of reduced magnetic confinement at 18 GHz. The x-ray power increased strongly for a mirror ratio of 2.55 (B_{min}/B_{ecr}=0.8) at 400 W further suggesting, along with the discussion in Sect. 4.1.2, that the plasma was particularly unstable.

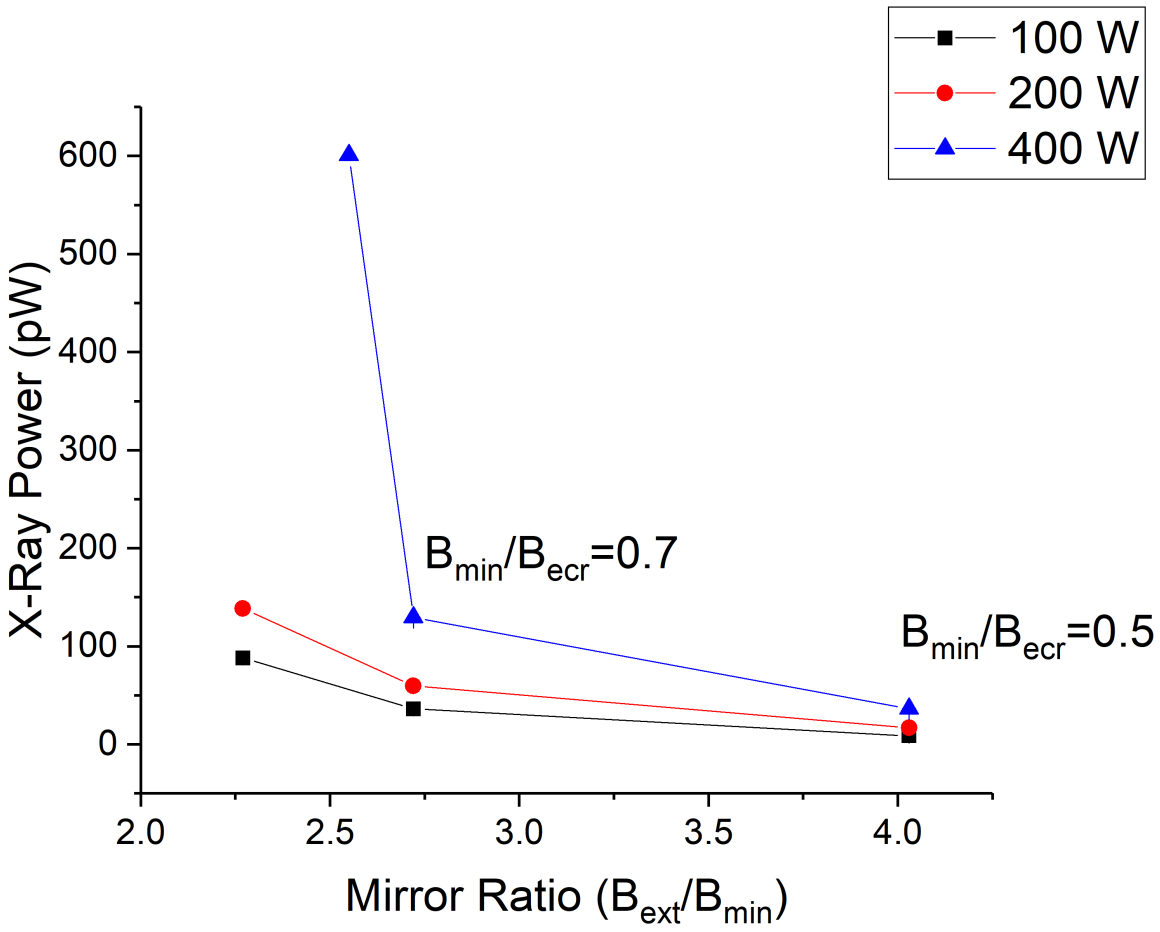

Figure 4.22: Energy integrated x-ray power as a function of mirror ratio.

Frequency (GHz)	Microwave Power (W)	B_{min}/B_{ecr}	Hot Electron Temperature (keV)	X-ray Power (pW)	Electron Energy Limit (keV)	
					Visual Inspection	Fitting Function
18 GHz	400 W	0.5	$26^{-1.9}_{+2.7}$	36.31±0.04	250	240
		0.7	$59.6^{-0.8}_{+1.4}$	129.4±0.1	600	520
		0.8	$64.1^{-0.5}_{+1.2}$	600.8±0.2	800	580
	200 W	0.5	$26^{-1.9}_{+2.1}$	16.94±0.03	250	250
		0.7	$55.2^{-0.8}_{+1.7}$	59.56±0.06	500	450
		0.9	$70.3^{+1.0}_{-0.3}$	138.3±0.1	700	800
	100 W	0.5	$26^{-1.7}_{+2.0}$	8.55±0.03	250	230
		0.7	$55^{-1.4}_{+1.7}$	36.10±0.05	450	420
		0.9	$69.0^{+1.1}_{-0.1}$	88.03±0.07	650	670
13 GHz	100 W	0.5	$19.8^{+0.3}_{+1.0}$	8.02±0.04	200	200
		0.7	$26^{-2.7}_{+3.1}$	11.63±0.03	250	240
		0.9	$46.2^{-2.1}_{+2.6}$	33.11±0.04	350	370

Table 4.5: Hot electron characteristics calculated from bremsstrahlung spectra. The subscript temperature a -10% deviation from fitting mask energy (125 keV in most cases) while the superscript was a +10% deviation. X-ray power was calculated by summing the power detected per energy bin starting at 50 keV. Electron energy limit is provided, estimated by visual inspection and fitting function.

4.3.2 Beam Current Decay time and Microwave Power at 18 GHz

The effect of microwave power on decay time for different charge states of gold was studied for two different magnetic fields: B_{min}/B_{ecr}=0.5 and B_{min}/B_{ecr}=0.7. Both magnetic fields were between 100-400 W but only the case where B_{min}/B_{ecr}=0.5, produced a smooth change of the decay time and CSD for each microwave power. In contrast, B_{min}/B_{ecr}=0.7 provided remarkably similar results for both the 100 W and 200 W and a strong change at 400 W.

Figure 4.23 shows how increased microwave power can push the CSD towards higher charge states and was likely caused by increased electron density thereby reducing the density of neutrals contributing to charge exchange as proposed in Ref. [82]. The dependence of the decay time as a function of charge state and microwave power is presented in Figs. 4.24 and 4.25. The main features are an increase of the decay time with charge state and a decrease as a function of microwave power. The trend observed with charge state was observed for all plasmas measured, and is strong evidence that the beam current waveform decay time is representative of an ion confinement process. The x-ray emission was measured co-incidentally with the decay time and is shown in Fig. 4.26. Emitted x-ray power increased linearly with microwave power, and the hot electron temperature (from x-ray fitting) remained fixed at $26^{-1.8}_{+2.3}$ keV as can be seen in Fig. 4.20 of Sect. 4.3.1 suggesting that the electron density increased with microwave power.

Five charge states of gold ranging from Au^{23+} to Au^{30+} had a beam current sufficiently above background for the three power levels used for these measurements. Figure 4.25 shows how decay time decreased as microwave power increased. The most probable explanation for this trend is that a higher electron density increases the ionization reaction rate, contributing to a smaller beam current decay time for a fixed confinement time suggested by Eq. (4.9).

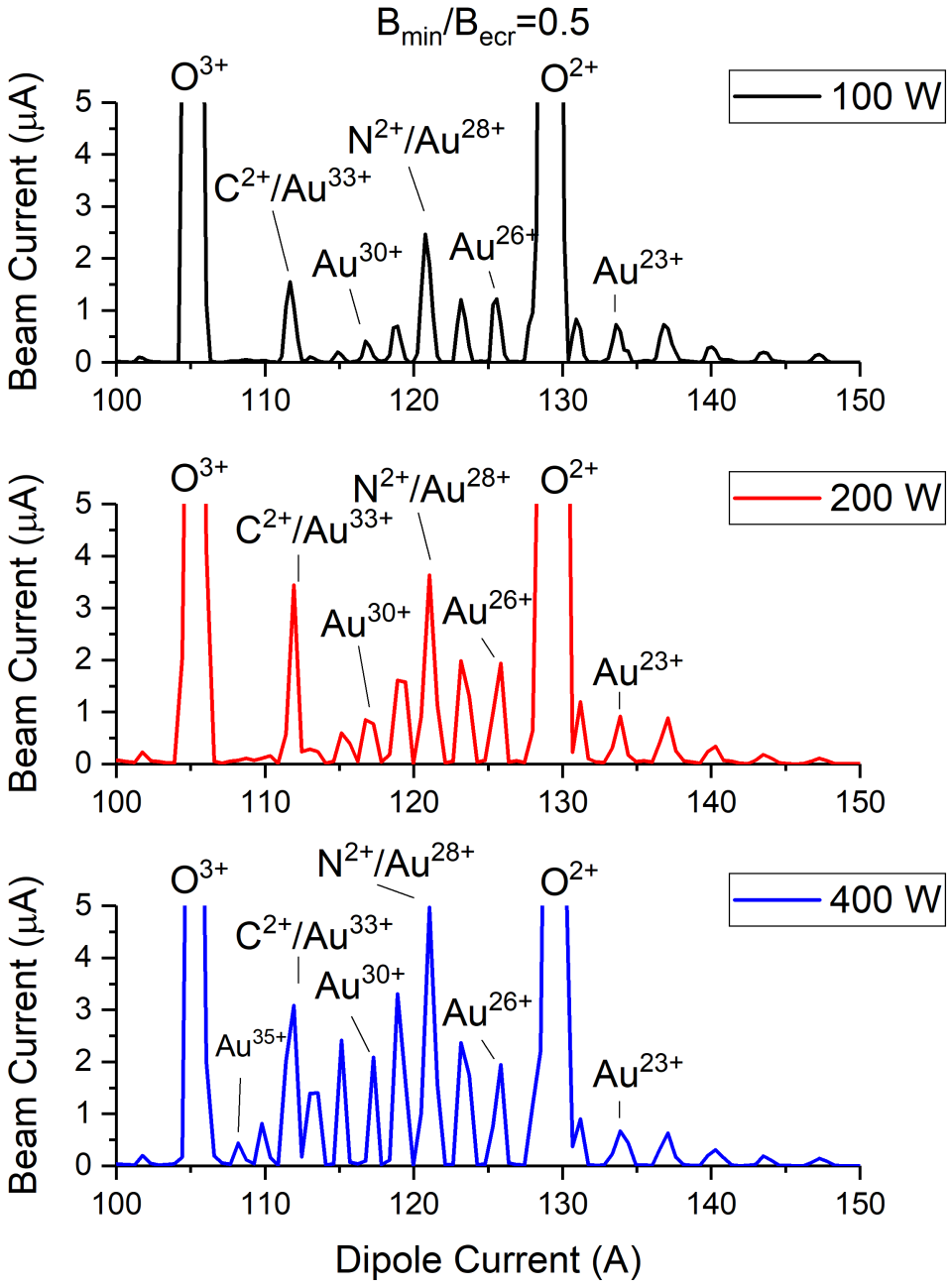

Figure 4.23: Charge state distribution for 100 W, 200 W, and 400 W at 18 GHz and for B_{min}/B_{ecr}=0.5. As the microwave power is increased the distribution tends towards higher charge states.

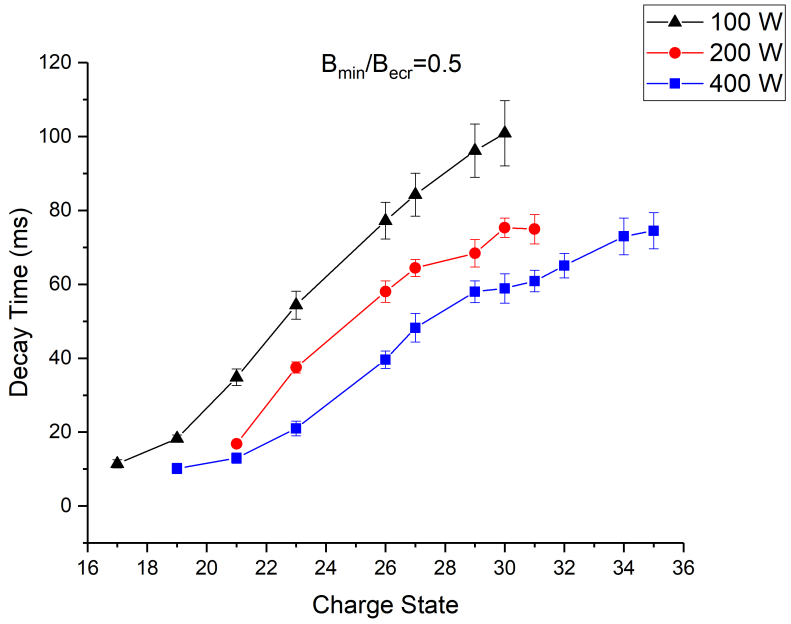

Figure 4.24: Decay time for all sampled charge states at a constant field of B_{min}/B_{ecr}=0.5 and increasing microwave power. Each decay time curve tends towards smaller values with increasing microwave power. The decay time curves appear to saturate at the high and low charge state tails.

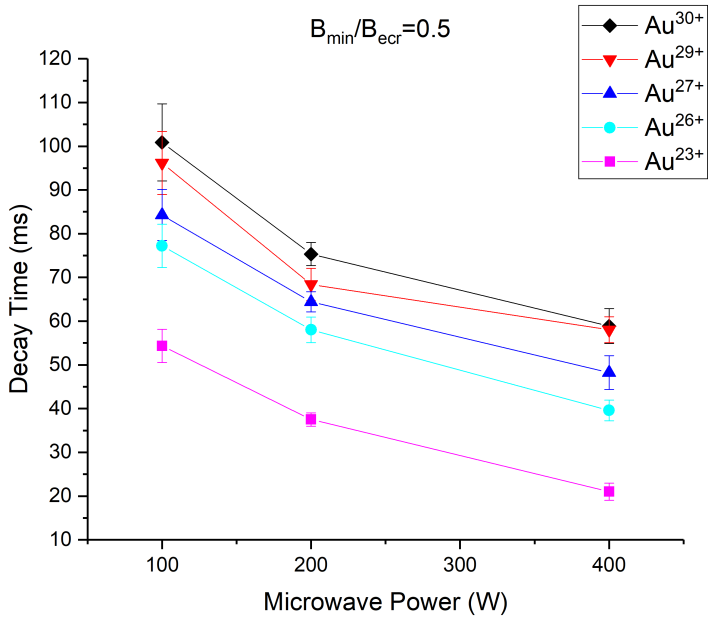

Figure 4.25: Decay time for the five charge states sampled that were expressed at all microwave power levels for B_{min}/B_{ecr}=0.5. Decay time increased with charge state and decreased with microwave power.

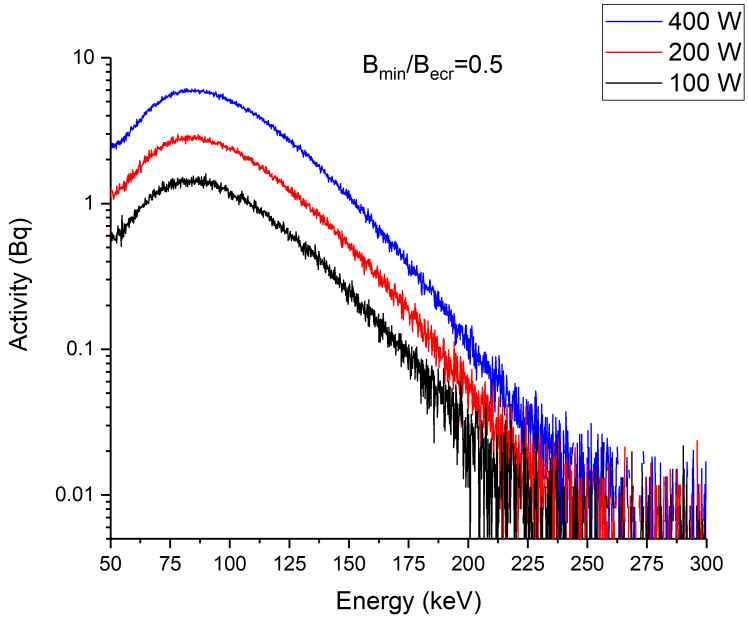

Figure 4.26: Bremsstrahlung spectra for different microwave powers at B_{min}/B_{ecr}=0.5 each representing a half hour exposure. The hot electron temperature remained fixed at $26^{-1.8}_{+2.3}$ keV while the x-ray power increased linearly with microwave power reaching 36.31±0.04 pW at 400 W applied microwave power.

It is interesting that decay time did not decrease linearly with microwave power, a different slope can be seen between the 200 W and 400 W microwave power levels.

The magnetic field B_{min}/B_{ecr}=0.7 was insensitive to the microwave power between 100 W and 200 W, and a finer resolution in microwave power would likely have resolved more of the structure. Decay time in Fig. 4.27 shows no significant change in decay time between 100 W and 200 W plasmas, while the 400 W plasma decays at half the rate. This jump was also expressed in the gold CSD (see Fig. 4.28) where the distributions at 100 W and 200 W were remarkably similar, but currents of highly charged gold dramatically increased between 200 W and 400 W plasmas. The x-ray spectra in Fig. 4.29 smoothly increased in intensity with microwave power and did not show evidence of a jump between 200 W and 400 W operating points. The x-ray power increased linearly with microwave power, and the

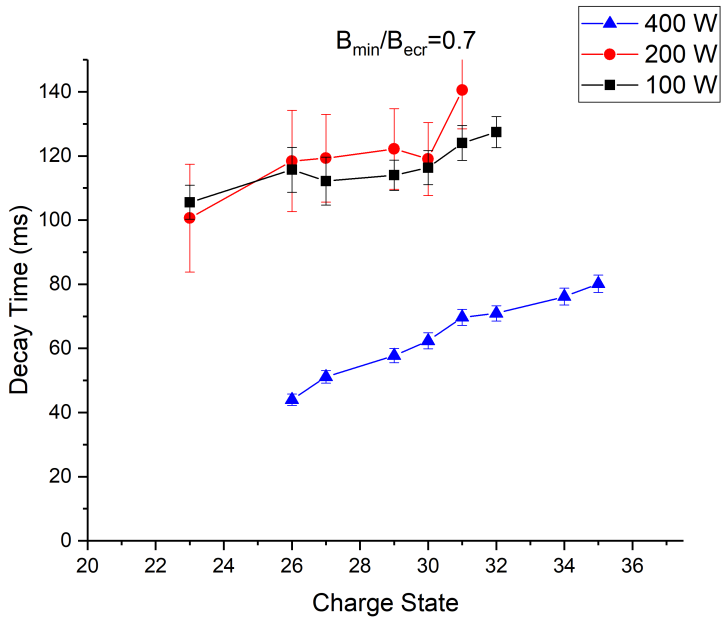

Figure 4.27: Decay times of gold charge states for B_{min}/B_{ecr}=0.7 for three different microwave power levels.

hot electron temperature remained largely fixed across the three power levels (see Fig. 4.20 in Sect. 4.3.1).

It is unclear why 100 W and 200 W plasmas produced such similar CSDs and decay times for B_{min}/B_{ecr}=0.7. Furthermore, it was unclear why such a large jump occurred in CSD and decay time between 200 W and 400 W operating points for this field. However, the results do corroborate the general trends found for B_{min}/B_{ecr}=0.5, mainly: decay time increased with charge state and decreased with microwave power (at least between 200 W and 400 W operating points).

Decay time generally decreased with increasing microwave power, with the best example for B_{min}/B_{ecr}=0.5 where a smooth decrease was seen in Fig. 4.25. In the case where two different operating points had the same mirror ratio, x-ray power increased with microwave power. This suggests that the additional electron losses were from a denser plasma. The ion

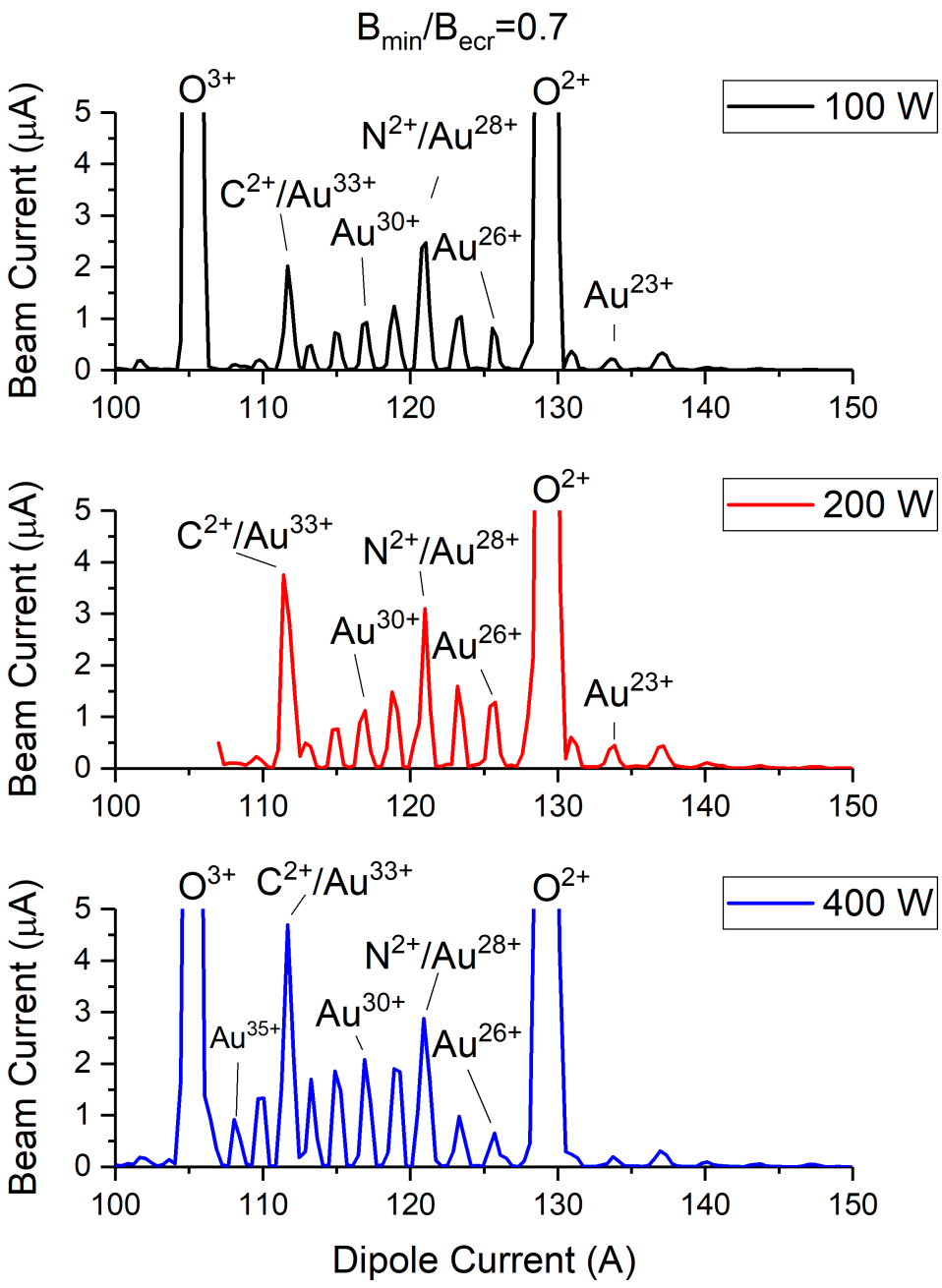

Figure 4.28: Charge state distribution for 100 W, 200 W, and 400 W at 18 GHz and for B_{min}/B_{ecr}=0.7. As the microwave power increased, the distribution tended towards higher charge states.

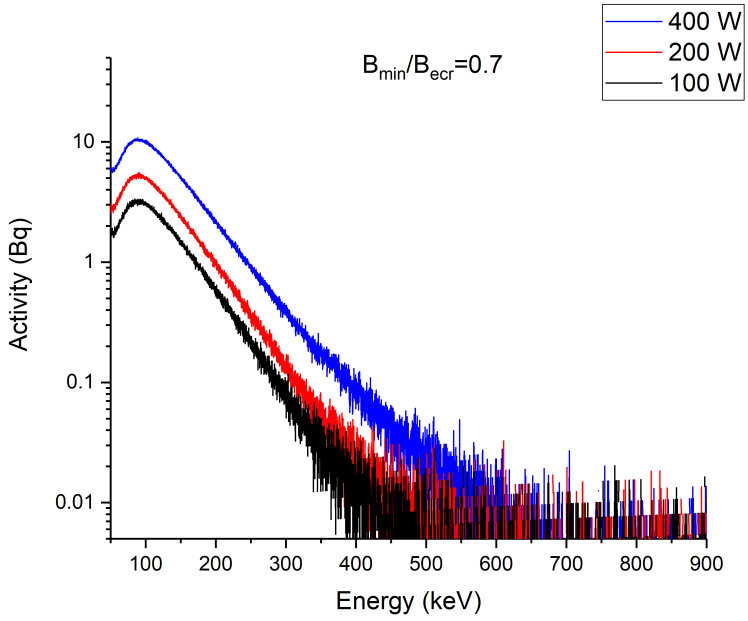

Figure 4.29: Bremsstrahlung spectra at three different microwave power levels for B_{min}/B_{ecr}=0.7.

confinement time, for a given charge state, likely remained fixed with microwave power and the decrease in decay time was the result of increasing electron density.

4.3.3 Decay Time and Magnetic Field for 13 GHz Operation

The effect of magnetic field on decay time was studied at 13 GHz for constant microwave power. Decay time increased with charge state for all of the three different magnetic fields as seen in Fig. 4.30. Moreover, Decay time steadily increased with magnetic minimum as shown in Fig. 4.31, with an approximately linear relationship. Each magnetic field produced a different hot electron temperature, with the hottest and coolest at $46.2^{-2.1}_{+2.6}$ keV and $19.8^{+0.3}_{+1.0}$ keV respectively as shown in Fig. 4.32. Furthermore, the emitted x-ray power increased linearly with hot electron temperature. The bremsstrahlung spectra for each field are shown in Fig. 4.20. The gold CSD was shifted to higher charge states with the increasing

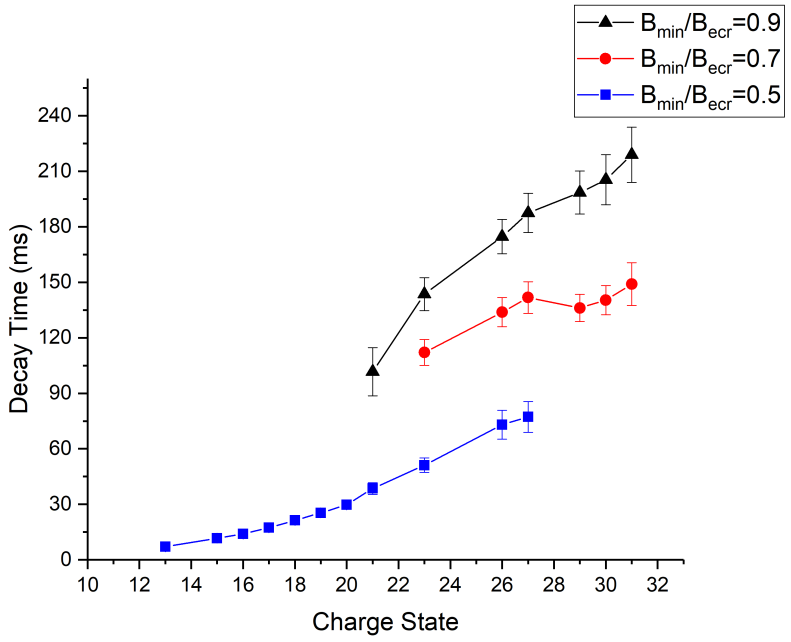

Figure 4.30: Decay time from fitting of gold beam current as a function of charge state and magnetic minimum for 100 W applied microwave power at a frequency of 13 GHz.

magnetic field (and hot electron temperature) as can be seen in Fig. 4.33.

The primary finding for 13 GHz operation at 100 W was that the measured decay time of the beam current waveform increased with B_{min}/B_{ecr}ratio and therefore increased with the hot electron temperature. The increase in decay time could have been caused by reduced ionization or charge exhange rates (see Eq. (4.9) in Sect. 4.2.2) but this is unlikely because the CSD was shifted to higher charge states for increasing B_{min}/B_{ecr}ratio. Most likely the decay time increased with ion confinement time from a deeper confinement potential generated by the hotter hot electron population. This suggests that hot electrons play a role in ion confinement.

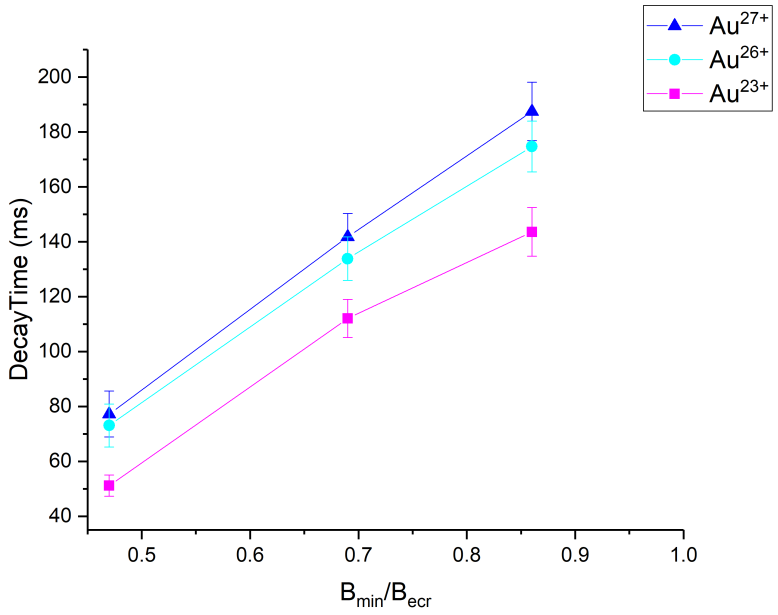

Figure 4.31: Decay time as a function of magnetic minimum for operation at 13 GHz and 100 W.

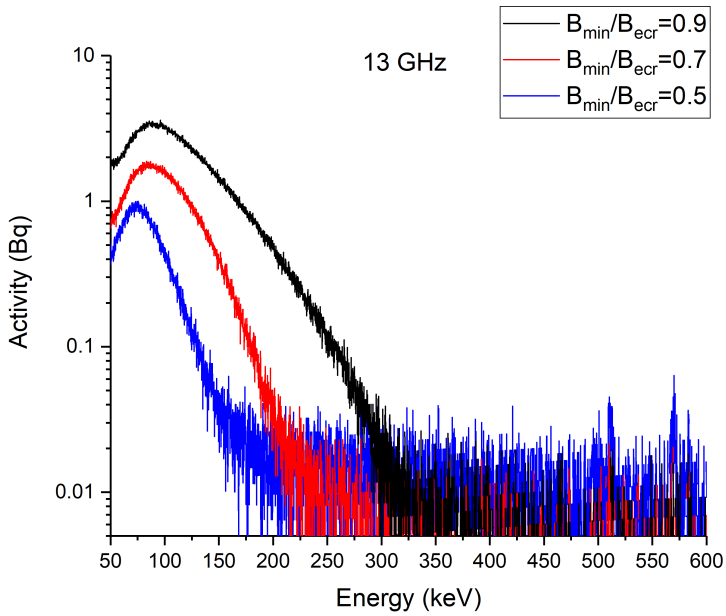

Figure 4.32: Bremsstrahlung spectra for three different magnetic minima at 13 GHz for a constant microwave power level of 100 W. The fitted hot electron temperatures for B_{min}/B_{ecr}=0.9, 0.7, and 0.5 were respectively: $46.2^{-2.1}_{+2.6}$ keV, $26^{-2.7}_{+3.1}$ keV, and $19.8^{+0.3}_{+1.0}$ keV.

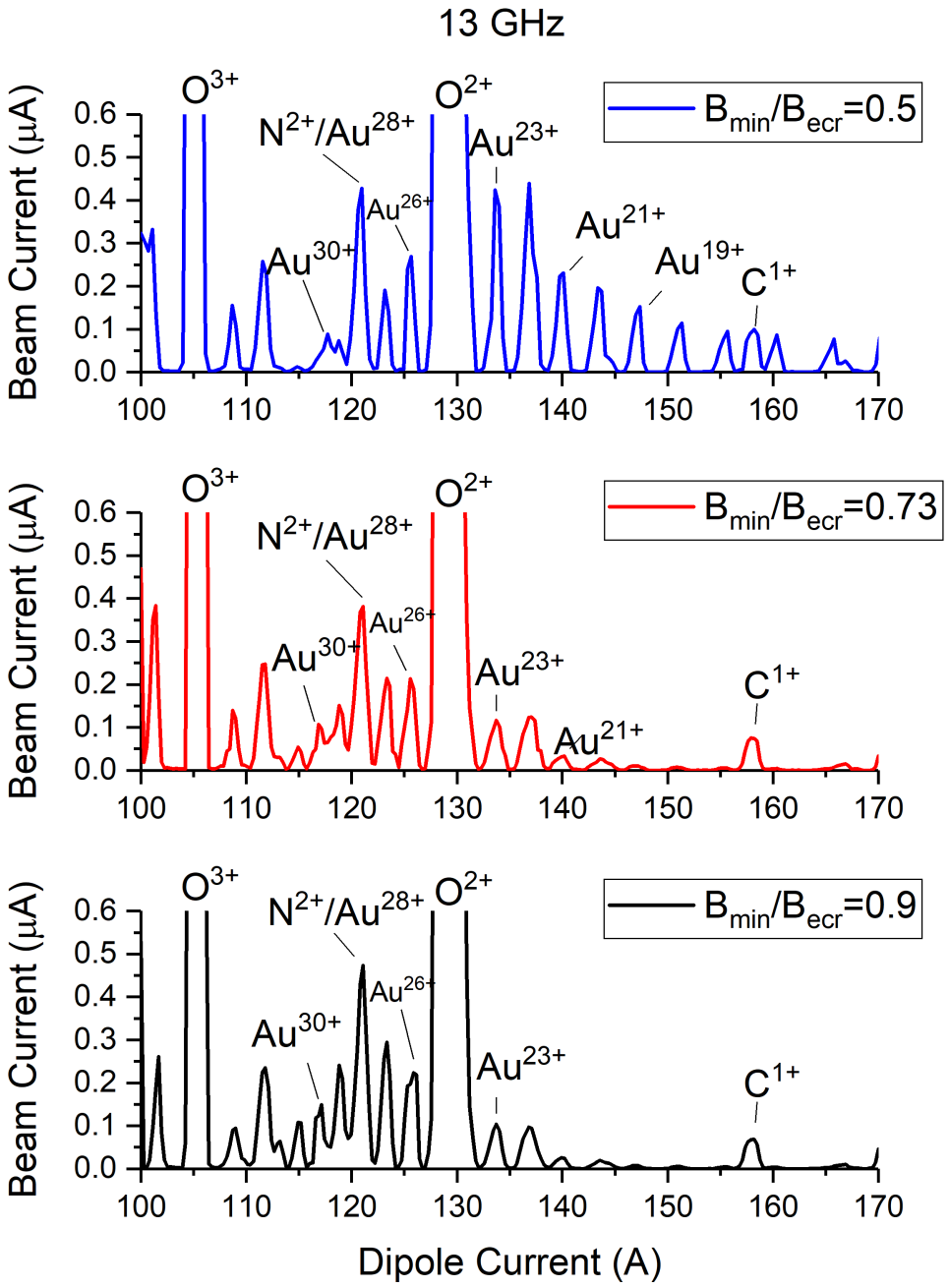

Figure 4.33: Charge state distributions for 13 GHz operation at 100 W. Higher magnetic minima produced a charge state distribution shifted towards higher charge states.

4.3.4 Decay Time and Magnetic Field for 18 GHz Operation

Operation at 18 GHz presented unique challenges. Beam current for 18 GHz operation at 100 W and 200 W produced bursts of current at B_{min}/B_{ecr}=0.9, likely the result of an instability absent for 13 GHz operation. An example of the current burst is shown for Au^{26+} in Fig. 4.34. Fitting of the beam current at 200 W required masking of the instability, otherwise the 1/e decay time was artificially increased. The beam current instability increased 1/e artificially by up to 20% in some cases as shown in Fig. 4.35. Masking of this instability was typically applied between 500-700 ms after the high voltage pulse was triggered (500-700 ms on Fig. 4.34), and was optimized in a case-by-case basis to each beam current waveform. Masking removed the artifact between Au^{26+} and Au^{27+} where 1/e decay time appears to decrease with increasing charge state. The use of smoothing functions was investigated for the 200 W dataset as an alternative to masking but, it was found to be ineffective. For the 100 W dataset, masking was found to be unnecessary because decay times were identical for masked and non-masked waveforms.

The CSD for gold ions shifted to higher charge states in both the 100 W case shown in Fig. 4.37 and 200 W case in Fig. 4.38. Figure 4.36a and Fig. 4.36c show the bremsstrahlung spectra becoming progressively hotter with increasing magnetic minimum. The CSDs and bremsstrahlung spectra show the same basic behavior of that observed for 13 GHz operation however, the decay times at 18 GHz operation did not have the same linear increase with magnetic minimum as was observed for 13 GHz operation. Instead, in both the 100 W and 200 W cases the decay times for the highest B_{min} (B_{min}/B_{ecr}=0.9) were significantly lower (about a factor of two) when compared to B_{min}/B_{ecr}=0.7 as can be seen in Fig. 4.36b and Fig. 4.36d. This was likely the result of kinetic instabilities further discussed in Sect. 4.3.5.

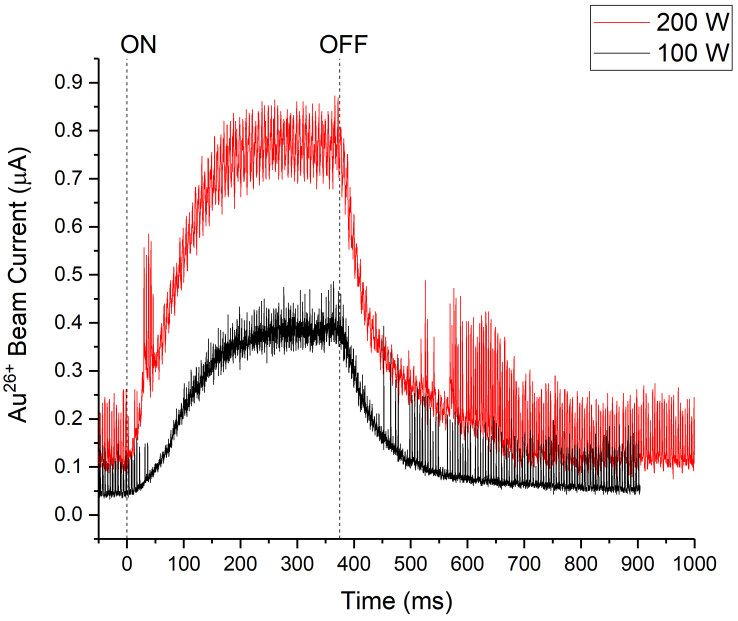

Figure 4.34: Instability observed at 18 GHz for B_{min}/B_{ecr}=0.9. Au^{26+} is shown but it was present in all measured charge states (except oxygen). It was necessary for the 200 W dataset to mask the region in time where the instability first appears as the beam current decays. Masking the instability at 100 W did not change the 1/e decay time.

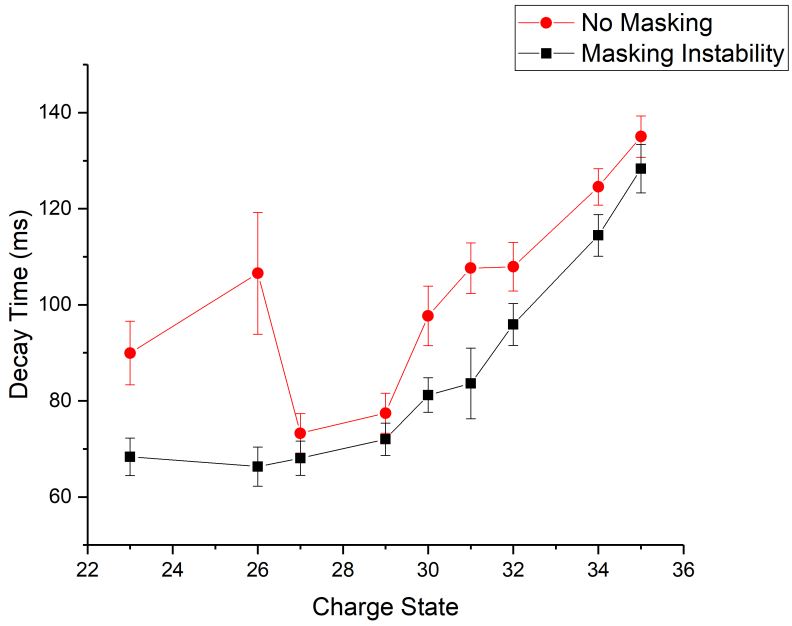

Figure 4.35: Decay time for masked and unmasked instabilities at 200 W. For various charge states of gold ranging from Au^{23+} to Au^{35+}. Masking of the beam current instability made a significant change to the fitted decay time and eliminated what appeared to be a decrease in decay time between Au^{26+} and Au^{27+}.

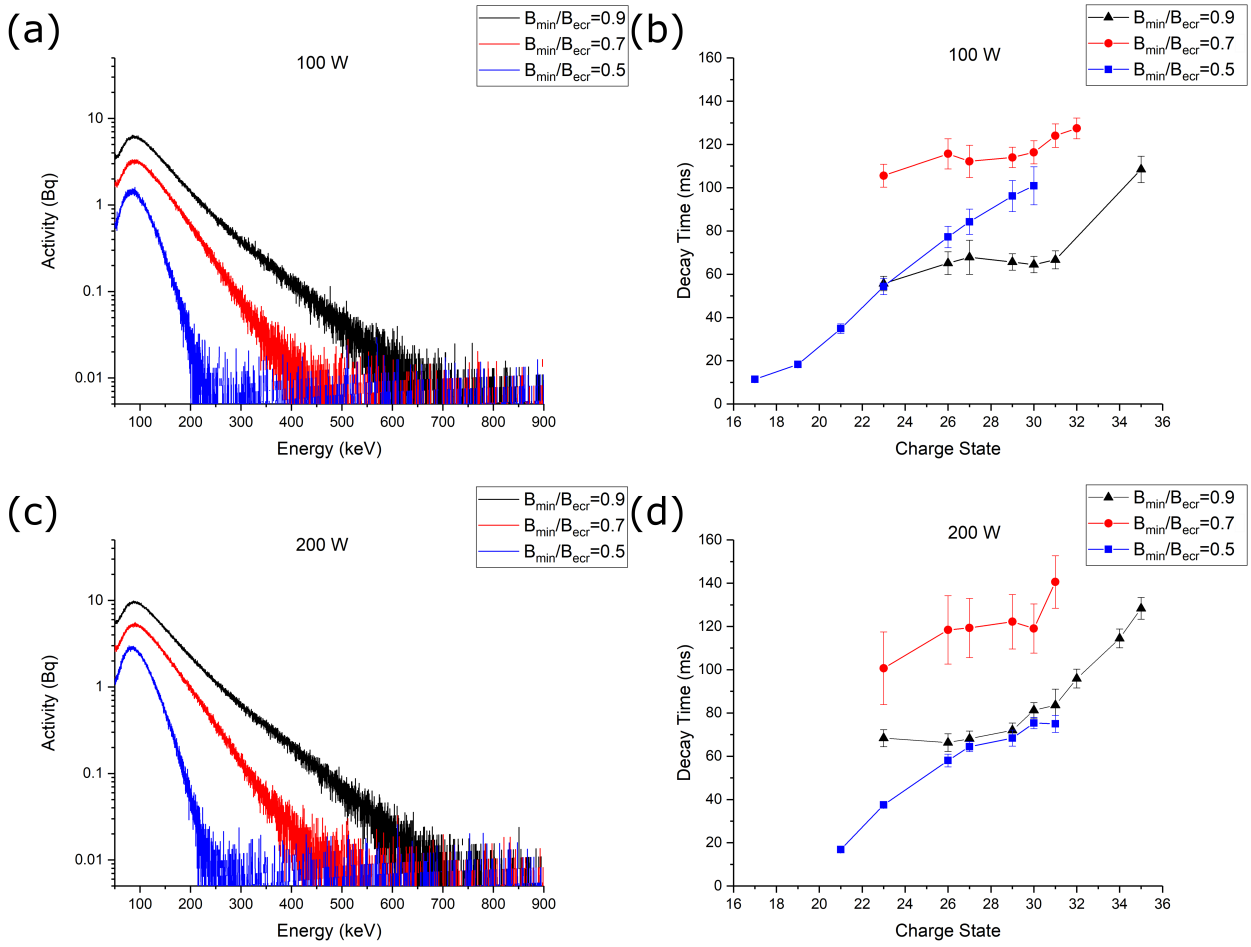

Figure 4.36: Bremsstrahlung spectra for 100 W (a) and 200 W (c) presented alongside the 100 W (b) and 200 W (d) 1/e decay times at 18 GHz. Table 4.5 provides specific quantities of hot electron temperature for the plasmas represented here. The hot electron temperature was the same (within each ±10% deviation) between 100 W and 200 W plasmas. The x-ray power at B_{min}/B_{ecr}=0.5 increased by a factor of two between 100 W and 200 W, but for B_{min}/B_{ecr}=0.9 and B_{min}/B_{ecr}=0.7 the increase was only about 60%. Note how For the magnetic field with the hottest hot electron temperature and highest x-ray power, B_{min}/B_{ecr}=0.9, the measured decay time is lower than for B_{min}/B_{ecr}=0.7.

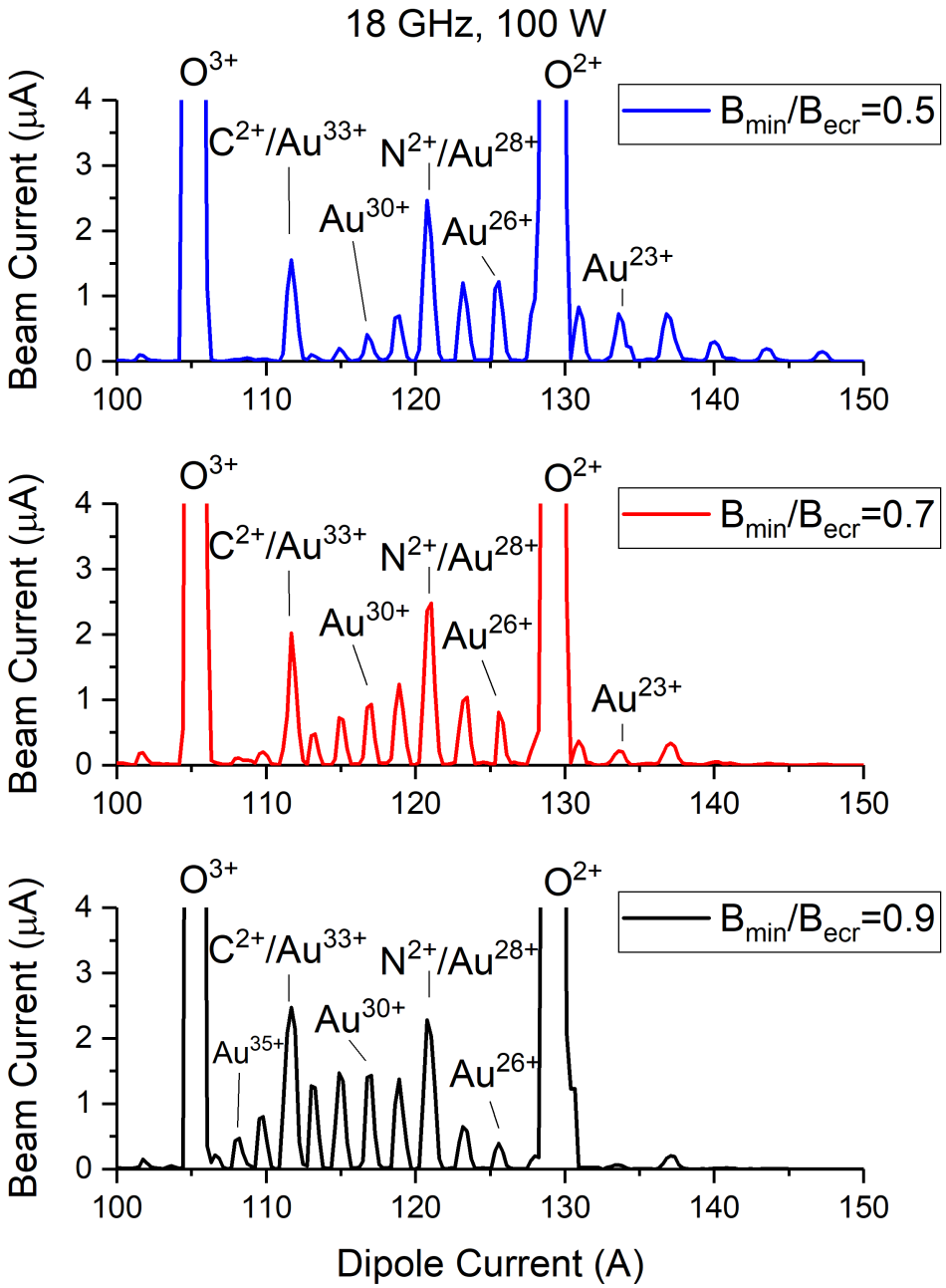

Figure 4.37: Charge state distribution for three different magnetic fields: B_{min}/B_{ecr}=0.5, B_{min}/B_{ecr}=0.7, and B_{min}/B_{ecr}=0.9 for 18 GHz operation at 100 W. 18 GHz operation at 100 W illustrated very clearly how the CSD shifts to higher charge states with increasing magnetic minimum observed in the study.

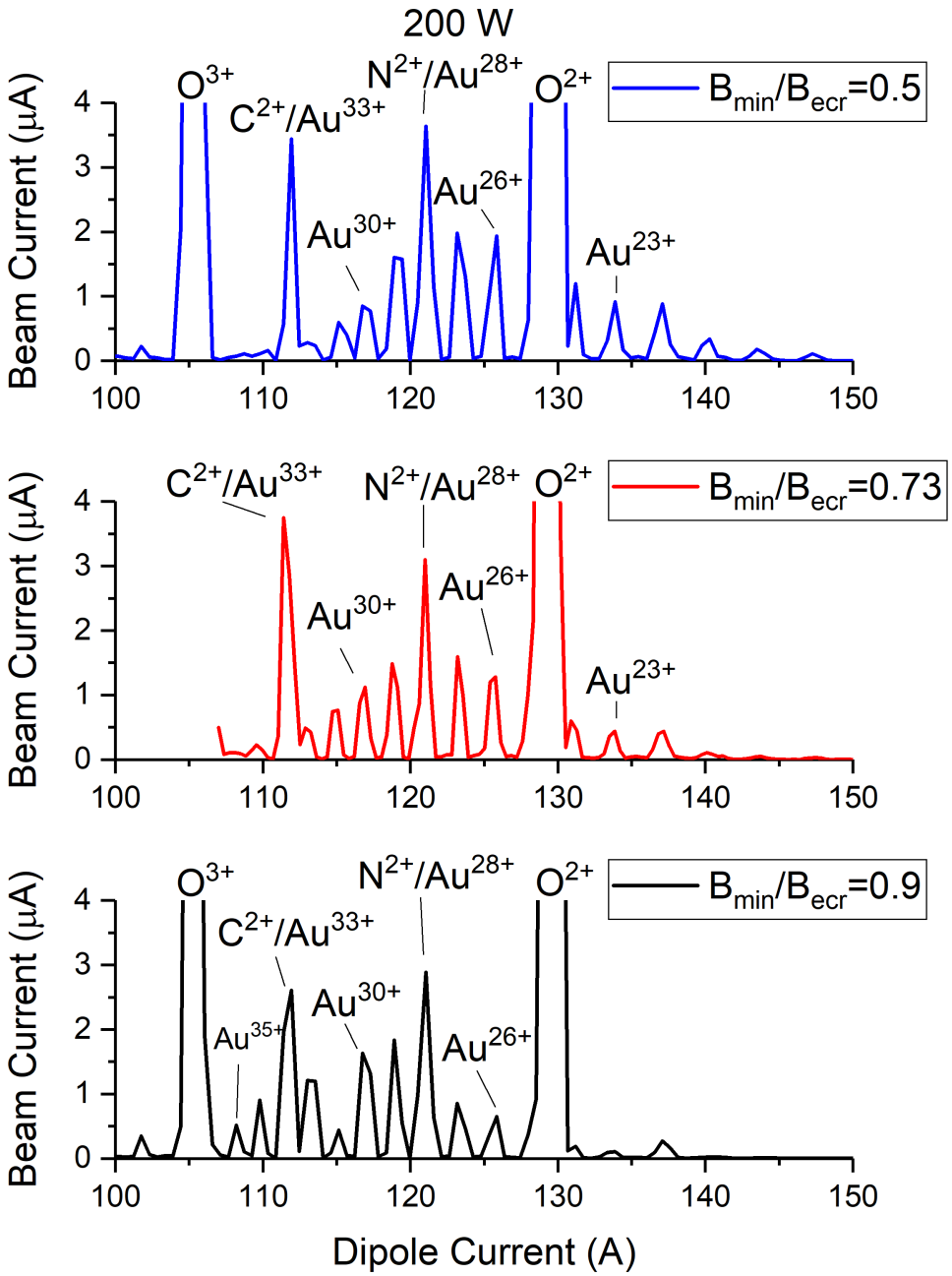

Figure 4.38: Charge state distribution for three different magnetic fields: B_{min}/B_{ecr}=0.5, B_{min}/B_{ecr}=0.7, and B_{min}/B_{ecr}=0.9 for 18 GHz operation at 200 W The Au^{31+} current measured for B_{min}/B_{ecr}=0.9 appears lower than its neighbors due to a data acquisition error.

4.3.5 The Effect of Cyclotron Instabilities on Decay Time for 18 GHz Operation

Decay time for 18 GHz operation did not increase smoothly with magnetic minimum as was the case for 13 GHz. The drop in characteristic decay time for 18 GHz operation at B_{min}/B_{ecr}=0.9 was likely the result of cyclotron instabilities. These instabilities were identified to occur in ECRIS plasmas for B_{min}/B_{ecr}> 0.7 [91]. It has been observed that cyclotron instabilities lead to losses of energetic electrons from the plasma through emission of microwave and x-ray radiations with a time scale of hundreds of nanoseconds (ns) and tens of microseconds (μs) respectively [31]. These instabilities depopulate hot electrons from magnetic confinement [23] converting the electron kinetic energy into microwave energy, and lead to a decrease in ion beam current particularly for high charge states with characteristic times in the millisecond range [91]. The diagnostics employed in the pulsed sputtering experiments were either time averaged (x-ray measurement), or as in the case of beam current measurement, presented insufficient time resolution due to the RC time constant of the measurement circuit (see Sect. 2.6.1). Figure 4.39 illustrates O^{6+} beam current oscillations observed for 200 W microwave power at B_{min}/B_{ecr}=0.9 which had a waveform similar in shape and frequency to that identified in [91] as characteristic of cyclotron instabilities. Figure 4.40 shows where the O^{6+} beam current oscillations fall in context of the sputtering time used during the experiment.

Decay time for 18 GHz operation was shown in Sect. 4.3.4 to decrease with B_{min}/B_{ecr}ratio from 0.7-0.9 for both 100 W (Fig. 4.36b) and 200 W (4.36d) microwave power levels. In contrast, Sect. 4.3.3 of this chapter demonstrated that at 13 GHz decay time increased with magnetic field and hot electron temperature. It is likely that the development of cyclotron

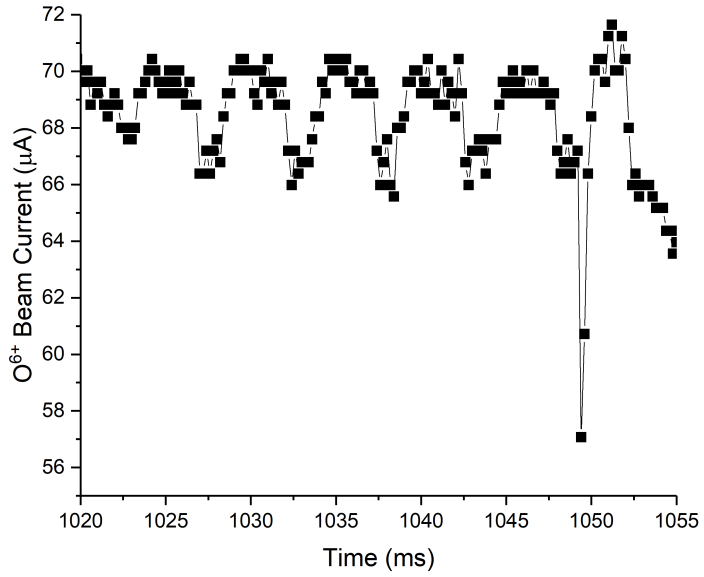

Figure 4.39: O^{6+} beam current for B_{min}/B_{ecr}=0.9 at 18 GHz with 200 W applied microwave power from Fig. 4.40. This shows the the fast periodic instabilities.

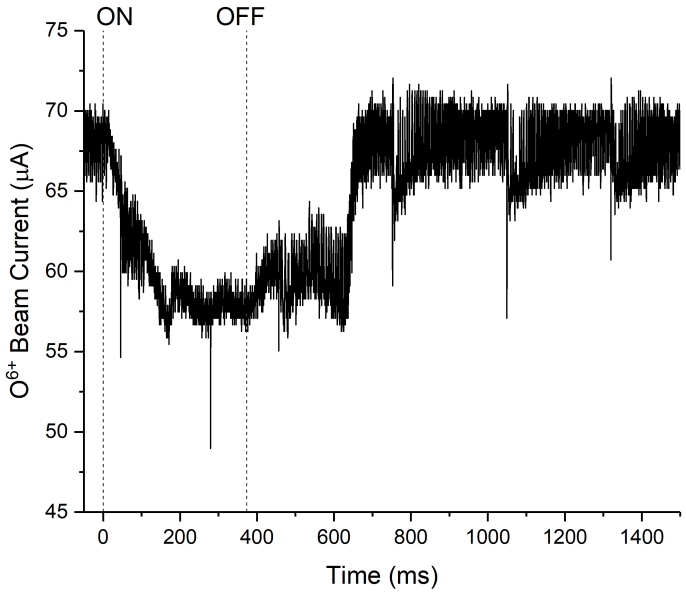

Figure 4.40: O^{6+} beam current for B_{min}/B_{ecr}=0.9 at 18 GHz for 200 W applied microwave power, in reference to the applied sputtering voltage, with beam dropouts seen at regular intervals.

instabilities reduced the electrostatic confinement potential by ejecting hot electrons from the plasma and lowering the measured decay time. As decay time is proportional to ion confinement time from Eq. (4.9) the ion confinement time was lower for B_{min}/B_{ecr}=0.9 than B_{min}/B_{ecr}=0.7 and was likely caused by cyclotron instabilities that according to Ref. [23] impact hot electrons more than cold electrons.

Further indication that plasma instabilities were present when operating the ion source with B_{min}/B_{ecr}=0.9 may be found by plotting the emitted x-ray power as a function of electron temperature as shown in Fig. 4.41. In particular, it can be seen that the x-ray power strongly increased when changing the B_{min}/B_{ecr}ratio from 0.7 to 0.9 compared to the trend observed between 0.5 and 0.7. The 13 GHz plasma did not have this structure and hot electron temperature linearly increased with x-ray power at a constant rate for all three magnetic field configurations. The fact that decay time for 13 GHz operation also increased linearly with magnetic field configuration further suggests that an instability (likely cyclotron instabilities) changed the ion confinement time at 18 GHz.

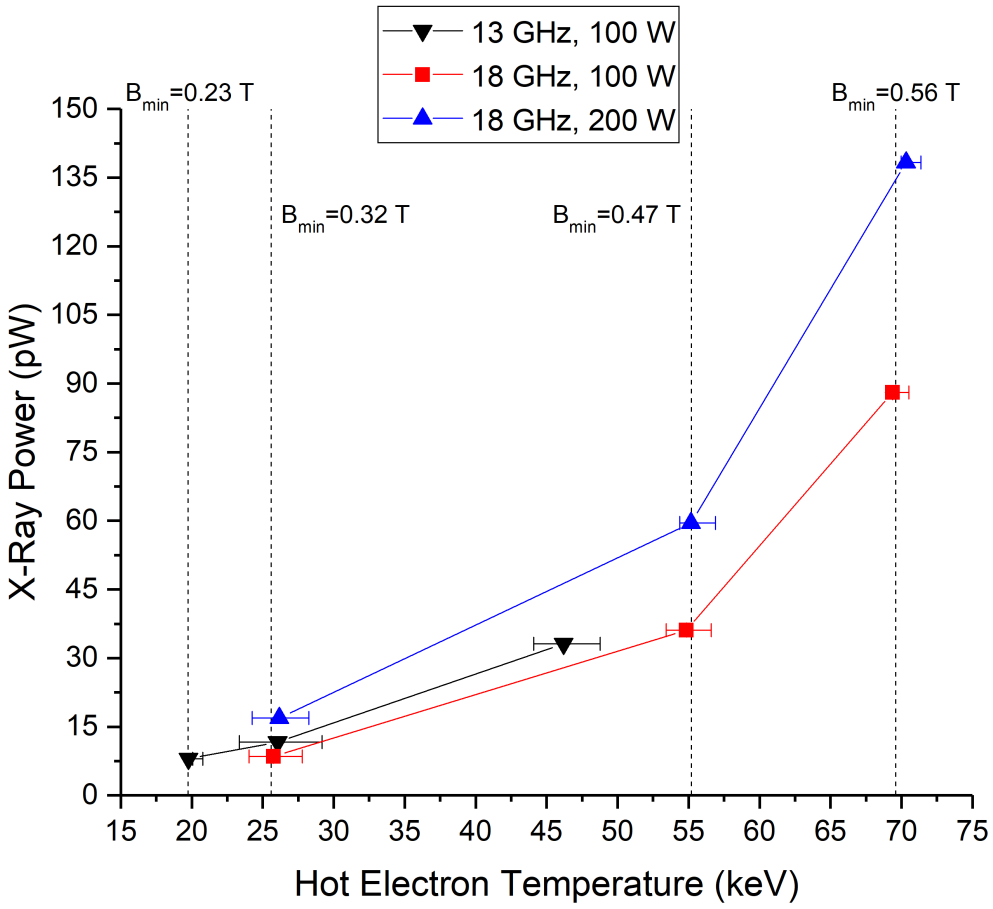

Figure 4.41: X-ray power as a function of hot electron temperature for 13 GHz and 18 GHz operation. The 400 W dataset was not included because the x-ray power for B_{min}/B_{ecr}=0.8 necessitated an increase in scale that rendered detail for the other operating points difficult to see. X-ray power increased linearly with hot electron temperature for all plasmas sampled at 13 GHz. However, for 18 GHz operation, the B_{min}/B_{ecr}=0.9 operating point produced disproportionately more x-rays than the trend established for lower B_{min}/B_{ecr}ratios suggesting plasma instabilities played an increased role at that magnetic field configuration.

4.4 Discussion of Results

Beam current decay times were related to ion confinement time using a fitting model in Sect. 4.2.2. The resulting 1/e decay time is less than the ion confinement time in the plasma. Decay times of gold increased with charge state for every plasma studied, and the decay time magnitudes measured in the study were fairly long with the range of values spanning between 7.1±0.8 ms for Au^{13+} and 220±15 ms for Au^{31+} (incidentally found for 13 GHz operation over all operating points). Decay times of gold increased with hot electron temperature for all magnetic fields, except for 18 GHz operation at B_{min}/B_{ecr}=0.9, wherein a significant decrease in decay time was observed (see Figs. 4.42 and 4.43). This was likely the result of kinetic cyclotron instabilities that were identified to arise for such a high B_{min}/B_{ecr}ratio [91]. Supporting this idea, hot electron temperature began to saturate with an increased x-ray power emission between B_{min}/B_{ecr}=0.7 and 0.9 when compared to trends established between B_{min}/B_{ecr}=0.5 and B_{min}/B_{ecr}=0.7 in Fig. 4.41. This suggested the plasma traded stored energy for increased electron losses at this operating point. Additionally, the oxygen beam current appeared to have a saw tooth waveform in Fig. 4.39 characteristic of cyclotron instabilities reported in Ref. [91]. The culmination of the evidence presented within this chapter suggests that ion confinement in ECR ion source is electrostatic as proposed by Refs. [68, 18]. The fact that decay time sagged in this region of instability further supports the idea that hot electrons are critical to maintain long ion confinement times.

Furthermore, when compared against the collisional model proposed in Refs. [9, 99] which may be described by the proportionality:

$$\tau_i \propto L^2 i^2 \frac{\sum_i i^2 n_i}{T_i^{5/2}}. \tag{4.10}$$

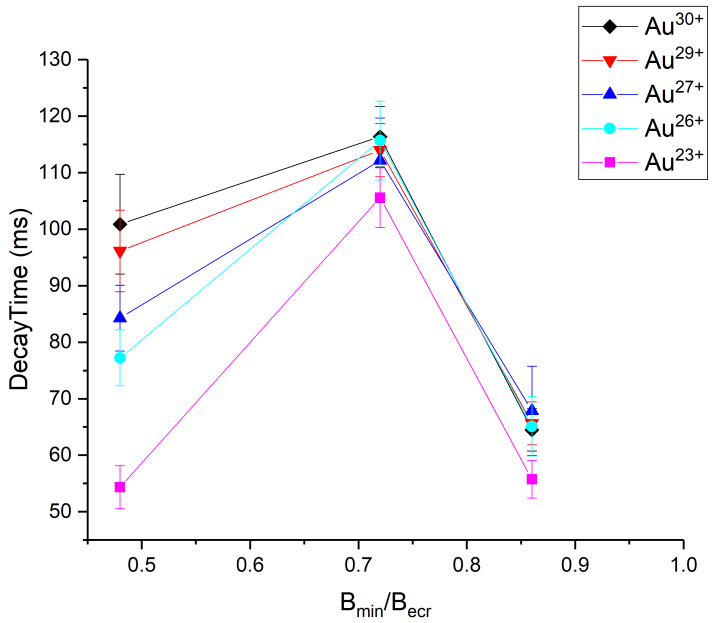

Figure 4.42: Decay time vs. B_{min}/B_{ecr}ratio at 18 GHz 100 W for all charge states with measurable current at the three selected fields.

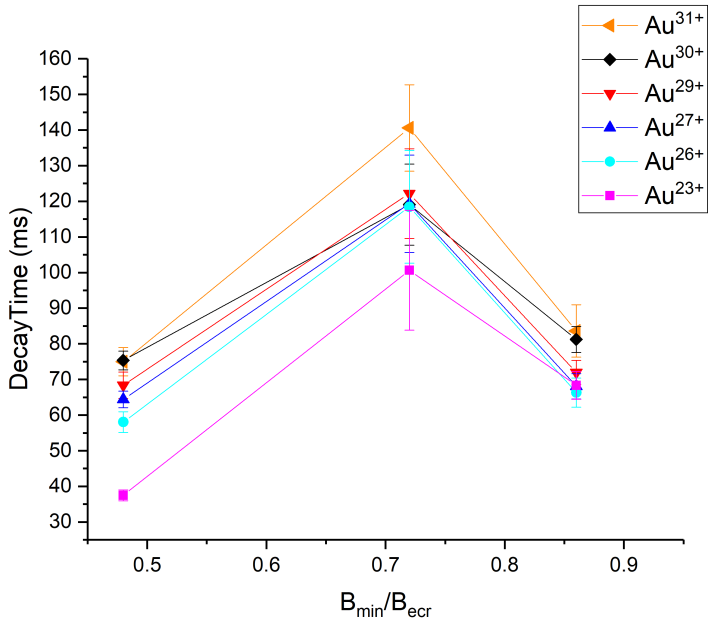

Figure 4.43: Decay time vs. B_{min}/B_{ecr}ratio at 18 GHz 200 W for all charge states with measurable current at the three selected fields.

Here, T_i is ion temperature, L is an axial plasma half length, n_i ion density as seen before, and i the charge state. Eq. (2.20) predicts confinement time should decrease with the square of plasma length, but the results for 13 GHz across all magnetic fields show decay time increasing with decreasing plasma length. Furthermore, 18 GHz results corroborate this trend between the operating points of B_{min}/B_{ecr}=0.5 (plasma length of 16.3 cm) and B_{min}/B_{ecr}=0.7 (plasma length of 12.8 cm). Decay time is proportional to ion confinement time, so to find decay time increasing with decreasing plasma length is mutually exclusive from the predictions of the diffusion model. By comparison, the electrostatic model depends on an effective electrostatic potential generated by a well-confined hot electron core and is more consistent with the trend of decay time increasing with hot electron temperature. It is worth mentioning that decay time did decrease from B_{min}/B_{ecr}=0.7 to B_{min}/B_{ecr}=0.9 for 18 GHz operation, which is believed to be caused by plasma instabilities. It would be interesting to see how decay time changes with magnetic fields that change only the plasma length leaving the magnetic minimum fixed, but unfortunately these field parameters were not explored in this study.

One interesting finding was that steady state gold sputtering currents for 13 GHz operation were a factor of 4-9 times lower than what was obtained for 18 GHz operation as can be seen in Table 4.5. Sputtering is particularly sensitive to plasma density, plasma ions are pulled onto the sputter sample making the sputtering rate density dependent. The capture probability of the sputtered neutral material is again dependent on plasma density. The decrease in current likely comes from a decrease in plasma density. The decay times for 13 GHz operation, with the same magnetic minimum (B_{min}=0.3 T), were higher for each comparable charge state than 18 GHz operation as seen in Fig. 4.44. The measured decay time would decrease with an increased electron density for similar ion confinement time,

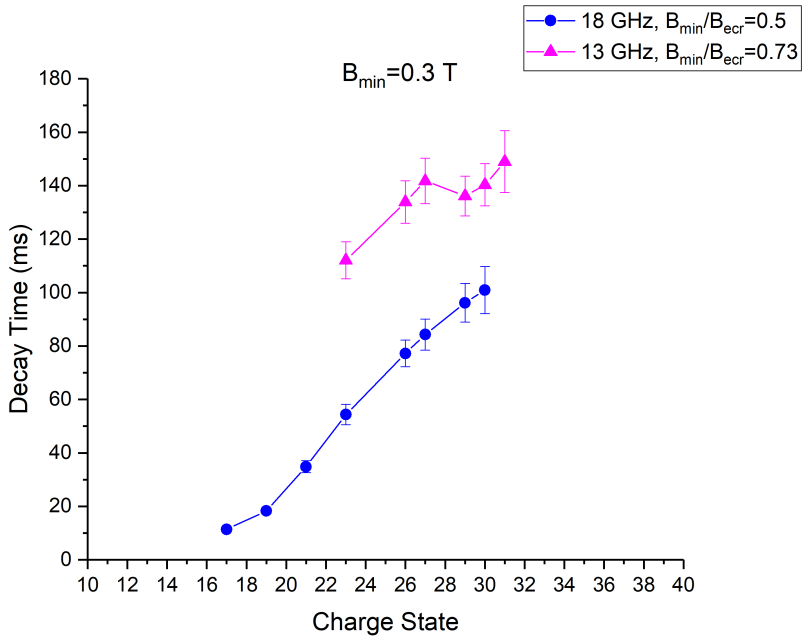

Figure 4.44: Decay times for 18 GHz and 13 GHz operation compared for B_{min}=0.3 T (hot electron temperature was 26 keV).

ionization rate, and charge exchange rate. In agreement with this idea, the decay times for 13 GHz operation were larger than 18 GHz operation for the same hot electron temperature, and could have been a result of the increased electron density for 18 GHz operation. It is worth mentioning that the vacuum pressures for 13 GHz operation at 100 W were about 30% lower than for 18 GHz operation suggesting that the charge exchange reaction rate was reduced for 13 GHz operation and may have contributed to the higher decay times at this operating point.

In summary, pulsed sputtering experiments on SuSI suggested that ion confinement in a 3^{rd} generation ECR ion source is electrostatic. The key evidence leading to that conclusion follows:

1. Decay time τ_{im} increased with charge state under all conditions suggesting it is proportional to ion confinement time τ_i.

2. Decay time increased with hot electron temperature except for B_{min}/B_{ecr}=0.9 with 18 GHz operation which was identified as an unstable operating point.

   (a) Plasma instabilities were identified by comparing x-ray power (electron losses) to hot electron temperature (energy storage). The region of instability produced x-ray power at a higher rate with hot electron temperature than for trends established at other magnetic field configurations.

   (b) O. Tarvainen et al. in Ref. [91] found magnetic field configurations with $B_{min}/B_{ecr}>$ 0.7 to be characterized by cyclotron instabilities.

   (c) S. Golubev et al. in Ref [23] found that cyclotron instabilities extract energy from hot electrons in a bi-Maxwellian plasma model.

In the electrostatic ion confinement model, well confined hot electrons create a potential dip that ions populate to maintain plasma quasi-neutrality. Although direct measurement of hot electron density was not possible with our instrumentation, the correlation of hot electron temperature and ion decay time suggests that hot electrons play a role in ion confinement.

A fast sputtering experiment described in Ref. [52] was conducted at the University of Jyväskylä using a copper sputtering sample on the 14 GHz ECR2 (see Sect. 2.5.3). Some of the same general trends were observed: decay times increased with charge state, decreased with microwave power, and increased with magnetic minimum. However, the change in decay times with magnetic minimum or microwave power was not very strong. This could have been the result of lower (relative to the gold results presented in this dissertation) charge states measured, thereby reducing the measurement sensitivity to small changes in the confinement well. In Fig. 4.30 the decay times appear to flatten towards zero as the charge state decreased to Au^{13+} (the lowest gold charge state measured in the study) suggesting that the ability of

these charge states to detect changes in the plasma is reduced, and could be the reason why the trends in decay time with microwave power and magnetic minimum in [52] were fairly mild.

Chapter 5

Amplitude Modulation of Microwave Power on the 14 GHz ECR Ion Source ECR2

Amplitude Modulation (AM) of microwave power explores how the plasma responds to changes in microwave power. The difference between amplitude modulation and afterglow is that with AM the microwave power is not turned off so the plasma is always sustained (180 W in this case) in between pulses. In essence AM is a new variation on the afterglow technique discussed in Sect. 2.4.3.

The first AM experiments were carried out on SuSI in 2014 and 2016 to determine if amplitude modulation in microwave power from the 24 GHz gyrotron, around 50 kHz, would be observable in the extracted beam. The amplitude modulation in the 24 GHz gyrotron for SuSI was the result of AM in the cathode high voltage from use of a switching power supply. Early AM experiments on SuSI modulated the 18 GHz klystron sinusoidally. These early experiments, although heavily influenced by the RC characteristics of the measurement circuit (Sect. 2.6.1), were encouraging. Systematic investigations were conducted in collaboration with the ion source group at the University of Jyväskylä physics department (JYFL) and are presented herein. Out of the large quantity of data obtained during the experiment a

portion is presented focusing on the effects of magnetic field, vacuum pressure, and plasma species.

One of the motivators for studying amplitude modulation was the idea that the plasma electron density could be perturbed by the microwave power, leaking ions from the source that would experience the confinement potential. In essence it was thought that AM could emulate a pulsed sputtering experiment but not incur the penalty of using a heavy element to witness the plasma and change its characteristics. The experimenter could measure the increase in characteristic time for ions on a pure gaseous plasma by modulating the electron density. However, at most AM frequencies the ions followed the x-ray signal (electrons) suggesting the measurement probed the behavior of electrons and their effect on ion extraction from the source instead of ion confinement.

A preliminary study is presented with the goal to explore sensitivity of the plasma to AM that was indented to point towards areas of interest for future investigation. The findings strongly suggest that AM does not probe ion confinement and production timescales rather, AM appears to provide insight to electron confinement and production times although the exact relationship remains an area of further investigation.

5.1 Experimental Set-up

5.1.1 Experimental Equipment Used in the Study

The microwave power level into the ion source provided by the klystron was determined by the intensity of the 14 GHz seed oscillation input to the klystron bunching cavity. The oscillator was a Keysight N5173B set to oscillate at 14.056 GHz and supported sinusoidal and square wave amplitude modulation. Frequencies for AM were purposefully selected to

avoid interference from harmonics of 50 Hz (the power station alternating current frequency) below ≈1 kHz. The average microwave power level injected was 350 W with a maximum of 530 W and a minimum of 180 W as measured from the bi-directional couplers at the klystron. Forward and reflected microwave power were monitored on an oscilloscope through Schottky diodes buffered with isolation amplifiers (gain of 1). Beam current was measured on the Faraday cup after mass to charge separation with a commercial low-noise current preamplifier (Stanford Research Systems model SR570) which had a sensitivity up to 200 kHz and was monitored on the oscilloscope. X-ray power was sampled radially in between the injection and extraction solenoids with a bismuth germanate scintillator crystal coupled to a sodium doped cesium iodide photomultiplier tube operating in current mode [91] culminating in the measurement of a voltage on the oscilloscope. The voltage was not calibrated to quantitative units such as watts because the photon energy was not counted in the measurement. The x-rays impinged on the scintillating crystal after transmission through the plasma chamber wall, hexapole magnet, and vacuum vessel so it is unlikely x-rays below in energy of about 30 keV were observable during the measurement. The x-ray detector measured the energy integrated power flux exceeding the energy threshold and represented a relative measure of x-ray power. A schematic of the set-up is provided in Fig. 5.1 for reference.

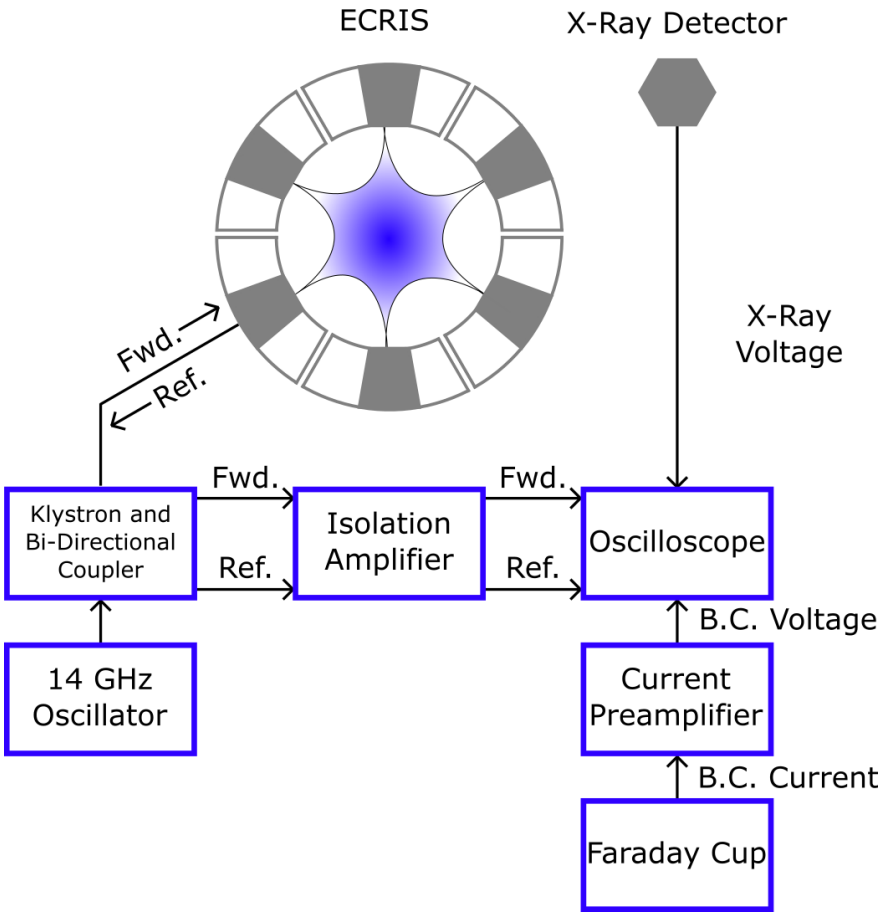

Figure 5.1: Schematic of the experimental set-up for the amplitude modulation experiment on ECR2 at the University of Jyväskylä Physics Department (JYFL).

5.1.2 Experimental Methodology

The main focus of the study was to quantify the plasma response to sinusoidal modulation of the microwave power at different modulation frequencies and for different charge states. Around 20 fixed frequencies were selected to measure the plasma response. However, not every frequency was used if the beam current did not oscillate. The ion source magnetic field was found to play a major role in the beam current amplitude response during the experiment. Amplitude modulation of the microwave power resulted in strong attenuation of the measured beam current amplitude when increasing the modulation frequency for B_{min}/B_{ecr}=0.72. Two additional magnetic field configurations were used, B_{min}/B_{ecr}=0.67 and B_{min}/B_{ecr}=0.77, that were separated by and equal magnitude about B_{min}/B_{ecr}=0.72. Modulation of the beam current amplitude was observed to extend to higher frequencies for these two fields. Table 5.1 lists some of the common characteristics of these magnetic field configurations. The x-ray power modulated similarly for all measured plasma species. The largest x-ray power amplitudes were measured for the lowest frequencies for any given operating point.

B_{min}/B_{ecr}	0.67	0.72	0.76	0.77
B_{min} (T)	0.34	0.36	0.38	0.39
B_{inj} (T)	1.89	1.95	1.99	2.01
B_{ext} (T)	0.88	0.92	0.95	0.97
ECR Length (cm)	11.8	10.7	9.9	9.5
B_{ext}/B_{min}	2.62	2.55	2.51	2.49
I_{inj}=I_{ext} (A)	480	510	530	540

Table 5.1: Table of magnetic field parameters calculated using the Finite Element Method Magnetics (FEMM) software with ECR2 model developed by the ion source group at JYFL. The injection solenoid current (I_{inj}) equaled the extraction solenoid current (I_{ext}).

5.1.3 Overview of the Plasmas Studied

One of the major goals during the experiment was to determine if AM could probe ion confinement times and as a result many charge states were selected particularly the extremely high and low charge states. Argon was the most studied gas species followed by neon and krypton. Krypton provided some of the smoothest beam current waveforms although it was measured for only for one magnetic field configuration.

The ion source was setup with a platform potential of 10 kV and the bias disc was set to -160 V for all experiments presented within this chapter. The source was optimized for an Ar^{13+} plasma at 350 W CW with a vacuum pressure of $4.5 \cdot 10^{-7}$ mbar which provided a drain current of 0.84 mA. The overall distribution of argon charge states did not change strongly with the plasma operating points explored. The neon plasma was tuned to produce approximately the same drain current as for argon (0.84 mA) arriving at a vacuum pressure of $2.2 \cdot 10^{-7}$ mbar. Over time the drain current of the neon plasma increased to 0.9 mA. Krypton was specifically tuned for maximum Kr^{23+} current at 350 W CW which included using the magnetic field configuration of B_{min}/B_{ecr}=0.77 which was well studied by argon and neon plasmas. The drain current for krypton was 0.7 mA with a vacuum pressure of $7.4 \cdot 10^{-7}$ mbar.

5.1.4 Methods of Data Processing, Error Identification, and Screening

Over the course of the experiment over eight thousand oscilloscope waveforms were exported containing oscillatory information of the forward power, reflected power, x-ray power, and beam current. With such a large quantity of information it was impractical to extract

basic quantities such as amplitude and relative phase (between any two channels) by visual inspection alone. Instead the measured waveforms were fitted automatically with a sinusoidal function using OriginLab. The forward microwave power was fitted reliably by the software with its highly sinusoidal behavior. The fitting function frequency was cross-checked with the experimentally applied frequency. Beam current however, experiencing more noise than any of the other sampled parameters (and nonlinear response for some operating points) proved often difficult for the fitting function to converge on the correct amplitude and frequency. This was remedied with the application of a binomial filter [51] to the beam current waveform that increased the reliability of beam current fitting. Figure 5.2a-c shows an example of the beam current fitting function in relation to the measured beam current (non smoothed) along with a Fast Fourier Transform (FFT) (Fig. 5.2d) of the beam current, demonstrating how the fitting function converged onto a generally good solution for beam current in spite of the noise and in some cases (Ne^{3+}) high harmonic content. The fitting functions of each of the four measurements, beam current, x-ray power, forward microwave power, and reflected microwave power were plotted along with the raw data allowing for manual inspection of the fit on a case-by-case basis.

In spite of the increased fitting reliability by filtering beam current, errors still occurred and were identified by plotting the fitting function frequencies against the known modulation frequencies. In the cases where the beam current frequency did not match one-to-one the driving AM frequency the data point was discarded. X-ray power responded most strongly to modulation at low frequency and in most cases completely attenuating for frequencies in the 2 kHz range. The quality of fit for x-ray power was evaluated by comparing the predicted oscillation frequency with the known AM frequencies. No smoothing of x-ray power was required for reliable fitting. A comparison between fitting function frequencies and known

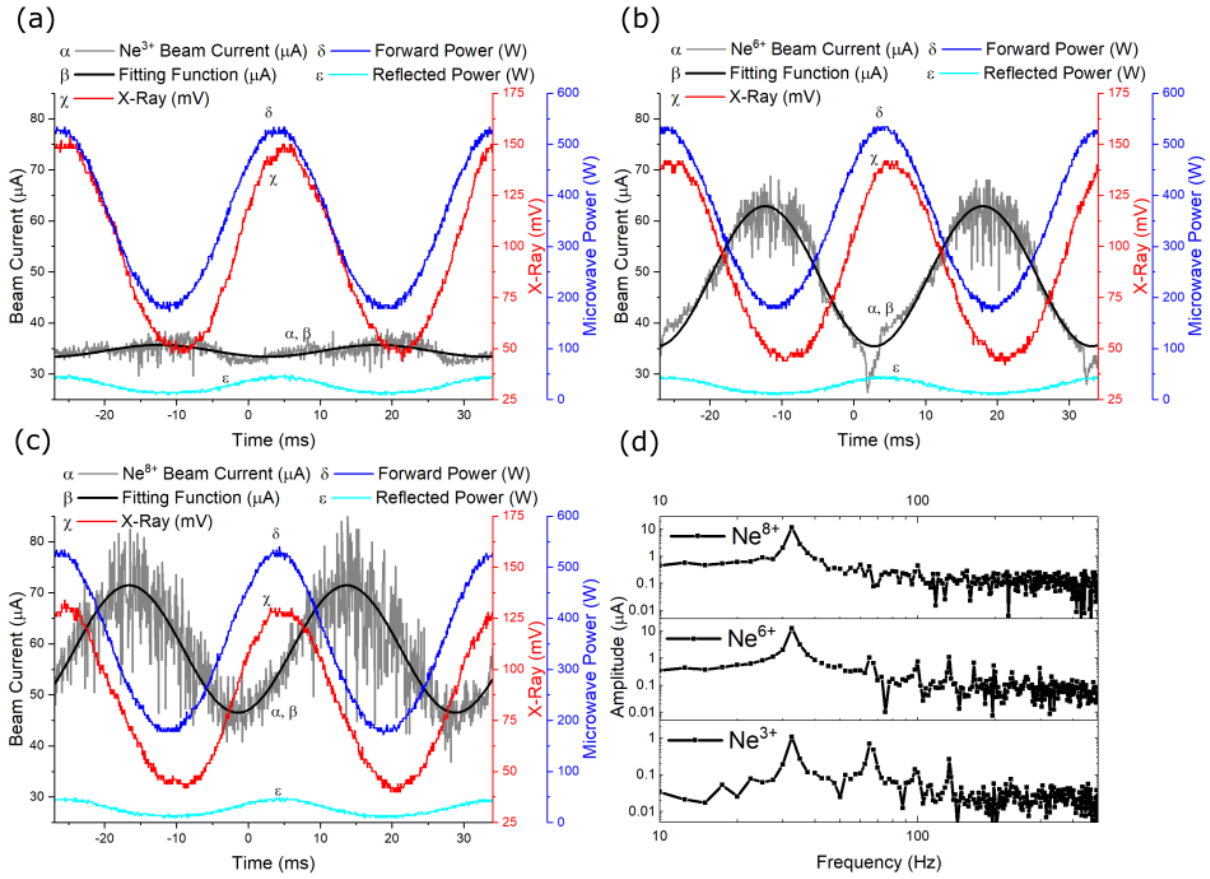

Figure 5.2: Beam current of three charge states Ne^{3+} (a), Ne^{6+} (b), and Ne^{8+} (c) plotted together with the fitting function, the microwave power, and the x-rays responding at 33 Hz for a magnetic field where B_{min}/B_{ecr}=0.77. A FFT of beam current (d) with 2.5 Hz resolution is shown for the total sampled time of 400 ms, and shows higher harmonic content for Ne^{3+} when compared to Ne^{6+} and Ne^{8+}. The CW beam current of Ne^{3+}, Ne^{6+}, and Ne^{8+} was 35.0±0.9 μA, 46.3±0.9 μA, and 56.5±4.2 μA respectively.

modulation frequencies was sufficient to determine where x-ray oscillations were no longer detectable. In general, comparing the fitting frequencies with the applied AM frequencies was the most reliable method of identifying erroneous fitting across all of the measurements. In a few cases, Fast Fourier Transform (FFT) analysis was performed on a case-by-case basis to better understand how nonlinear beam current waveforms were constructed.

Beam current and X-ray amplitude measurements helped determine to what extend the ECR plasma responded to the modulation of microwave power and was particularly useful

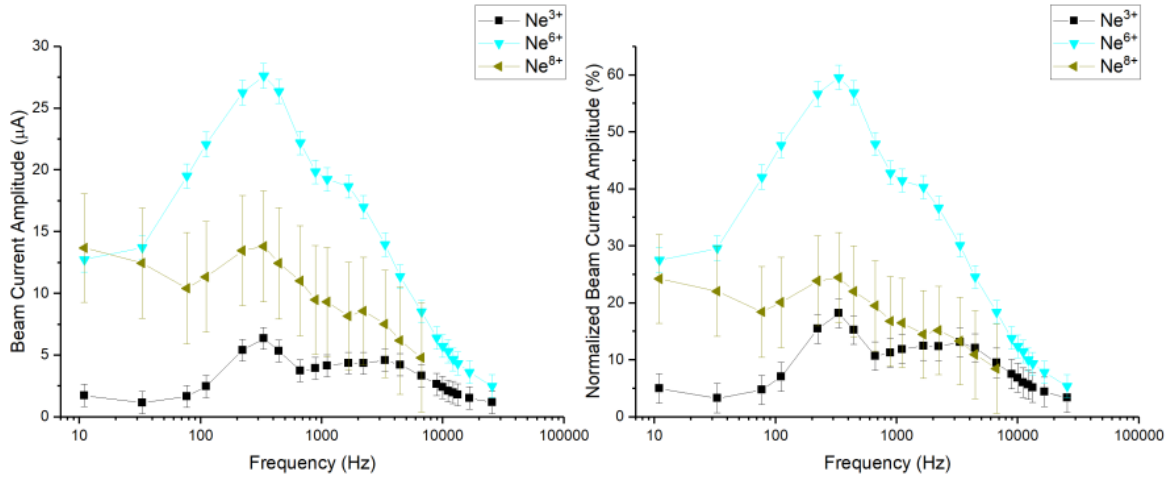

Figure 5.3: Beam current amplitude plotted alongside normalized beam current amplitude of Ne^{3+}, Ne^{6+}, and Ne^{8+} for sinusoidal microwave power modulation between 530 W and 180 W. The beam current was normalized to the CW current at 350 W, and was useful to compare all charge states for operating points such as with krypton where the current magnitudes differ by up to two orders of magnitude with charge state. The CW currents for Ne^{3+}, Ne^{6+}, and Ne^{8+} were 35.0 ± 0.9 μA, 46.3 ± 0.9 μA, and 56 ± 4 μA respectively.

to find the frequencies were it was no longer significant. Figure 5.3 shows typical amplitudes (one half the peak-to-peak amplitude) for three neon charge states for a magnetic field configuration of B_{min}/B_{ecr}=0.77. The beam current amplitude was typically reported as a percentage normalized to the CW current at 350 W which was useful for plasmas like krypton and argon with large disparity in steady state current between the highest charge states and the charge states with the highest currents. Figure 5.3 shows how normalized beam current relates to the beam current amplitudes for argon.

The amplitude error was estimated from the standard deviation of the average current during CW operation at 350 W. Frequencies where modulation was no longer significant were determined when the beam current amplitude equaled the standard deviation of the CW current at 350 W. In the case of Fig. 5.3 the frequencies where modulation was no longer significant were greater than 25 kHz for Ne^{3+} and Ne^{6+} but 6.7 kHz for Ne^{8+}.

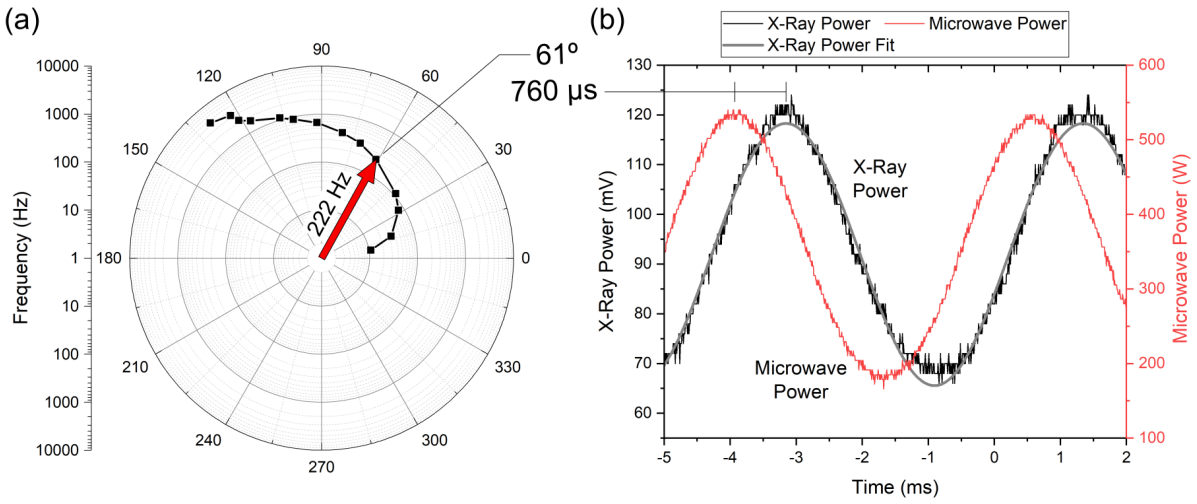

Figure 5.4: Phase between x-ray and microwave power for a neon plasma with B_{min}/B_{ecr}=0.77 (a). X-ray and microwave power waveforms for modulation at 222 Hz (b).

Phase of the beam current and x-ray power was calculated in relation to the microwave power. The relative phase between quantities (ex. x-ray power and microwave power) was calculated by subtracting the time delays from fitting and then normalizing to the frequency to obtain phase. The phase between x-ray power and microwave power is shown in Fig. 5.4a for a neon plasma with the 222 Hz data point marked with the red arrow. The waveforms corresponding to the 222 Hz data point are shown in Fig. 5.4b. The x-ray power lagged behind the microwave power by about 760 μs resulting in a phase angle of 61°. An absolute time delay can only be resolved to the period of the oscillating frequency. For a constant time delay, the phase difference increases with the frequency. On a polar plot such as that in Fig. 5.4a, a constant time delay spirals from the origin with increasing frequency. Figure 5.20 in Sect. 5.4.1 plots various constant time delays with respect to the x-ray power phase.

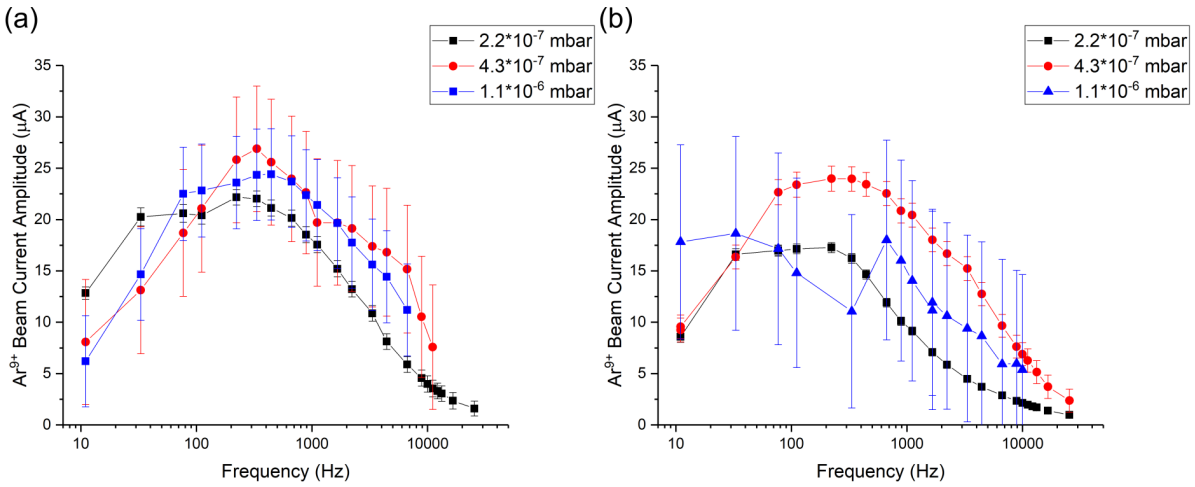

Figure 5.5: Beam current amplitude of Ar^{9+} for the magnetic field configuration B_{min}/B_{ecr}=0.67 (a) and B_{min}/B_{ecr}=0.77 (b).

5.2 Results of Initial Exploration

5.2.1 Beam Current and X-Ray Response to Vacuum Pressure

The effect of vacuum pressure on amplitude modulation was studied for argon plasmas. Three different magnetic field configurations were used B_{min}/B_{ecr}=0.67, B_{min}/B_{ecr}=0.72, and B_{min}/B_{ecr}=0.77. The Ar^{9+} beam current was studied because it had the largest current of any other charge state in the CSD. For this charge state, various pressures ranging as high as $1.1{\cdot}10^{-6}$ mbar and as low as $2.2{\cdot}10^{-7}$ mbar were used. For all other charge states, the amplitude modulation measurements were only carried out at $4.3{\cdot}10^{-7}$ mbar as reported in Sect. 5.4.2. Finally, three magnetic field configurations B_{min}/B_{ecr}=0.67, B_{min}/B_{ecr}=0.72, and B_{min}/B_{ecr}=0.77 were used for the study of the plasma response to changes in the vacuum pressure. Overall, the analysis of the data showed that vacuum pressure appeared to play a role in determining the beam current modulation behavior.

Two magnetic field configurations, B_{min}/B_{ecr}=0.67 and B_{min}/B_{ecr}=0.77, behaved in a similar way. The Ar^{9+} beam current reached a maximum amplitude for a middle frequency

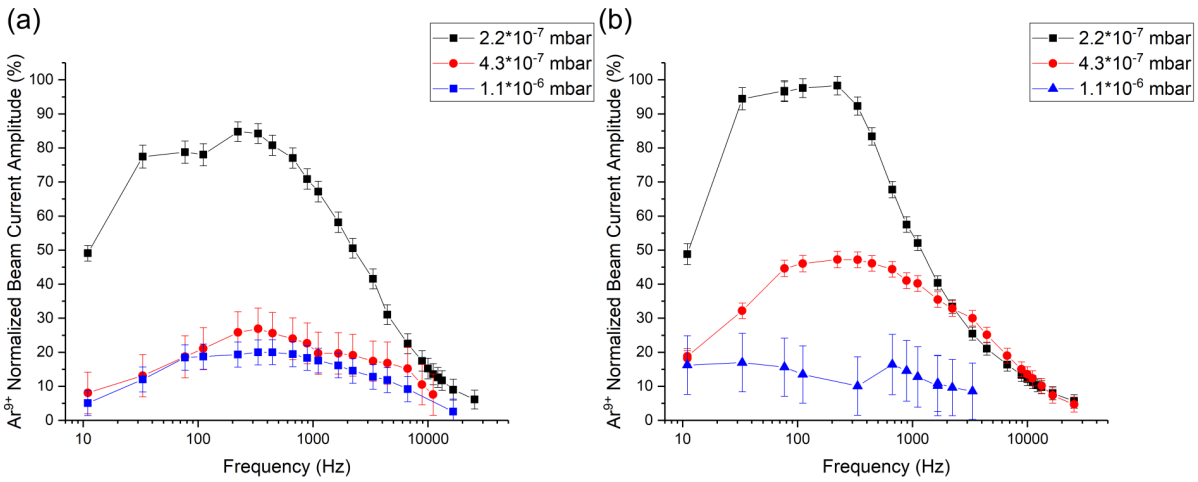

Figure 5.6: Beam current amplitude of Ar^{9+} normalized to the CW current at 350 W for the magnetic field configuration B_{min}/B_{ecr}=0.67 (a) and B_{min}/B_{ecr}=0.77 (b).

B_{min}/B_{ecr}	0.67	0.72	0.77
$2.2{\cdot}10^{-7}$ mbar	26.1 ± 0.7 μA	30 ± 2 μA	17.6 ± 0.4 μA
$4.3{\cdot}10^{-7}$ mbar	66 ± 6 μA	68 ± 5 μA	51 ± 1 μA
$1.1{\cdot}10^{-6}$ mbar	122 ± 5 μA	173 ± 10 μA	110 ± 9 μA

Table 5.2: The Ar^{9+} CW current at 350 W for three different vacuum pressures and magnetic field configurations.

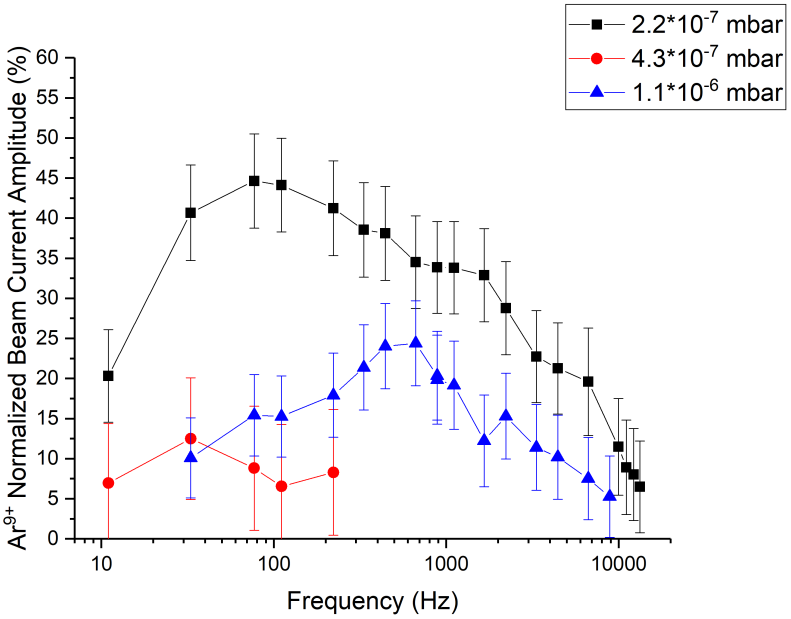

Figure 5.7: Beam current amplitude of Ar^{9+} normalized to the CW current at 350 W for the magnetic field configuration B_{min}/B_{ecr}=0.72. This magnetic field configuration was notable for its ability to suppress beam current modulation at $4.3 \cdot 10^{-7}$ mbar.

(in the range studied) while modulating weakly for high and low frequencies. This was a typical behavior for most operating points (see Sections 5.2.2 and 5.4.1 to 5.4.3). Increasing the vacuum pressure increased the Ar^{9+} beam current magnitude for any particular magnetic field configuration (see Table 5.2). However, beam current amplitude was approximately fixed as shown for B_{min}/B_{ecr}=0.67 in Fig. 5.5a with a similar behavior observed for B_{min}/B_{ecr}=0.77 Fig. 5.5b. As a result, the normalized amplitudes decreased with pressure (see Fig. 5.6a-b) becoming a smaller percentage of the CW current.

One of the most striking results was obtained for B_{min}/B_{ecr}=0.72. The Ar^{9+} beam current amplitude was highly sensitive to vacuum pressure as seen in Fig. 5.7. One such pressure, $4.3 \cdot 10^{-7}$ mbar, almost completely suppressed the of Ar^{9+} beam current response to amplitude modulation. Beam current modulation was no longer significant for frequencies higher than around 200 Hz at this pressure. The other two pressures $2.2 \cdot 10^{-7}$ mbar and

B_{min}/B_{ecr}	0.67	0.72	0.77
$2.2{\cdot}10^{-7}$ mbar	15.5 ± 0.8 mV	24.5 ± 0.8 mV	73 ± 1.4 mV
$4.3{\cdot}10^{-7}$ mbar	12.1 ± 0.8 mV	31 ± 1 mV	80 ± 1.3 mV
$1.1{\cdot}10^{-6}$ mbar	11.9 ± 0.8 mV	31.1 ± 0.9 mV	66 ± 1.2 mV

Table 5.3: The x-ray power at 350 W for three different vacuum pressures and magnetic field configurations.

$1.1{\cdot}10^{-6}$ mbar exhibited beam current modulation out to around 10 kHz just under two orders of magnitude higher frequency than for $4.3{\cdot}10^{-7}$ mbar. Furthermore, vacuum pressure appeared to shift the frequency where the largest beam current amplitudes were observed. The peak amplitude for $2.2{\cdot}10^{-7}$ mbar was 90 Hz while for $1.1{\cdot}10^{-6}$ mbar was 600 Hz. The pressure of $4.3{\cdot}10^{-7}$ mbar did not generate a frequency in the range studied where the Ar^{9+} beam current modulated with a distinct maximum amplitude (outside the range of the error bars). This particular magnetic field configuration (B_{min}/B_{ecr}=0.72) produced the largest CW beam currents of Ar^{9+} for each vacuum pressure as seen in Table 5.2.

The x-ray power magnitude was primarily determined by the magnetic field configuration. Table 5.3 reports the CW x-ray powers for each pressure and magnetic field operating point with the highest power for the highest B_{min} with B_{min}/B_{ecr}=0.77. X-ray power amplitude, when modulated at different frequencies, was the largest for the lowest AM frequencies. Additionally, B_{min}/B_{ecr}=0.77 was the most impacted by changes in vacuum pressure as seen in Fig. 5.8. The largest amplitudes were observed for $4.3{\cdot}10^{-7}$ mbar even when normalized to the CW x-ray emission. The higher vacuum pressure, $1.1{\cdot}10^{-6}$ mbar, had the lowest x-ray power magnitudes and amplitudes at this magnetic field configuration. The x-ray power amplitude across the three vacuum pressures equalized at around 200 Hz decaying rapidly with increasing frequency. The x-ray power no longer exhibited modulation for frequencies higher than 3.3 kHz for any operating point, and it is interesting to not that the

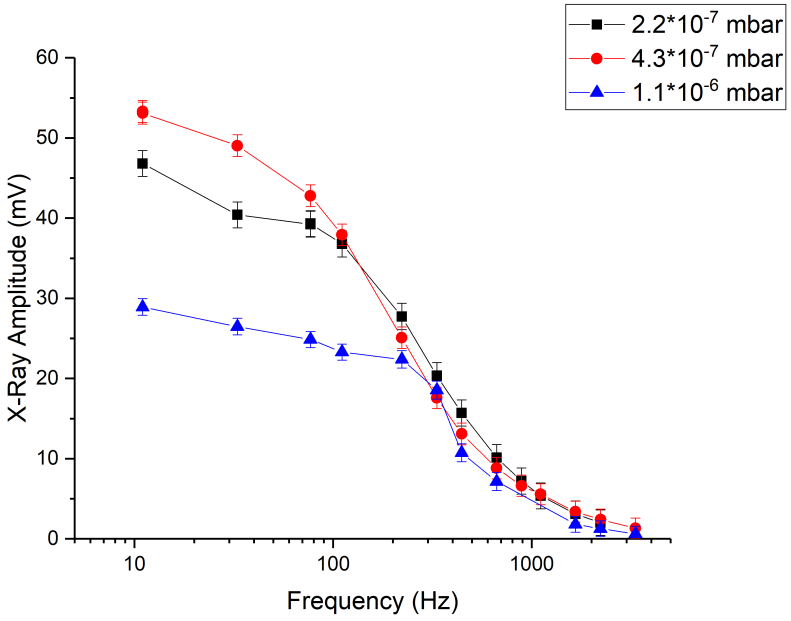

Figure 5.8: X-ray amplitude for B_{min}/B_{ecr}=0.77 as a function of modulation frequency for three different vacuum pressures. The CW x-ray emission for $2.2{\cdot}10^{-7}$ mbar, $4.3{\cdot}10^{-7}$ mbar, and $1.1{\cdot}10^{-6}$ mbar was 74 ± 1.4 mV, 80 ± 1.3 mV, and 66 ± 1.2 mV respectively.

x-ray power oscillations for the other two magnetic field configurations B_{min}/B_{ecr}=0.67 and B_{min}/B_{ecr}=0.72 was not observed to change with vacuum pressure.

5.2.2 Beam Current and X-Ray Response to Magnetic Field

The magnetic field played a significant role in how the beam current responded to amplitude modulation and was studied for an argon plasma with a vacuum pressure of $4.3{\cdot}10^{-7}$ mbar. The magnetic field was swept in three different ways:

1. The injection solenoid current was changed maintaining the extraction current fixed,

2. The extraction coil current was changed maintaining the injection coil current fixed,

3. Both the injection and extraction coil currents were changed with equal values.

The magnetic field configurations reported in Table 5.1 and referred to in the text by

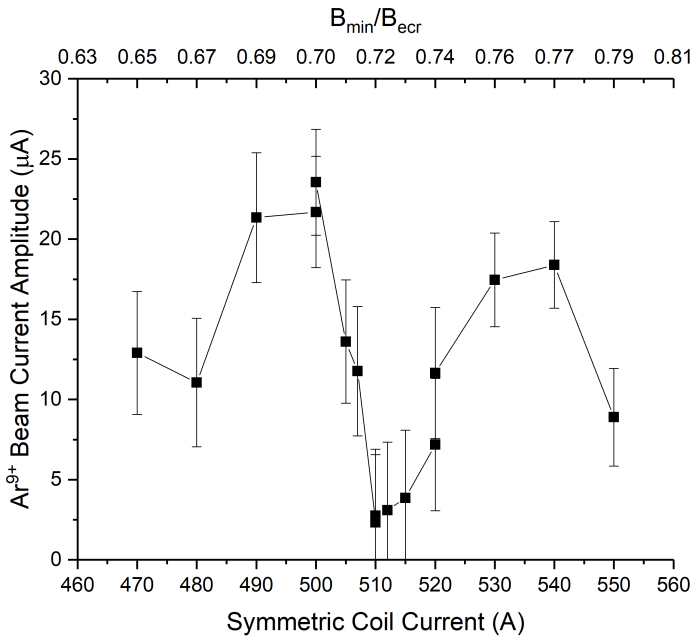

Figure 5.9: Amplitude of Ar^{9+} at a modulation frequency of 2.22 kHz for different magnetic minima obtained by increasing the injection and extraction solenoid currents symmetrically.

B_{min}/B_{ecr}ratio, were obtained for symmetric currents in the injection and extraction solenoids. For fields with $B_{min}/B_{ecr} \gtrapprox 0.77$, instabilities were observed in the x-ray and beam current similar to that reported in Ref. [91].

The microwave power was modulated at a constant 2.22 kHz with a peak power of 530 W and minimum of 180 W (as was the case in every section of this chapter). Ar^{9+} was selected because it produced the most current in the CSD at any of the three magnetic field configurations. The amplitude error for the intermediate magnetic fields was estimated here (within this subsection) from the average error from CW beam current measurements (6%) taken at the three magnetic field configurations.

The beam current amplitude was sensitive to the magnetic field. In particular, one magnetic field configuration (B_{min}/B_{ecr}=0.72), almost completely suppressed the beam current amplitude. Figure 5.9 shows the sharp decrease in the observed beam current modulation at

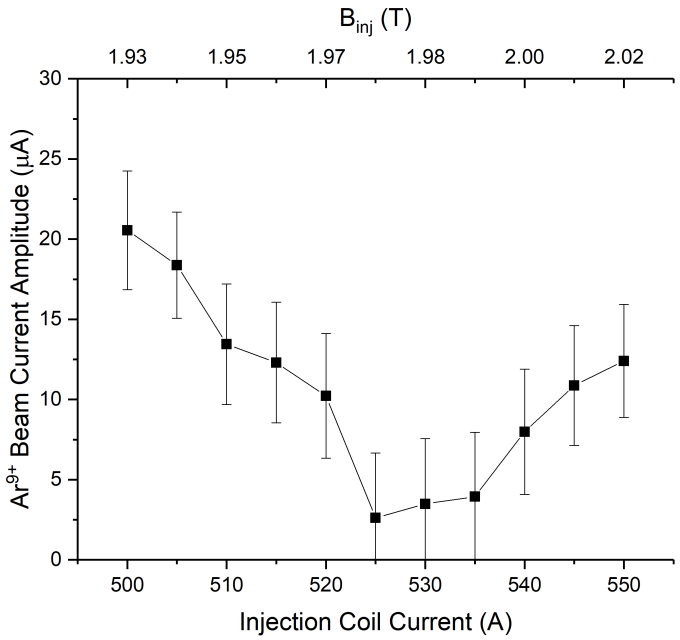

Figure 5.10: Amplitude of Ar^{9+} at a modulation frequency of 2.22 kHz for different injection magnetic field magnitudes with the extraction approximately fixed at 0.912 T deviating by about ± 3 mT at the extremes.

this magnetic field configuration. The modulation frequency 2.22 kHz was selected because the amplitude of the measured Ar^{9+} beam current would decrease dramatically at a specific magnetic field configuration unlike what was observed at lower modulation frequencies in the 100 Hz to 400 Hz range where the modulation in the beam current amplitude was attenuated. However, in the subsequent data analysis a lower frequency such as 200 Hz may have yielded better resolution as the beam current amplitude reached its maximum values here for most magnetic field configurations as shown in Sect. 5.4.2. In post processing, the ≈ 5 A steps in solenoid current appeared to be fairly coarse to resolve well the different amplitudes expressed in the beam current.

The injection solenoid was slightly more effective at suppressing the beam current modulation as seen in Fig. 5.10 than the extraction solenoid shown in Fig. 5.11 however, the extraction solenoid still produced a notable decrease in beam current amplitude. The 5 A

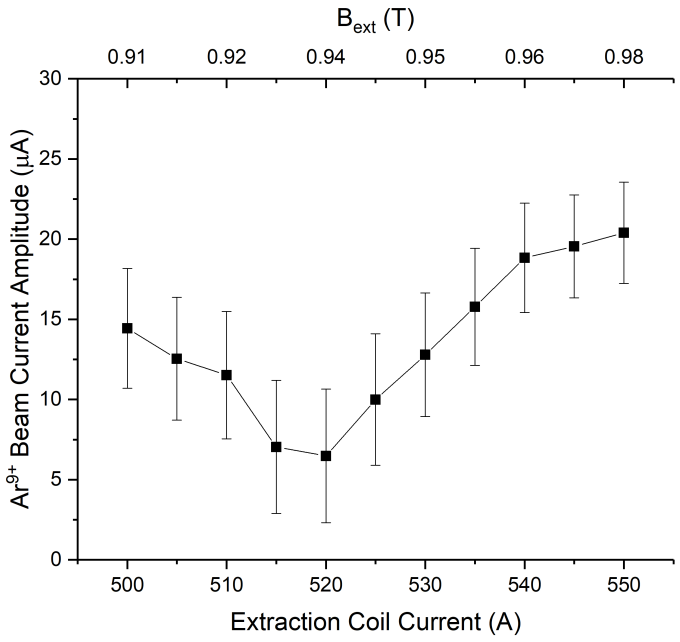

Figure 5.11: Amplitude of Ar^{9+} at a modulation frequency of 2.22 kHz for different extraction magnetic field magnitudes with the injection approximately fixed at 1.936 T deviating by about ±3 mT at the extremes.

steps selected for the sweep in injection and extraction magnetic field resolved well the structure in beam current amplitude unlike for the case where both coils were set to the same current shown in Fig. 5.9.

The magnetic field that suppressed the 2.22 kHz modulation in the beam current, also produced the highest average currents over all the fields studied. Figure 5.12 shows the data included from Figs. 5.9 to 5.11 but expressed as a function of the length of the ECR resonance volume. The peak in CW current corresponded to a minima in beam current amplitude and occurred for an ECR length of around 106 mm. For the purely symmetric sweep in magnetic field in Fig. 5.9 care was taken to minimize the beam current amplitude, the resulting magnetic field configuration: B_{min}/B_{ecr}=0.72, generated an ECR length of 106.6 mm and was 5.00 times the vacuum wavelength of the for the 14.056 GHz microwave power frequency.

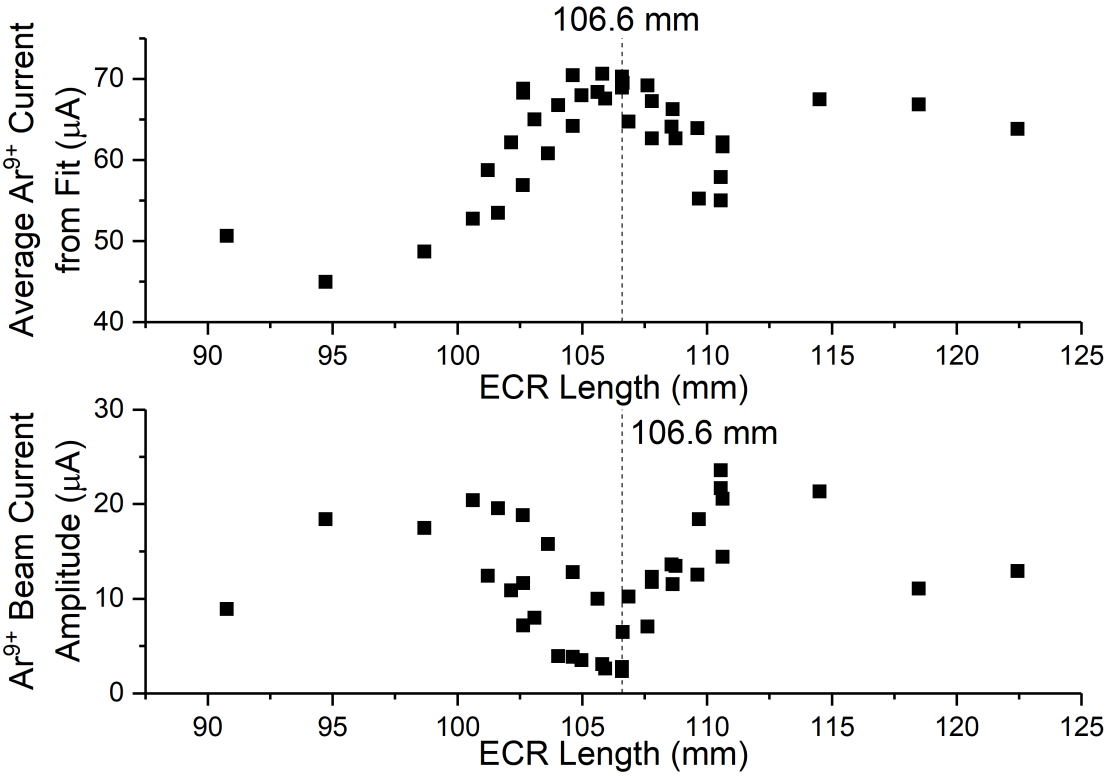

Figure 5.12: The total average current and amplitude of Ar^{9+} at a modulation frequency of 2.22 kHz for different ECR lengths and magnetic minima combined from Figs. 5.9 to 5.11.

5.3 Average X-Ray Power and Beam Current with Amplitude Modulation

Amplitude modulation was unable to increase the average beam current intensity extracted from the ion source for any frequency or plasma operating point studied. Charge states of krypton are shown as an example in Figs. 5.13a-d for B_{min}/B_{ecr}=0.77. At best, AM produced beam currents with the same intensity as CW operation. Kr^{15+} in Fig. 5.13b is a good example particularly for frequencies above 400 Hz. However, in most cases, AM produced average beam current intensities lower than for CW operation with the same average power (350 W). Figures. 5.13a-d all show frequencies where AM under performed CW operation. The error bars generated from simple processing of the beam current data file for the average current illustrate the oscillatory behavior of the beam current during AM.

Although beam current was not increased by AM with respect to the average microwave power, the x-ray power was. Figure 5.14 compares the average x-ray power during AM with CW operation at 350 W (the average power during AM). Amplitude modulation at any of the frequencies studied generated a higher average x-ray power than for CW operation at 350 W. In this case, the fitting function was unable to converge on an oscillatory solution (with the correct frequency) for frequencies higher than 3.3 kHz and is the reason the average x-ray power from fit in Fig. 5.14 stops here. In a similar manner to the beam current error in Figs. 5.13a-d, the average x-ray power error in Fig. 5.14 illustrates the oscillation envelope of the x-ray power and is similar to the trends in Fig. 5.8. The average power from fit accounts for the sinusoidal modulation behavior in x-ray power and is much more suitable as the average x-ray power magnitude. For frequencies higher than 3.3 kHz the fitting function was unable to converge on a correct solution and the fitting function result is truncated. In

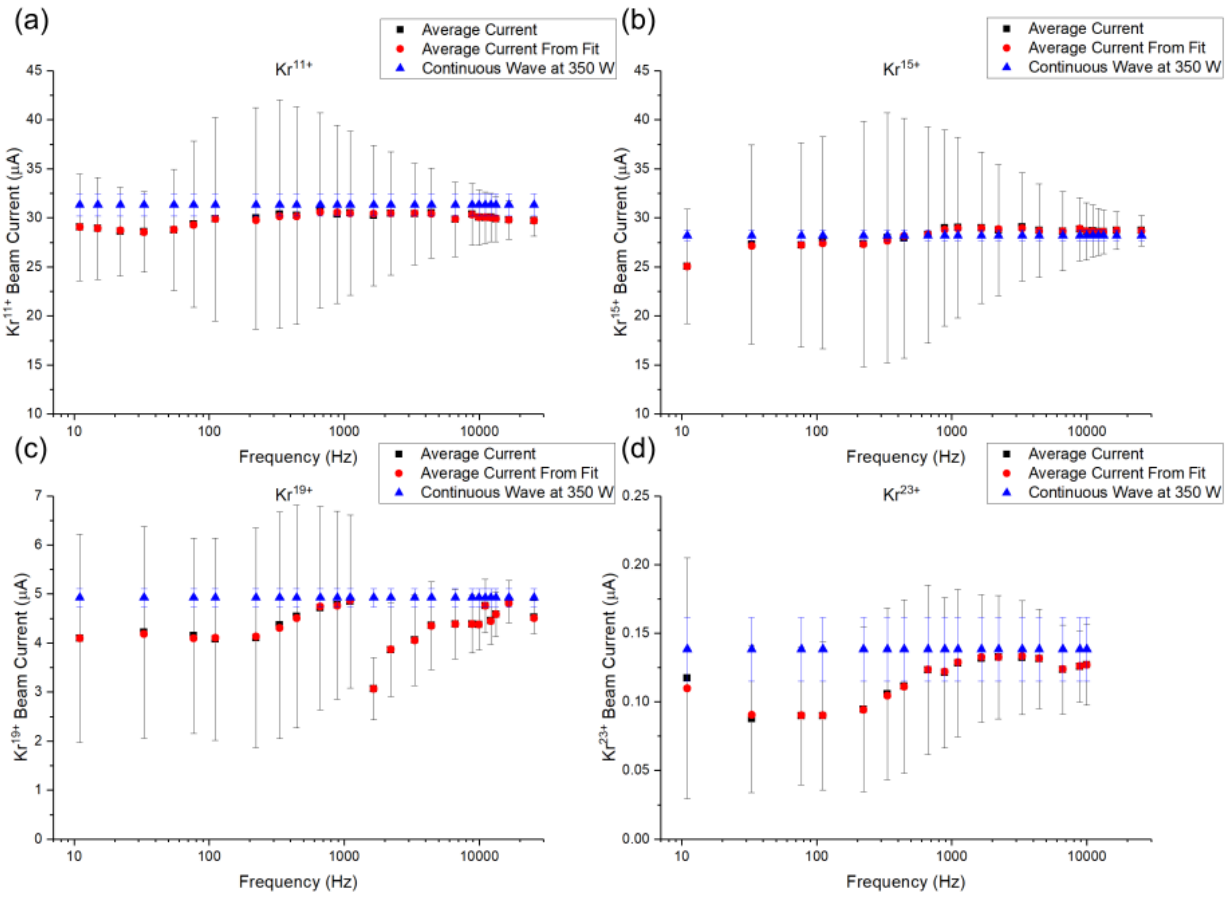

Figure 5.13: Average current from simple processing of the data file, average current from fitting, and CW beam current at 350 W microwave power for: Kr^{11+} (a), Kr^{15+} (b), Kr^{19+} (c), and Kr^{23+} (d). Note the smaller scales of the vertical axis for (c) and (d) compared to (a) and (b) as the current magnitudes decreased.

this region, the error bars in the average x-ray power become representative of actual error instead of oscillation amplitude.

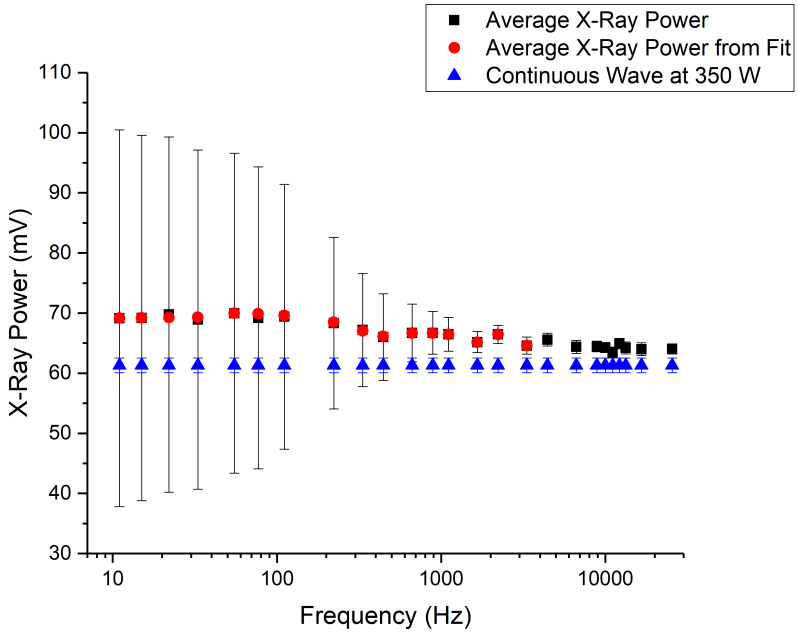

Figure 5.14: Average x-ray power from simple processing of the data file, average x-ray power from fitting, and CW x-ray power at 350 W.

5.4 Sinusoidal Amplitude Modulation

5.4.1 Krypton

Krypton was the heaviest noble gas studied and provided a good example of the amplitude modulation response for B_{min}/B_{ecr}=0.77. Every other charge state in the Continuous Wave (CW) charge state distribution (see Fig. 5.15) was sampled starting from Kr^{23+} terminating at Kr^{11+}. Kr^{12+} was avoided due to likely contamination with nitrogen.

The beam current modulated strongly with the microwave power as apparent in Fig. 5.16 showing a clear peak in amplitude at 333 Hz. As frequency increased amplitude exponentially decreased. Kr^{13+}-Kr^{21+} modulated with amplitudes on the order of beam noise up to 25 kHz which was the highest frequency sampled. Kr^{23+} was the highest charge state that could be measured in the CSD but as a result the fluctuations in the CW beam current was 17%,

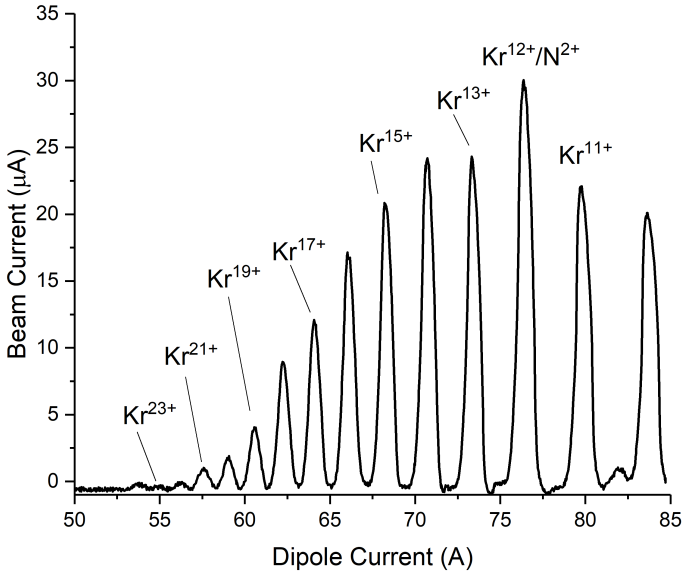

Figure 5.15: Charge state distribution of krypton for CW operation at 350 W.

which was high considering that for other charge states such as Kr^{11+} the fluctuations in the CW beam current were 4%.

High charge states Kr^{23+} and Kr^{21+} responded strongly to low frequency modulation, Fig. 5.16 shows the largest amplitudes of these charge states were measured at 11 Hz. Kr^{19+} and the other lower charge states oscillated with maximum amplitude at around 300-400 Hz. The beam current of the lowest charge state measured (Kr^{11+}) and for the lowest frequency (11 Hz) exhibited a "double peak" in Fig. 5.17. As charge states progressively increased the first peak gradually decreased in amplitude and was still observable in Kr^{17+} but undetectable in Kr^{19+}. The "double peak" structure was characteristic of low charge states during sinusoidal AM. Kr^{23+} by comparison in Fig. 5.17, only shows one peak in current as the microwave power decreases which is more or less in phase with the first peak of Kr^{11+}.

Fourier analysis was performed for the Kr^{11+} beam current waveform in Fig. 5.18. The highest harmonic observable was the 3^{rd} at 44 Hz decreasing in amplitude approximately

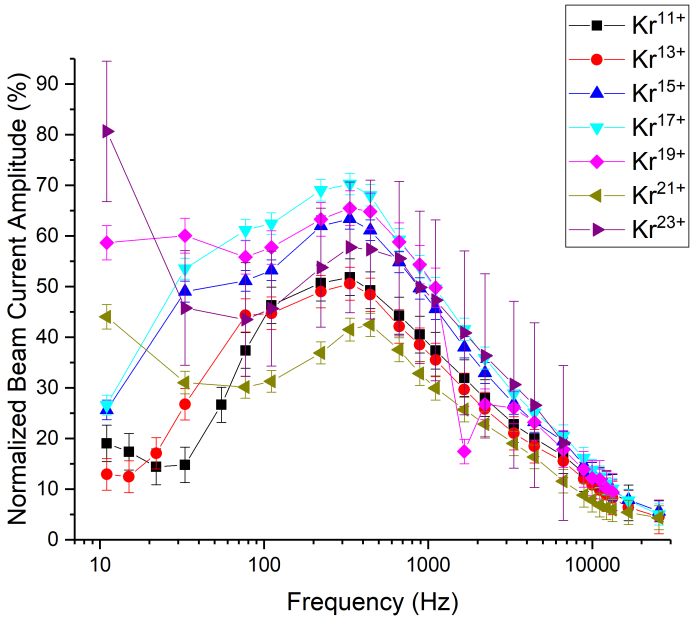

Figure 5.16: Beam current amplitude normalized to the CW current at 350 W for various krypton charge states as a function of modulation frequency.

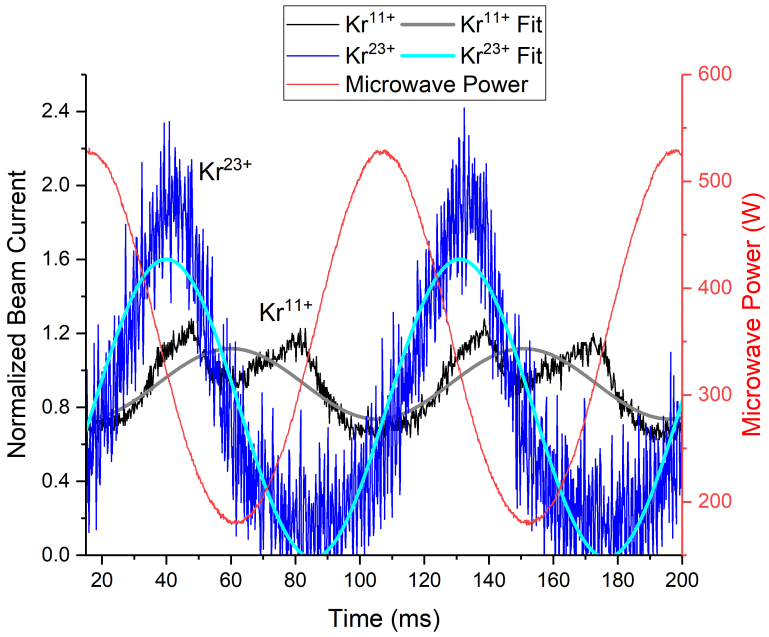

Figure 5.17: Kr^{23+} and Kr^{11+} beam currents normalized to CW at 350 W plotted with respect to the microwave power for modulation at 11 Hz.

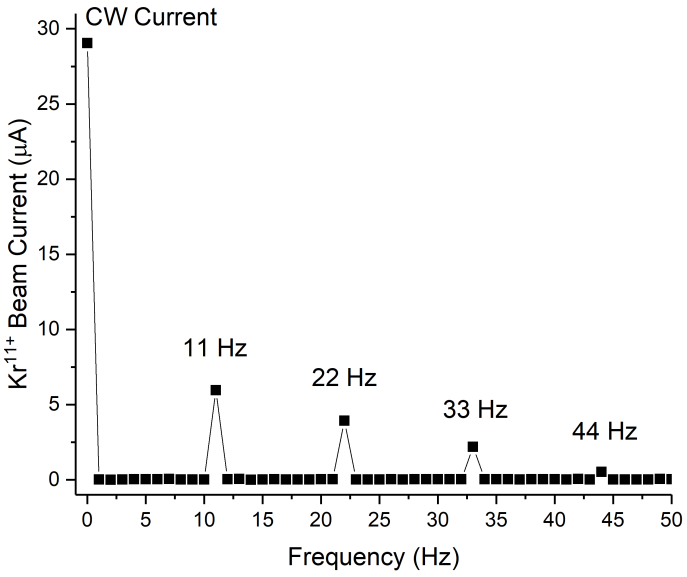

Figure 5.18: Fast Fourier transform of Kr^{11+} beam current waveform in Fig. 5.17 with 1 Hz resolution. The Kr^{11+} current exhibits a double peak lowering the amplitude. The waveform is constructed from harmonics of the fundamental 11 Hz modulation frequency.

linearly from the fundamental frequency (11 Hz). Both even and odd harmonics generated the Kr^{11+} beam current waveform. Fourier analysis was performed for Kr^{11+} at the 11 Hz modulation frequency because of its well defined double peak structure.

The beam current phase to the microwave power followed a uniform spiral structure for frequencies higher than about 100 Hz where the phase equalized across charge states. Figure 5.19a shows nicely the spiral phase structure. A phase disparity appeared between charge states for the lower frequencies and in particular for the 11 Hz measurement where Kr^{11+} appears delayed from the higher charge states. Figure 5.17 shows that two distinct peaks in beam current existed for Kr^{11+} and the fitting function split the difference and converged on a phase in between the two. This issue appeared at only low frequencies $\lessapprox$ 100 Hz and for the low charge states where the beam current waveforms had harmonic content in the beam current waveform (see Fig. 5.18). Figure 5.19b calculates the phase of

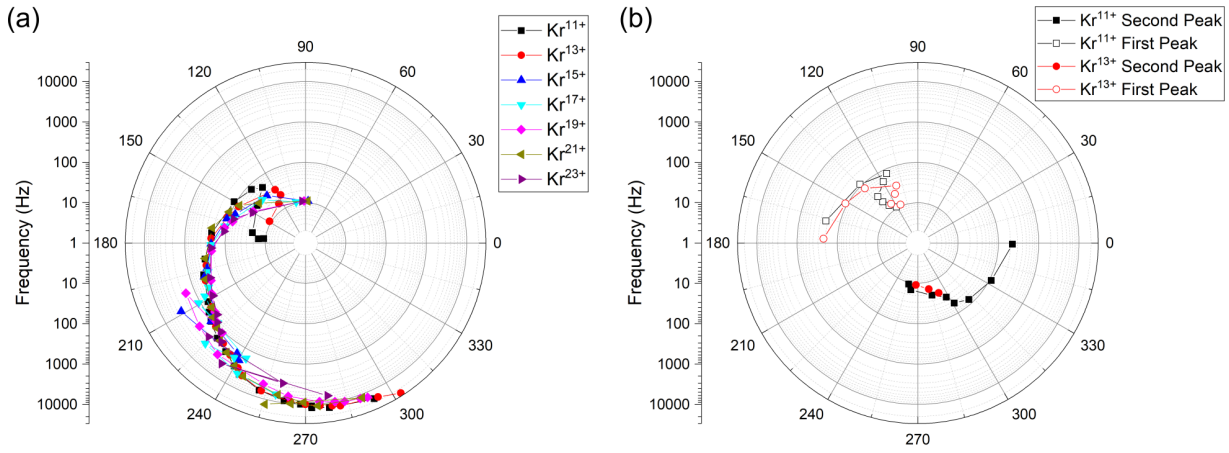

Figure 5.19: Phase between the beam current and microwave power with frequency on the radius (a) calculated from the fitting functions. Phase between beam current and microwave power with frequency on the radius calculated from the first and second peak (see the Kr^{11+} waveform in Fig. 5.17) for Kr^{11+} and Kr^{13+} by visual inspection (b).

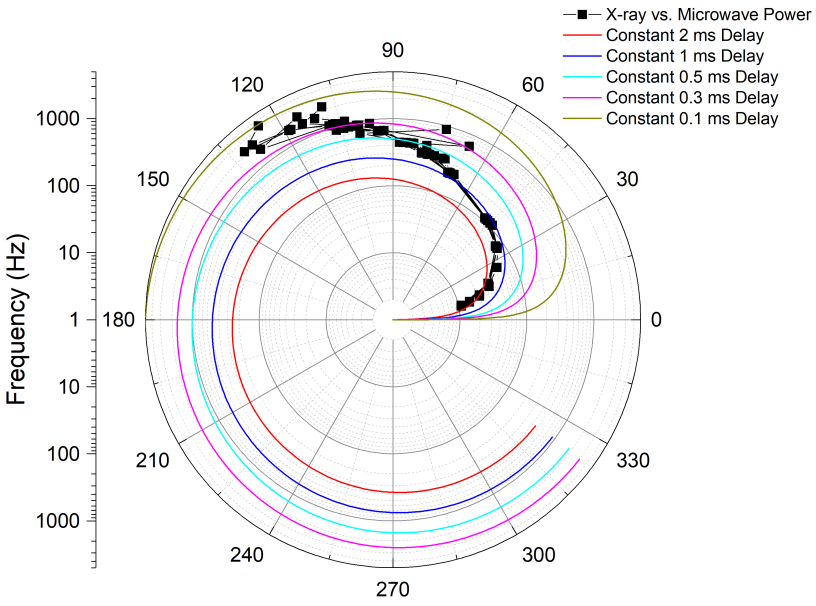

Figure 5.20: Phase between the x-ray power and microwave power with frequency on the radius. Various constant time delays are plotted alongside the x-ray phase to provide a reference to the significance of the spiral shape.

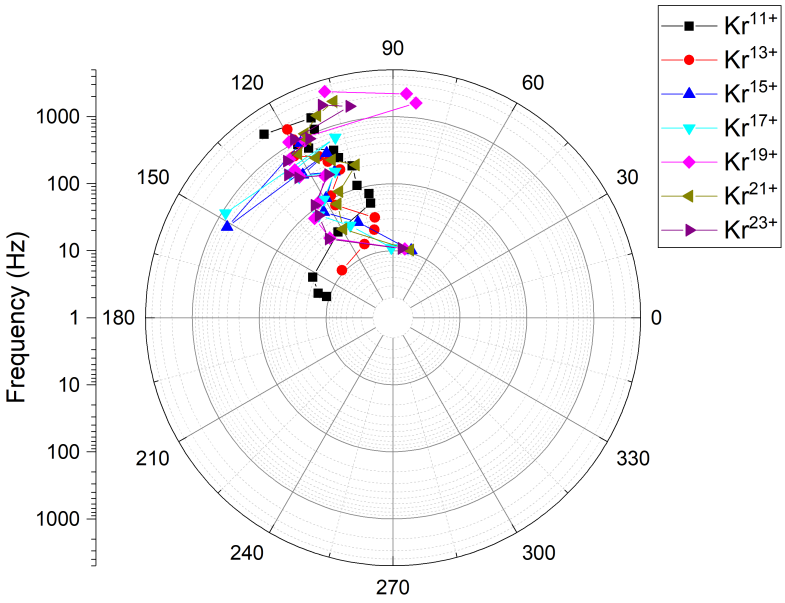

Figure 5.21: Phase between beam current and x-ray power with frequency on the radius. Measurements from all charge states are plotted.

the first and second peaks in the Kr^{11+} and Kr^{13+} waveforms with respect to the microwave power. The second peak, when observable, was nearly $3\pi/2$ out of phase at 11 Hz and spiraled with increasing phase with a similar relationship to that found from the fitting functions in Fig. 5.19a.

The spiral shape of the beam current phase was imparted from the electrons as evident in Fig. 5.20 showing the phase between the x-ray power and microwave power. The spiral shape in Fig. 5.20 and Fig. 5.19a is similar to how a constant time delay manifests on a phase plot with frequency. Several different constant time delays are plotted alongside the x-ray phase in Fig. 5.20 for comparison. The x-ray power lagged behind the microwave power with different time delays depending on frequency. For example, modulation at low frequency (11 Hz) the x-ray power lagged about 3 ms behind the microwave power whereas for the highest frequency (3.33 kHz) the time delay was 150 μs. The effective time delay of the

x-ray power decreased with increasing frequency and could have been caused by a mapping of electron energy onto frequency. The electrons with higher energy, longer production times, and confinement times did not contribute to the oscillatory part of the x-ray power if the period of oscillation was higher than the characteristic production and confinement time. Further investigations, with the ability to resolve x-ray energy, would be required to determine if AM could be used to map electron production and confinement times.

The beam current, within the range of frequencies studied (11 Hz to $\approx$ 25 kHz), appeared to follow the x-ray power. When the spiral shape of the x-ray power phase (Fig. 5.20) was subtracted from the beam current phase Fig. 5.19a phase, Fig. 5.21 results. The beam current, independent of charge state, appeared at an approximately constant phase ($\approx 120^{\circ}$) to the x-ray power. A discussion of the likely reason for this behavior may be found in Sect. 5.6.

5.4.2 Argon

Argon was used to study the impact of vacuum pressure on the beam current amplitude modulation response in Sect. 5.2.1 and with magnetic field configuration in Sect. 5.2.2. These sections only studied the response of Ar^{9+} to AM. In this section, three charge states of argon were studied Ar^{5+}, Ar^{9+}, and Ar^{13+} at each of three different magnetic field configurations B_{min}/B_{ecr}=0.67, B_{min}/B_{ecr}=0.72, and B_{min}/B_{ecr}=0.77. The CSD of argon did not change significantly with magnetic field. The spectrum was contaminated with nitrogen from a leak in the gas feed line as seen in Fig. 5.22 (for CW operation at 350 W). The nitrogen leak did not significantly impact the resulting beam current or x-ray response to amplitude modulation, but most likely impacted the high charge state performance of the source overall.

The beam current amplitude responded in a similar way to different modulation frequen-

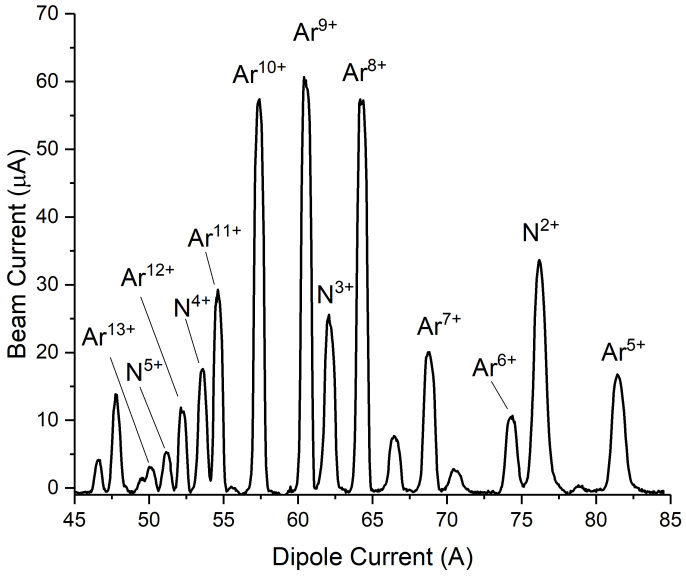

Figure 5.22: Charge state distribution of argon for B_{min}/B_{ecr}=0.67 and 350 W microwave power.

cies for B_{min}/B_{ecr}=0.67 and B_{min}/B_{ecr}=0.77 shown in Fig. 5.23 and Fig. 5.24 respectively. The Ar^{13+} beam current amplitude was the largest for the lowest frequency measured (11 Hz) reaching a local maxima around 200-400 Hz. In a similar way, Ar^{9+} reached its maximum amplitude for a modulation frequency around 200-400 Hz. Both Ar^{9+} and Ar^{13+} beam current amplitudes decayed exponentially with increasing frequency after the peak. Ar^{5+} did not respond strongly to modulation at any frequency or magnetic field configuration.

One magnetic field configuration, B_{min}/B_{ecr}=0.72, highly suppressed the beam current response to amplitude modulation as seen in Fig. 5.25 with Sect. 5.2.2 covering this topic in more detail. All charge states measured had reduced amplitudes and ceased modulating significantly at reduced frequencies. Ar^{9+} and Ar^{5+} no longer showed significant modulation at 222 Hz while Ar^{13+} was even less responsive with no significant modulation observed higher than 77 Hz. The largest Ar^{13+} normalized amplitude was measured was at this

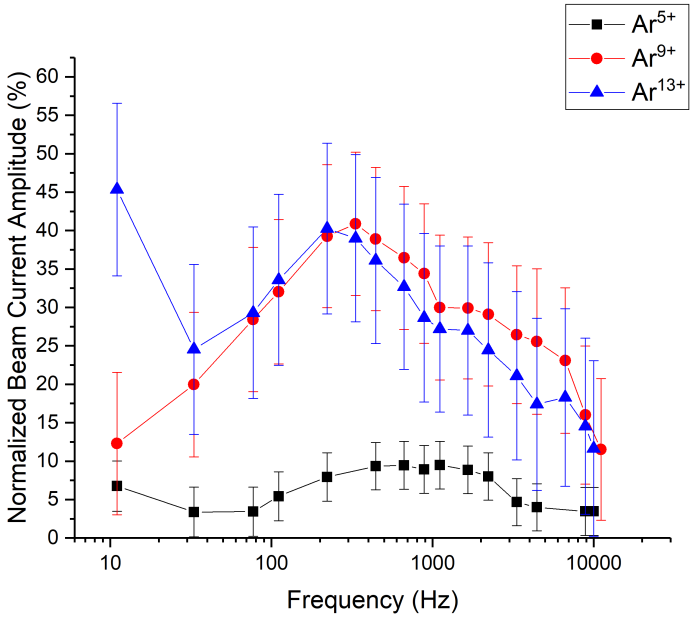

Figure 5.23: Beam current amplitude of three argon charge states as a function of modulation frequency for a magnetic field configuration of B_{min}/B_{ecr}=0.67.

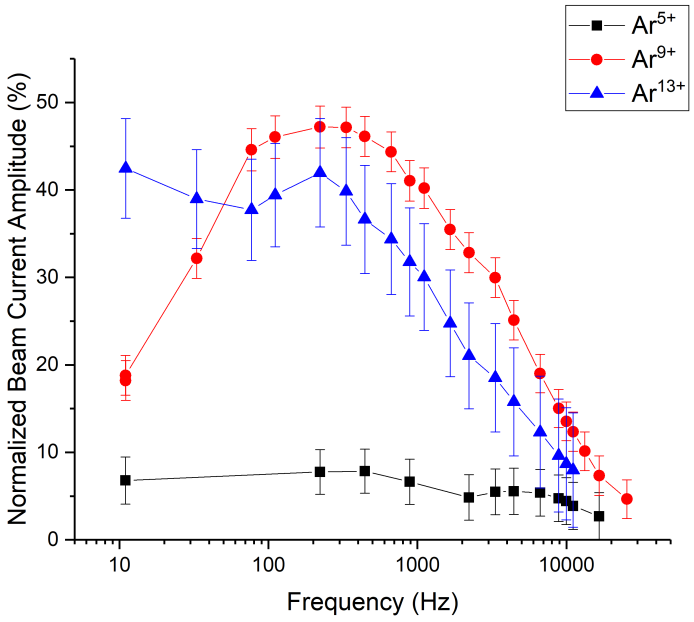

Figure 5.24: Beam current amplitude of three argon charge states as a function of modulation frequency for a magnetic field configuration of B_{min}/B_{ecr}=0.77.

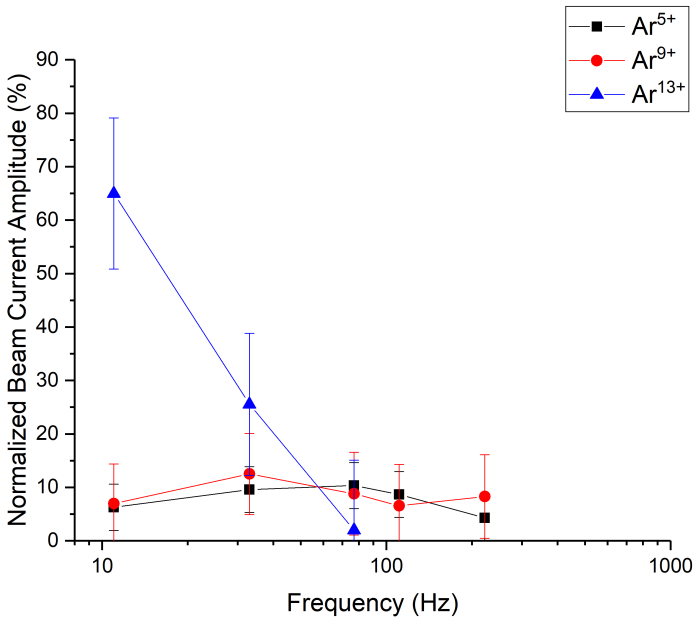

Figure 5.25: Beam current amplitude of three argon charge states as a function of modulation frequency for a magnetic field configuration of B_{min}/B_{ecr}=0.72.

magnetic field, 65% the CW current, however the largest magnitudes of Ar^{13+} amplitude and CW current were found for B_{min}/B_{ecr}=0.77 with 2.7 ± 0.3 μA and 6.3 ± 0.4 μA respectively where the normalized amplitude was 43% the CW current.

Beam current phase showed variation with magnetic field configuration and charge state but only for frequencies less than around 100 Hz. Unfortunately, the point density for these low frequencies was very low consisting of 3 measurements 11 Hz, 33 Hz, and 77 Hz. The low point density in this range was less of an issue for B_{min}/B_{ecr}=0.77 shown in Fig. 5.26c where the phase shifting with frequency is relatively smooth. However, Fig. 5.26a for B_{min}/B_{ecr}=0.67 shows that the Ar^{5+} phase was significantly under sampled for frequencies below 100 Hz. The phase for either magnetic field configuration or charge state followed a similar relationship for frequencies higher than around 100 Hz. The Ar^{5+} had the most varied response with magnetic field configuration of the three charge states studied. It is

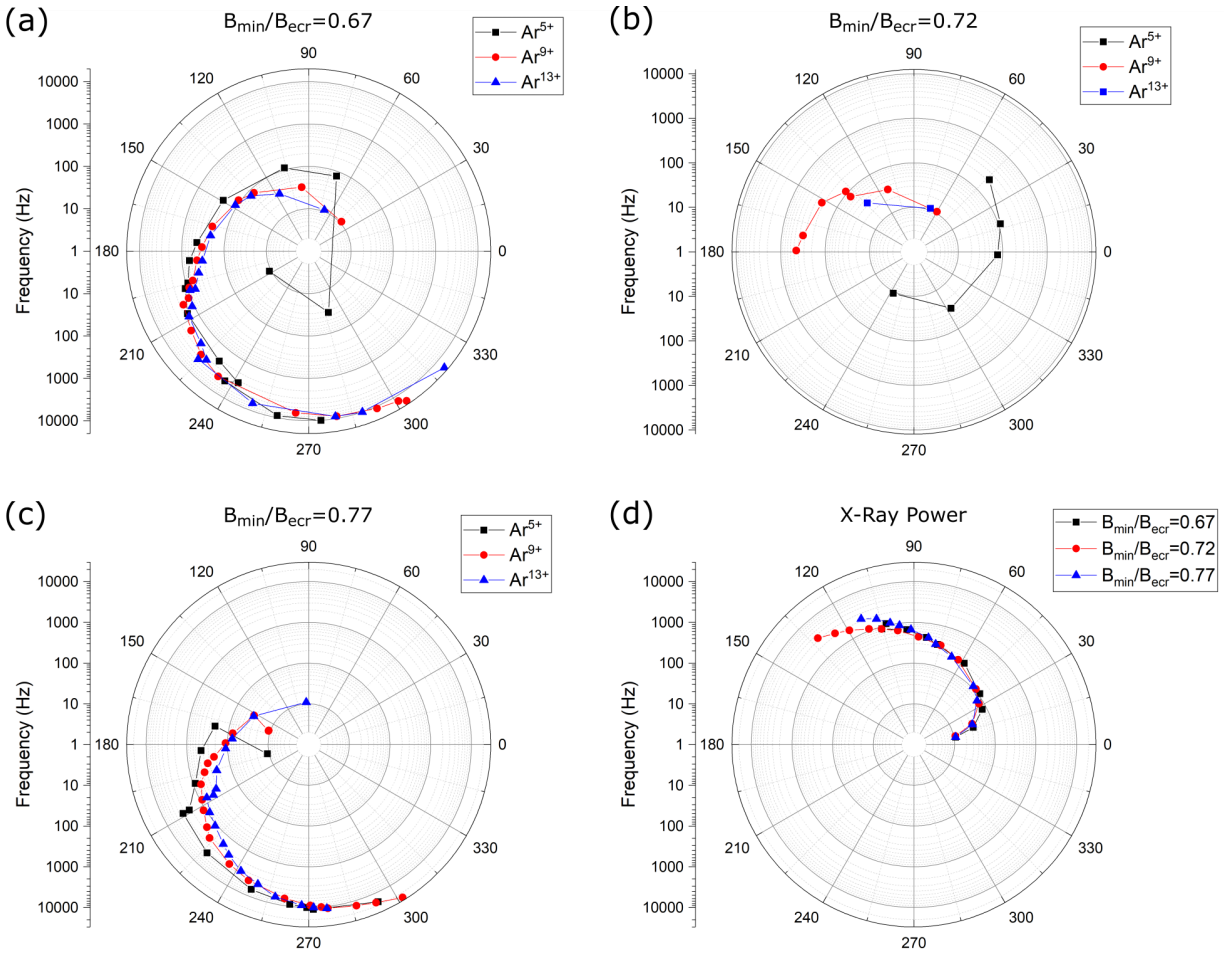

Figure 5.26: Beam current phase of argon plasmas to microwave power for B_{min}/B_{ecr}=0.67 (a), B_{min}/B_{ecr}=0.72 (b), and B_{min}/B_{ecr}=0.77 (c). The x-ray amplitude normalized to the CW x-ray emission as a function of magnetic field configuration (d). The spiral shape in the beam current phase is the same structure as found in the x-ray emission.

unclear why for B_{min}/B_{ecr}=0.72 Ar^{5+} in Fig. 5.26b phase is continuous with frequency but significantly under sampled in Fig. 5.26a. A clear double peak was observed in the Ar^{5+} waveform for low frequency operation ($\lessapprox 100\ Hz$) for B_{min}/B_{ecr}=0.77 similar to that found in Kr^{11+} at the same field (see Fig. 5.17). The magnetic fields B_{min}/B_{ecr}=0.67 and B_{min}/B_{ecr}=0.72 did not have double peaks in the Ar^{5+} waveform.

phase did not change significantly with magnetic field configuration for the frequency selected for study of how magnetic field impacted beam current modulation: 2.22 kHz. This

turned out to be an unfortunate choice because Figs. 5.26a-c demonstrate that the beam current phase was fixed in the kHz range with magnetic field configuration.

5.4.3 Neon

Neon, the lightest noble gas presented in this chapter was studied for three different magnetic field configurations B_{min}/B_{ecr}=0.67, B_{min}/B_{ecr}=0.72, and B_{min}/B_{ecr}=0.77. Unique to neon, every charge state available in the CSD was sampled at each magnetic field configuration. The CSD of neon is shown for B_{min}/B_{ecr}=0.67 in Fig. 5.27 and did not change significantly with magnetic field for CW operation at 350 W.

Neon beam current amplitude responded to AM in a similar way to argon and krypton. However, neon beam currents for B_{min}/B_{ecr}=0.67 experienced higher than average CW beam noise when compared to B_{min}/B_{ecr}=0.72 or B_{min}/B_{ecr}=0.77 as evident by the large error bars in Fig. 5.28. In general, magnetic fields B_{min}/B_{ecr}=0.67 and B_{min}/B_{ecr}=0.77 produced beam current modulation that behaved similarly with charge state and frequency. The beam current amplitude for B_{min}/B_{ecr}=0.67 in Fig. 5.28 and B_{min}/B_{ecr}=0.77 in Fig. 5.29 peaked on a frequency in the range of 100-300 Hz for Ne^{3+}-Ne^{6+}. The highest charge states, Ne^{7+} and Ne^{8+}, had the largest beam current amplitudes with the lowest frequency modulation (11 Hz). No optimization for beam current amplitude was found at higher frequencies unlike the case for Ar^{13+} in Sect. 5.4.2 or Kr^{23+} in Sect. 5.4.1.

In the case of B_{min}/B_{ecr}=0.77, a clear peak in beam current amplitude was observed at around 300 Hz for each charge state as seen in Fig. 5.29. This field was also unique in producing the highest frequency beam current oscillations for Ne^{5+}, exhibiting modulation out to around 80 kHz however with very low amplitude. The double peak found in Kr^{11+}, Kr^{13+}, and Ar^{5+} for low frequency operation was not apparent in Ne^{3+} at any field although

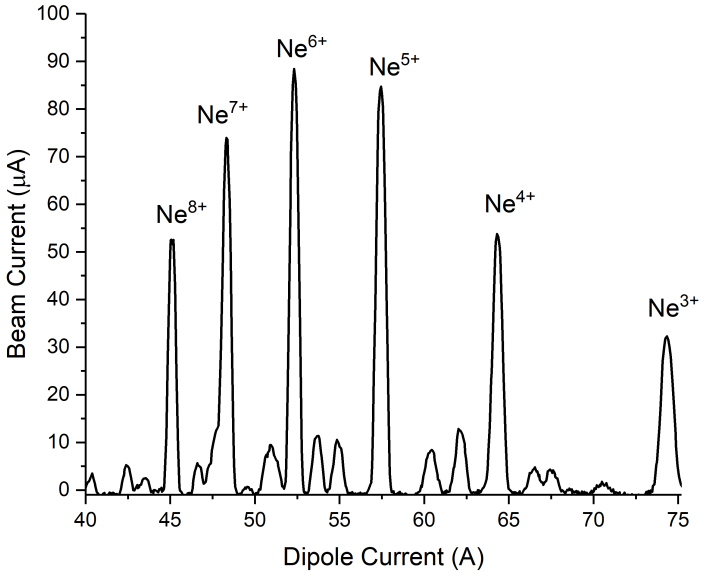

Figure 5.27: Charge state distribution of a neon plasma for 350 W at B_{min}/B_{ecr}=0.67 operating in CW.

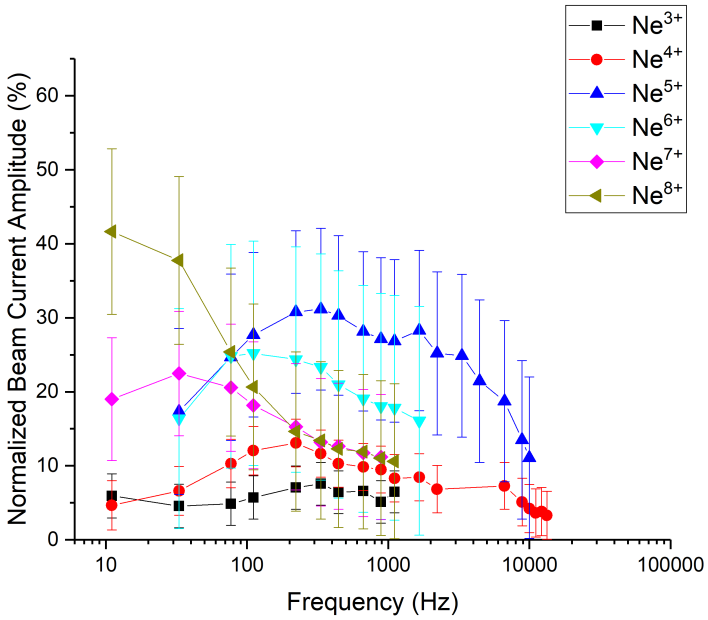

Figure 5.28: Beam current amplitude of neon charge states as a function of modulation frequency for all the neon charge states measurable with ECR2 for a magnetic field configuration of B_{min}/B_{ecr}=0.67.

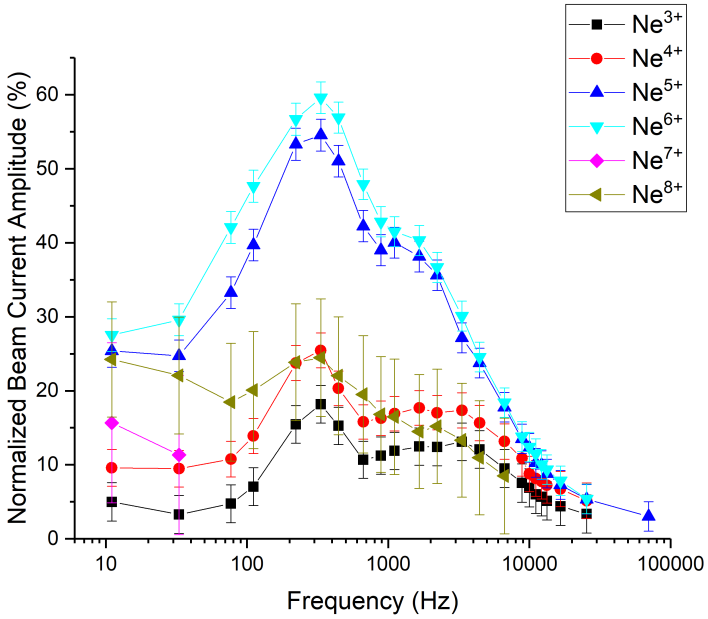

Figure 5.29: Beam current amplitude of neon charge states as a function of modulation frequency for all the neon charge states measurable with ECR2 for a magnetic field configuration of B_{min}/B_{ecr}=0.77.

the waveform was frequently deformed from the sinusoidal shape.

One magnetic field configuration, B_{min}/B_{ecr}=0.72, suppressed the beam current amplitude for any modulation frequency and reduced the highest frequency where modulation was observable. The same effect was observed with argon plasmas covered in Sect. 5.2.2 and Sect. 5.4.2. Ne^{7+} and Ne^{8+} were severely impacted by this magnetic field and no longer exhibited signs of modulation for frequencies higher than 77 Hz. In contrast, Ne^{4+} and Ne^{5+} modulated out to around 10 kHz. The Ne^{4+} beam current amplitude remained unchanged at B_{min}/B_{ecr}=0.72 (Fig. 5.30) compared to B_{min}/B_{ecr}=0.67 (Fig. 5.28) either in magnitude or shape and was the only such example found in the study. The waveforms of Ne^{4+} were distinguishable at either field with B_{min}/B_{ecr}=0.72 possessing more of an afterglow like shape for 33 Hz modulation (similar to the Ne^{6+} example in Fig. 5.32), and more of a sawtooth shape for 11 Hz modulation. In contrast the Ne^{4+} waveform for B_{min}/B_{ecr}=0.67

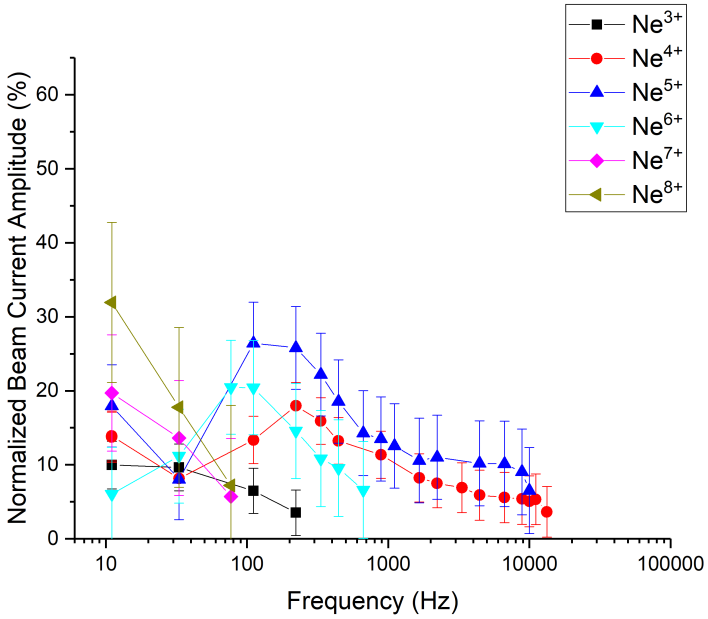

Figure 5.30: Beam current amplitude of neon charge states as a function of modulation frequency for all the neon charge states measurable with ECR2 for a magnetic field configuration of B_{min}/B_{ecr}=0.72.

was largely sinusoidal at any frequency studied.

The beam current phase to microwave power followed similar relationships as observed for argon and krypton plasmas, mainly all charge states oscillated in phase with each other for frequencies higher than about 1 kHz as seen in Figs. 5.31a-c with the characteristic shape of the x-ray phase Fig 5.31d. Beam current phase for the lowest frequency studied (11 Hz) decreased for the highest charge state and can be seen in Fig. 5.31a for B_{min}/B_{ecr}=0.67. The beam current phase for low frequency operation suggests that lower charge states had longer characteristic times as compared to higher charge states in a similar manner to afterglow measurements in Ref. [93].

The beam current phase for B_{min}/B_{ecr}=0.72 was unusually chaotic due to afterglow like waveforms that appeared at this magnetic field configuration during AM. The jagged features in phase in Fig. 5.31b demonstrates the failure of the fitting function to reliably interpret the

phase of waveforms that responded in a nonlinear way to the sinusoidally varying microwave power. Figure 5.32 illustrates the afterglow like shape of the beam current oscillation in Ne^{6+} at 33 Hz. Lower charge states like Ne^{4+} experienced the afterglow like current burst later in time with respect to the microwave power and was reflected in the beam current phase in Fig. 5.31a-c where lower charge states are phase shifted more than higher charge states for low frequency operation.

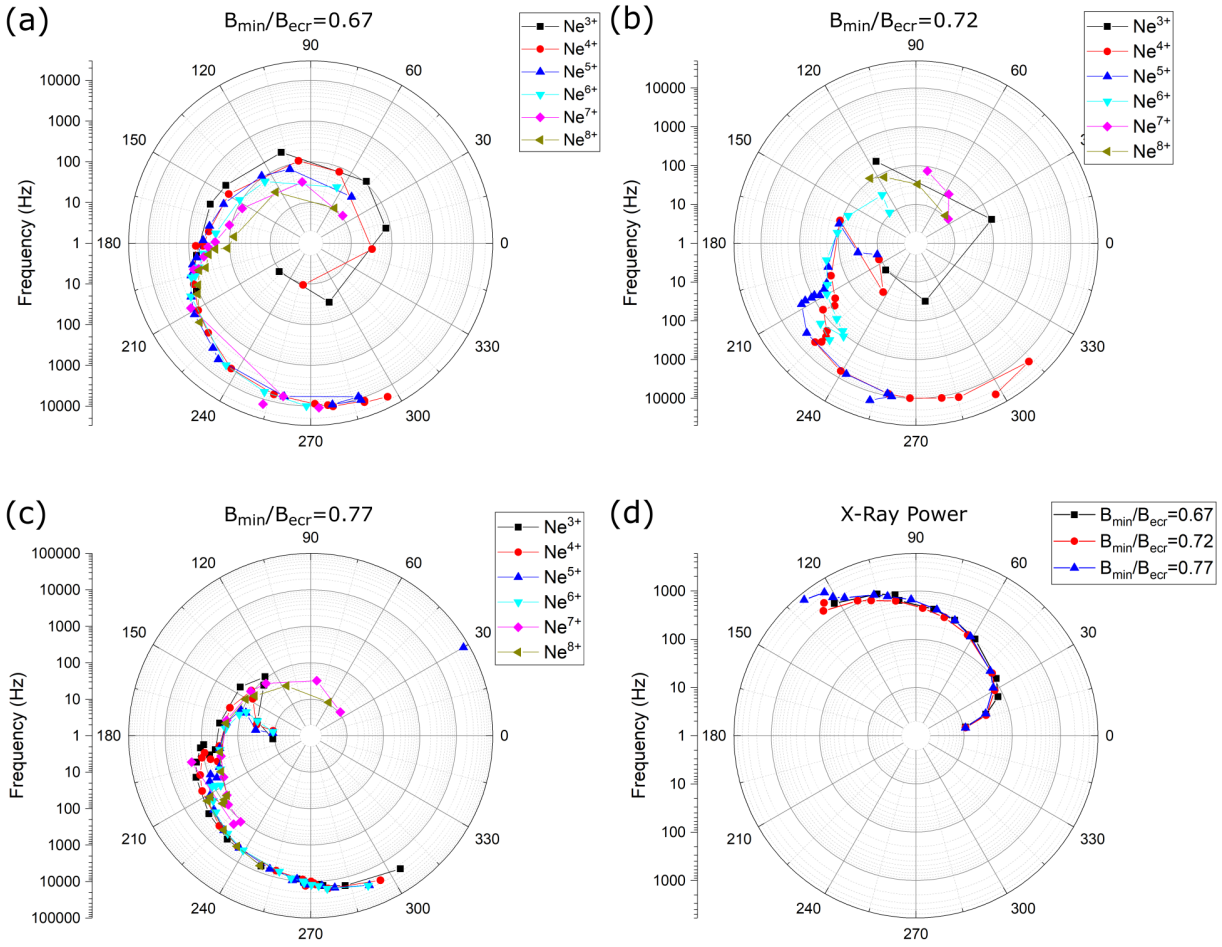

Figure 5.31: Beam current phase of neon plasmas to microwave power for B_{min}/B_{ecr}=0.67 (a), B_{min}/B_{ecr}=0.72 (b), and B_{min}/B_{ecr}=0.77 (c). The x-ray amplitude normalized to the CW x-ray emission as a function of magnetic field configuration (d). The spiral shape in the beam current phase (a-c) is the same structure as found in the x-ray emission (d), note the radial scale terminates at 6 kHz to better display the lower frequency response of the x-ray power.

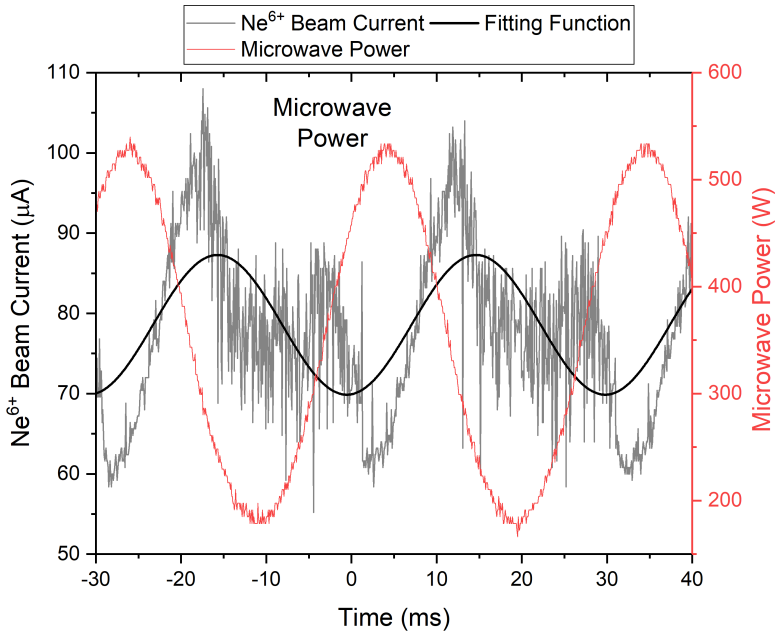

Figure 5.32: Beam current, beam current fitting function, and microwave power of Ne^{6+} for B_{min}/B_{ecr}=0.72 at 33 Hz.

5.5 Square Wave Amplitude Modulation

This section presents the plasma response to a sharp decrease in microwave power for the three plasma species studied krypton, argon, and neon. The microwave power was modulated with a square wave between 180 W and 530 W at a frequency of 3 Hz. This allowed the plasma 167 ms to equalize to the high or low power state. The beam current and x-ray response to step decreases in microwave power were studied, on a limited scale, to better understand some of the observed phenomenon from sinusoidal modulation. Krypton and argon were studied for $B_{min}/B_{ecr} > 0.72$ whereas neon plasmas were studied at all three magnetic field configurations B_{min}/B_{ecr}=0.67, B_{min}/B_{ecr}=0.72, and B_{min}/B_{ecr}=0.77.

Krypton provided a nice example of the beam current responses for sharp changes in microwave power. A pumping effect was observed shortly after the microwave power increased from 180 W to 530 W (see Fig. 5.33a). The beam initial current decrease had the same time

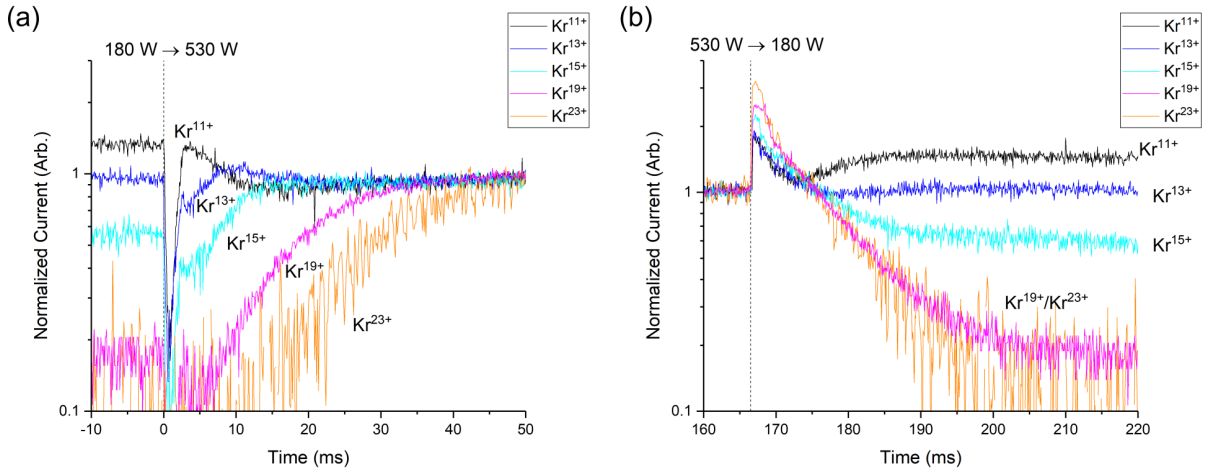

Figure 5.33: Krypton beam current of various charge states normalized to the CW current at 530 W plotted logarithmically for B_{min}/B_{ecr}=0.77. Krypton currents are shown from low to high microwave power (a), and high to low microwave power (b).

structure across all charge states, however the current recovery took an increasingly long time for each increasing charge state. Kr^{11+} was particularly interesting because it returned to nearly its previous current (at 180 W) before redistributing to a lower value for the 530 W operating point. This suggests that the density of Kr^{11+} did not significantly change during the sharp decrease in current and therefore was likely due to the ion flow out of the source being temporarily stopped as the plasma redistributed to the high power state. The Kr^{11+} current, at its minimum, decreased by a factor of nine with a FWHM of 1.2 ms.

Every charge state exhibited an afterglow like pulse of current as the microwave power decreased. Higher charge states experienced a larger current burst as seen in Fig. 5.33b. The actual beam current decay rate of low charge states such as Kr^{11+} was unclear because the current increased rapidly after the current burst as the plasma redistributed the CSD for the lower power configuration. The decay rate of Kr^{15+}, Kr^{19+}, Kr^{23+} was 7.4 ± 0.1 ms, 8.4 ± 0.3 ms, and 8.1 ± 1 ms respectively when fitted with an exponential decay function from the current burst peak through the end of the file. The three fitted charge states decayed at

a nearly identical rate with no trend in charge state. The error in decay time was generated by the CW beam current noise for 350 W operation.

Argon produced similar results to krypton when modulated with a square wave at low frequency (3 Hz). In error, a slightly different magnetic field configuration of B_{min}/B_{ecr}=0.76 was used as compared to the B_{min}/B_{ecr}=0.77 for krypton. The slight difference in magnetic field configuration was unfortunate but the results are likely still comparable to the B_{min}/B_{ecr}=0.77 as both fields are very similar as seen in Table 5.1. Figure 5.34 shows the beam current response of Ar^{9+} and Ar^{13+} to microwave power decreasing from 530 W to 180 W. Both charge states experienced an afterglow like current burst. The decay rate of Ar^{9+} was difficult to determine because the beam current increased after the current burst ended as the CSD from the plasma accommodated the lower microwave power condition. Ar^{13+} decayed with a characteristic time of 9.0 ± 0.6 ms when fitted with an exponential decay function from the current burst peak through to the end of the file, the error was propagated from the CW beam noise for operation at 350 W. For comparison, the pure afterglow experiment in Ref. [93] on ECR2 measured the afterglow 1/e decay time as 8 ± 1 ms. The Ar^{13+} decay time from the AM experiment is in agreement with that obtained during afterglow.

The effect of magnetic field configuration on the afterglow like beam current pulse was studied for neon. Figure 5.35 shows how for Ne^{8+} the beam current burst disappears for B_{min}/B_{ecr}=0.72 along with optimizing the CW current at 530 W. In an interesting result specific to neon, the current bursts of Ne^{8+} for the other fields B_{min}/B_{ecr}=0.67 and B_{min}/B_{ecr}=0.77 approximately reach the magnitude of the CW current at 530 W for B_{min}/B_{ecr}=0.72. This was similar to the relationship observed in Fig. 5.12 where the field that minimized sinusoidal modulation also maximized the CW current. The same effect

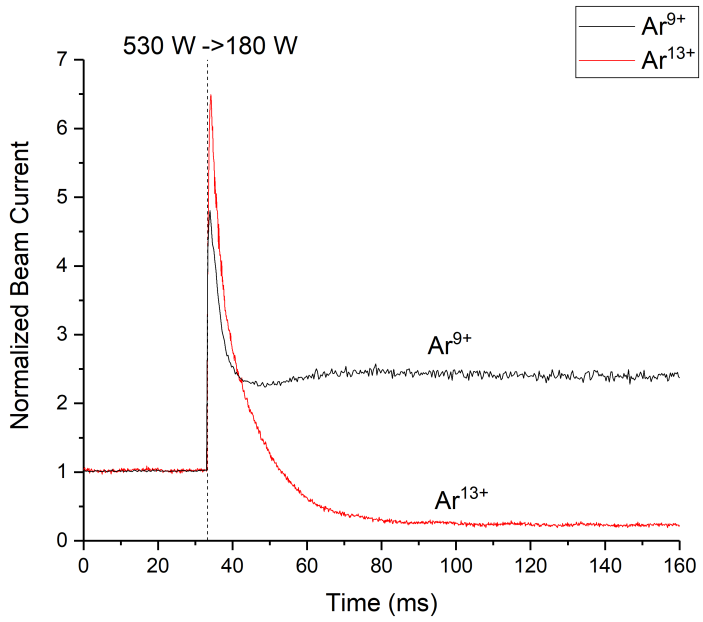

Figure 5.34: Ar^{9+} and Ar^{13+} beam current normalized to the current preceding the decrease in microwave power for B_{min}/B_{ecr}=0.76.

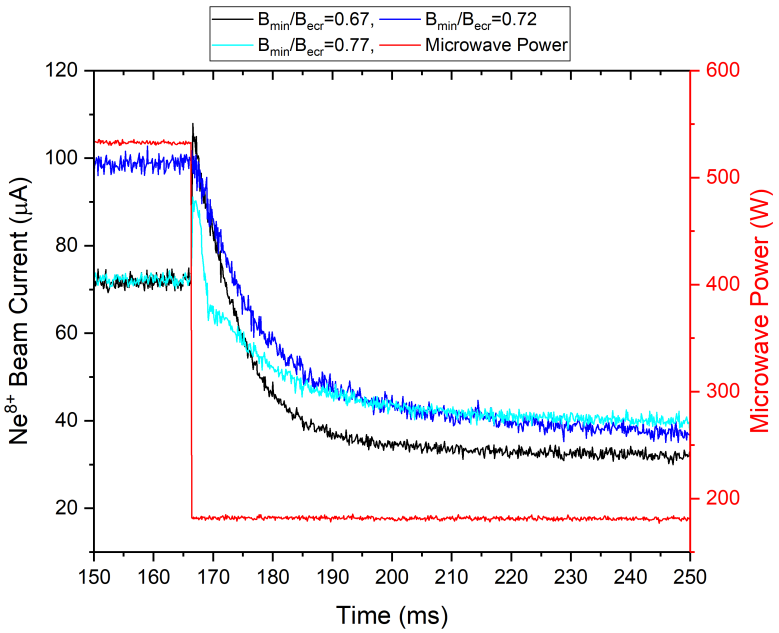

Figure 5.35: Ne^{8+} beam current modulated by a sudden decrease in microwave power for three different magnetic field configurations. One field, B_{min}/B_{ecr}=0.72, did not produce an afterglow like burst when the microwave power decreased.

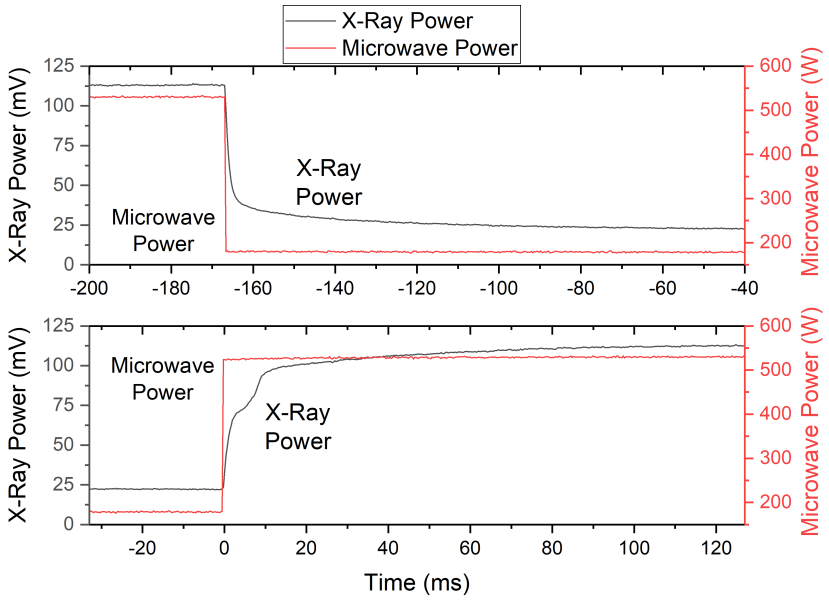

Figure 5.36: X-ray power for a sharp increase and decrease in microwave power. The x-ray power responds to the microwave quickly at first but takes tens of milliseconds to saturate to its CW value at either high or low microwave power.

shown in Fig. 5.35 for Ne^{8+} was also observed with Ne^{6+}.

X-ray power responded smoothly to the step increase and decrease in microwave power as seen in Fig. 5.36. The x-ray power response was very fast with an initial time delay within the 300 μs time resolution of the waveforms. X-ray power saturated to its CW values slowly requiring tens of milliseconds at either 530 W or 180 W power levels. This suggested there were different production rates and confinement times expressed in the x-ray power.

5.5.1 Variable Slope Modulation

For one specific operating point, with an argon plasma with a magnetic field configuration of B_{min}/B_{ecr}=0.76, the impact of microwave power slope on the beam current burst of Ar^{13+} was studied. The sharp corner of the 3 Hz square wave (see Sect. 5.5) was "clipped" to make a linear slope in microwave power of various rates (see Fig. 5.37). The larger the microwave power rate of change (slope) the more time the plasma experienced the high power level

(530 W). In the case of the smallest microwave power rate of change (3.50 W/ms), the plasma spent 20% less time at 530 W than for the highest power rate of change ($>$ 2660 W/ms with the 3 Hz square wave).

The time characteristics of the Ar^{13+} beam current burst were modified by changing the microwave power rate of decrease. Figure 5.37 shows the Ar^{13+} beam current response for four different microwave power rates. The current burst "fired" at the specific power level of about 390 W for each different microwave power rate of change. The steepest slope in microwave power rate of change generated the largest peak current of Ar^{13+} and the shortest burst duration. Conversely, the smallest microwave power slope produced the smallest peak current of Ar^{13+} but the longest burst duration (see Fig. 5.38). The current bursts were integrated (Grey shaded area) finding the total charge in each burst to remain approximately fixed. Furthermore the relationship in Fig 5.38 between peak current and burst duration suggests the total charge contained per burst was conserved.

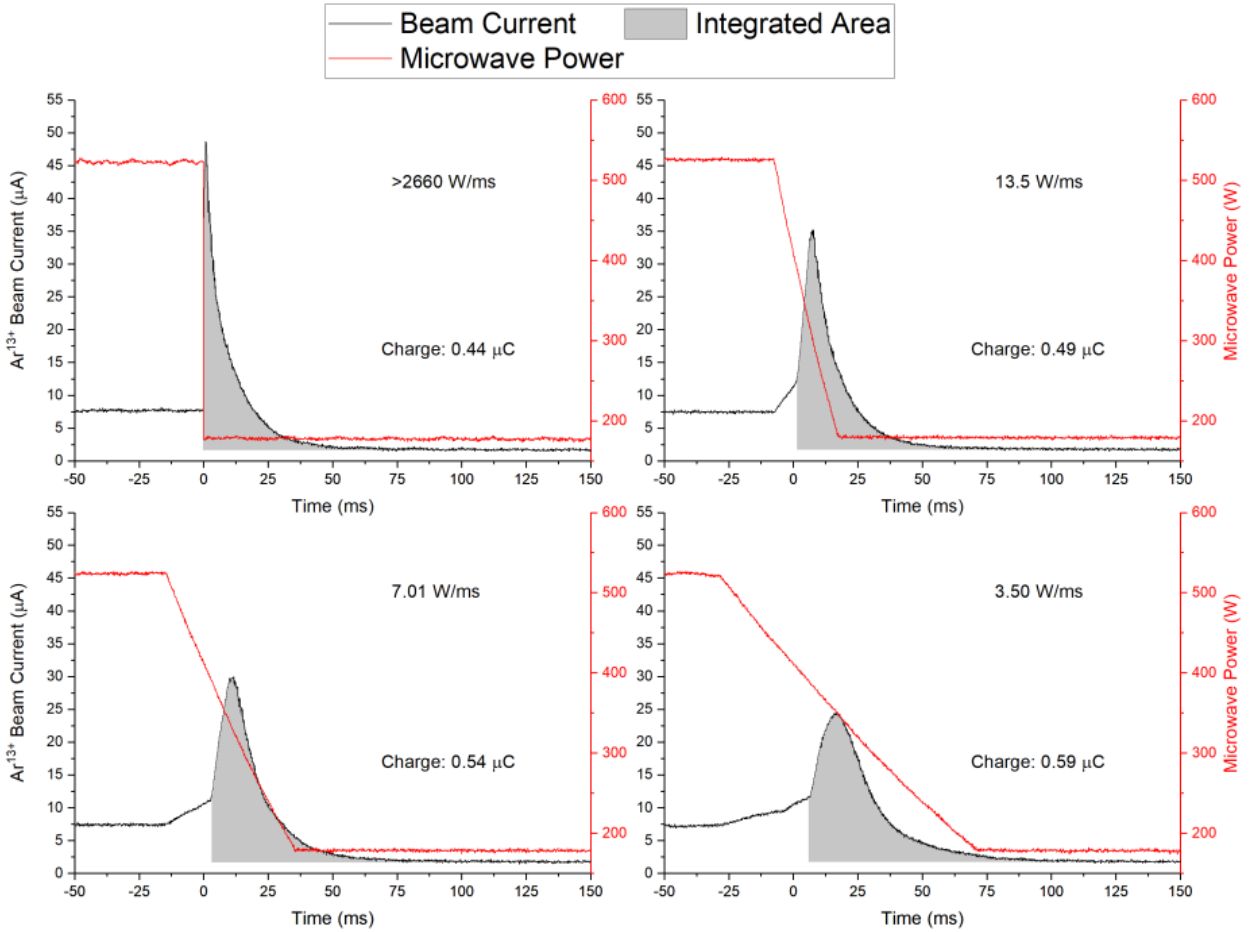

Figure 5.37: Ar^{13+} beam current for different rates of linear microwave power decrease with a magnetic field configuration of B_{min}/B_{ecr}=0.76. Approximately the same amount of charge was released with each afterglow like current burst with the rate of microwave power decrease impacting the rate of release of the charge, the Grey shading denotes the integration region. The time for the microwave power to decrease from 530 W to 180 W was less than 128 μs, 24.8 ms, 50.1 ms, and 101 ms in ascending order. The main current burst was initiated at about the same power level.

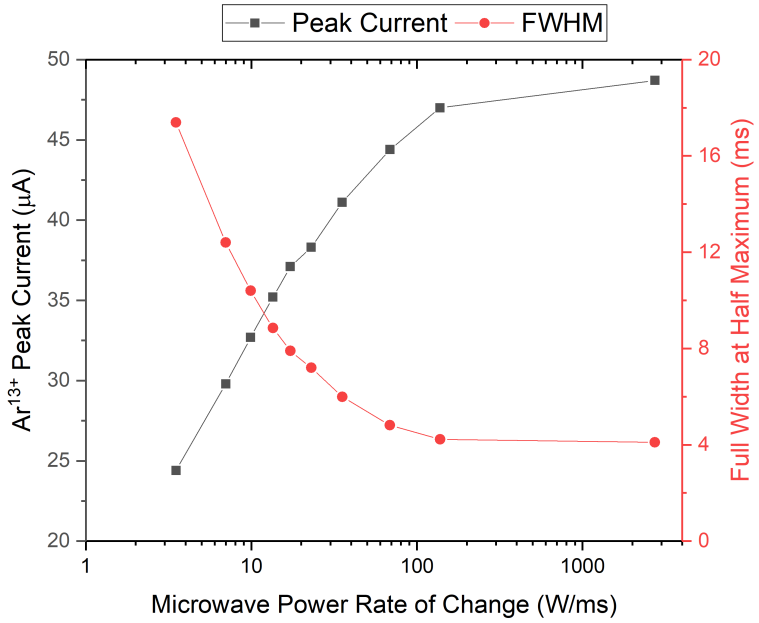

Figure 5.38: Ar^{13+} peak current and Full Width at Half Maximum (FWHM) for different microwave power rates of change (decrease) for B_{min}/B_{ecr}=0.76. The balance point maximizing peak current while minimizing FWHM is similar to the effect observed during sinusoidal modulation where the largest amplitudes were observed in the 200-400 Hz range.

5.6 Discussion and Outlook

Beam current and x-ray responses to microwave power modulation were studied for three different noble gases, and followed trends general across plasma species:

1. One magnetic field configuration, B_{min}/B_{ecr}=0.72, highly suppressed amplitude modulation in the beam current (see Sect. 5.2.2).

2. Beam current amplitude, when not highly suppressed from B_{min}/B_{ecr}=0.72, reached a local maxima around 200-400 Hz and exponentially decreased in amplitude for higher frequencies.

3. The beam current amplitude was always highly suppressed for frequencies greater than 10 kHz and was never more than 15% of the CW current at this frequency.

4. The x-ray power phase was insensitive to magnetic field, plasma species, and vacuum pressure.

5. All the beam current charge states oscillated in phase with each other for modulation frequencies higher than around 400 Hz.

    (a) The beam current phase followed the same shape as the x-ray power phase.

These results suggest that the ions were following the electrons. It may not appear clear why the local maxima in beam current amplitude around 200-400 Hz, observed for most plasma operating points during sinusoidal modulation, is evidence supporting this explanation. One of the best examples comes out of the variable slope modulation result in Fig. 5.38 where the time structure of the Ar^{13+} beam current burst lengthened as the microwave power rate of change decreased. This same effect was likely taking place during sinusoidal modulation. In the case of low frequencies such as 11 Hz, the plasma had a lot of time to produce ions at the high power level but due to the long time to transition between high and low power states, the plasma could only release the accumulated charge slowly (long FWHM). Whereas for high frequencies such as 10 kHz, the microwave power transitioned quickly and the time structure in the current burst was short but because the sinusoidal waveform spent equal times at high and low power states, the plasma did not have enough time at the high power level to build up a significant amount of ions to release resulting in low peak beam currents and low amplitudes. The balance point between these two extremes appeared, in most cases, to occur in the 200-400 Hz range.

In the case of square wave modulation, particularly of krypton, the ion currents were highly perturbed as the microwave power transitioned between levels. For example, as the microwave power went from low to high, the beam currents decreased to nearly zero for a

short time as seen in Fig. 5.33a. Conversely, there was a beam current burst as the power went from high to low. and the charge states of krypton shared similar time characteristics as seen in Fig. 5.33b. This was likely due to the plasma maintaining quasi-neutrality as the electron density was modulated.

Notably, one magnetic field configuration, B_{min}/B_{ecr}=0.72, highly suppressed beam current modulation in argon as seen in Fig. 5.7. One unique feature of B_{min}/B_{ecr}=0.72 was its ability to provide a small boost to the CW beam current (see Fig. 5.12). It is curious that the length of the ECR resonance zone for B_{min}/B_{ecr}=0.72 was 5.00 times the vacuum wavelength of the driving microwave power, and could be evidence of a limited resonance structure provided by the magnetic ECR surface. If this is true, then similar magnetic fields should exist at other multiples of the driving RF frequency that suppress the beam current amplitude to AM. It is also worth reiterating that the effect was pressure dependent (as demonstrated in Sect. 5.2.1) for reasons that remain, at the time of writing, unclear. Unfortunately, the x-ray power did not provide evidence in waveform shape, amplitude, or phase that singled out B_{min}/B_{ecr}=0.72 as unique, and as a result the suppression of beam current modulation from this field does not appear to be the direct result of hot electron behavior within the sensitivity of this measurement.

Amplitude modulation did not appear to provide useful information about steady state ion confinement time. In cases where characteristic time, such as phase, scaled smoothly with charge state (see the neon result in Fig. 5.31a), the lowest charge states experienced a longer phase shift in a manner more consistent with afterglow and inconsistent with ion confinement. For most plasmas, the low charge state and low frequency operating point produced a double peak in the waveform (see Fig. 5.17) resulting in a less clear analysis of the phase. However, in the case of neon at B_{min}/B_{ecr}=0.67 no double peak structure was observed and a smooth

transition in phase occurred between charge states (see Fig. 5.31a), the lowest charge state Ne^{3+} was phase delayed by about 180° to the highest charge state Ne^{8+}. This type of phenomenon is more similar to that observed during afterglow experiments where low charge states decayed with a much longer characteristic time than high charge states [93]. There was not a clear disparity as a function of charge state for 1/e decay time during square wave measurements, but the current burst frequently observed as microwave power transitioned from high to low power levels was suggestive of afterglow.

5.6.1 Final Thoughts on Amplitude Modulation and Future Work

The culmination of the evidence suggests that amplitude modulation of the microwave power probes an electron effect. Most compelling, was that major structures in beam current amplitude were shared amongst different charge states, gases, and following the same x-ray phase structure. The simplest explanation seems to be the most plausible, mainly that the microwave power modulates the plasma electron density. The effect is best exemplified by Fig. 5.33a and Fig. 5.33b with square wave modulation of krypton. As microwave power decreases (Fig. 5.33b) the electron density decreases from steady state (at high power) and the ions are expelled from the plasma to maintain quasi neutrality (beam current burst). When the microwave power increases (Fig. 5.33a) the increased electron density, to maintain quasi neutrality, temporarily confines the ions until the ion density can "catch up" to the more mobile electrons. In general, for sinusoidal modulation, the ions followed the x-ray power (electrons) as modulation frequency increased.

Unfortunately, amplitude modulation was unable to increase the average beam current from the ECR ion source (see Figs. 5.13a-d). However, the x-ray power magnitude increased from amplitude modulation seen in Fig. 5.14. The average x-ray power was larger than its

steady state value during AM even when modulation was unobservable in the x-ray power waveform. This was likely due to asymmetry between electron heating and confinement rates with electrons being pumped into states with longer confinement times than the period of modulation. The time delay between the x-ray power and microwave power decreased as a function of frequency (see Fig. 5.20), and was no longer measurable for frequencies in the 2-4 kHz range. The combination of increased x-ray power during AM and the sliding time delay value as a function of frequency suggests that the modulation in x-ray power was smoothed out by electron confinement time. If this was the case, then the frequency cutoff observed in the 2-4 kHz range was likely proportional to the electron confinement time associated with the low energy cutoff of the x-ray detector (estimated to be 30 keV), and the long time delay (2 ms) for low frequency operation (11 Hz) was the result of modulation in the highest energy electrons.

If amplitude modulation is in fact an indirect measurement of electron confinement time, then it could be used to measure the relationship between electron energy and electron confinement. This could be performed by using an energy and time resolved x-ray measurement similar to the method employed by T. Ropponen et al. in Ref. [73]. An energy resolved x-ray detector such as the one described in Sect. 2.6.2 could be set-up to discriminate against x-ray detections outside of a specific phase window on the x-ray oscillation. The energy resolved x-ray spectra at minimum and maximum x-ray power would be compared for equal detection windows by comparing the difference in energy resolved spectra on the crest and trough of the x-ray power waveform. As AM frequency is changed, the highest energy electron modulating at the AM frequency could be mapped. An idea of how the experiment might work is sketched out in Fig. 5.39. An alternative approach could be to measure the extracted electrons from the source, as was demonstrated by I. Izotov et al. in Ref. [32], during amplitude

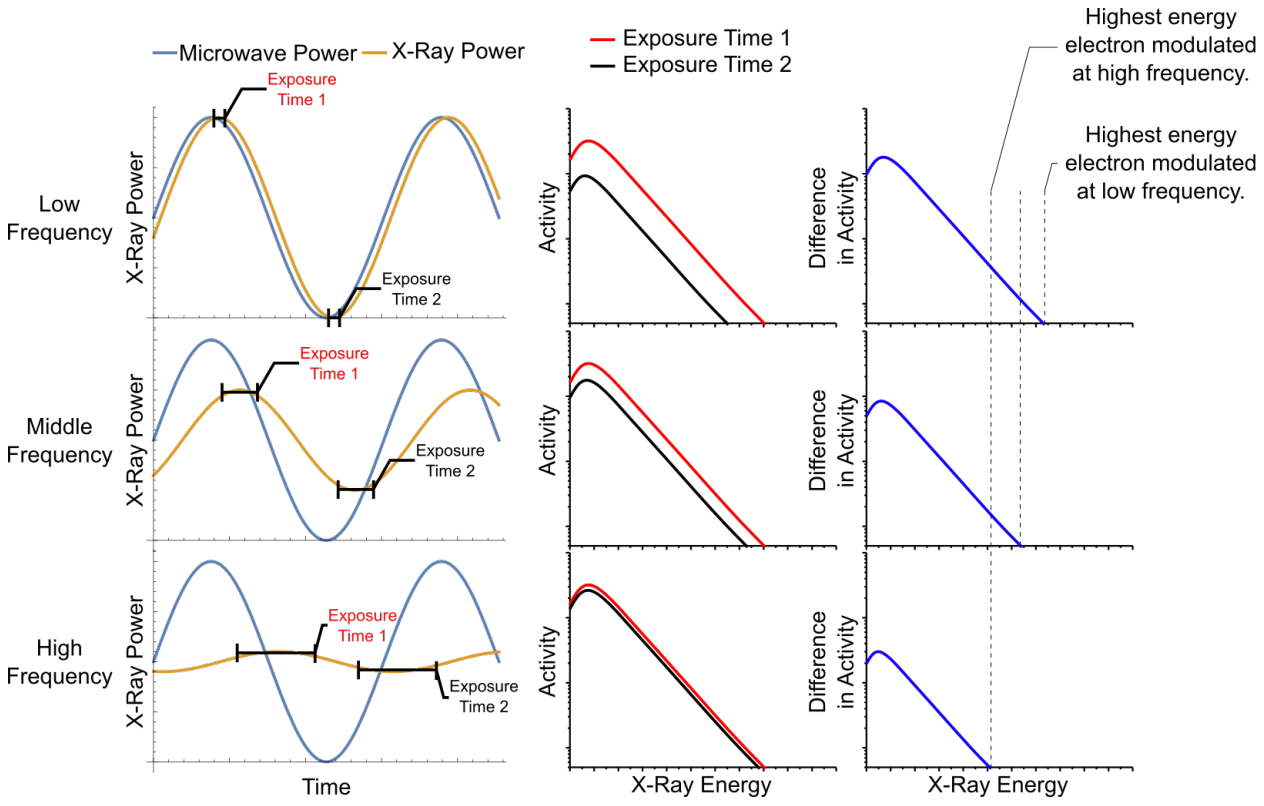

Figure 5.39: A schematic of how amplitude modulation could be used to map out electron confinement with energy resolved x-ray measurements. This method would work if the x-ray behavior observed in this chapter was from mapping of electron confinement time onto the x-ray power as a function of frequency. One difficulty with this method could be obtaining useful statistics for high (kilohertz) modulation frequencies where the exposure windows would need to be sub-millisecond, and small separation between spectra.

modulation. For discretized electron energies (set by the dipole magnet), the amplitude of modulation in electron beam intensity would be measured. As the frequency is increased, the high energy electrons should no longer modulate while the low energy electrons should still modulate but at lower amplitude.

APPENDIX

Energy Resolved X-ray Processing

The x-rays measured in the bremsstrahlung detector used in Chapter 3 and Chapter 4 were corrected for the detector efficiency in post processing. The detector efficiency was measured using a source of ^{152}Eu of known activity measured 1 m from the detector end-cap The resulting spectral lines were compared to branching ratios obtained from [2]. The gamma spectra of ^{152}Eu were fitted and integrated after background subtraction using View Specra [13] finding the total number of detections of each energy line. The solid angle subtended by the detector was taken into account. The resulting detector efficiency curve is shown in Fig. A.40 along with the polynomial fitting function that transferred the shape onto the bremsstrahlung spectra from the ECR ion source. Figure A.41 shows an example of bremsstrahlung corrected for efficiency as opposed to background subtracted over the entire energy range the detector was sensitive to for 18 GHz operation at 100 W microwave power for B_{min}/B_{ecr}=0.9. The data near zero energy were caused by noise and do not represent real detections.

Hot Electron Temperature and Magnetic Minimum

The hot electron temperature was demonstrated in Ref. [3] to depend on magnetic minimum instead of the gradient of the magnetic field at the resonance zone. Figure 3 from that paper is reproduced here in Fig. A.42 with the hot electron temperatures from SuSI overlaid onto it. The trend and magnitudes measured on SuSI are consistent with that found on the VENUS source.

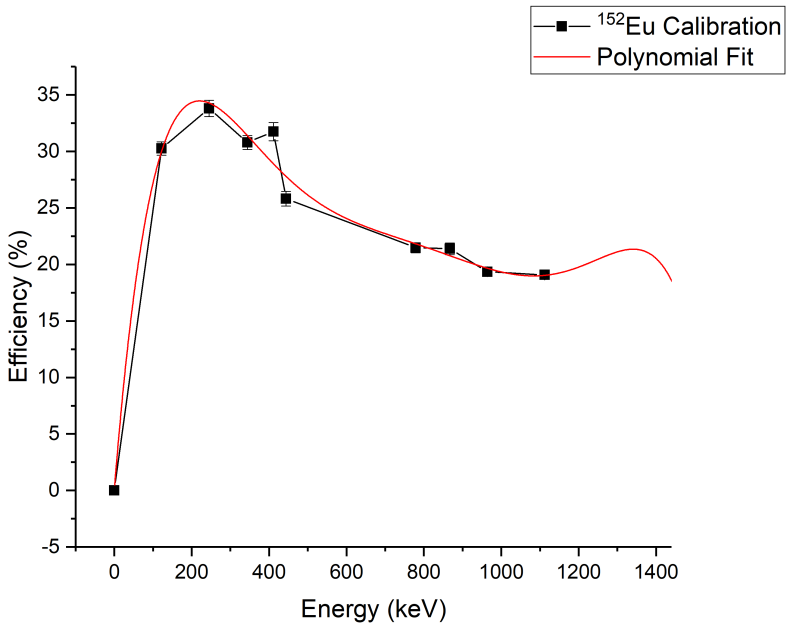

Figure A.40: X-ray efficiency calibration applied to bremsstrahlung spectra in Chapter 3 and Chapter 4.

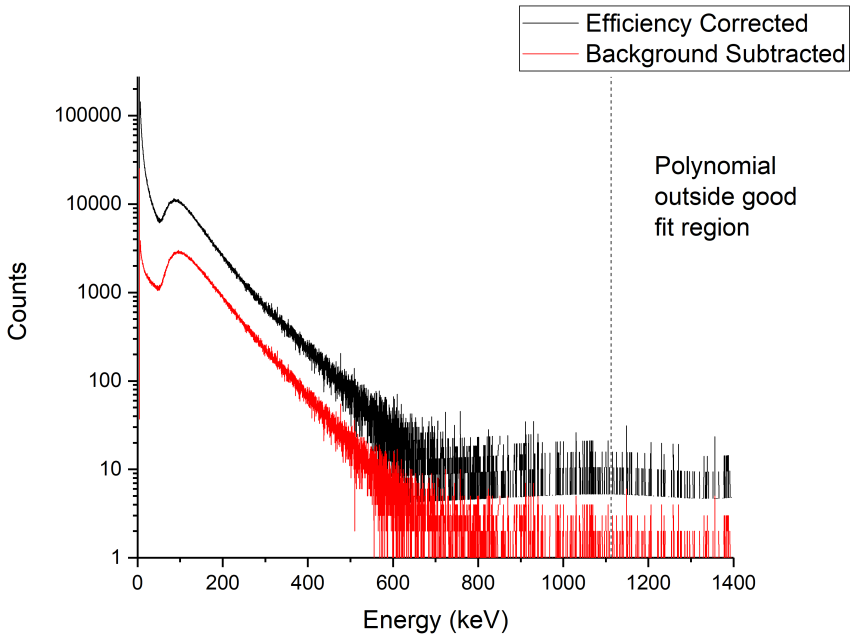

Figure A.41: Bremsstrahlung spectra showing background subtracted raw counts and efficiency corrected over the entire sensitive energy range. The counts near zero energy are caused by noise and do not represent real data. The efficiency calibration increases the count rate to account for the less than one detector efficiency.

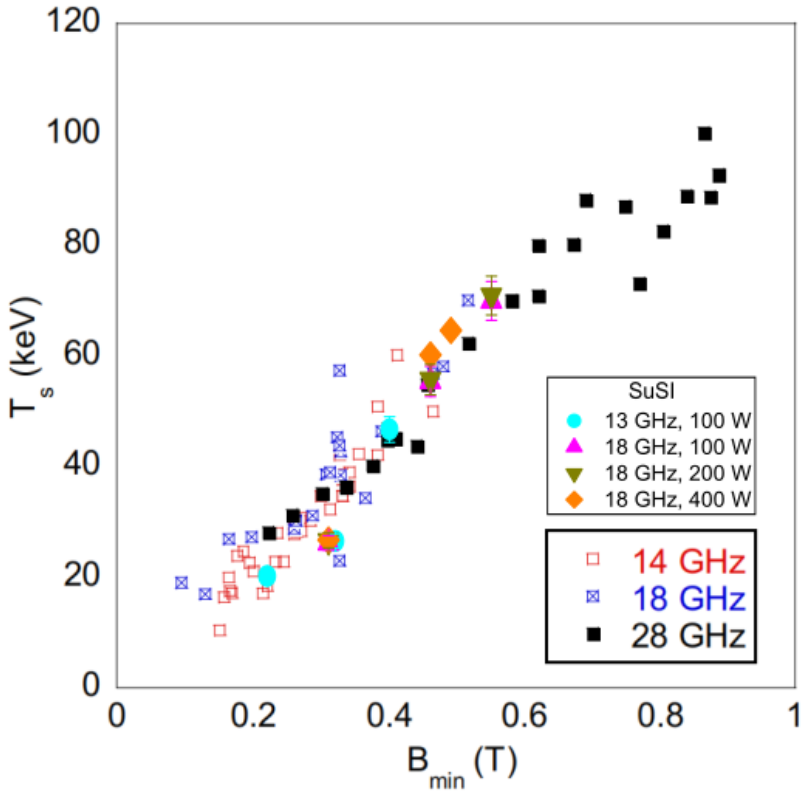

Figure A.42: The hot electron temperature measured on VENUS from Ref. [3] with the hot electron temperature from SuSI reported in Sect. 4.3.1 of this dissertation overlaid onto it.

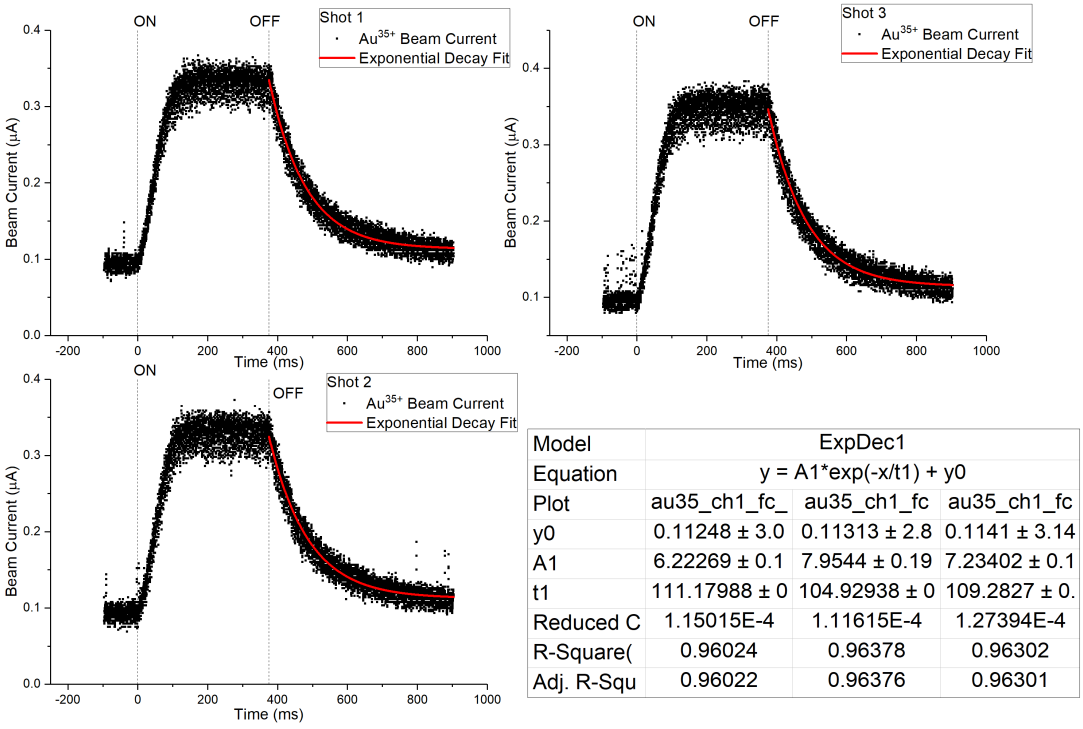

Model	ExpDec1		
Equation	y = A1*exp(-x/t1) + y0		
Plot	au35_ch1_fc_	au35_ch1_fc	au35_ch1_fc
y0	0.11248 ± 3.0	0.11313 ± 2.8	0.1141 ± 3.14
A1	6.22269 ± 0.1	7.9544 ± 0.19	7.23402 ± 0.1
t1	111.17988 ± 0	104.92938 ± 0	109.2827 ± 0.
Reduced C	1.15015E-4	1.11615E-4	1.27394E-4
R-Square(	0.96024	0.96378	0.96302
Adj. R-Squ	0.96022	0.96376	0.96301

Figure A.43: All three shots obtained of Au^{35+} for 18 GHz operation at B_{min}/B_{ecr}=0.9 and for 100 W applied microwave power.

Pulsed Sputtering Raw Data

An example of all 3 shots of Au^{35+} is shown in Fig. A.43. The corresponding plasma operating point was with 18 GHz operation for 100 W applied microwave power and with a magnetic field configuration of B_{min}/B_{ecr}=0.9. The decay time of the three shots were averaged with the standard deviation contributing to the error bar generation of decay time along with the CW beam current average and standard deviation.

BIBLIOGRAPHY

BIBLIOGRAPHY

[1] J. Baumgaertel. "Simulating the effects of stellarator geometry on gyrokinetic drift-wave turbulence." PhD thesis. Princeton University, 2012.

[2] M. Bé, V. Chechev, R. Dersch, O. Helene, R. Helmer, M. Herman, S. Hlavác, A. Marcinkowski, G. Molnár, A. Nichols, E. Schönfeld, V. Vanin, and M. Woods. "Volume 1: recommended decay data, high energy gamma ray standards and angular correction coefficients." In: *Update of x-ray and gamma ray decay data standards for detector calibration and other applications*. Vienna, Austria: International Atomic Energy Agency (IAEA), 2007, p. 38.

[3] J. Benitez, C. Lyneis, L. Phair, D. Todd, and D. Xie. "Recent bremsstrahlung measurements from the superconducting electron cyclotron resonance ion source VENUS." In: *Proc. ECRIS'16*. JACoW Conference Proceedings MOCO04. Busan, Korea, 2016.

[4] J. Benitez, J. Noland, D. Leitner, C. Lyneis, D. Todd, and J. Verboncoeur. "High energy component of x-ray spectra in ECR ion sources." In: *Proc. ECRIS'08*. JACoW Conference Proceedings MOPO-08. Chicago, IL, USA, 2008.

[5] K. Bernhardi, G. Fuchs, M. Goldman, H. Herbert, D. Obermann, and W. Walcher. "Resonance zone effects on electron heating of an electron-cyclotron-resonance plasma." In: *Phys. Lett.* 50A.5 (1974), p. 324.

[6] J. Bittencourt. "Fundamentals of plasma physics 3rd ed." In: New York, NY, USA: Springer-Verlag, 2004.

[7] S. Braccini. "Compact medical cyclotrons and their use for radioisotope production and multi-disciplinary research." In: *Proc. CYCLOTRONS'16*. JACoW Conference Proceedings TUD01. Zurich, Switzerland, 2016.

[8] F. Chen. In: *Introduction to plasma physics and controlled fusion 2nd ed.* Ed. by I. G. Brown. Vol. 1. New York, NY, USA: Plenum Press, 1984, p. 352.

[9] G. Douysset, H. Khodja, A. Girard, and J. Briand. "Highly charged ion densities and ion confinement properties in an electron-cyclotron-resonance ion source." In: *Phys. Rev. E* 61.3 (2000), p. 3015.

[10] D. Edgell, J. Kim, I. Bogatu, R. Pardo, and R. Vondrasek. "Modeling of electron cyclotron resonance ion source plasmas." In: *Proc. PAC'01*. 2135. Chicago, IL, USA, 2001.

[11] D. Edwards and M. Syphers. "An introduction to the physics of high energy accelerators." In: Hoboken, NJ, USA: John Wiley & Sons, 2008.

[12] M. Farley, P. Rose, and G. Ryding. "Freeman and Bernas ion sources." In: *The physics and technology of ion sources 2nd ed.* Ed. by I. G. Brown. Weinheim, Germany: WILEY-VCH, 2004, p. 133.

[13] A. Fitzler. "Tv user manual." In: Cologne, Germany: University of Cologne, 2003.

[14] A. Fridman. "Plasma chemistry." In: Cambridge, UK: Cambridge University Press, 2008.

[15] S. Gammino, G. Civola, L. Celona, D. Hitz, A. Girard, and G. Melin. "Operation of the SERSE superconducting electron cyclotron resonance ion source at 28 GHz." In: 72.11 (2001), p. 4090.

[16] S. Gammino, J. Sijbring, and A. Drentje. "Experiment with a biased disc at the K.V.I. ECRIS." In: *Rev. Sci. Instrum.* 63 (1992), p. 2872.

[17] N. Gavrilov. "High current gaseous ion sources." In: *The physics and technology of ion sources 2nd ed.* Ed. by I. G. Brown. Weinheim, Germany: WILEY-VCH, 2004, p. 107.

[18] R. Geller. "Electron cyclotron resonance ion sources and ECR plasmas." In: Bristol, UK: IOP Publishing, 1996.

[19] D. Goebel and I. Katz. "Fundamentals of electric propulsion: ion and hall thrusters." In: ed. by J. Yuen. Pasadena, CA, USA: Jet Propulsion Laboratory & California Institute of Technology, 2008, p. 429.

[20] K. Golovanivsky. "Autoresonant acceleration of electrons at nonlinear ECR in a magnetic field which is smoothly growing in time." In: *Phys. Scr.* 22 (1980), p. 126.

[21] K. Golovanivsky. "Gyromagnetic autoresonance at ultrarelativistic energies." In: *Trans. Plas. Sci.* PS-10.2 (1982), p. 120.

[22] K. Golovanivsky. "The gyromagnetic autoresonance." In: *Trans. Plas. Sci.* PS-11.1 (1983), p. 28.

[23] S. Golubev and A. Shalashov. "Cyclotron-resonance MASER with adiabatic magnetic pumping in a low-density plasma." In: *JETP Letters* 86.2 (2007), p. 91.

[24] K. Halbach and R. F. Holsinger. "SUPERFISH - a computer program for evaluation of RF cavities with cylindrical symmetry." In: *Part. Acc.* 7 (1976), p. 213.

[25] R. Harkewicz, P. Billquist, and R. Pardo. “Recent developments in ECRIS technology at Argonne National Laboratory and the new ATLAS 14 GHz ECRIS project.” In: *Proc. ECRIS'95*. Saitama, Japan, 1995.

[26] B. Henke, E. Gullikson, and J. Davis. “X-ray interactions: photoabsorption, scattering, transmission, and reflection at E=50-30000 eV, Z=1-92.” In: *At. Data Nucl. Data Tables* 54.2 (1993), p. 181.

[27] Y. Higurashi, J. Ohnishi, H. Haba, M. Kidera, K. Ozeki, and T. Nakagawa. “Recent developments of RIKEN 28 GHz SC-ECRIS.” In: *Proc. ECRIS'16*. JACoW Conference Proceedings MOBO04. Busan, Korea, 2016.

[28] C. Hill and K. Langbein. “Experiments on a 14.5 GHz electron cyclotron resonance source.” In: *Rev. Sci. Instrum.* 69.2 (1998), p. 643.

[29] D. Hitz, A. Girard, G. Melin, S. Gammino, G. Ciavola, and L. Celona. “Results and interpretation of high frequency experiments at 28 GHz in ECR ion sources, future prospects.” In: *Rev. Sci. Instrum.* 73 (2002), p. 509.

[30] B. Isherwood. Email to author. Dec. 2017.

[31] I. Izotov, O. Tarvainen, D. Mansfeld, V. Skalyga, H. Koivisto, T. Kalvas, J. Komppula, R. Kronholm, and J. Laulainen. “Microwave emission related to cyclotron instabilities in a minimum-B electron cyclotron resonance ion source plasma.” In: *Plas. Sourc. Sci. Technol.* 24 (2015), p. 045017.

[32] I. Izotov, O. Tarvainen, V. Skalyga, D. Mansfield, T. Kalvas, H. Koivisto, and R. Kronholm. “Measurement of the energy distribution of electrons escaping minimum-B ECR plasmas.” In: *Plas. Sourc. Sci. Technol.* 27 (2018), p. 025012.

[33] F. Jaeger, A. Lichtenberg, and M. Lieberman. “Theory of electron cyclotron resonance heating. I. Short time and adiabatic effects.” In: *Plas. Phys.* 14 (1972), p. 1073.

[34] T. Kalvas, H. Koivisto, and O. Tarvainen. “Status of new 18 GHz ECRIS HIISI.” In: 2011 (2018), p. 040006.

[35] G. Knoll. “Radiation detection and measurement 3rd ed.” In: Hoboken, NJ, USA: John Wiley & Sons, 2000.

[36] H. Koivisto, D. Cole, A. Fredell, C. Lyneis P. Miller, J. Moskalik, B. Nurnberger, J. Ottarson, A. Zeller, J. DeKamp, R. Vondrasek, P. Zavodszky, and D. Xie. *ARTEMIS the new room temperature ECR ion source at MSU*. Tech. rep. East Lansing, Michigan: NSCL/MSU, 2006.

[37] H. Koivisto, P. Heikkinen, V. Hänninen, A. Lassila, H. Leinonen, V. Nieminen, J. Pakarinen, K. Ranttila, J. Ärje, and E. Liukkonen. "The first results with the new JYFL 14 GHz ECR ion source." In: *Nucl. Instrum. Meth. Phys. Res. B* 174 (2001), p. 379.

[38] A. Kojevnikov. "David Bohm and collective movement." In: *Hist. Stud. Phys. Biol. Sci.* 33.1 (2002), p. 161.

[39] M. Lamoureux and P. Charles. "General deconvolution of thin-target and thick-target bremsstrahlung spectra to determine electron energy distributions." In: *Rad. Phys. Chem.* 75 (2006), p. 1220.

[40] D. Leitner and C. Lyneis. "ECR ion sources." In: *The physics and technology of ion sources 2nd ed.* Ed. by I. G. Brown. Weinheim, Germany: WILEY-VCH, 2004, p. 207.

[41] D. Leitner, D. Winklehner, and M. Strohmeier. "Some aspects of electron dynamics in electron cyclotron resonance ion sources." In: *J. Inst.* 6 (2011), P07010.

[42] M. Lieberman and A. Lichtenberg. "Theory of electron cyclotron resonance heating. II. Long time and stochastic effects." In: *Plas. Phys.* 15 (1973), p. 125.

[43] W. Lotz. "Electron-impact ionization cross-sections and ionization rate coefficients for atoms and ions from hydrogen to calcium." In: *Z. Phys.* 216 (1968), p. 241.

[44] C. Lyneis, D. Leitner, D. Todd, S. Virostek, T. Loew, A. Heinen, and O. Tarvainen. "Measurements of bremsstrahlung production and x-ray cryostat heating in VENUS." In: *Rev. Sci. Instrum.* 77 (2006), 03A302.

[45] G. Machicoane. Email to author. May 2018.

[46] G. Machicoane. Email to author. Jan. 2019.

[47] G. Machicoane, D. Cole, K. Holland, D. Leitner, D. Morris, D. Neben, and L. Tobos. "First results at 24 GHz with the superconducting source for ions (SuSI)." In: *Proc. ECRIS'14*. JACoW Conference Proceedings MOOMMH03. Nizhny Novgrod, Russia, 2014.

[48] G. Machicoane, D. Cole, J. Ottarson, J. Stetson, and P. Zavodszky. "ARTEMIS-B: A room-temperature test electron cyclotron resonance ion source for the National Superconducting Cyclotron Laboratory at Michigan State University." In: *Rev. Sci. Instrum.* 77 (2006), 03A322.

[49] G. Machicoane, M. Doleans, G. Humenik, F. Marti, P. Miller, M. Steiner, J. Stetson, X. Wu, and P. Zavodszky. "R&D effort at NSCL with the off-line ECR ion source ARTEMIS-B." In: *High Energ. Phys. Nuc.* 31.1 (2007), p. 187.

[50] G. Machicoane, H. Felice, J. Fogleman, R. Hafalia, G. Morgan, H. Pan, S. Prestmon, E. Pozdeyev, X. Rao, H. Ren, and L. Tobos. "Status of ECR ion sources for the Facility for Rare Isotope Beams (FRIB)." In: *Rev. Sci. Instrum.* 87 (2016), 02A743.

[51] P. Marchand and L. Marmet. "Binomial smoothing filter: A way to avoid some pitfalls of least-squares polynomial smoothing." In: *Rev. Sci. Instrum.* 54 (1983), p. 1034.

[52] M. Marttinen. "Transient sputtering method for estimating ion confinement times in ECRIS plasma." MA thesis. University of Jyväskylä, 2018.

[53] G. Melin, C. Barué, F. Bourg, P. Briand, J. Debernardi, M. Delaunay, R. Geller, A. Girard, K. Golovanivsky, D. Hitz, B. Jacquot, P. Ludwig, J. Mathonnet, T. Nguyen, L. Pin, M. Pontonnier, J. Rocco, and F. Zadworny. "Recent developments and future projects on ECR ion sources at Grenoble." In: *Proc. ECRIS'91*. Oak Ridge, TN, USA, 1991.

[54] G. Melin, F. Bourg, P. Briand, J. Debernardi, M. Delaunay, R. Geller, B. Jacquot, P. Ludwig, T. N'Guyen, L. Pin, M. Pontonnier, J. Rocco, and F. Zadworny. "Some particular aspects of the physics of the ECR sources for multicharged ions." In: *Rev. Sci. Instrum.* 61.1 (1990), p. 236.

[55] G. Melin, G. Drentje, A. Girard, and D. Hitz. "Ion behavior and gas mixing in electron cyclotron resonance plasmas as sources of highly charged ions." In: *J. Appl. Phys.* 86 (1999), p. 4772.

[56] V. Mironov, S. Bogomolov, A. Bondarchenko, A. Efremov, and V. Loginov. "Numerical simulations of gas mixing effect in electron cyclotron resonance ion sources." In: *Phys. Rev. Accel. Beams* 20 (2017), p. 013402.

[57] V. Mironov, S. Bogomolov, A. Bondarchenko, A. Efremov, and V. Loginov. "Simulations of charge-breeding processes in ECRIS." In: (2017). arXiv: `1706.07591`.

[58] V. Mironov, S. Bogomolov, A. Bondarchenko, A. Efremov, and V. Loginov. "Some aspects of electron dynamics in electron cyclotron resonance ion sources." In: (2017). arXiv: `1702.00237`.

[59] V. Mironov, O. Hohn, S. Runkel, L. Schmidt, G. Shirkov, K. Stiebing, H. Schmidt-Böcking, and A. Schempp. "Laser ablation plasma injeciton into the Frankfurt 14 GHz ECRIS." In: *Proc. ECRIS'99*. CERN/PS/99-52 EXT-2000-114. Geneva, Switzerland, 1999.

[60] A. Müller and E. Salzborn. "Scaling of cross sections for multiple electron transfer to highly charged ions colliding with atoms and molecules." In: *Phys. Lett.* 62A.6 (1977), p. 391.

[61] M. Niimura, A. Chutjian, S. Smith, M. Lamoureaux, A. Goto, and Y. Yano. "Physics and control of the afterglow HCI-beam pulsewidths for synchrotron and atomic physics." In: *Proc. PAC'01*. JACoW Conference Proceedings 2141. Chicago, IL, USA, 2001.

[62] J. Noland, J. Benitez, D. Leitner, C. Lyneis, and J. Verboncoeur. "measurement of radial and axial high energy x-ray spectra in electron cyclotron resonance ion source plasmas." In: *Rev. Sci. Instrum.* 81 (2010), 02A308.

[63] K. Ozeki, Y. Higurashi, J. Ohnishi, and T. Nakagawa. "Effect of biased disc on brightness of highly charged uranium ions from RIKEN 28 GHz superconducting electron cyclotron resonance ion source." In: *Jpn. J. Appl. Phys.* 52 (2013), p. 068001.

[64] T. Palchan, R. Pardo, F. Kondev, S. Kondrashev, C. Nair, R. Scott, R. Vondrasek, M. Paul, W. Bauder, P. Collon, G. Youinou, M. Salvatores, G. Palmotti, J. Berg, T. Maddock, and G. Imel. "Laser ablation of solids into an electron cyclotron resonance ion sources for accelerator mass spectroscopy." In: *Proc. HIAT'12*. JACoW Conference Proceedings TUC03. Chicago, IL, USA, 2010.

[65] *Pantechnik monogan M100*. www.pantechnik.com. Mar. 2013.

[66] V. Pastukhov. "Classical longitudinal plasma losses from open adiabatic traps." In: *Rev. Plas. Phys.* 13 (1984), p. 203.

[67] P. Patnaik. In: *Handbook of inorganic chemicals*. Ed. by K. McComb and D. Penikas. New York, USA: McGraw-Hill, 2002, p. 1086.

[68] C. Petty, D. Goodman, D. Smith, and D. Smatlak. "Physics of multiply charged oxygen in the Constance B Quadrupole Mirror." In: *J. Phys. Coll.* 50.C1 (1989), p. 783.

[69] D. Pozar. "Microwave engineering 4th ed." In: Hoboken, NJ, USA: John Wiley & Sons, 2012.

[70] *RIA Physics White Paper*. July 2000. URL: `https://fribusers.org/frib/docs/2000-DurhamWhitePaperRIAPhysics.pdf`.

[71] T. Rognlien and T. Cutler. "Transition from Pastukhov to collisional confinement in a magnetic and electrostatic well." In: *Nucl. Fusion* 20.8 (1980), p. 1003.

[72] T. Ropponen, D. Cole, G. Machicoane, A. Stolz, L. Sun, and L. Tobos. "Bremstrahlung and ion beam current measurements with SuSI ECR ion source." In: *Proc. ECRIS'10*. JACoW Conference Proceedings WECOAK04. Grenoble, France, 2010.

[73] T. Ropponen, O. Tarvainen, I. Izotov, J. Noland, V. Toivanen, G. Machicoane, D. Leitner, H. Koivisto, T. Kalvas, P. Peura, P. Jones, V. Skalyga, and V. Zorin. "Studies

of plasma breakdown and electron heating on a 14 GHz ECR ion source through measurement of plasma bremsstrahlung." In: *Plas. Sourc. Sci. Technol.* 20 (2011), p. 055007.

[74] T. Ropponen, O. Tarvainen, P. Suominen, T. Koponen, T. Kalvas, and H. Koivisto. "Hybrid simulation of electron cyclotron resonance heating." In: *Nucl. Instrum. Meth. Phys. Res. A* 587 (2008), p. 115.

[75] S. Runkel, O. Hohn, K. Stiebing, A. Schempp, H. Schmidt-Böcking, V. Mironov, and G. Shirkov. "Time resolved experiments at the Frankfurt 14 GHz electron cyclotron resonance ion source." In: *Rev. Sci. Instrum.* 71 (2000), p. 912.

[76] E. Rutherford. "The scattering of α and β particles by matter and the structure of the atom." In: *Philos. Mag.* 21.6 (1911), p. 669.

[77] M. Schlapp, R. Vondrasek, J. Szczech, P. Billquist, Z. Xie, R. Harkewicz, and R. Pardo. "A new 14 GHz Electron-Cyclotron-Resonance Ion Source (ECRIS) for the heavy ion accelerator facility atlas." In: *Proc. PAC'97*. JACoW Conference Proceedings 6W003. Vancouver, BC, Canada, 1997.

[78] K. Shepard, L. Bollinger, and R. Pardo. "The ATLAS positive ion injector." In: *Proc. LINAC'90*. JACoW Conference Proceedings WE102. Albuquerque, New Mexico, USA, 1990.

[79] G. Shirkov. "Electron and ion confinement conditions in the open magnetic trap of ECR ion source." In: *CERN Technical Report* PS-94-13 (1994), p. 1.

[80] G. Shirkov. "Techniques for the measurement of ionization times in ECR ion sources using a fast sputter sample and fast gas valve." In: *Plas. Sourc. Sci. Tchnol.* 2 (1993), p. 250.

[81] G. Shirkov. "The multiply charged ion production in ECR ion sources." In: *Rev. Sci. Instrum.* 63.4 (1992), p. 2894.

[82] G. Shirkov, C. Mühle, G. Musiol, and G. Zschornack. "Ionization and charge dispersion in electron cyclotron resonance ion sources." In: *Nucl. Instrum. Meth. Phys. Res. A* 302 (1991), p. 1.

[83] G. Shirkov and A. Philippov. "A computer model of particle balance in ECR ion sources." In: *Phys. Part. Nuclei Lett.* 5.7 (2008), p. 645.

[84] G. Shirkov and G. Zschornack. "Simulation of ion confinement in an ECR ion source under electron injection." In: *Nucl. Instrum. Meth. Phys. Res. B* 95 (1995), p. 527.

[85] M. Silva, S. Herdade, P. Lammoglia, P. Costa, and R. Terini. "Determination of the voltage applied to x-ray tubes from the bremsstrahlung spectrum obtained with a silicond PIN photodiode." In: *Med. Phys.* 27.11 (2000), p. 2617.

[86] J. Stetson. Email to author. June 2017.

[87] J. Stetson, G. Machicoane, P. Miller, M. Steiner, and P. Zavodszky. "Experimental studies of electrostatic and solenoidal focusing of low-energy, heavy-ion ECRIS beams at the NSCL/MSU." In: *Proc. LINAC'06*. JACoW Conference Proceedings TUP046. Knoxville, TN, USA, 2006.

[88] K. Stiebing, O. Hohn, S. Runkel, L. Schmidt, and H. Schmidt-Böcking. "Time resolved measurements of the biased disk effect at an electron cyclotron resonance ion source." In: *Phys. Rev. Accel. Beams* 2 (1999), p. 123501.

[89] L. Sun, H. Zhao, W. Lu, J. Guo, Y. Feng, W. Zhang, X. Zhang, Y. Yang, C. Qian, X. Fang, Z. Shen, W. Wu, L. Zhu, and L. Ma. "Intense beam production of highly charged ions by the superconducting ECR ion source SECRAL for heavy ion LINACS." In: *Proc. LINAC'16*. JACoW Conference Proceedings FR1A03. East Lansing, MI, USA, 2016.

[90] O. Tarvainen. "Studies of electron cyclotron resonance ion source plasma physics." PhD thesis. University of Jyväskylä, 2005.

[91] O. Tarvainen, I. Izotov, D. Mansfeld, V. Skalyga, S. Golubev, T. Kalvas, H. Koivisto, J. Komppula, R. Kronholm, J. Laulainen, and V. Toivanen. "Beam current oscillations driven by cyclotron instabilities in a minimum-B electron cyclotron resonance ion source plasma." In: *Plas. Sourc. Sci. Technol.* 23 (2014), p. 025020.

[92] O. Tarvainen, T. Ropponen, V. Toivanen, J. Ärje, and H. Koivisto. "Plasma breakdown diagnostics with the biased disc of electron cycotron resonance ion source." In: *Plas. Sourc. Sci. Tchnol.* 18 (2009), p. 035018.

[93] O. Tarvainen, T. Ropponen, V. Toivanen, T. Kalvas, J. Ärje, and H. Koivisto. "Diagnostics of plasma decay and afterglow transient of an electron cyclotron resonance ion source." In: *Plas. Sourc. Sci. Technol.* 19 (2010), p. 045027.

[94] O. Tarvainen, P. Suominen, and H. Koivisto. "A new plasma potential measurement instrument for plasma ion sources." In: *Rev. Sci. Instrum.* 75 (2004), p. 3138.

[95] K. Tinschert, J. Blosser, R. Lang, K. Langbein, H. Schulte, and P. Spädtke. "Investigation of the afterglow mode with the Caprice ECRIS for the GSI heavy-ion-synchotron operation." In: *Proc. ECRIS'99*. CERN/PS/99-52 EXT-2000-095. Geneva, Switzerland, 1999.

[96] K. Tinschert, R. Lannucci, J. Bossler, and R. Lang. "Experimental studies of the afterglow mode with xenon in a CAPRICE ECRIS." In: *Rev. Sci. Instrum.* 75.5 (2004), p. 1407.

[97] R. Vondrasek, R. Scott, R. Pardo, and D. Edgell. "Techniques for the measurement of ionization times in ECR ion sources using a fast sputter sample and fast gas valve." In: *Rev. Sci. Instrum.* 73.2 (2002), p. 548.

[98] R. Watson, D. Church, R. Tribble, L. Yang, B. Bandong, and T. Lotze. "Atomic physics with the Texas A&M ECR ion source." In: *Nucl. Instrum. Meth. Phys. Res. B* 56 (1991), p. 223.

[99] D. Whaley and W. Getty. "Ion temperature effects on ion charge-state distributions of an electron cyclotron resonant ion source." In: *Phys. Fluids B* 2.6 (1990), p. 1195.

[100] D. Wutte, M. Leitner, and C. Lyneis. "The Berkeley 88-inch cyclotron injector system." In: *Proc. EPAC'00*. JACoW Conference Proceedings THP6A02. Vienna, Austria, 2000.

[101] D. Xie, W. Lu, J. Benitez, C. Lyneis, and D. Todd. "Recent production of intense high charge ion beams with VENUS." In: *Proc. ECRIS'16*. JACoW Conference Proceedings THAO01. Busan, Korea, 2016.

[102] Z. Xie. "Production of highly charged ion beams from electron cyclotron resonance ion sources." In: *Rev. Sci. Instrum.* 69 (1998), p. 625.

[103] P. Zavodszky, B. Arend, D. Cole, J. DeKamp, G. Machicoane, F. Marti, P. Miller, J. Moskalik, W. Nurnberger, J. Ottarson, J. Vincent, X. Wu, and A. Zeller. "Design, construction and commissioning of the SuSI ECR." In: *Proc. PAC'07*. JACoW Conference Proceedings FRXAB03. Albuquerque, NM, USA, 2007.

[104] P. Zavodszky, B. Arend, D. Cole, J. DeKamp, G. Machicoane, F. Marti, P. Miller, J. Moskalik, J. Ottarson, J. Vincent, A. Zeller, and N. Kazarinov. "Status report on the design and construction of the Superconducting Source for Ions at the National Superconducting Cyclotron Laboratory/Michigan State University." In: *Rev. Sci. Instrum.* 77 (2006), 03A334.

[105] H. Zhao, L. Sun, J. Guo, W. Lu, D. Xie, D. Hitz, X. Zhang, and Y. Yang. "Intense highly charged ion beam production and operation with a superconducting electron cyclotron resonance ion source." In: *Phys. Rev. Accel. Beams* 20 (2017), p. 094801.